Marta Galbiati

Molecular Spintronics

From Organic Semiconductors to Self-Assembled Monolayers

Springer

Springer Theses

Recognizing Outstanding Ph.D. Research

Aims and Scope

The series "Springer Theses" brings together a selection of the very best Ph.D. theses from around the world and across the physical sciences. Nominated and endorsed by two recognized specialists, each published volume has been selected for its scientific excellence and the high impact of its contents for the pertinent field of research. For greater accessibility to non-specialists, the published versions include an extended introduction, as well as a foreword by the student's supervisor explaining the special relevance of the work for the field. As a whole, the series will provide a valuable resource both for newcomers to the research fields described, and for other scientists seeking detailed background information on special questions. Finally, it provides an accredited documentation of the valuable contributions made by today's younger generation of scientists.

Theses are accepted into the series by invited nomination only and must fulfill all of the following criteria

- They must be written in good English.
- The topic should fall within the confines of Chemistry, Physics, Earth Sciences, Engineering and related interdisciplinary fields such as Materials, Nanoscience, Chemical Engineering, Complex Systems and Biophysics.
- The work reported in the thesis must represent a significant scientific advance.
- If the thesis includes previously published material, permission to reproduce this must be gained from the respective copyright holder.
- They must have been examined and passed during the 12 months prior to nomination.
- Each thesis should include a foreword by the supervisor outlining the significance of its content.
- The theses should have a clearly defined structure including an introduction accessible to scientists not expert in that particular field.

More information about this series at http://www.springer.com/series/8790

Marta Galbiati

Molecular Spintronics

From Organic Semiconductors
to Self-Assembled Monolayers

Springer

Author
Dr. Marta Galbiati
Institute of Molecular Science
University of Valencia
Valencia, Paterna
Spain

Supervisors
Prof. Frédéric Petroff
Unité Mixte de Physique CNRS/Thales
University Paris-Sud
Palaiseau Cedex
France

Prof. Pierre Sénéor
Unité Mixte de Physique CNRS/Thales
University Paris-Sud
Palaiseau Cedex
France

Parts of this thesis have been published in the following journal articles:

- **Unveiling Self-Assembled Monolayers' Potential for Molecular Spintronics: Spin Transport at High Voltage**
  M. Galbiati, C. Barraud, S. Tatay, K. Bouzehouane, C. Deranlot, E. Jacquet, A. Fert, P. Seneor, R. Mattana, and F. Petroff
  Adv. Mater. 24, 6429 (2012); DOI: 10.1002/adma.201203136

- **Self-Assembled Monolayer-Functionalized Half-Metallic Manganite for Molecular Spintronics**
  S. Tatay, C. Barraud, M. Galbiati, P. Seneor, R. Mattana, K. Bouzehouane, C. Deranlot, E. Jacquet, A. Forment-Aliaga, P. Jegou, A. Fert, and F. Petroff
  ACS Nano 6, 8753 (2012); DOI: 10.1021/nn302458z

- **Spinterface: Crafting spintronics at the molecular scale**
  M. Galbiati, S. Tatay, C. Barraud, A. V. Dediu, F. Petroff, R. Mattana, and P. Seneor
  MRS Bull. 39, 602 (2014); DOI: http://dx.doi.org/10.1557/mrs.2014.131

- **Is spin transport through molecules really occurring in organic spin valves? A combined magnetoresistance and inelastic electron tunnelling spectroscopy study**
  M. Galbiati, S. Tatay, S. Delprat, H. Le Khanh, B. Servet, C. Deranlot, S. Collin, P. Seneor, R. Mattana, and F. Petroff
  Appl. Phys. Lett. 106, 082408 (2015); DOI: 10.1063/1.4913908

- **Recovering ferromagnetic metal surfaces to fully exploit chemistry in molecular spintronics**
  M. Galbiati, S. Delprat, M. Mattera, S. Mañas-Valero, A. Forment-Aliaga, S. Tatay, C. Deranlot, P. Seneor, R. Mattana, and F. Petroff
  AIP Adv. 5, 057131 (2015); DOI: 10.1063/1.4921241

- **Influence of alkylphosphonic acid grafting on the electronic and magnetic properties of $La_{2/3}Sr_{1/3}MnO_3$ surfaces**
  M. Galbiati, S. Tatay, S. Delprat, C. Barraud, V. Cros, E. Jacquet, F. Coloma, F. Choueikani, E. Otero, P. Ohresser, N. Haag, M. Cinchetti, M. Aeschlimann, P. Seneor, R. Mattana, and F. Petroff
  Appl. Surf. Sci. 353, 24–28, (2015); DOI: 10.1016/j.apsusc.2015.06.051

- **Self-Assembled Monolayers based spintronics: from ferromagnetic surface functionalization to spin-dependent transport**
  S. Tatay, M. Galbiati, S. Delprat, C. Barraud, K. Bouzehouane, S. Collin, C. Deranlot, E. Jacquet, P. Seneor, R. Mattana, and F. Petroff
  (submitted)

Supervisors' Foreword

Molecular or organic spintronics is an emerging research field at the frontier between organic chemistry and spintronics. This thesis targets this new field and more particularly the spin polarization tailoring opportunities which arise from the ferromagnetic metal/molecule hybridization at interfaces: the new concept of spinterface.

The manuscript is divided into three parts. The first one introduces the basic concepts of spintronics and advantages that molecules can bring to this field. A state of the art in organic and molecular spintronics is also given with a special emphasis on the physics and experimental evidence of spinterfaces. The second and third parts are dedicated to the two main experimental topics investigated in the thesis: self-assembled monolayers (SAMs) and organic semiconductors (OSCs). The study of SAMs-based magnetic tunnel nanojunctions reveals the potential to modulate "at will" the properties of such devices since each part of the molecule can be tuned independently as a "LEGO" building block. The study of Alq_3-based spin valves reveals magnetoresistance effects at room temperature and aims at understanding the respective roles of the two interfaces. Through the development of those systems, their potential for spintronics is demonstrated and gives a solid foundation towards spin polarization engineering at the molecular level.

Palaiseau Cedex
May 2015

Prof. Pierre Sénéor
Dr. Richard Mattana
Dr. Frédéric Petroff

Preface

Organic spintronics is an emerging research field at the frontier between organic chemistry and spintronics. Exploiting the peculiarity of these two fields, this young branch of spintronics presents a great potential combining the flexibility, versatility, and low production cost of organic materials with the nonvolatility, spin degree of freedom and beyond CMOS capabilities offered by spintronics. While the interest in organic materials was mainly initiated by the expected longer spin lifetime of spin polarized carriers, it has been recently unveiled that new spintronics tailoring opportunities, unachievable or unthinkable of with inorganic materials, could arise from the chemical versatility brought by molecules and molecular engineering. It was shown that the molecular structure, the local geometry at the molecule–electrode interface, and more importantly the ferromagnetic metal/molecule hybridization can strongly influence the interfacial spin properties. This makes organic systems highly promising for the envisaged possibility to engineer at molecular level the spintronic properties of these devices. The increasing attention towards these exciting effects has, during my Ph.D., resulted in the development of a new field called "spinterface," whose aim is to investigate the metal–molecule interface properties for spin polarization manipulation. The work of this thesis follows from the fascinating opportunities predicted and offered by spin hybridization and giving birth to the spinterface field.

This manuscript is divided into three parts. In the first one, a preliminary introduction to the basic concepts of spintronics and the advantages that molecules can bring to this field will be presented. A general state of the art in organic and molecular spintronics will be also reported and a special attention will be given to the physics and experimental evidence of spinterfaces.

The second and third parts of the manuscript will be dedicated to the two main experimental topics investigated during the thesis: self-assembled monolayers (SAMs) and organic semiconductors (OSCs).

The first experimental part will focus on the study of SAMs-based magnetic tunnel nanojunctions. We will see how this system looks like a promising candidate to modulate "at will" the properties of the device since each part of the molecule

can be tuned independently, as a "LEGO" barrier. Through the development of these systems we will demonstrate their validity for spintronics and set the bases towards the engineering of the spin polarization properties of spintronic devices at the molecular level.

The second experimental part will focus on the study of organic semiconductors spintronic devices, here Alq_3-based spin valves. We will investigate magnetoresistance (MR) effects at room temperature using conventional ferromagnetic (FM) materials. These investigations were done wishing to improve the understanding on the two interfaces and disentangle their contributions on the spin polarization properties of the devices.

Acknowledgments

First of all, I would like to thank all the members of the jury for having accepted to attend to my defense. I would also like to acknowledge A.F., F.N.V.D., and F.P. for having received me in their laboratory and for having allowed UMR being what it is today.

Most of my gratitude goes to my supervisors P.S. and R.M. that with their excellent scientific qualities and great humanity motivated me, taught me a lot, and they have always been ready to help and support me all along this thesis and afterwards. I really have no words to express my gratitude and admiration. Thanks!

Special thanks to F.P. for having been always there for any problem and having supported me all along this thesis. On Thales side, I would like to thank P.B. for his help, supervision, and support.

Also, a big thanks to all the people whose help, suggestions, and discussions contributed to the successful development of this thesis. Special thanks to S.T., K.B., C.D., and E.J. without whom this work would not have been possible.

More in general, I would really like to thank the entire UMR where everybody contributes to create its great environment, founded on team work and good humor that have made the work here a real pleasure.

To conclude, a big thanks also to my friends, close and far, who have been close to me during this adventure. A final special thanks to my family, especially to my parents, for being always there for me and having supported and encouraged me all along these years.

Contents

Part II   Self-Assembled Monolayers for Molecular Spintronics

Symbols

$6T$	Sexithienyl molecule
$\bar{\varphi}$	Mean value of the barrier height
β	Decay coefficient
β_0	Bias-independent decay coefficient
β_N	Decay coefficient expressed in C^{-1}
β_v	Bias-dependent decay coefficient
$\Delta E^{\uparrow(\downarrow)}$	Difference between molecular level energy and metal Fermi level for spin $\uparrow$ ($\downarrow$)
Δs	Barrier width at the Fermi level of the electrodes
$\delta\mu$	Shift of the chemical potential
$\delta\varepsilon_{R(L)}$	Spin-dependent shift contributions at the right (left) interface to the position ε_0 of the molecular level
ε	Vacuum permittivity
ε_r	Relative dielectric constant
η	Position of the level inside the organic barrier and takes into account the different weights of left and right electrodes at molecular level
Γ	Molecular energy level broadening
γ	Bias asymmetry
$\Gamma^{\uparrow(\downarrow)}$	Energy level broadening for spin $\uparrow$ ($\downarrow$)
$\Gamma_{R(L)}$	Contributions to the molecular level broadening at the right (left) interface
$\hbar$	Reduced Planck constant
μ	Carrier mobility
ω	Frequency of AC signal
$\sigma^{-(+)}$	Left (right) circularly polarized X-ray
τ	Lifetime of the molecular level
θ	Angle between the direction of the applied magnetic field and the device in the plane
$\varepsilon_{eff}^{\uparrow(\downarrow)}$	Effective molecular level energy for spin $\uparrow$ ($\downarrow$)
ε_0	Isolated molecular level energy

ε_{eff}	Effective molecular level energy when coupled to the surface
φ_0	Height of a rectangular potential barrier
AFM	Atomic force microscopy
Alq₃	Tris(8-hydroxyquinolinato)aluminum molecule
AMR	Anisotropic magnetoresistance
BLAG	Buffer layer assisted growth
C12P	Dodecyl-phosphonic acid molecule
CB	Conduction band
d	Length of the molecule
$D_{FM}^{\uparrow(\downarrow)}$	Density of states in a ferromagnetic metal for spin $\uparrow$ ($\downarrow$)
$D_{int}^{\uparrow(\downarrow)}$	Density of states at the ferromagnetic metal/molecule interface (effective electrode) for spin $\uparrow$ ($\downarrow$)
DOS	Density of states
e	Elementary charge
E_F	Fermi energy
FM	Ferromagnetic
FN	Fowler–Nordheim plot
GMR	Giant magnetoresistance
H	Magnetic field
h	Planck constant
HE	Hanle effect
HOMO	Highest occupied molecular orbital
I_P	Tunnel current in the parallel magnetic configuration of the device
I_{AP}	Tunnel current in the antiparallel magnetic configuration of the device
IBE	Ion beam etching
IETS	Inelastic electron tunneling spectroscopy
IPES	Inverse photoemission spectroscopy
IR	Infrared spectroscopy
IRRAS	Infrared reflection spectroscopy
J	Current density
JMR	Junction magnetoresistance
LAO	LaAlO
LSMO	$La_{0.7}Sr_{0.3}MnO_3$
LUMO	Lowest unoccupied molecular orbital
m_e	Free electron mass
MR	Magnetoresistance
MRAM	Magnetic random access memory
MTB	Multibarrier tunneling model
MTJs	Magnetic tunnel junctions
N	Number of carbon atoms
$N_L^{\uparrow(\downarrow)}$	Density of states of spin $\uparrow$ ($\downarrow$) at the Fermi level for the left electrode
$N_R^{\uparrow(\downarrow)}$	Density of states of spin $\uparrow$ ($\downarrow$) at Fermi level for the right electrode
$N_{\uparrow(\downarrow)}$	Density of states of spin $\uparrow$ ($\downarrow$) at Fermi level
NM	Nonmagnetic

NPs	Nanoparticles
OFETs	Organic field effect transistors
OLEDs	Organic light emitting diodes
OPVs	Organic photovoltaic cells
OSCs	Organic semiconductors
P	Spin polarization
P_{FM}	Spin polarization of the ferromagnetic metal
P_{int}	Spin polarization at the ferromagnetic metal/molecule interface
$P_{R(L)}$	Spin polarization of the right (left) electrode
Pc	Phthalocyanine molecule
PLD	Pulsed laser deposition
R_0	Contact resistance
$R_\perp$	Resistance corresponding to an orthogonal magnetization to the magnetic field
R_{AP}	Resistance of the device in the antiparallel magnetic configuration
R_{mol}	Resistance of the molecule
R_P	Resistance of the device in the parallel magnetic configuration
RA	Resistance area product
SAMs	Self-assembled monolayers
SMM	Single molecular magnet
$SP - PES$	Spin-polarized photoemission spectroscopy
$SP - STM$	Spin-polarized scanning tunneling microscope
SQUID	Superconducting quantum interference device
STO	SrTiO
SV	Spin Valve
TAMR	Tunneling anisotropic magnetoresistance
TB	Tunnel barrier
TEM	Transition electron microscopy
TEY	Total electron yield
TMR	Tunnel magnetoresistance
TVS	Transition voltage spectroscopy
UPS	Ultraviolet photoelectron spectroscopy
V	Bias voltage
V_t	Voltage transition between the direct tunneling regime and the FN conduction
$V_{1/2}$	Bias voltage at which the MR is reduced by a factor of two
$V_{d(a)}$	DC (AC) voltage applied to the junction
V_i	Image potential
VB	Valence band
XAS	X-ray absorption spectroscopy
XMCD	X-ray magnetic circular dichroism
XPS	X-ray photoelectron spectroscopy
ZBA	Zero-bias anomaly
ZMP	Zinc methyl phenalenyl molecule

Part I
Introduction to Organic and Molecular Spintronics

This first part of the manuscript is dedicated to a general introduction on the key concepts that later will allow to contextualize and understand the main results of this thesis.

In Chap. 1 we will start with an introduction on the basics of spintronics. In Chap. 2 we will briefly introduce the peculiarities of molecular systems and in particular the difference between organic and inorganic materials. Finally we will explore the advantages that organics could bring to spintronics field. In Chap. 3 we will present a general state of the art in organic and molecular spintronics fields and we will conclude with the description of interface spin polarization manipulation effects studied by spinterface field, whose investigation represents one of the main aims of this thesis.

Chapter 1
Introduction to Spintronics

Spintronics was born in 1988 with the discovery of GMR (Fig. 1.1a) provided simultaneously by A. Fert [1] and P. Grünberg [2] and rewarded in 2007 with the Nobel Prize in Physics. This field has since been largely exploited on the market, for example it has been at the base of every hard disk read head (Fig. 1.1b). These sensors consist of a stack of magnetic and non-magnetic layers that respond to the magnetic bits on the disk, which are as small magnets that point up (1) or down (0). The current through the stack is different depending on the orientation of the magnets (this effect is called GMR) and it allows the stored data to be read electronically using the spin-dependent interactions of the electrons. Many other devices based on spintronic effects are already on the market or in development. Some examples are the non-volatile magnetic random access memory (MRAM), "racetrack" memories, magnetic-field sensors, or even applications as quantum-computing [3–5].

Spintronics field is extremely active and interesting from both a fundamental point of view and for technological applications. Currently, with the aim at new functionalities there is an increased activity from materials research perspective to understand and develop spintronics devices using materials with new properties like carbon nanotubes, graphene, topological insulators and molecules.

In Sect. 1.1 we will start with the description of the electronic structure of ferromagnetic metals. In Sect. 1.2, we will present the principle of a basic spintronic device and finally, in Sect. 1.3, we will focus on magnetic tunnel junctions (MTJs) with a more detailed description of the tunneling magnetoresistance (TMR) effect proper to these systems.

1.1 Electronic Structure of Ferromagnetic Metals

1.1.1 Conduction in Ferromagnetic Metals

Contrarily to a normal metal (Fig. 1.2a), in a ferromagnetic (FM) metal the density of states (DOS) at the Fermi level is different for the spin up and the spin down directions
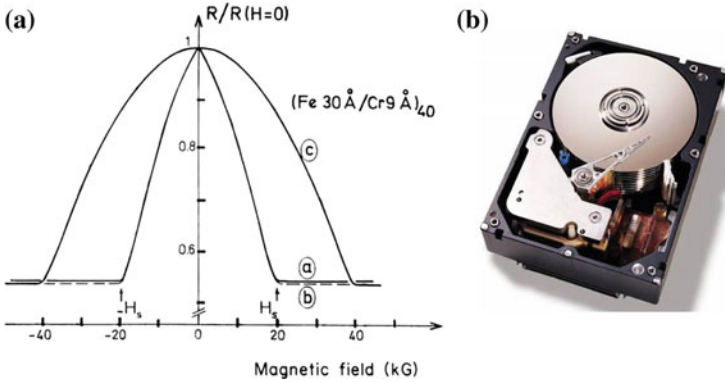
Fig. 1.1 **a** GMR effect measured in Fe/Cr multilayers by Baibich et al. [1]. Reprinted figure with permission from [1], copyright 1988 by the American Physical Society. **b** Inside view of a hard disk commercialized on the market. The working principle of these devices is based on the GMR effect
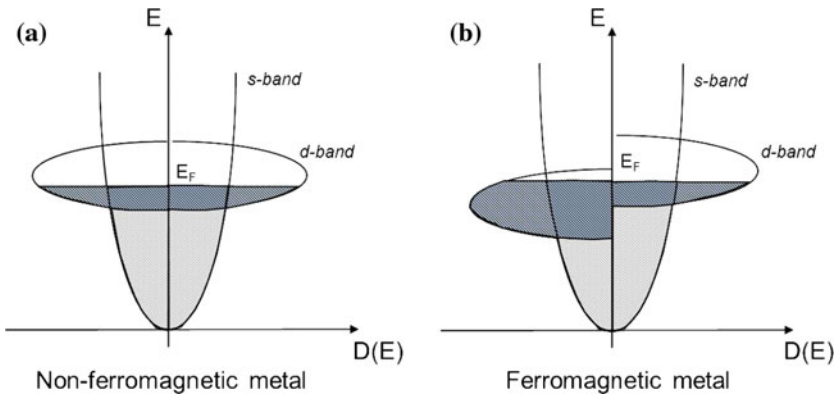
Fig. 1.2 Schematic representation of s and d bands **a** in a normal metal and **b** in a ferromagnetic metal. The DOS at the Fermi level is different for spin ↑ and ↓ in a FM metal. d-bands have a narrower bandwidth than s-bands and a higher contribution at the Fermi level. In a simple vision d-electrons are thus localized and responsible for magnetism, while s-electrons are delocalized and responsible for transport

(Fig. 1.2b). As one can see in the picture, in 3d-transition ferromagnetic metals such as Fe, Co or Ni, the d-bands lie close to the Fermi level and have smaller bandwidths than the delocalized s-bands. Due to the narrow bandwidth, the contribution of d-bands DOS at the Fermi level is higher. In a simplified vision we can consider that the electrical transport occurs via the delocalized s-band electrons, while magnetism is due to the d-bands. However, due to a significant s-d coupling at the Fermi energy, the conduction s-electrons become spin-polarized.

The spin polarization of a material expresses the imbalance between the populations of spin ↑ and ↓ at the Fermi level and it can be defined as:

$$P = \frac{N_\uparrow - N_\downarrow}{N_\uparrow + N_\downarrow} \qquad (1.1)$$

where $N_\uparrow$ and $N_\downarrow$ are the DOS of spin $\uparrow$ and $\downarrow$ at the Fermi level.

Typical spin polarization values for 3-d transition FM metals are 35 % for Co, 40 % for Fe and 23 % for Ni [6]. Some others ferromagnetic materials called "half-metals" also exist and one example is $La_{0.7}Sr_{0.3}MnO_3$ (LSMO) that will be used in our devices. In these materials the d-bands present only one spin direction at the Fermi level and hence their spin polarization is $\sim$100 %.

1.1.2 Spin Polarization Measurement

The spin polarization of a FM metal was measured for the first time in 1971 by P. Tedrow and R. Meservey [7]. These researchers discovered that in a super-conductor/tunnel barrier/FM metal device two different channels tunnel from the ferromagnetic metal through the tunnel barrier and could be associated to the two spin populations ($\uparrow$ and $\downarrow$). The two channels were highlighted by applying a strong magnetic field to the system and observing the split of spin population in the supercon-ductor Al layer due to the Zeeman effect. In Fig. 1.3a, b are illustrated the electronic
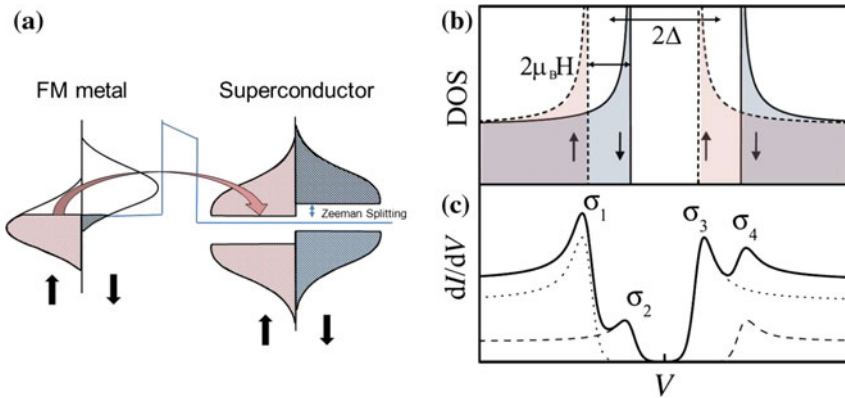
Fig. 1.3 **a** Schematic representation of the system with a superconductor electrode used by Meser-vey and Tedrow in their experiment to measure spin polarization. In the case represented in the picture only the majority spins can tunnel through the insulating barrier from the FM electrode to the superconductor one. This occurs since minority spin states present a gap at the Fermi level in the superconductor structure due to the Zeeman splitting. **b** Band structure of the superconductor electrode under the application of a magnetic field H on the junction plane. **c** Conductance mea-surement performed in the FM metal/insulator/superconductor system in (**a**). The different peaks correspond to the activation of the different spin channels in the system. The different contributions of spin up and down are represented in *dotted lines* and correspond to the bands represented in (**b**). Figure reprinted from [8] © IOP Publishing. Reproduced by permission of IOP Publishing. All rights reserved. Figure adapted from [9]

structure of the device with the peculiar BCS gap of the superconductor material. The superconductor electrode plays the role of a spin detector since the tunnel conduction between the two electrodes can take place only if the spins coming from the FM metal find an empty state with the same spin direction in the superconductor electrode. By changing the bias voltage, empty states of one or the other spin direction become available and the band structure is reflected on the conductivity peaks shown in Fig. 1.3c. These peaks correspond to the subsequent activation of spin ↑ and ↓ channels and their intensity reflects the different DOS at the Fermi level for spin ↑ and spin ↓ in the FM material. From this observation Tedrow and Meservey could define the spin polarization of the tunnel current as

$$P \sim \frac{(\sigma_4 - \sigma_2) - (\sigma_1 - \sigma_3)}{(\sigma_4 - \sigma_2) + (\sigma_1 - \sigma_3)} \simeq \frac{N_\uparrow - N_\downarrow}{N_\uparrow + N_\downarrow} \tag{1.2}$$

where $\sigma_1, \sigma_2, \sigma_3, \sigma_4$ are the peaks shown in Fig. 1.3c.

1.2 Principle of a Basic Spintronic Device

After having introduced the concept of spin polarization, we will see here how it can be exploited in a device. In Fig. 1.4 is shown the schematic representation of a basic spintronic device. It consists in a non-magnetic spacer embedded between two ferromagnetic electrodes. The first one is used as a spin injector, the spin polarized current is propagated along the non-magnetic spacer and finally detected by the second FM electrode. The detection occurs depending on the relative orientation of the magnetization direction of the two electrodes.

The typical curve expected in this kind of devices is represented in Fig. 1.5. When a large positive magnetic field is applied in the plane of the junction both FM electrodes are forced to point in the same direction (parallel configuration) and this results in a
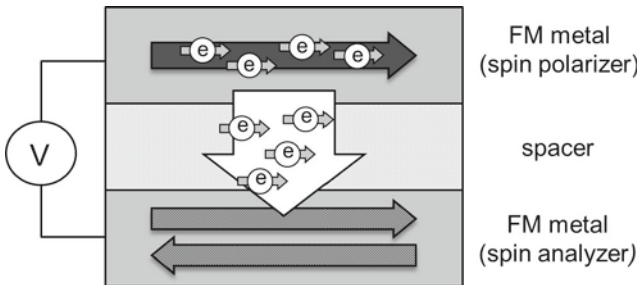
Fig. 1.4 Schematic representation of a basic spintronic device. The first FM electrode acts as a spin polarizer. Spin polarized current is transported through the spacer and it is finally detected by the second FM electrode
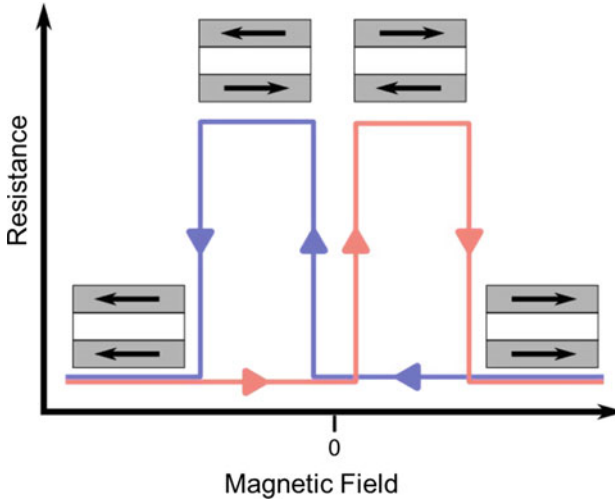
Fig. 1.5 Representation of a classical MR curve expected to be observed by sweeping the applied magnetic field on these spintronic devices. Depending on the relative orientation of the two electrodes magnetization there are two resistance states. One corresponding to the parallel configuration and the other corresponding to the antiparallel one

low resistance state. On the contrary, when decreasing the magnetic field below zero (blue curve), the electrode with the smallest coercive field switches its magnetization first, resulting in an antiparallel configuration and a high resistance state. The same process is repeated symmetrically in the other direction (red curve). The relative change of resistance between the parallel and antiparallel configurations is called *magnetoresistance (MR)* and it is defined as:

$$MR = \frac{R_{AP} - R_P}{R_P} \tag{1.3}$$

where R_{AP} and R_P are respectively the resistance of the device in the antiparallel and parallel magnetic configurations. The magnetoresistance phenomenon has revealed to be extremely useful for applications since it can be used as "0" and "1" states of a bit.

Depending on the nature and the thickness of the non-magnetic (NM) spacer we can have two kind of devices that behave as described before:

Spin valves: If the spacer consists of a NM conductor or semiconductor, the device is called a *spin valve* (SV) and the signal measured is *giant magnetoresistance* (GMR). This device is characterized by a current propagation through the NM layer. During the transport from one FM electrode to the other FM electrode, the spin polarization is gradually lost by spin flip events. This loss typically follows an exponential decay that is characterized by the spin diffusion length.

Magnetic tunnel junction: If the spacer consists of a thin insulating layer, the device is called *magnetic tunnel junction* (MTJ) and the signal measured is *tunnel magnetoresistance* (TMR). In this case there is no current propagation through the NM layer but a tunnel current flows directly between the two FM electrodes.

The principles of tunneling magnetoresistance will be described in more details in the following section since most of my work relates to magnetic tunnel junctions.

1.3 Tunnel Magnetoresistance

1.3.1 Jullière's Model

The first measurement of tunnel magnetoresistance was provided by M. Jullière in 1975 on a Fe/Ge(10–15 nm)/Co device [10]. His work was based on the one of Meservey and Tedrow but instead of the superconductor material, Jullière created a FM/tunnel barrier/FM junction then called "magnetic tunnel junction". With two FM electrodes he could exploit into a device the physical concept of spin polarized tunnel effect and he developed a model that is now widely known as *Jullière's model*.

A schematic example to understand TMR phenomenon is shown in Fig. 1.6. Jullière attributed the change of resistance in the parallel and antiparallel configurations to the fact that, due to the spin conservation during the tunnel process, electrons can only tunnel from a given spin sub-band in the first FM electrode to the same spin sub-band in the second FM electrode. Hence, when the two electrodes are in a parallel configuration the DOS for spin ↑ is present at the Fermi level in both electrodes and electrons can easily tunnel from one electrode to the other resulting in a low resistance. On the contrary, if the two electrodes are in the antiparallel configuration, spin ↑ are present at the Fermi level for the first electrode but there are no available states for this direction in the second electrode. Therefore, the current flow in the junction is lower due to the significant spin scattering at the interface and the device resistance is high.

The tunnel current in the parallel and antiparallel configurations as a function of the DOS of electrodes with spin ↑ and spin ↓ can be written as:

$$\begin{aligned} I_p &\propto N_L^\uparrow \cdot N_R^\uparrow + N_L^\downarrow \cdot N_R^\downarrow \\ I_{ap} &\propto N_L^\uparrow \cdot N_R^\downarrow + N_L^\downarrow \cdot N_R^\uparrow \end{aligned} \tag{1.4}$$

where the sum of the two terms in each equation corresponds to the two separate spin channels, with $N = N(E_F)$.

From these observations Jullière defined the tunnel magnetoresistance (TMR) as:

$$TMR = \frac{R_{AP} - R_P}{R_P} = \frac{I_P - I_{AP}}{I_{AP}} = \frac{2 P_R P_L}{1 - P_R P_L} \tag{1.5}$$
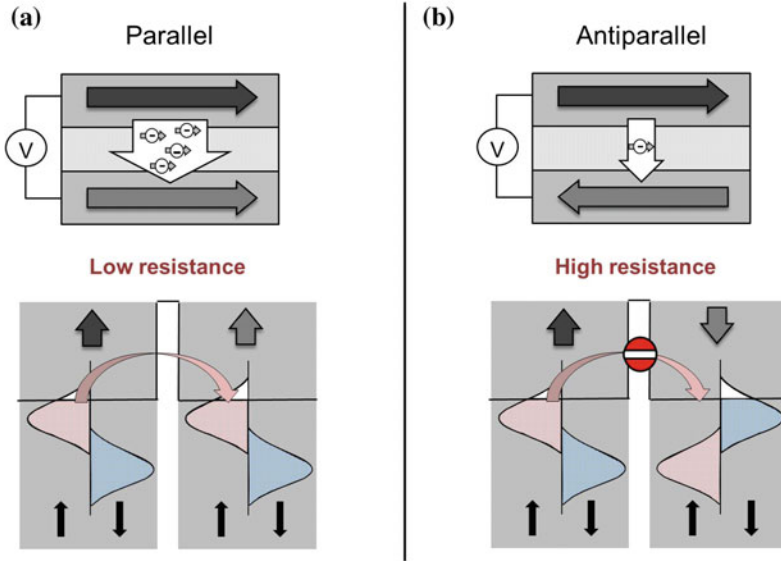
Fig. 1.6 Schematic description (*top*) and spin dependent DOS as a function of energy (*bottom*) for: **a** MTJ in the parallel configuration. Since spin ↑ states (DOS) are present at the Fermi level in both electrodes, spin ↑ electrons can easily tunnel and a large current flows through the tunnel barrier, corresponding to a low resistance state. **b** MTJ in the antiparallel configuration. Spin ↑ states (DOS) are present at the Fermi level in the first electrodes but there are not empty states for this channel in the second one. The resistance of the junction is high

where $P_{L(R)} = \dfrac{N^{\uparrow}_{L(R)} - N^{\downarrow}_{L(R)}}{N^{\uparrow}_{L(R)} + N^{\downarrow}_{L(R)}}$ is the spin polarization of the tunnel current for left (L) and right (R) electrode.

One important remark is that the sign of TMR effect depends on the product between the spin polarization of the two electrodes. Moreover we highlight that in this case the spin polarization is only dependent on the ferromagnetic metals, while we will see later that this is not exactly the case.

Although the Jullière's model gives a good basic insight, it cannot explain a number of experimental observations like the dependence on temperature, on bias voltage, on the tunnel barrier material or the height and width of the barrier. A model incorporating all these effects is still missing.

1.3.2 Development of Magnetic Tunnel Junctions

A turning point in the development of these devices arrived in 1995 when two important results were provided by J. Moodera [11] in CoFe/Al$_2$O$_3$/Co MTJs (Fig. 1.7a) [11] and by Miyazaki and Tezuka in Fe/Al$_2$O$_3$/Fe MTJs (Fig. 1.7b) [12]. Both groups fabricated MTJs with an Al$_2$O$_3$ tunnel barrier. The relevance of these results lies in
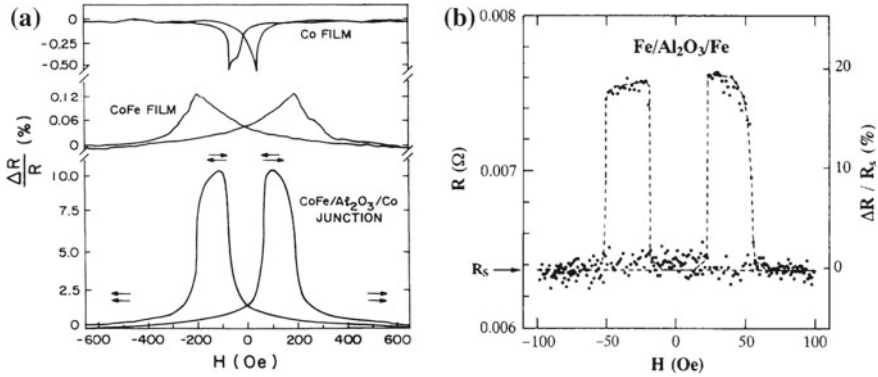
Fig. 1.7 a TMR curve recorded at room temperature in a CoFe/Al$_2$O$_3$/Co MTJ. Above the TMR curve are also represented the curves of anisotropic MR of the Co and CoFe layers. Reprinted figure with permission from [11], copyright 1995 from the American Physical Society. **b** TMR curve recorded at room temperature in Fe/Al$_2$O$_3$/Fe MTJ. Reprinted from [12], copyright 1995, with permission from Elsevier

the quite remarkable intensity of TMR effect (above 10 %) and, most important, the fact that the effect could be observed at room temperature. This improvement can be ascribed to the refinement of the quality of device interfaces with Al$_2$O$_3$ films with a better homogeneity, roughness and with a significant decrease in the number of defects in the junction.

These results gained a lot of attention and since then a large effort has been produced to achieve high MR in these devices. For example, one direction has been to go towards ferromagnetic electrodes with a higher spin polarization than 3d FM metals, such as LSMO, CrO$_2$ and Fe$_3$O$_4$ that present a spin polarization $\simeq$100 %.

The highest TMR value obtained with an Al$_2$O$_3$ barrier at room temperature is 70 % observed in a CoFeB/Al$_2$O$_3$/CoFeB MTJ [13]. Thanks to symmetry filtering, changing the amorphous Al$_2$O$_3$ tunnel barrier for crystalline MgO, much higher TMR values could be observed. Currently a TMR signal up to 600 % has been obtained at room-temperature in CoFeB/MgO/CoFeB MTJs [14] which has now made its way to hard disk read heads. We will see that such a large signal can not be simply explained by Jullière, revealing one first limitation of his model.

1.3.3 Characteristics of Tunnel Magnetoresistance, Beyond Jullière's Model

In this section we will present and discuss the most important features of TMR observed experimentally and that often can not be explained by a simple model. We will focus in particular on the TMR dependence on bias voltage, on temperature and on the material of the tunneling barrier.
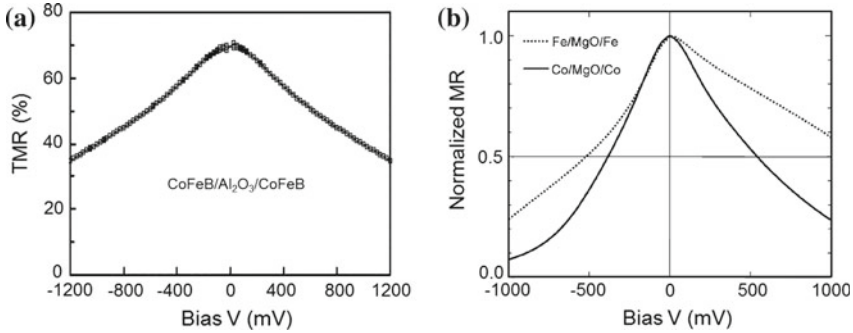
Fig. 1.8 TMR dependence with bias voltage measured in MTJs based on an Al_2O_3 (**a**) and MgO (**b**) barrier. Figure **a** reprinted from [13]. **b** Reprinted with permission from [15]. Copyright 2006, AIP Publishing LLC

Voltage and temperature dependence: In most of the MTJs the TMR magnitude is observed to drop by applying an increasing bias voltage.

In Fig. 1.8 are reported examples of MTJs made using Al_2O_3 and MgO barriers. As one can note, in such devices the TMR effect is generally maximum at zero bias and it decreases in an almost symmetric way when increasing the positive or negative applied bias.

The suppression of TMR with bias voltage is a critical feature when operating MTJ devices. One figure of merit in this regard is $V_{1/2}$ that corresponds to the voltage at which the TMR is reduced by a factor of two. In the first works on MTJs this value reached a bias of only few mV. Later, with the improving of the barrier control, this value could be increased to 300–600 mV for an Al_2O_3 barrier and sometimes even higher than 1 V for a well optimized MgO barrier.

The phenomena governing the V dependence of TMR are still unclear, however several mechanisms have been proposed to describe it. The most common ones ascribe the cause of TMR decreasing to the magnon excitation at the ferromagnetic/insulator interface, to defects and impurity states in the barrier region or to the density of states.

Concerning magnon hypothesis, it has been generally observed in MTJs that both the conductances in parallel and anti-parallel configurations strongly deviate from the parabolic law at low bias voltage, as shown in Fig. 1.9. This behaviour is called "Zero-Bias Anomaly" (ZBA) and was explained by Zhang et al. [16] and Bratkovsky [17] with the opening of an inelastic tunnel channel due to magnon excitations at the ferromagnet/insulator interface. At non-zero bias, electrons can tunnel and can loose part of their energy by emitting a magnon in any of the FM electrodes which in turn flips their spin. When increasing the bias voltage more magnons can be emitted resulting in the reduced TMR values. It is also expected that this excitation has a linear variation with bias voltage until it reaches a threshold value in the 100 mV range (which is FM material dependent) where all the modes are saturated [16].

Fig. 1.9 Resistance as a
function of bias voltage at
T = 4.2 K for parallel and
antiparallel magnetization
configurations of the two
electrodes in a
$Co/Al_2O_3/CoFe$ junctions.
The drop in resistance for
V < 150 mV is referred to as
the zero bias anomaly
(ZBA). Reprinted figure with
permission from [16].
Copyright 1997 by the
American Physical Society
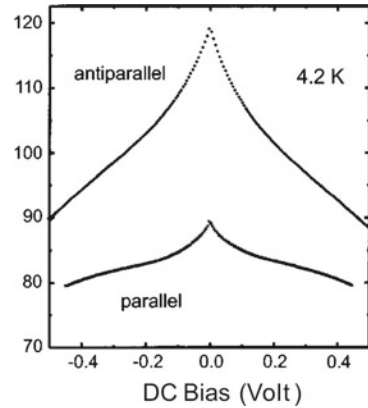
On the other hand, another hypothesis suggests that the voltage drop in TMR
could be due to localized trap states in the amorphous barrier [18–20]. This had
been proposed after a work was published where a spin-polarized scanning tunneling
microscope (SP-STM) was used to study TMR in a MTJ formed by the ferromagnetic
STM tip, a Co electrode and vacuum as a "perfect" insulating barrier. Despite this
system does not prevent the excitation of magnons, no variation in TMR was reported
up to ±0.9 V. For this reason it was concluded that most of the voltage dependence
is probably not related to magnon excitations at the interface but due to impurities.

Another feature of TMR that caught a strong attention both from the fundamental
point of view as well as for device applications is the TMR dependence with temper-
ature. This occurs since the possibility to have devices working at room temperature
plays a key role for their industrial development.

A typical behaviour is shown in Fig. 1.10a and in general in every MTJ it is
observed that TMR decreases with increasing temperature. The cause of this phe-
nomenon is mainly ascribed to electron-magnon scattering at the barrier interface
[21]. At higher temperature, the Fermi distribution of the tunneling electrons is broad-
ened and allows electrons with higher energy to tunnel across the barrier. For this
reason the TMR decreasing with temperature has been ascribed to similar contribu-
tions than the bias ones.

All these effects can be reinforced at the interface such as in the case of LSMO
where the breaking of symmetry at the interface leads to a different behaviour of the
surface to the bulk material. For example, this explains the faster decreasing of the
surface magnetization in LSMO as shown in Fig. 1.10b [22, 23].

Influence of the barrier: It is important to remark that, contrarily to what was
predicted by Jullière's model, in a MTJ the spin polarization of the tunnelling current
is different from the global DOS of the electrodes and it depends on the insulating
barrier.
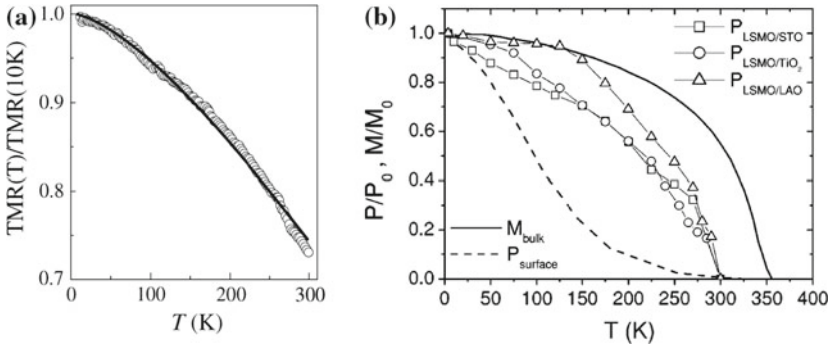
Fig. 1.10 a Temperature dependence of TMR for a Co/Al$_2$O$_3$/Co MTJ (*circles*) and a fit to the model of Shang et al. [21] (*solid line*). Figure reprinted from [8] © IOP Publishing. Reproduced by permission of IOP Publishing. All rights reserved. **b** Temperature dependence of the LSMO surface spin polarization and the spin polarization in LSMO/SrTiO$_3$(STO), LSMO/LaAlO$_3$(LAO) and LSMO/TiO$_2$ bilayers. The drop of the surface spin polarization with temperature is faster than the bulk one thus meaning a different behaviour between the surface and bulk of a magnetic material. Reprinted figure with permission from [22]. Copyright 2004 by the American Physical Society

For example, the DOS found by spin polarization of field-emitted electrodes in FM metals as Co or Ni [24], determined a negative sign for the spin polarization of these materials. On the contrary, experiments similar to the ones performed by Meservey and Tedrow through the Al$_2$O$_3$ barrier always determined a positive spin polarization for materials as Co, Ni, Fe and CoFe [6].

These observations raised a first question on the spin polarization sign of the TMR effect.

A turning point in this regard arrived in 1999 with a work presented by de Teresa et al. [25] where authors compared results on three different MTJs based on LSMO and Co electrodes. LSMO is a half-metal and its spin polarization is positive. In this way it was used to probe the spin polarization of Co when coupled to different insulating barriers. In Fig. 1.11 are shown the results for LSMO/tunnel barrier/Co junctions with Al$_2$O$_3$, SrTiO$_3$ (STO) and STO/Al$_2$O$_3$ tunnel barriers. As one can see, a positive or negative TMR signal was observed in these junctions formed by identical FM materials as electrodes. Knowing that spin polarization of LSMO is always positive, how can it be explained that the spin polarization of Co is sometimes positive and sometimes negative?

This phenomenon can be better understood if we look at the calculated DOS for d and s bands of Co. In Fig. 1.12a are shown the d bands of Co. They are localized, large at the Fermi level and shifted for spin up and down due to the exchange interaction that is at the origin of magnetism. One peculiarity of Co is that the d band for the majority electrons (spin ↑) is almost fully filled and hence almost zero at the Fermi level, while the band for the minority electrons (spin ↓) prevails at the Fermi level. This results in a globally negative spin polarization of the Co metal.
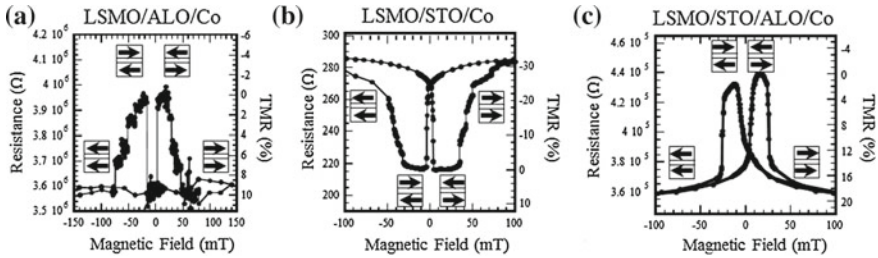
Fig. 1.11 TMR curves in MTJs with an Al$_2$O$_3$ (**a**), STO (**b**) and STO/Al$_2$O$_3$ barrier. These junctions have the same electrodes but different sign of TMR and they can not be explained by Jullière's model. Figure reprinted from [25]
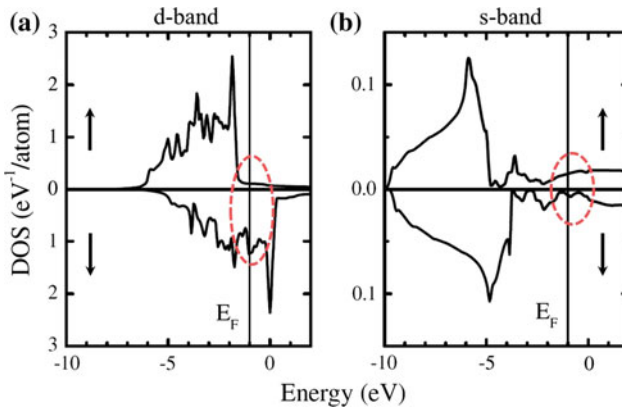
Fig. 1.12 DOS for bulk fcc Co projected to the *d* orbitals (**a**) and the *s* orbitals (**b**). The minority electrons population is larger at the Fermi level in d-bands but it is the opposite for the s-bands. Figure reprinted from [8] © IOP Publishing. Reproduced by permission of IOP Publishing. All rights reserved

On the contrary, in Fig. 1.12b is shown the DOS of *s* bands of Co. As described in Sect. 1.1, in this case bands are delocalized, narrow at the Fermi level and almost not shifted. The "s" electrons are mainly responsible for transport. In *s* bands at the Fermi level the spin ↑ population is nearly higher than the spin ↓ one. However, for what concerns the global spin polarization of Co material the "d$_↓$" electrons are still more numerous and they prevail on the total effect. A similar phenomenon is also observed in others ferromagnetic materials as Ni, CoFe or NiFe.

Based on these observations de Teresa and co-authors studied the hybridization of the interface states between the tunnel barrier and the Co electrode of their junctions as shown in Fig. 1.13. They explained the different TMR sign in LSMO/tunnel barrier/Co magnetic tunnel junctions by the fact that, depending on the hybridization between the tunnel barrier and the ferromagnetic metal, different states could be selected. Following their results, in the case of an Al$_2$O$_3$ barrier the *s* states of Co would be selected (Fig. 1.13b) and, since they are positively polarized, this results in
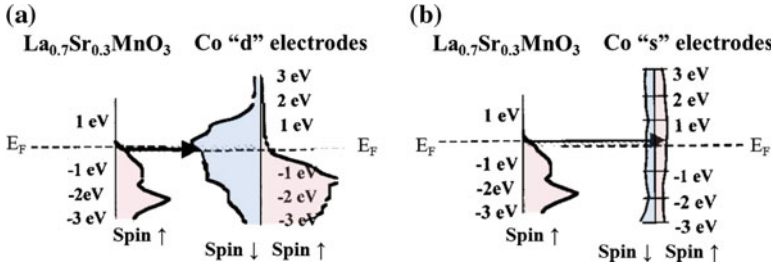
Fig. 1.13 Explanation of the different TMR sign found in LSMO/STO/Co and LSMO/STO/Al$_2$O$_3$/Co MTJs by de Teresa et al. [25]. **a** STO/Co interface would select *d*-bands of Co resulting in a negative spin polarization. **b** Al$_2$O$_3$/Co interface would select *s*-bands of Co resulting in a positive spin polarization. Figure reprinted from [25]

a positive TMR signal. On the contrary, in the case of a STO barrier the *d* states of Co would be selected and this explains the negative sign of a Co/STO/LSMO junction.

Crystalline symmetry filtering: Another very important effect highlighting the convoluted role of the ferromagnet and the tunnel barrier was observed in MgO based MTJs. This time the effect of the barrier was the spin filtering of the FM orbital, leading to an increase of the TMR signal. As shown in Fig. 1.14a, giant values above 200 % could be reported for example in Fe/MgO/Fe MTJs [26, 27]. This effect can not be explained by Jullière's model but its cause must be searched in symmetry filtering effects of the MgO barrier [28]. Indeed, theoretical calculations predicted that the different orbital symmetries at the Fermi level of the Fe (001) electrode, which correspond to the different hybridizations ($\Delta_1(spd)$, $\Delta_2(d)$, $\Delta_5 (sp)$), are not attenuated in the same way by the MgO(001) barrier. In Fig. 1.14b is shown the calculated symmetry dependent attenuation in a Fe/MgO/Fe MTJ. As one can see, symmetry Δ_1 is the less attenuated in the barrier. If we look at the band structure of Fe (001) represented in Fig. 1.14c, one can see that symmetry Δ_1 presents a half-metallic structure since only $\Delta_{1\uparrow}$ band is at the Fermi level while $\Delta_{1\downarrow}$ is well above it. Hence, the spin polarization of this symmetry is 100 %. If we now consider again the different symmetry attenuations in MgO, it becomes clear that a sufficiently thick MgO barrier can lead to a filtering effect where almost only the Δ_1 is transmitted, thus allowing a simple FM such as Fe to be transformed into an almost "half-metal". This filtering effect is at the base of very high TMR signals up to 600 % observed at room temperature in the case of a CoFeB/MgO/CoFeB MTJ [14].

In conclusion, we have seen here how TMR can be affected by the tunneling barrier in inorganic devices. These effects are beyond Jullière's model and highlight the necessity to refine it. Indeed, instead of talking about the spin polarization of the electrode, we have seen that it is necessary to talk at least about the *spin polarization of the FM metal/tunnel barrier interface*.
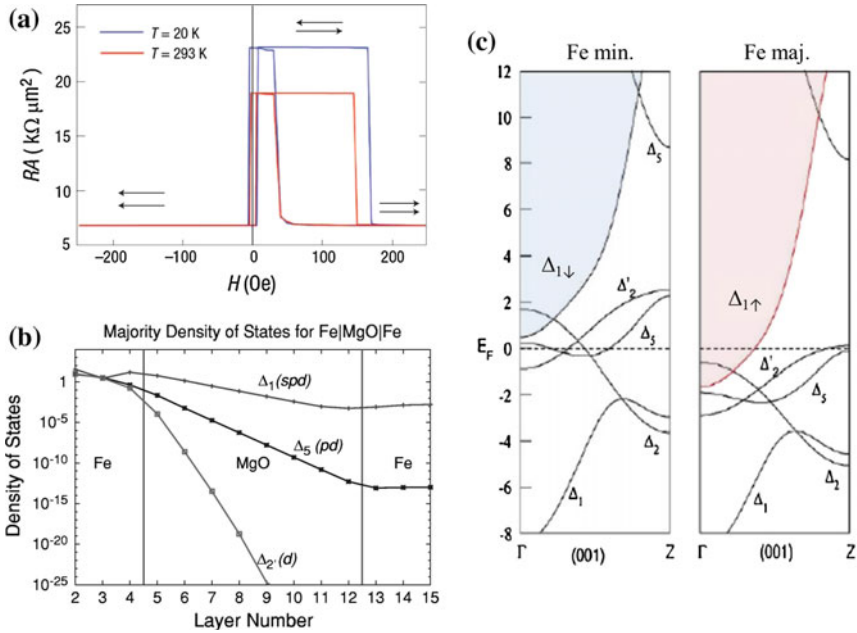
Fig. 1.14 **a** TMR curves measured in a Fe/MgO/Fe junction at 20 K (*blue*) and 293 K (*red*) where a signal up to 180 % can be observed at this temperature. Reprinted by permission from Macmillan Publishers Ltd: Nature Materials [27], copyright 2004. **b** Fe DOS attenuation in a MgO barrier for the different symmetries Δ_1, Δ_5 and Δ_2. At the interface with the second Fe electrode several orders of magnitude in transmission separate the different symmetries highlighting the filtering effect of the MgO barrier. Reprinted figure with permission from [28]. Copyright 2001 by the American Physical Society. **c** Density of states of Fe for the different symmetries. Δ_1 symmetry presents a half-metallic behaviour with only spin up at the Fermi level. Since this symmetry is the less filtered from the MgO barrier, this effect results in an artificially enhanced spin polarization (color figure online)

References

1. M.N. Baibich, J.M. Broto, A. Fert, F.N.V. Dau, F. Petroff, P. Etienne, G. Creuzet, A. Friederich, J. Chazelas, Giant magnetoresistance of (001)Fe/(001)Cr magnetic superlattices. Phys. Rev. Lett. **61**(21), 2472–2475 (1988)
2. G. Binasch, P. Grunberg, F. Saurenbach, W. Zinn, Enhanced magnetoresistance in layered magnetic structures. Phys. Rev. B **39**(7), 4828–4830 (1989)
3. C. Chappert, A. Fert, F. Nguyen Van Dau, The emergence of spin electronics in data storage. Nat. Mater. **6**, 813–823 (2007)
4. I. Žutić, S. Das Sarma, Spintronics: fundamentals and applications. Rev. Mod. Phys. **76**, 323–410 (2004)
5. S.A. Wolf, D.D. Awschalom, R.A. Buhrman, J.M. Daughton, S. von Molnár, M.L. Roukes, A.Y. Chtchelkanova, D.M. Treger, Spintronics: a spin-based electronics vision for the future. Science **294**, 1488–1495 (2001)
6. J.S. Moodera, G. Mathon, Spin polarized tunneling in ferromagnetic junctions. J. Magn. Magn. Mater. **200**, 248–273 (1999)

7. P.M. Tedrow, R. Meservey, Spin-dependent tunneling into ferromagnetic nickel. Phys. Rev. Lett. **26**, 192–195 (1971)

8. E.Y. Tsymbal, O.N. Mryasov, P.R. LeClair, Spin-dependent tunnelling in magnetic tunnel junctions. J. Phys. Condens. Matter **15**, R109–R142 (2003)

9. R. Meservey, P.M. Tedrow, Spin-polarized electron tunneling. Phys. Rep. **238**(4), 173–243 (1994)

10. M. Julliere, Tunneling between ferromagnetic films. Phys. Lett. A **54**(3), 225–226 (1975)

11. J.S. Moodera, L.R. Kinder, T.M. Wong, R. Meservey, Large magnetoresistance at room temperature in ferromagnetic thin film tunnel junctions. Phys. Rev. Lett. **74**, 3273–3276 (1995)

12. T. Miyazaki, N. Tezuka, Spin polarized tunneling in ferromagnet/insulator/ferromagnet junctions. J. Magn. Magn. Mater. **151**, 403–410 (1995)

13. D. Wang, C. Nordman, J. Daughton, Z. Qian, J. Fink, 70 % TMR at room temperature for SDT sandwich junctions with CoFeB as free and reference layers. IEEE Trans. Magn. **40**, 2269–2271 (2004)

14. S. Ikeda, J. Hayakawa, Y. Ashizawa, Y.M. Lee, K. Miura, H. Hasegawa, M. Tsunoda, F. Matsukura, H. Ohno, Tunnel magnetoresistance of 604 % at 300 K by suppression of Ta diffusion in CoFeB/MgO/CoFeB pseudo-spin-valves annealed at high temperature. Appl. Phys. Lett. **93**(8), 082508 (2008)

15. S. Yuasa, A. Fukushima, H. Kubota, Y. Suzuki, K. Ando, Giant tunneling magnetoresistance up to 410 % at room temperature in fully epitaxial Co/MgO/Co magnetic tunnel junctions with bcc Co(001) electrodes. Appl. Phys. Lett. **89**, 042505 (2006)

16. S. Zhang, P.M. Levy, A.C. Marley, S.S.P. Parkin, Quenching of magnetoresistance by hot electrons in magnetic tunnel junctions. Phys. Rev. Lett. **79**, 3744–3747 (1997)

17. A.M. Bratkovsky, Assisted tunneling in ferromagnetic junctions and half-metallic oxides. Appl. Phys. Lett. **72**, 2334–2336 (1998)

18. J. Zhang, R.M. White, Voltage dependence of magnetoresistance in spin dependent tunneling junctions. J. Appl. Phys. **83**, 6512 (1998)

19. R. Jansen, J.S. Moodera, Influence of barrier impurities on the magnetoresistance in ferromagnetic tunnel junctions. J. Appl. Phys. **83**, 6682 (1998)

20. R. Jansen, J. Moodera, Magnetoresistance in doped magnetic tunnel junctions: effect of spin scattering and impurity-assisted transport. Phys. Rev. B **61**, 9047–9050 (2000)

21. C. Shang, J. Nowak, R. Jansen, J. Moodera, Temperature dependence of magnetoresistance and surface magnetization in ferromagnetic tunnel junctions. Phys. Rev. B **58**, R2917–R2920 (1998)

22. V. Garcia, M. Bibes, A. Barthélémy, M. Bowen, E. Jacquet, J.-P. Contour, A. Fert, Temperature dependence of the interfacial spin polarization of $La_{2/3}Sr_{1/3}MnO_3$. Phys. Rev. B **69**, 052403 (2004)

23. J.-H. Park, E. Vescovo, H.-J. Kim, C. Kwon, R. Ramesh, T. Venkatesan, Magnetic properties at surface boundary of a half-metallic ferromagnet $La_{0.7}Sr_{0.3}MnO_3$. Phys. Rev. Lett. **81**(9), 1953 (1998)

24. G. Chrobok, M. Hofmann, G. Regenfus, R. Sizmann, Spin polarization of field-emitted electrons from Fe Co, Ni, and rare-earth metals. Phys. Rev. B **15**(1), 429–440 (1977)

25. J.M. De Teresa, Role of metal-oxide interface in determining the spin polarization of magnetic tunnel junctions. Science **286**, 507–509 (1999)

26. S.S.P. Parkin, C. Kaiser, A. Panchula, P.M. Rice, B. Hughes, M. Samant, S.-H. Yang, Giant tunnelling magnetoresistance at room temperature with MgO (100) tunnel barriers. Nat. Mater. **3**(12), 862–867 (2004)

27. S. Yuasa, T. Nagahama, A. Fukushima, Y. Suzuki, K. Ando, Giant room-temperature magnetoresistance in single-crystal Fe/MgO/Fe magnetic tunnel junctions. Nat. Mater. **3**, 868–871 (2004)

28. W. Butler, X.-G. Zhang, T. Schulthess, J. MacLaren, Spin-dependent tunneling conductance of Fe/MgO/Fe sandwiches. Phys. Rev. B **63**, 054416 (2001)

Chapter 2
Why Bring Organic and Molecular Electronics to Spintronics

In the previous chapter we introduced few spintronic concepts that will allow to understand the effects observed in this work. Before starting the discussion on the organic spintronics field, a brief introduction on organic and molecular electronics and the specificities of molecules is also necessary to understand the advantages that these systems can bring to spintronics.

2.1 Introduction to Organic and Molecular Electronics

Since the '70s the electronic properties of organic materials have raised an increasing interest in the scientific community. While organics were traditionally considered insulating, in 1977 A.J. Heeger, A. MacDiarmid and H. Shirakawa [1] discovered the possibility to dope a polymer and make it semiconductor. This discovery opened a new conception of organic materials and the idea to replace classical silicon with organic semiconductors to fabricate low cost electronic components arose. The important discovery of conductive polymers was rewarded in 2000 with the Nobel prize in Chemistry and nowadays this research field is called **organic electronics**. Products based on active thin-film organic devices are already in the market place and other devices are being developed. Some examples are the very bright and colourful thin displays based on organic light emitting diodes (OLEDs), the organic photovoltaic cells (OPVs) for low-cost solar energy generation and the organic field effect transistors (OFETs). This technology sets great promise for the near future with an entirely new generation of *ultralow-cost*, *lightweight* and *flexible* electronic devices. An example is shown in Fig. 2.1a.

Another highly promising branch of organic systems is **molecular electronics**: looking at the ultimate downscaling for behind CMOS and relating to the study of devices formed by single or few molecules. This field was born in 1971 when B. Mann and H. Kuhn measured the tunnel current through an insulating molecule with the objective to study its electronic properties [3]. In 1974 M. Ratner and A. Aviram proposed a method to make a rectifier based on a single organic molecule
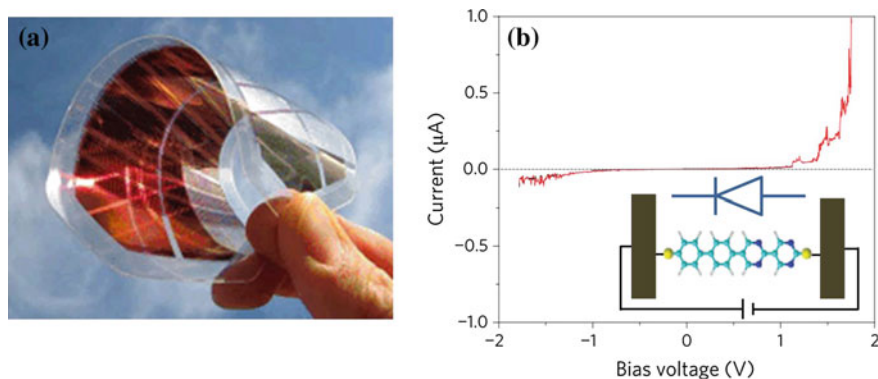
Fig. 2.1 **a** Example of flexible organic photovoltaic cell. **b** Example of a molecular rectifier formed by a non-symmetric dipyrimidinyl-diphenyl molecule bound to two electrodes. In the graph is represented the typical I–V characteristic. A schematic of the device and its electrical equivalent are represented in the inset. Adapted by permission from Macmillan Publishers Ltd: Nature Chemistry [2], copyright 2009

[4]. Their work sets the basis to the idea that, if it is possible to link the chemical structure of a molecule to its electrical behaviour, it must be potentially possible to replace every electric component with the appropriate molecule. One example of molecular rectifier device is shown in Fig. 2.1b. The possibility to replace an electrical component with one single molecule could represent a final *miniaturization* for devices. For these reasons molecular electronics is often proposed as a candidate to overcome the possible downscaling limitations in silicon. Very interestingly, since the electrical properties of organic molecules can be altered by molecular design and synthesis, this offers in theory unlimited possibilities for technological development of functional devices based on the properties of a single molecule.

The *versatility* of chemistry is thus one strong advantage since it is relatively simple from a chemical point of view to change properties from one molecule to the other with just very small variations.

2.2 Main Difference Between Organic and Inorganic Materials

To understand the key advantages brought by molecules to organic spintronics, it is important to remark the substantial difference that exists between an organic and inorganic material, as represented in Fig. 2.2.

While inorganic materials are formed by a continuum of states and electrons are delocalized within the bands (Fig. 2.2a), organics are composed by discrete levels (Fig. 2.2b). Every level is associated to a molecular orbital that can be strongly localized on a group or bond of the molecule, or delocalized on the whole (or large part)
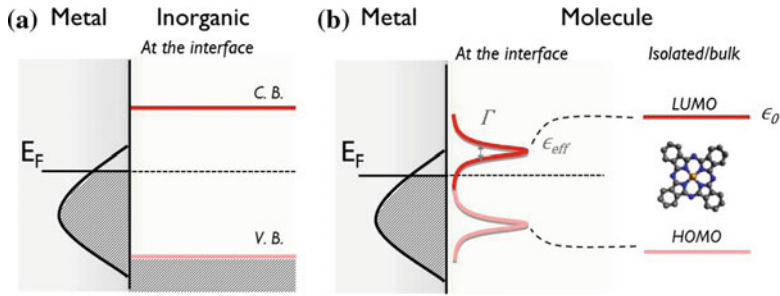
Fig. 2.2 Schematic representation of **a** the interface between a metal and an inorganic material such as a semiconductor or insulator versus **b** what happens when an isolated molecule is brought in proximity with a metallic surface. For simplicity, a flat band configuration is used for the semiconductor in the first few nanometers from the interface. As opposed to the inorganic materials, molecules present discrete levels. When interacting with the metal, the initial discrete levels of the isolated molecule broaden and shift relative to the density of states of the metal. Reference [5], reproduced with permission

of it. The two orbitals that are involved in the charge transport are the "Highest Occupied Molecular Orbital" (HOMO) and the "Lowest Unoccupied Molecular Orbital" (LUMO) that are separated by a "gap". These orbitals can be compared to the valence and conduction bands of inorganic semiconductors. In the case of inorganic materials electrons are delocalized on the crystal and give rise to bands, while this is mainly not the case in a molecule.

2.2.1 Behaviour at the Interface

Let see now what happens when a molecule, from isolated, is brought in proximity to a metal. First we consider a discrete and isolated molecular level, for example the LUMO of Fig. 2.2b. Being isolated, the lifetime of this state is infinite, and its energy ε_0 is precisely known (the time-energy equivalent to the Heisenberg uncertainty principle). But, what happens to this at an interface in a device? When brought in proximity to a metallic electrode, the initially isolated molecular level gets progressively hybridized by coupling with the many states of the metal. This leads to two main effects:

- the lifetime (τ) of the molecular level becomes finite since the charge has a certain probability to escape to the metal. As a consequence, the energy δE is no more completely defined, resulting in the level **energy broadening** with a finite width $\Gamma \approx \hbar/\tau$ which, in the first approximation, is proportional to the density of states (DOS) of the metal. Depending on the strength of the interaction this broadening can range from below the meV up to the eV range [6].

- an **energy shift** of the molecular level from the initial position of the isolated molecule ε_0 to the final ε_{eff} one also results from the interaction with the metal. This shift is dependent on the metal DOS and includes, among other contributions, the combined effects of interfacial dipoles or image forces [7].

2.2.2 Electronic Properties of Molecules

We will briefly review here some ideas about the main features of transport properties through isolated molecules and molecules organized in a thin layer.

Isolated Molecule

We start by considering the simple case of an isolated molecule. The properties of a molecule depend on its chemical structure and on the energy position of its orbitals. For example, in the case of an alkane and alkene chain, the different electronic properties of the two molecules depend on the orbital hybridization of carbon atoms.

In Fig. 2.3a is shown the structure of an alkane chain which is insulating. Carbon atoms present an hybridization sp^3 and their σ orbitals are bonded to two neighbour carbons and to two hydrogen atoms. As shown in Fig. 2.3b, the σ orbitals of two carbons are frontally overlapped and they form a node on each carbon atom which prevents the electron delocalization on the whole chain. The molecule is thus insulating and the HOMO-LUMO gap has been calculated and experimentally measured [8] to be around 8–9 eV. Since the orbital overlap is too weak, gap value is not expected to change a lot with the chain length of the molecule.

On the contrary, one example of semiconductor molecule is an alkene chain (Fig. 2.4a) where carbon atoms present an hybridization sp^2. Here the three σ orbitals are bonded to two neighbour carbons and one hydrogen atom, while the p_z orbital out of plane overlaps with the neighbouring p_z orbitals (Fig. 2.4b). This overlap results in the formation of π-bonds that allow a delocalization of the π-electrons along the molecule. This leads to the formation of two thin energy bands. The delocalized electrons occupy the bonding π-orbitals, while the anti-bonding π-orbitals remain
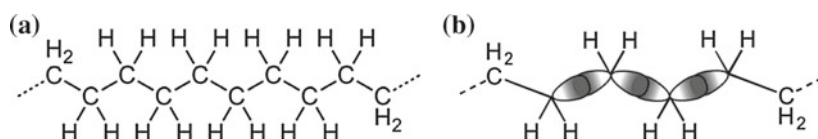
Fig. 2.3 **a** Structure of an alkane chain. Carbon atoms present an hybridization sp^3 and they are bonded one to each other through σ orbitals. **b** This forms a node on each carbon and prevents electron delocalization, making the molecule insulating
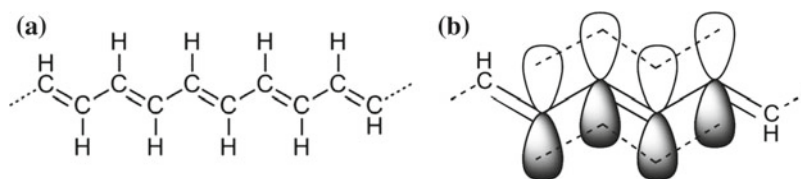
Fig. 2.4 **a** Structure of an alkene chain. Carbon atoms present an hybridization sp^2. They form σ-bonds with the adjacent carbons and the p_z orbital out of plane overlaps with the neighbouring p_z orbitals **b** allowing the delocalization of electrons on the molecule. This makes the molecule to be semiconductor

empty. The gap for these molecules is smaller than the saturated chain and its value is about 1–3 eV. Moreover, since the orbitals are overlapped, in this case the value of the gap is expected to change with the length of the molecule.

Molecular Layer

We will see now what happens if molecules are grouped to form a thin molecular layer. Molecules can be organized in an amorphous, polycrystalline or crystalline phase depending on the deposition conditions. They interact each other through Van der Waals interactions and this assures the layer cohesion. Van der Waals forces that exist between molecules are weaker than covalent or ionic bondings, that are typical of inorganic crystals, and this is the cause of the lower rigidity of molecules in comparison to inorganic materials.

Moreover, the orbital overlap between adjacent molecules is often weak and it prevents (or almost prevents) the electrons delocalization on more molecules. Depending on the orbital overlapping there can be two conduction regimes: (i) *band transport* when the overlap between π-orbitals is strong enough to allow the delocalization of charges in an energy band formed by a quasi-continuum of states (Fig. 2.5a). (ii) *Hopping transport* where charges jump from one localized state of a molecule to another (Fig. 2.5b).
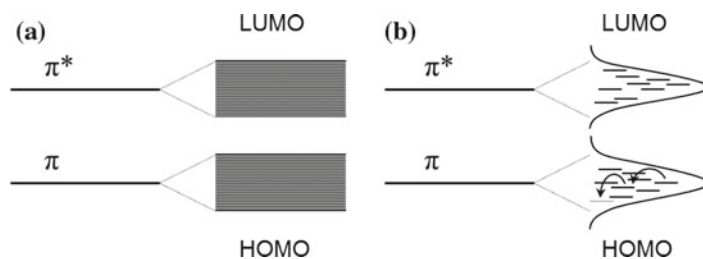
Fig. 2.5 **a** Representation of the structure for band transport. If the overlap between molecules is strong enough, the overlap of bonding and anti-bonding π orbitals leads to the formation of energy bands formed by a quasi-continuum of states. **b** Representation of the structure for hopping transport. In an amorphous material disorder leads to a dispersion of localized states. Transport occurs by hopping and it is assisted by phonons

Depending on the molecule itself, its interactions and defects (as dopants…), it is possible to find molecules with every characteristic: insulators, semiconductors, metallic and even superconductors.

However, in reality no many molecules behave as a metallic or semiconducting inorganic crystal with band transport such as TTF-TCNQ [9] but the majority of molecules presents a hopping transport. This is often due to an amorphous organisation of the molecules and the weak interaction between them. The charge hopping between localized sites can be described by phonon assisted tunneling. One example of semiconductor molecule behaving like this is the largely used Alq_3.

The weak orbital overlap is also at the origin of the low charge mobility that is usually find in organic materials. Normal values are between $10^{-6} - 10^{-3}$ $cm^2/V \cdot s$ (for example charge mobility in Alq_3 is $\mu_e = 1.4 \times 10^{-6} cm^2/V \cdot s$ [10]). The limit value between hopping transport and band transport is normally fixed around $1 cm^2/V \cdot s$ [11]. Examples of high mobility molecules are rubrene ($10 cm^2/V \cdot s$) [12] or C8-BTBT [13] with a record mobility around $43 cm^2/V \cdot s$. To compare, mobility values usually found in inorganic semiconductors as Si are $\mu_e \approx 1500 cm^2/V \cdot s$ and $\mu_h \approx 500 cm^2/V \cdot s$.

In conclusion, we have seen in this section that the different structure between an organic material, formed by discrete levels instead of a continuum of states, and an inorganic one, leads to fundamental differences. These can be summarized with:

(i) an energy shift and broadening of the molecular states at the interface with a metal.

(ii) weak Van der Waals interactions resulting in a transport in the bulk material mainly governed by charges hopping, leading to a lower mobility of molecules in comparison to inorganics. But, as a counterpart, the weak Van der Waals interactions are also at the base of molecules flexibility properties.

We will see in the next section how some of these characteristics give rise to specific advantages for organic spintronics that are not achievable with inorganic materials.

2.3 Advantages of Organic and Molecular Materials for Spintronics

Organic spintronics is a very recent and promising field that combines the potential of chemistry to the non-volatility and the spin degree of freedom of spintronics towards electronics for beyond CMOS applications.

From the merging of these two domains the main advantages of organic spintronics can be resumed in three baselines:

- The first advantages are the ones of organic electronics vs. classical electronics. They can be resumed in the potentiality to implement *flexible*, *low production cost* and *large area easy-processing* electronics.
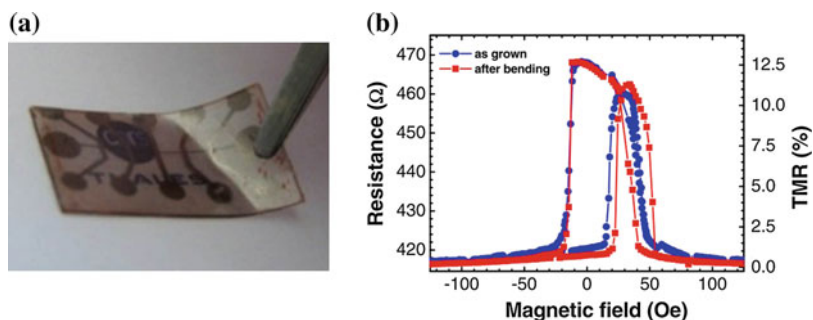
Fig. 2.6 **a** Picture of a flexible Co/Al$_2$O$_3$/Co MTJ grown on a polyester organic substrate. **b** TMR curves recorded before and after the device bending. No difference could be recorded in the signal demonstrating that bending is not damaging the device. Reprinted with permission from [14]. Copyright 2010, AIP Publishing LLC

The possibility to combine spintronic devices with flexible substrates was first proposed in 1992 [15] and has been already demonstrated with prototype devices [16–19].

For example, in Fig. 2.6 is shown a Co/Al$_2$O$_3$/Co magnetic tunnel junction grown on a polyester organic substrate [14]. After twisting and bending the MTJs, the TMR signal is maintained unchanged. This indicates that spin dependent tunneling properties are preserved and demonstrates that MTJs based spintronic devices are compatible with embodied flexible organic electronics.

- One of the main advantages that initially attracted much of the attention to organic materials is their expected *longer spin lifetime* [20, 21]. At the origin of this effect is the low spin-orbit coupling due to the low-weight atoms from which organic materials are composed of (spin-orbit coupling scales with Z^4, where Z is the atomic number). Moreover, hyperfine interactions are also weak in organic materials since transport mainly occurs through π-orbitals and the spin of mobile carriers is weakly sensible to spins of the nuclear atoms of the molecule. As a consequence, the spin of a carrier weakly interacts in the organic environment and the spin information can be potentially maintained for a long time. For these materials, spin lifetimes in the µs range and higher have been predicted [22] and deduced by experiments [23]. To compare, the typical spin lifetime in an inorganic metal or semiconductor is in the *ps* range or maximum *ns* range.

  This property of organic materials could be exploited for spin manipulation into molecules and for the spin transport. However, spin transport has to face with the drawback of low carrier mobility presented by most of the organic materials (normally $\mu \simeq 10^{-5}-10^{-2}$ cm^2/V·s) that limits the spin diffusion length to some tens of nanometers. Very interesting materials in this regard are carbon nanotubes and graphene that present a high mobility around 10^4 cm^2/V·s and where long spin diffusion lengths >100 µm could be measured [24].

- Finally, it has been recently unveiled that new spintronics tailoring opportunities, unachievable or unthinkable with inorganic materials could arise from the chemical versatility brought by molecules and molecular engineering. It has been
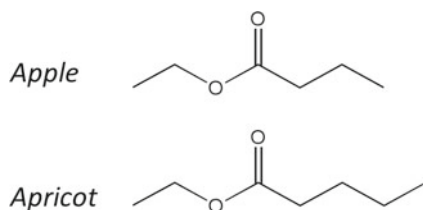
Fig. 2.7 Chemical structure of the molecule responsible for **a** apple flavour and **b** apricot flavour. The difference of just a carbon atom in the molecule leads to completely different properties

shown that spin-polarized hybridization at the ferromagnetic metal/molecule interface can drastically influence the spin transport properties of molecular spintronic devices and provide new functionalities beyond that of conventional inorganic ones. Indeed, the interface hybridization can be used to tune the spin polarization and thus the spintronic device properties [25].

As already remarked before, chemistry is extremely *versatile* and it is possible to find molecules with all the functionalities of inorganic materials. The choice of molecules is unlimited and molecules present very reach functionalities as optical switchers or molecular magnets. It is also relatively simple from a chemical point of view to change properties from one molecule to the other. One example is reported in Fig. 2.7 where adding just one C atom, the molecule changes from the flavour of apple to the one of apricot. Hence, thanks to chemistry versatility it is possible to envisage the possibility to *engineer at the molecular level* the spintronic properties of the devices.

All these advantages motivated an increasing interest in the field of organic spintronics. However, this field not only combines the advantages of the two domains that it fusions but also, unfortunately, their technological problems. For example from spintronics it gets the high sensitivity to interfaces, while from molecular electronics it gets the difficulty to fabricate contacts on molecules. All these points will be described more in details later in the manuscript. In the next section we will start by briefly presenting the state of the art in organic spintronics.

References

1. C.K. Chiang, C.B. Fincher, J.Y.W. Park, A.J. Heeger, H. Shirakawa, E.J. Louis, S.C. Gau, A.G. MacDiarmid, Electrical conductivity in doped polyacetylene. Phys. Rev. Lett. **39**(17), 1098–1101 (1977)
2. I. Díez-Pérez, J. Hihath, Y. Lee, L. Yu, L. Adamska, M.A. Kozhushner, I.I. Oleynik, N. Tao, Rectification and stability of a single molecular diode with controlled orientation. Nat. Chem. **1**, 635–641 (2009)
3. B. Mann, H. Kuhn, Tunneling through fatty acid salt monolayers. J. Appl. Phys. **42**, 4398–4405 (1971)
4. A. Aviram, M.A. Ratner, Molecular rectifiers. Chem. Phys. Lett. **29**(2), 277–283 (1974)
5. M. Galbiati, S. Tatay, C. Barraud, A.V. Dediu, F. Petroff, R. Mattana, P. Seneor, Spinterface: crafting spintronics at the molecular scale. MRS Bull. **39**, 602–607 (2014)

6. H. Vazquez, R. Oszwaldowski, P. Pou, J. Ortega, R. Pérez, F. Flores, A. Kahn, Dipole formation at metal/PTCDA interfaces: role of the charge neutrality level. EPL (Europhys. Lett.) **65**(6), 802 (2004)

7. M.L. Perrin, C.J.O. Verzijl, C.A. Martin, A.J. Shaikh, R. Eelkema, J.H. van Esch, J.M. van Ruitenbeek, J.M. Thijssen, H.S.J. van der Zant, D. Dulić, Large tunable image-charge effects in single-molecule junctions. Nat. Nanotechnol. **8**, 282–287 (2013)

8. C. Boulas, J. Davidovits, F. Rondelez, D. Vuillaume, Suppression of charge carrier tunneling through organic self-assembled monolayers. Phys. Rev. Lett. **76**, 4797–4800 (1996)

9. M. Cohen, L. Coleman, A. Garito, A. Heeger, Electrical conductivity of tetrathiofulvalinium tetracyanoquinodimethan (TTF) (TCNQ). Phys. Rev. B **10**, 1298–1307 (1974)

10. R.G. Kepler, P.M. Beeson, S.J. Jacobs, R.A. Anderson, M.B. Sinclair, V.S. Valencia, P.A. Cahill, Electron and hole mobility in tris(8-hydroxyquinolinolato-N1, O8) aluminum. Appl. Phys. Lett. **66**, 3618 (1995)

11. G. Horowitz, Organic field-effect transistors. Adv. Mater. **10**, 365–377 (1998)

12. C. Reese, Z. Bao, High-resolution measurement of the anisotropy of charge transport in single crystals. Adv. Mater. **19**, 4535–4538 (2007)

13. Y. Yuan, G. Giri, A.L. Ayzner, A.P. Zoombelt, S.C.B. Mannsfeld, J. Chen, D. Nordlund, M.F. Toney, J. Huang, Z. Bao, Ultra-high mobility transparent organic thin film transistors grown by an off-centre spin-coating method. Nat. Commun. **5**, 3005 (2014)

14. C. Barraud, C. Deranlot, P. Seneor, R. Mattana, B. Dlubak, S. Fusil, K. Bouzehouane, D. Deneuve, F. Petroff, A. Fert, Magnetoresistance in magnetic tunnel junctions grown on flexible organic substrates. Appl. Phys. Lett. **96**, 072502 (2010)

15. S.S.P. Parkin, K.P. Roche, T. Suzuki, Giant magnetoresistance in antiferromagnetic Co/Cu multilayers grown on kapton. Jpn. J. Appl. Phys. **31**(9A), 1246–1249 (1992)

16. S.S.P. Parkin, Flexible giant magnetoresistance sensors. Appl. Phys. Lett. **69**(20), 3092–3094 (1996)

17. F. Yan, G. Xue, F. Wan, A flexible giant magnetoresistance sensor prepared completely by electrochemical synthesis. J. Mater. Chem. **12**, 2606–2608 (2002)

18. T. Uhrmann, L. Bär, T. Dimopoulos, N. Wiese, M. Rührig, A. Lechner, Magnetostrictive GMR sensor on flexible polyimide substrates. J. Magn. Magn. Mater. **307**(2), 209 (2006)

19. A. Bedoya-Pinto, M. Donolato, M. Gobbi, L.E. Hueso, P. Vavassori, Flexible spintronic devices on Kapton. Appl. Phys. Lett. **104**, 062412 (2014)

20. D.R. McCamey, H.A. Seipel, S.Y. Paik, M.J. Walter, N.J. Borys, J.M. Lupton, C. Boehme, Spin Rabi flopping in the photocurrent of a polymer light-emitting diode. Nat. Mater. **7**, 723–728 (2008)

21. C.G. Yang, E. Ehrenfreund, Z.V. Vardeny, Polaron spin-lattice relaxation time in pi-conjugated polymers from optically detected magnetic resonance. Phys. Rev. Lett. **99**, 157401 (2007)

22. S. Sanvito, A.R. Rocha, Molecular-spintronics: the art of driving spin through molecules. J. Comput. Theor. Nanosci. **3**, 624–642 (2006)

23. V.I. Krinichnyi, S.D. Chemerisov, Y.S. Lebedev, EPR and charge-transport studies of polyaniline. Phys. Rev. B **55**(24), 16233 (1997)

24. B. Dlubak, M.-B. Martin, C. Deranlot, B. Servet, S. Xavier, R. Mattana, M. Sprinkle, C. Berger, W.A. De Heer, F. Petroff, A. Anane, P. Seneor, A. Fert, Highly efficient spin transport in epitaxial graphene on SiC. Nat. Phys. **8**, 557–561 (2012)

25. C. Barraud, P. Seneor, R. Mattana, S. Fusil, K. Bouzehouane, C. Deranlot, P. Graziosi, L. Hueso, I. Bergenti, V. Dediu, F. Petroff, A. Fert, Unravelling the role of the interface for spin injection into organic semiconductors. Nat. Phys. **6**, 615–620 (2010)

Chapter 3
State of the Art in Organic and Molecular Spintronics

3.1 Introduction to Organic and Molecular Spintronics

Organic spintronics was born in 2002 with the pioneer work presented by the group of C. Taliani and A.V. Dediu [1] on a lateral LSMO/sexithienyl (6T)/LSMO junction (Fig. 3.1a). In this work authors investigated the MR dependence on the channel length at room temperature. MR values up to 30 % could be recorded for a channel of 140 nm, while the effect disappeared for channels above 250 nm (Fig. 3.1b).

Since the two electrodes were the same, MR could not be measured by the independent switching of their magnetization but it had to be deduced by the resistance change in the junction between zero and strong magnetic field. In reality, it is not easy to directly link the resistance change upon the application of a magnetic field to a MR effect that corresponds to the spin injection, propagation and detection in the parallel and antiparallel magnetic states. In any case, this remains a fundamental work for the domain since it linked for the first time the spintronic and organic chemistry community estimating a spin relaxation time in this system in the order of 1 μs.

A second fundamental work was presented by the group of Z.V. Vardeny [3] in 2004 where for the first time MR could be observed in a vertical organic spin valve formed by LSMO/Alq_3(130 nm)/Co (Fig. 3.2a). Alq_3 is an organic semiconductor largely used in OLEDs and the thickness of the nominal barrier in this study was 130 nm. As shown in Fig. 3.2b, a negative magnetoresistance of −40 % could be observed at low temperature (11 K). The low resistance state can be identified as the antiparallel magnetic configuration between the two electrodes, while the high resistance state as the parallel one. The effect was also observed to vanish at T > 200 K.

Many works succeeded in this direction with the study of vertical spin valves. In a first time the attention was mainly focused on the study of long spin lifetime properties of organic materials and the investigation was centred on the spin injection, propagation and detection in organic spin valves, trying to understand the mechanisms affecting spin-related phenomena and improving performances. In this regard
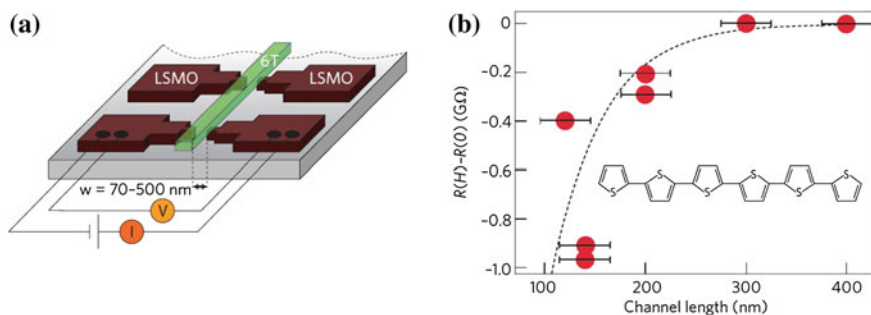
Fig. 3.1 **a** Schematic structure of a lateral LSMO/6T/LSMO junction. The length of the organic channel can vary from 70 to 500 nm. **b** MR effect calculated as the difference between the device resistance subjected to a strong magnetic field and at zero magnetic field. The molecule of sexithiophene is also represented in the picture. Reprinted by permission from Macmillan Publishers Ltd: Nature Materials [2], copyright 2009, adapted from [1]
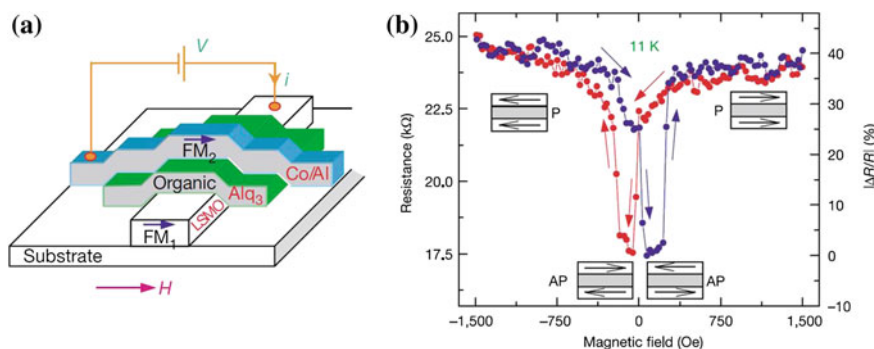
Fig. 3.2 **a** Schematic structure of a vertical LSMO/Alq$_3$/Co OSV. **b** MR curve measure in a LSMO/Alq$_3$ (130 nm)/Co junction at 11 K. Reprinted by permission from Macmillan Publishers Ltd: Nature [3], copyright 2004

many works have been performed using Alq$_3$ organic semiconductor to compare with Vardeny's group measurements [4–8]. A more detailed discussion on results obtained in devices based on this molecule will be treated in Chap. 7.

In the meanwhile the spin transport through some other molecules has been also investigated. We will not enter here in the details but the interested reader can find more informations in reviews or thesis works as [2, 9, 10]. For example, some work exist on Rubrene [11–13], C$_{60}$ [14–19], 6T [2], α-NPD [20], CuPc [21], perylene derivatives [22, 23], pentacene [24, 25], BF3 [26] and TPP [4]. Some studies have been also performed on polymers: P3HT [27, 28] and PPV [29]. A general trend that emerges from all these studies is a positive or negative MR signal with a magnitude often <30 %. One exception is represented by polymers where a magnetoresistance up to 80 % could be recorded at low temperature [30]. A behaviour with bias voltage and temperature similar to the one described in Sect. 1.3 is generally reported. MR
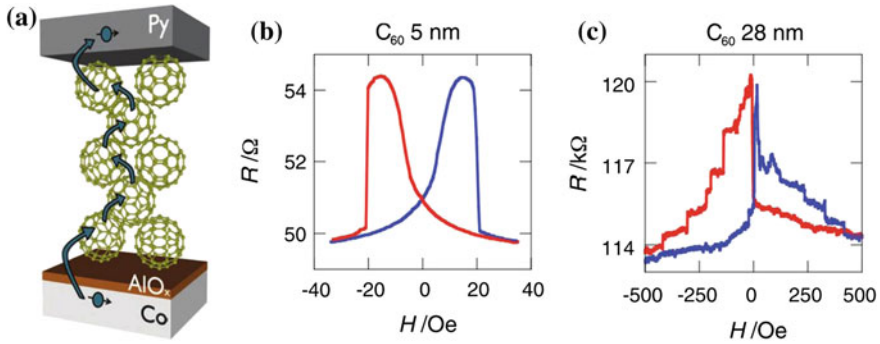
Fig. 3.3 **a** Schematic representation of a Co/Al$_2$O$_3$/C$_{60}$/Py OSV. **b** MR signal observed at room temperature in a Co/Al$_2$O$_3$/C$_{60}$/Py OSV with a C$_{60}$ thickness of 5 nm and **c** 28 nm. Reprinted with permission from [15], copyright 2011

signal decreases with increasing bias and it usually completely disappears below 1 V. MR signal also decreases with increasing temperature and often it completely vanishes well below room temperature. In conclusion, despite different molecules have been investigated, up to now no one really emerges among the others.

Nowadays a big effort is focused on the achievement of clear MR signal at room temperature in OSVs in order to be able to exploit them for applications. In this direction results could be obtained relying on the insertion of an oxide barrier at one FM electrode/organic interface in the device. For example with this method Dediu et al. [2] could report 0.15 % MR signal at room temperature in a LSMO/Alq$_3$/Al$_2$O$_3$/Co junction. As shown Fig. 3.3, in another work Gobbi et al. [15] could obtain +9 and +5.5 % of MR at room temperature in Co/Al$_2$O$_3$/C$_{60}$/Py OSVs with a thickness of the organic layer respectively of 5 and 28 nm. One other result at room temperature was reported by Zhang et al. [31] in a Fe$_3$O$_4$/Al$_2$O$_3$/C$_{60}$(80 nm)/Co junction where they could observe a MR signal up to 8 % highlighting C$_{60}$ as a good candidate for organic spintronic devices. Finally, few other results exist on MR effect at room temperature measured in OSVs without the oxide barrier [14, 28, 30, 32], however the magnitude of the measured signal is still very limited (<1.5 %).

In parallel to the investigation of spin injection and propagation in devices with a thick organic layer, some groups also started to explore the possibility to use these materials as spin-tunnel barrier in MTJs. One first example is the work reported by Santos et al. [33] on a Co/Al$_2$O$_3$/Alq$_3$(1.6 nm)/NiFe MTJ where 4.6 % TMR was measured at room temperature. Other examples are works presented by Li et al. [22] where authors observed a MR signal up to 12 % in a NiFe/CoFe/Al$_2$O$_3$(0.6 nm)/PTCDA(1.25 nm)/Al$_2$O$_3$(0.6 nm)/CoFe MTJ, or the work reported by Yoo et al. [34] where authors studied a LSMO/LAO(1.2 nm)/rubrene (5 nm)/Fe MTJ. In this case MR signal was found to be 12 % at low temperature but it disappeared above 200 K. As one can note, all these results were obtained in devices where an oxide tunnel barrier was inserted at the interface. This is due to the extreme difficulty to avoid the short-circuit formation through such a thin molecular layer

in large-area devices. As it will be described later, one approach to avoid this problem has been to reduce the area of the device to the nanometric size. In this way Barraud et al. [35] could report an extremely high MR signal up to 300 % at 4.2 K in a LSMO/Alq$_3$(2 nm)/Co magnetic tunnel nanojunction. This large effect and its origin attributed to the FM metal/molecule hybridization at the interface attracted a strong interest on interface properties, such to give rise to a new branch of organic spintronics that is now called "spinterface" [36] and that will be presented more in details in the next section.

Finally, one other approach to fabricate MTJs is the one that could be called **molecular spintronics** in respect to molecular electronics. This field concerns devices realized by one or few molecules with the main aim to chemically engineer the device properties to manipulate their spins and charges. Nevertheless, working with nano-objects represents a considerable technological effort. In Fig. 4.7 we will summarize some of the most common techniques used in molecular electronics to contact molecules and we will see in Sect. 5.1 that contacting molecules in spintronic devices is even more difficult. One first result in this direction was the one presented in 2004 by Petta et al. [37] where authors fabricated a Ni/octanethiol/Ni magnetic tunnel nanojunction using the nanopore geometry and octanethiol self-assembled monolayer as tunnel barrier. This field represents an exciting challenge for the tailoring opportunities that it offers and its development will be treated more in details in Chap. 4 since it will represent one of the central aim of this thesis.

On the other hand, the opposite approach also exists where a single molecular magnet (SMM) is integrated in a device with ferromagnetic (or not) electrodes. One of the main interest of this kind of systems is their potential for applications in molecule-based information storage and processing [38].

3.2 Spinterface

In the very last years a new direction of organic spintronics is gaining increasing interest. Indeed, it was unveiled [35] that new spintronic functionalities, unavailable with conventional inorganic materials, could stem from the interface hybridization between ferromagnetic and molecular materials, giving rise to a new branch that is now called *spinterface* field [36]. These results can be found in a review [39].

3.2.1 A Model to Explain Spintronics Tailoring Through Molecular Spin Hybridization

A model which could explain the tailoring opportunities offered by organic materials was proposed in 2010 by Barraud et al. [35] who related these phenomena to the FM metal/molecule interface hybridization properties.
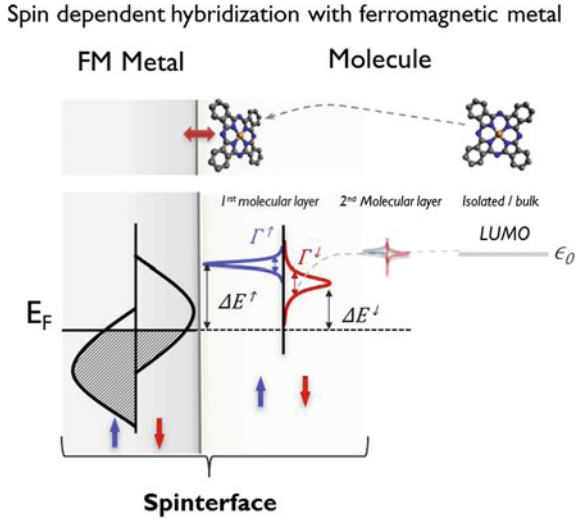
Fig. 3.4 Schematic representation of the molecular hybridization at an interface with a ferromagnetic metal. (*Top*) Representation of the molecule as it gets closer to the surface and is progressively coupled with the ferromagnetic metal. (*Bottom*) Representation of the metal density of states (DOS) and molecular orbitals for the corresponding position of the molecule. Molecules present discrete levels (far right) that shift and broaden as the hybridization with the metal get stronger towards chemi/physi-sorption. As the spin up and spin down density of states are different in the ferromagnetic metal, the broadening Γ and energy shifting ΔE become spin dependent on the molecule. This induces a spin polarization on the first molecular layer. A new effective electrode can be defined, including the first molecular layer, the spinterface. For simplicity, only the lowest unoccupied molecular orbital (LUMO) is represented for the molecule (the effect is also expected for the other orbitals); the 3d ferromagnet is represented with a simple band structure, whereas the s and d bands and anisotropy should be taken into account in the spin-dependent hybridization. Reference [39], reproduced with permission

Ferromagnetic Metal/Molecule Interaction

This model starts considering the different structure of a molecule in comparison to an inorganic material. As described in Sect. 2.2, molecules are formed by discrete levels and not from a continuum of states. We have seen in Sect. 2.2.1 the energy shift and broadening of a molecular state at the interface with a metal. We will see now what happens if the metal is ferromagnetic.

When instead of a non-magnetic metal one considers the interaction of the molecule with a *ferromagnetic* metal, the model predicts that the spin unbalance in the DOS of the metal is also reflected on the molecule, resulting in a spin-dependent energy shifting and broadening of the molecular level. This is represented in Fig. 3.4.

The DOS in a ferromagnetic metal is different for the spin $\uparrow$ and $\downarrow$ ($D_{FM}^{\uparrow}(E) \neq D_{FM}^{\downarrow}(E)$). As a consequence, the initially spin degenerated molecular level would split in two different energies $\varepsilon_{eff}^{\uparrow} \neq \varepsilon_{eff}^{\downarrow}$ and two different broadening widths $\Gamma^{\uparrow} \neq \Gamma^{\downarrow}$ for the two different spin directions $\uparrow$ and $\downarrow$.

The broadening and shifting are weighted by the individual coupling of each metallic state to the molecular one. The spin dependent broadening can thus be written as a weighted DOS:

$$\Gamma^{\uparrow(\downarrow)}(E) = 2\pi\Sigma_{i\uparrow(\downarrow)}|V_{i\uparrow(\downarrow)}|^2\delta(E_i - E) \tag{3.1}$$

where $V_{i\uparrow(\downarrow)}$ is the coupling between the spin-dependent state $i^{\uparrow(\downarrow)}$ of the metallic electrode and the discrete molecular state, and $\Sigma_{i\uparrow(\downarrow)}\delta(E_i - E)$ is the sum over all these states as shown in Fig. 3.4. Intuitively, one can obtain a simple picture and see that for a constant coupling, $V_{i\uparrow(\downarrow)} \approx V$, the broadening is now directly proportional to the FM electrode DOS with $\Gamma^{\uparrow(\downarrow)}(E) \propto D_{FM}^{\uparrow(\downarrow)}(E)$. In a more realistic picture, for example for a 3d ferromagnet (such as Co, Fe, and Ni), one would expect different contributions for s or d bands or even of different wave-function symmetries co-existing in the metal, as in crystalline MgO-based tunnel junctions.

To summarize, the effect of the ferromagnetic metal/molecule hybridization is to induce a spin polarization (spin-dependent broadening and shifting) on the molecular orbital and this depends on the nature of the FM metal/molecule coupling.

Redefinition of a New Effective Electrode

In this scenario, authors proposed to define a new *effective electrode* (spinterface) formed by the ferromagnetic electrode plus the first spin hybridized molecular layer at the interface (Fig. 3.4b). The DOS of this new effective electrode ($D_{int}^{\uparrow(\downarrow)}$) could be characterized using the two key parameters $\Gamma^{\uparrow(\downarrow)}$ and $\varepsilon_{eff}^{\uparrow(\downarrow)}$ derived above. The effect of these spin dependent broadening and shifting of the molecular level could be simply described as a Lorentzian distribution for its DOS:

$$D_{int}^{\uparrow(\downarrow)}(E) = \frac{\Gamma^{\uparrow(\downarrow)}/2\pi}{\left(E - \varepsilon_{eff}^{\uparrow(\downarrow)}\right)^2 + \left(\Gamma^{\uparrow(\downarrow)}/2\right)^2} \tag{3.2}$$

where $\Gamma^{\uparrow(\downarrow)}$ and $\varepsilon_{eff}^{\uparrow(\downarrow)}$ are characteristic parameters for each spinterface and they can be computed or extracted phenomenologically from transport measurements in solid-state devices or spintronics studies.

The redefinition of a new effective electrode results in the fact that now one must consider the spin polarization of this new spinterface instead of the one of the simple FM electrode. In similarity to the spin polarization calculation in FM metals, the spin polarization of the interface can be defined as:

$$P_{int} = \frac{D_{int}^{\uparrow} - D_{int}^{\downarrow}}{D_{int}^{\uparrow} + D_{int}^{\downarrow}} \tag{3.3}$$

where the spin-dependent DOS of the FM metal are substituted to the one of the effective electrode obtained by Eq. 3.2.

Spin Polarization Tailoring Through Molecular Hybridization

The spin-dependent hybridization between the FM electrode and the molecule leads to some tailoring opportunities that can be illustrated considering two limit examples for $D_{int}^{\uparrow(\downarrow)}$: $\Gamma \gg \Delta E$ and $\Gamma \ll \Delta E$ (where $\Delta E = E_F - \varepsilon_{eff}^{\uparrow(\downarrow)}$).

- **Case of $\Gamma \gg \Delta E$:**
  This situation is schematically illustrated in Fig. 3.5b and it is normally expected to happen for intermediate to strong coupling since it corresponds to a larger broadening Γ [40]. However, it could also happen for weaker Γ in a situation where cumulative effects as image forces or dipoles [41] would make $\varepsilon_{eff}^{\uparrow(\downarrow)} \rightarrow E_F$ and thus $\Delta E \rightarrow 0$.
  Considering $\Gamma \gg \Delta E$, from Eq. 3.2 the DOS of the spinterface can be rewritten as $D_{int}^{\uparrow(\downarrow)} \approx \frac{1}{\Gamma^{\uparrow(\downarrow)}}$ and hence $D_{int}^{\uparrow(\downarrow)} \propto \frac{1}{D_{FM}^{\uparrow(\downarrow)}}$. As one can see, the effective spinterface DOS is now inversely proportional to the electrode's original one and by substituting this in Eq. 3.3 we obtain:

$$P_{int} = -\frac{\Gamma^{\uparrow} - \Gamma^{\downarrow}}{\Gamma^{\uparrow} + \Gamma^{\downarrow}} \approx -\frac{D_{FM}^{\uparrow} - D_{FM}^{\downarrow}}{D_{FM}^{\uparrow} + D_{FM}^{\downarrow}} = -P_{FM} \qquad (3.4)$$

Inorganic interface: (a)

Molecular Spinterface:
(b) Spin polarization inversion $\Gamma \gg \Delta E$
(c) Spin polarization enhancement $\Gamma \ll \Delta E$

Spinterface "effective" electrode = metal + 1st interfacial molecular state
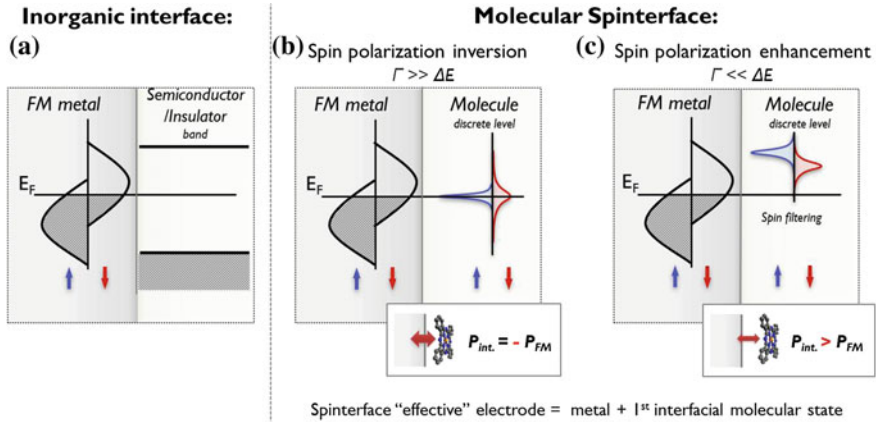
Fig. 3.5 Illustration of the spinterface. **a** Usual representation of an inorganic interface with the conduction and valence band structure. **b, c** Representation of two examples of molecular spinterface effect: inversion and enhancement. **b** Case of broadening being larger than the difference between molecular level energy and metal Fermi level ($\Gamma \gg \Delta E$). As the broadening area corresponds to only one spin state, a larger broadening ($\Gamma \propto D_{FM}^{\uparrow(\downarrow)}$) means a lower molecular density of states $D_{Int}^{\uparrow(\downarrow)}$. This induces an inversion of the spin polarization on the molecular orbital following Eq. 3.4. **c** Opposite case where the energy difference between molecular level energy and metal Fermi level is larger than the broadening ($\Gamma \ll \Delta E$). The induced spin polarization can then be enhanced compared to the original spin polarization of the ferromagnet and can be compared to a spin-filter following Eq. 3.5. Reference [39], reproduced with permission

In this case *the sign of the spin polarization at the interface results to be the* **opposite** *to the one of the original ferromagnetic electrode* (P_{FM}).

This can be physically understood looking at the schematic picture in Fig. 3.5b. The area of the broadening is constant for spin ↑ and ↓ of the molecular state since it derives from a single initial spin state. Hence, a larger broadening ($\Gamma^{\uparrow(\downarrow)} \propto D_{FM}^{\uparrow(\downarrow)}$) corresponds to a reduced maximum for the molecular DOS $D_{int}^{\uparrow(\downarrow)}$. This explains the DOS inversion between the FM electrode and the molecular state.

- **Case of $\Gamma \ll \Delta E$:**

  This situation is represented in Fig. 3.5c and it corresponds to the case where the molecular level is only slightly shifted and the broadening Γ is small enough to be neglected with respect to ΔE. This is more likely a common case for weak coupling between the molecule and the metal where the broadening is small respect to $\Delta E = E_F - \varepsilon_{eff}^{\uparrow(\downarrow)}$.

  Considering $\Gamma \ll \Delta E$, Eq. 3.2 can be rewritten as $D_{int}^{\uparrow(\downarrow)} \approx \frac{\Gamma^{\uparrow(\downarrow)}}{(\Delta E^{\uparrow(\downarrow)})^2}$ and hence $D_{int}^{\uparrow(\downarrow)} \propto \frac{D_{FM}^{\uparrow(\downarrow)}}{(\Delta E^{\uparrow(\downarrow)})^2}$. The effective spinterface DOS maintains in this case the same spin polarization sign of the electrode's original one but it becomes levered by $(\Delta E^{\uparrow(\downarrow)})^2$. Substituting the approximated $D_{int}^{\uparrow(\downarrow)}$ in Eq. 3.3 we obtain:

$$P_{int} = \frac{\frac{\Gamma^{\uparrow}}{\Delta E^{\uparrow 2}} - \frac{\Gamma^{\downarrow}}{\Delta E^{\downarrow 2}}}{\frac{\Gamma^{\uparrow}}{\Delta E^{\uparrow 2}} + \frac{\Gamma^{\downarrow}}{\Delta E^{\downarrow 2}}} > P_{FM} \tag{3.5}$$

Thus, *the spin polarization at the interface results to be* **enhanced** *in comparison to the one of the original ferromagnetic electrode* (P_{FM}).

This because the spin-dependent shift $\varepsilon_{eff}^{\uparrow(\downarrow)}$ (found in $(\Delta E^{\uparrow(\downarrow)})^2$) acts as a spin-filter effect [42]. Indeed, as shown in Fig. 3.5c, when the less (more) broadened level stays further away from (is brought closer to) the FM Fermi level one can obtain an enhancement effect for the spin polarization.

Summarizing, we have seen here how this simple model demonstrated that the spin response can be strongly modulated by the hybridization at the interface. In the next section we will present some experimental evidence that could confirm the two functionality cases described above.

3.2.2 Experimental Evidence of Spin Polarization Tailoring

The model described above does not represent just a theoretical prediction of what could happen at the ferromagnetic metal/molecule interface, but the spin dependent hybridization at the spinterface could be also experimentally observed using surface sensitive techniques and in spintronic devices. The study of ferromagnetic

metal/molecule interface mainly involved small molecules as phthalocyanines (Pc) [43–49], fullerene (C_{60}) [50–52] and Alq_3 [35, 53–55]. Here below we will present few examples, for a more complete review we will recall to [39].

3.2.2.1 Spectroscopy Measurements

Different spectroscopic techniques have been used to investigate the spin dependent hybridization, such as the spin-polarized scanning tunneling microscopy (SP-STM), the spin-polarized spectroscopy, X-ray magnetic circular dichroism (XMCD) and spin-resolved two-photon photoemission spectroscopy (SP-PES).

One example of spin polarization inversion is reported in Fig. 3.6a that shows a H_2Pc molecule absorbed on a Fe surface and studied by SP-STM technique [44]. The H_2Pc molecule is non-magnetic but when it is absorbed over the Fe surface a spin polarization could be observed over the molecule and its sign became opposite to that of the Fe surface. This phenomenon can be ascribed to the inversion case (Fig. 3.5b) at Fe/H_2Pc interface.

On the other hand, an example of spin polarization enhancement and energy shifting is reported in Fig. 3.6b. Here the spin dependent energy shifting of the molecular orbitals at the ferromagnetic interface could be directly measured on C_{60} molecules deposited on a chromium surface using SP-STM. The extracted TMR values calculated from this spectra reached a ratio up to 100 % [50]. The large magnetore-
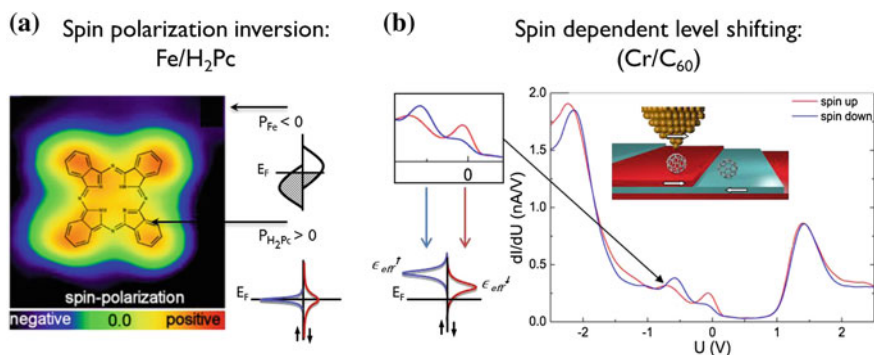
Fig. 3.6 Experimental evidences of an induced spin polarization inversion (**a**) and spin dependent energy shifting on a single molecule (**b**). **a** Image of the spin polarization of a H_2Pc molecule deposited on an iron surface done by spin polarized scanning tunneling microscopy experiments. Whereas the iron surface spin polarization is negative (*blue*) the spin polarization above the molecule is positive (*yellow-orange*) highlighting the spin polarization inversion on the H_2Pc orbitals. Figure adapted from [44]. **b** Spin polarized scanning tunneling spectroscopy measurements on a C_{60} molecule deposited on a chromium surface. The difference in the conductance curves for the spin up (*red*) and down (*blue*) shows a spin dependent energy shifting of the molecular levels up to 0.5 eV. Figure adapted from [50]. Copyright 2012 American Chemical Society. Reference [39], reproduced with permission

sistance in this system was ascribed to the spin dependent broadening and shifting of the molecular orbitals leading to the spin polarization enhancement presented in Fig. 3.5c.

3.2.2.2 Spintronics Devices

The spin polarization tailoring due to the ferromagnetic metal/molecule hybridization could be also observed in solid-state spintronic devices as MTJs.

One first example of spin polarization inversion could be measured in a Co/Co Pc/Co MTJ [9] and it is shown in Fig. 3.7b. As one can see, this junction presents a negative TMR signal even if it is symmetric with both Co electrodes. If the spin polarization was just due to the electrode spin polarization, the sign of TMR should be positive according to Jullière's model (Eq. 1.5). However, the negative sign of TMR suggests that the spin polarization is inverted at only one interface and thus, although there are two identical Co ferromagnetic electrodes, the Co/CoPc and CoPc/Co spinterfaces are drastically different.

On the other hand, one example of spin polarization enhancement is the one already cited before where an extremely high TMR value up to 300 % could be recorded in a LSMO/Alq$_3$/Co MTJ as shown in Fig. 3.7a.

Using Jullière's model (Eq. 1.5) and considering a spin polarization of 100 % for LSMO electrode, it has been calculated that spin polarization for the Alq$_3$/Co interface has a value at least of 60 %, corresponding to a 30 % enhancement compared to bare Co [35].
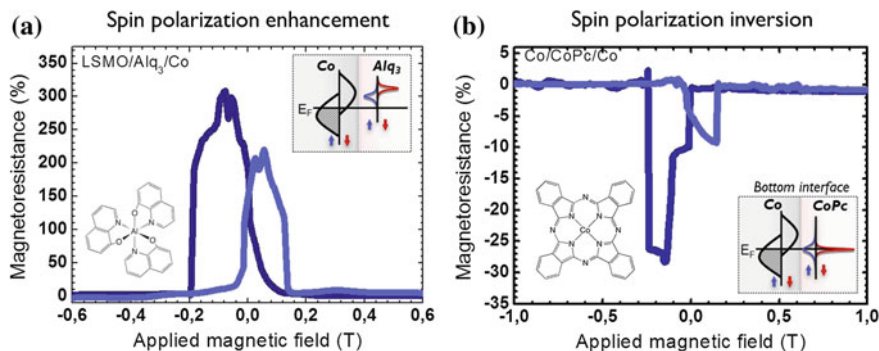
Fig. 3.7 Tunneling magnetoresistance (TMR) experiments highlighting the enhancement and the inversion of the spin polarization on the molecular levels. **a** High TMR in LSMO/Alq$_3$/Co magnetic tunnel junctions. The large TMR effect up to 300 % is ascribed to an enhancement of at least 30 % of the spin polarization at the Alq$_3$/Co interface. Figure adapted from [35]. **b** Inverse TMR in a Co/CoPc/Co magnetic tunnel junction. The inverse TMR means that the two interfacial spin polarizations have opposite signs. The inversion on the spin polarization occurs at the bottom Co/CoPc in agreement with spin-polarized STM measurement performed on a single CoPc molecule on a cobalt surface [43, 46]. Figure adapted from [9]. Reference [39], reproduced with permission
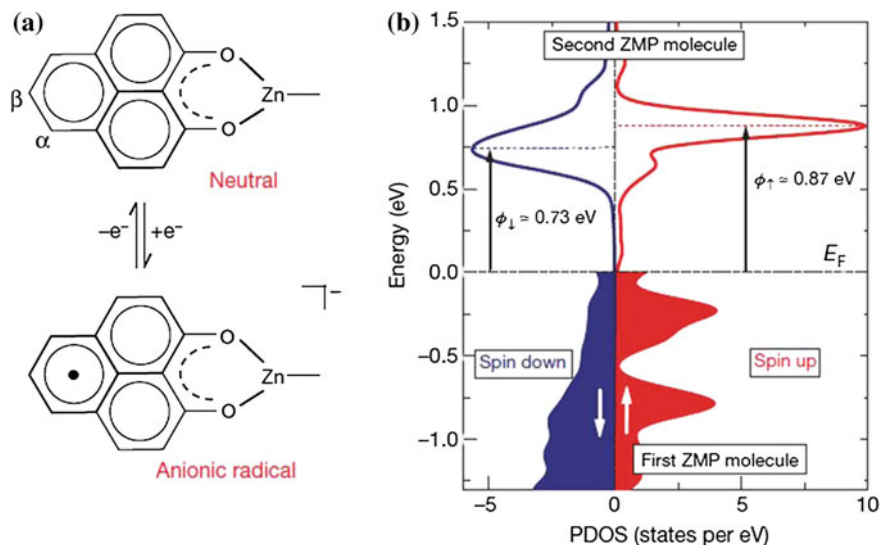
Fig. 3.8 **a** Structure of a zinc methyl phenalenyl (ZMP) molecule in a neutral state with no net spin (*top*). Charge transfer processes through hybridization on the ferromagnet surface can change the chemical state of the phenalenyl moiety from neutral to an anionic radical (*bottom*) with net moment. **b** Spin-resolved PDOS of the p-states for the first-layer (*bottom*) and second-layer (*top*) ZMP molecule of the relaxed interface system in the energy interval [−1.5, 1.5 eV]. Interface p_z-d hybridization creates spin-unbalanced electronic structure in the two molecules. The LUMO of the second ZMP molecule is spin-splitted by 0.14 eV, leading to a difference in the barrier height for the two spin channels. Reprinted by permission from Macmillan Publishers Ltd: Nature [56], copyright 2013

Finally, another example of how the spin dependent shifting of the molecular orbital can act as a spin filter was reported in a junction formed by zinc methyl phenalenyl (ZMP) molecules deposited on a Co electrode and with the second electrode that is non-magnetic. In this case it was shown that the induced spin polarization can spread up to the second molecular layer that naturally presents a weaker coupling strength [56] (Fig. 3.8). In this way a spin-valve like MR effect could be obtained in an organic spintronic device with only one inorganic ferromagnetic electrode. In this case, being the hybridization naturally weaker for the second molecular layer, the spin dependent shifting of the molecular orbitals leads to an effective organic "spin polarizer" acting as a spin filter junction.

3.3 Conclusion

In this chapter we presented the strong development seen in the last years in the field of organic spintronics. Despite many fundamental phenomena are still to be unravelled, as the spin relaxation mechanisms inside the organic material, the field has just begun to unveil an amazing potential.

As we saw, beyond to focus on the device and interface optimization in order to obtain a high MR especially at room temperature, new interesting phenomena had been highlighted such as the possibility to tune the interface spin polarization (from the enhancement to the reversal of its sign) depending on the ferromagnetic metal/molecule coupling strength. This exciting discovery promises properties unachievable with inorganic materials and gives rise to a new "spinterface" field paving the way for new multi-functionalities.

References

1. V. Dediu, M. Murgia, F.C. Matacotta, C. Taliani, S. Barbanera, Room temperature spin polarized injection in organic semiconductor. Solid State Commun. **122**, 181–184 (2002)
2. V.A. Dediu, L.E. Hueso, I. Bergenti, C. Taliani, Spin routes in organic semiconductors. Nat. Mater. **8**, 707–716 (2009)
3. Z.H. Xiong, D. Wu, Z.V. Vardeny, J. Shi, Giant magnetoresistance in organic spin-valves. Nature **427**, 821–824 (2004)
4. W. Xu, G.J. Szulczewski, P. LeClair, I. Navarrete, R. Schad, G.X. Miao, H. Guo, A. Gupta, Tunneling magnetoresistance observed in $La_{0.67}Sr_{0.33}MnO_3$/organic molecule/Co junctions. Appl. Phys. Lett. **90**(7), 72506 (2007)
5. G.Wang, T.-W.Kim, H. Lee, T. Lee, Influence of metal-molecule contacts on decay coefficients and specific contact resistances in molecular junctions. Phys. Rev. B **76**, 205320 (2007)
6. V.A. Dediu, L.E. Hueso, I. Bergenti, A. Riminucci, F. Borgatti, P. Graziosi, C. Newby, F. Casoli, M.P. De Jong, C. Taliani, Y. Zhan, Room-temperature spintronic effects in Alq_3-based hybrid devices. Phys. Rev. B **78**, 115203 (2008)
7. S. Majumdar, H.S. Majumdar, R. Laiho, R. Osterbacka, Comparing small molecules and polymer for future organic spin-valves. J. Alloys Compd. **423**, 169–171 (2006)
8. H. Vinzelberg, J. Schumann, D. Elefant, R.B. Gangineni, J. Thomas, B. Büchner, Low temperature tunneling magnetoresistance on (La, Sr)MnO$_3$/Co junctions with organic spacer layers. J. Appl. Phys. **103**, 93720 (2008)
9. C. Barraud, Spintronique moléculaire: rôle des interfaces dans le transport du spin. Ph.D. thesis, Université Pierre et Marie Curie, June 2011
10. M. Palosse, Élaboration et étude de vannes de spin organiques: vers le transport de spin à température ambiante. Ph.D. thesis, Université de Toulouse (2013)
11. J. Shim, K. Raman, Y. Park, T. Santos, G. Miao, B. Satpati, J. Moodera, Large spin diffusion length in an amorphous organic semiconductor. Phys. Rev. Lett. **100**, 226603 (2008)
12. J.-W. Yoo, H.W. Jang, V.N. Prigodin, C. Kao, C.B. Eom, A.J. Epstein, Giant magnetoresistance in ferromagnet/organic semiconductor/ferromagnet heterojunctions. Phys. Rev. B **80**, 205207 (2009)
13. R. Lin, F. Wang, J. Rybicki, M. Wohlgenannt, K.A. Hutchinson, Distinguishing between tunneling and injection regimes of ferromagnet/organic semiconductor/ferromagnet junctions. Phys. Rev. B **81**, 195214 (2010)
14. F. Wang, Z.V. Vardeny, Recent advances in organic spin-valve devices. Synth. Met. **160**(3–4), SI, 210–215 (2010)
15. M. Gobbi, F. Golmar, R. Llopis, F. Casanova, L.E. Hueso, Room-temperature spin transport in C-60-based spin valves. Adv. Mater. **23**(14), 1609 (2011)
16. R. Lin, F. Wang, M. Wohlgenannt, C. He, X. Zhai, Y. Suzuki, Organic spin-valves based on fullerene C-60. Synth. Met. **161**(7–8), 553–557 (2011)
17. T.L.A. Tran, T.Q. Le, J.G.M. Sanderink, W.G. van der Wiel, M.P. de Jong, The multistep tunneling analogue of conductivity mismatch in organic spin valves. Adv. Funct. Mater. **22**, 1180–1189 (2012)

18. X. Zhang, S. Mizukami, T. Kubota, Q. Ma, M. Oogane, H. Naganuma, Y. Ando, T. Miyazaki, Observation of a large spin-dependent transport length in organic spin valves at room temperature. Nat. Commun. **4**, 1392 (2013)

19. T.D. Nguyen, F. Wang, X.-G. Li, E. Ehrenfreund, Z.V. Vardeny, Spin diffusion in fullerene-based devices: morphology effect. Phys. Rev. B **87**(7), 75205 (2013)

20. F.J. Wang, C.G. Yang, Z.V. Vardeny, X.G. Li, Spin response in organic spin valves based on $La_{2/3}Sr_{1/3}MnO_3$ electrodes. Phys. Rev. B **75**, 245324 (2007)

21. Y. Liu, T. Lee, H.E. Katz, D.H. Reich, Effects of carrier mobility and morphology in organic semiconductor spin valves. J. Appl. Phys. **105**, 07C708 (2009)

22. K.-S. Li, Y.-M. Chang, S. Agilan, J.-Y. Hong, J.-C. Tai, W.-C. Chiang, K. Fukutani, P.A. Dowben, M.-T. Lin, Organic spin valves with inelastic tunneling characteristics. Phys. Rev. B **83**, 172404 (2011)

23. M. Palosse, M. Fisichella, E. Bedel-Pereira, I. Séguy, C. Villeneuve, B. Warot-Fonrose, J.F. Bobo, Spin-polarized transport in NiFe/perylene-3,4,9,10-tetracarboxylate/Co organic spin valves. J. Appl. Phys. **109**(7), 07C723 (2011)

24. T. Ikegami, I. Kawayama, M. Tonouchi, S. Nakao, Y. Yamashita, H. Tada, Planar-type spin valves based on low-molecular-weight organic materials with $La_{0.67}Sr_{0.33}MnO_3$ electrodes. Appl. Phys. Lett. **92**(15), 153304 (2008)

25. T. Shimada, H. Nogawa, T. Noguchi, Y. Furubayashi, Y. Yamamoto, Y. Hirose, T. Hitosugi, T. Hasegawa, Magnetotransport properties of Fe/Pentacene/Co:TiO$_2$ junctions with Fe top contact electrodes prepared by thermal evaporation and pulsed laser deposition. Jpn. J. Appl. Phys. **47**, 1184–1187 (2008)

26. M. Palosse, I. Séguy, E. Bedel-Pereira, C. Villeneuve-Faure, C. Mallet, P. Frère, B. Warot-Fonrose, N. Biziere, J.-F. Bobo, Spin transport in benzofurane bithiophene based organic spin valves. AIP Adv. **4**, 017117 (2014)

27. S. Majumdar, H. Huhtinen, H.S. Majumdar, R. Laiho, R. Österbacka, Effect of $La_{0.67}Sr_{0.33}MnO_3$ electrodes on organic spin valves. J. Appl. Phys. **104**(3), 33910 (2008)

28. N.A. Morley, A. Rao, D. Dhandapani, M.R.J. Gibbs, M. Grell, T. Richardson, Room temperature organic spintronics. J. Appl. Phys. **103**, 07F306 (2008)

29. F. Wang, C. Yang, E. Ehrenfreund, Z. Vardeny, Spin dependent reactions of polaron pairs in PPV-based organic diodes. Synth. Met. **160**, 297–302 (2010)

30. S. Majumdar, R. Laiho, P. Laukkanen, I.J. Väyrynen, H.S. Majumdar, R. Österbacka, Application of regioregular polythiophene in spintronic devices: effect of interface. Appl. Phys. Lett. **89**, 122114 (2006)

31. X. Zhang, S. Mizukami, Q. Ma, T. Kubota, M. Oogane, H. Naganuma, Y. Ando, T. Miyazaki, Spin-dependent transport behavior in C_{60} and Alq$_3$ based spin valves with a magnetite electrode (invited). J. Appl. Phys. **115**, 172608 (2014)

32. Y. Liu, S.M. Watson, T. Lee, J.M. Gorham, H.E. Katz, J.A. Borchers, H.D. Fairbrother, D.H. Reich, Correlation between microstructure and magnetotransport in organic semiconductor spin-valve structures. Phys. Rev. B **79**, 075312 (2009)

33. T.S. Santos, J.S. Lee, P. Migdal, I.C. Lekshmi, B. Satpati, J.S. Moodera, Room-temperature tunnel magnetoresistance and spin-polarized tunneling through an organic semiconductor barrier. Phys. Rev. Lett. **98**, 016601 (2007)

34. J.-W. Yoo, H. Jang, V. Prigodin, C. Kao, C. Eom, A. Epstein, Tunneling vs. giant magnetoresistance in organic spin valve. Synth. Met. **160**, 216–222 (2010)

35. C. Barraud, P. Seneor, R. Mattana, S. Fusil, K. Bouzehouane, C. Deranlot, P. Graziosi, L. Hueso, I. Bergenti, V. Dediu, F. Petroff, A. Fert, Unravelling the role of the interface for spin injection into organic semiconductors. Nat. Phys. **6**, 615–620 (2010)

36. S. Sanvito, Molecular spintronics: the rise of spinterface science. Nat. Phys. **6**, 562–564 (2010)

37. J.R. Petta, S.K. Slater, D.C. Ralph, Spin-dependent transport in molecular tunnel junctions. Phys. Rev. Lett. **93**, 136601 (2004)

38. D. Gatteschi, A. Cornia, M. Mannini, R. Sessoli, Organizing and addressing magnetic molecules. Inorg. Chem. **48**, 3408–3419 (2009)

39. M. Galbiati, S. Tatay, C. Barraud, A.V. Dediu, F. Petroff, R. Mattana, P. Seneor, Spinterface: crafting spintronics at the molecular scale. MRS Bull. **39**, 602–607 (2014)

40. H. Vazquez, R. Oszwaldowski, P. Pou, J. Ortega, R. Pérez, F. Flores, A. Kahn, Dipole formation at metal/PTCDA interfaces: role of the charge neutrality level. EPL (Europhys. Lett.) **65**(6), 802 (2004)

41. M.L. Perrin, C.J.O. Verzijl, C.A. Martin, A.J. Shaikh, R. Eelkema, J.H. van Esch, J.M. van Ruitenbeek, J.M. Thijssen, H.S.J. van der Zant, D. Dulić, Large tunable image-charge effects in single-molecule junctions. Nat. Nanotechnol. **8**, 282–287 (2013)

42. J.S. Moodera, T.S. Santos, T. Nagahama, The phenomena of spin-filter tunnelling. J. Phys. Condens. Matter **19**, 165202 (2007)

43. C. Iacovita, M.V. Rastei, B.W. Heinrich, T. Brumme, J. Kortus, L. Limot, J.P. Bucher, Visualizing the spin of individual cobalt-phthalocyanine molecules. Phys. Rev. Lett. **101**, 116602 (2008)

44. N. Atodiresei, J. Brede, P. Lazic, V. Caciuc, G. Hoffmann, R. Wiesendanger, S. Blugel, Design of the local spin polarization at the organic-ferromagnetic interface. Phys. Rev. Lett. **105**, 066601 (2010)

45. J. Brede, N. Atodiresei, S. Kuck, P. Lazić, V. Caciuc, Y. Morikawa, G. Hoffmann, S. Blügel, R. Wiesendanger, Spin- and energy-dependent tunneling through a single molecule with intramolecular spatial resolution. Phys. Rev. Lett. **105**, 47204 (2010)

46. J. Brede, R. Wiesendanger, Spin-resolved characterization of single cobalt phthalocyanine molecules on a ferromagnetic support. Phys. Rev. B **86**, 184423 (2012)

47. S. Schmaus, A. Bagrets, Y. Nahas, T.K. Yamada, A. Bork, M. Bowen, E. Beaurepaire, F. Evers, W. Wulfhekel, Giant magnetoresistance through a single molecule. Nat. Nanotechnol. **6**, 185–189 (2011)

48. S. Lach, A. Altenhof, K. Tarafder, F. Schmitt, M.E. Ali, M. Vogel, J. Sauther, P.M. Oppeneer, C. Ziegler, Metal-organic hybrid interface states of a ferromagnet/organic semiconductor hybrid junction as basis for engineering spin injection in organic spintronics. Adv. Funct. Mater. **22**, 989–997 (2012)

49. F. Djeghloul, F. Ibrahim, M. Cantoni, M. Bowen, L. Joly, S. Boukari, P. Ohresser, F. Bertran, P. Le Fèvre, P. Thakur, F. Scheurer, T. Miyamachi, R. Mattana, P. Seneor, A. Jaafar, C. Rinaldi, S. Javaid, J. Arabski, J.-P. Kappler, W. Wulfhekel, N.B. Brookes, R. Bertacco, A. Taleb-Ibrahimi, M. Alouani, E. Beaurepaire, W. Weber, Direct observation of a highly spin-polarized organic spinterface at room temperature. Sci. Rep. **3**, 1272 (2013)

50. S.L. Kawahara, J. Lagoute, V. Repain, C. Chacon, Y. Girard, S. Rousset, A. Smogunov, C. Barreteau, Large magnetoresistance through a single molecule due to a spin-split hybridized orbital. NANO Lett. **12**, 4558–4563 (2012)

51. T.L.A. Tran, P.K.J. Wong, M.P. de Jong, W.G. van der Wiel, Y.Q. Zhan, M. Fahlman, Hybridization-induced oscillatory magnetic polarization of C-60 orbitals at the C-60/Fe(001) interface. Appl. Phys. Lett. **98**(22), 222505 (2011)

52. K. Yoshida, I. Hamada, S. Sakata, A. Umeno, M. Tsukada, K. Hirakawa, Gate-tunable large negative tunnel magnetoresistance in Ni–C60–Ni single molecule transistors. NANO Lett. **13**, 481–485 (2013)

53. Y. Zhan, E. Holmstrom, R. Lizárraga, O. Eriksson, X. Liu, F. Li, E. Carlegrim, S. Stafström, M. Fahlman, E. Holmström, Efficient spin injection through exchange coupling at organic semiconductor/ferromagnet heterojunctions. Adv. Mater. **22**, 1626 (2010)

54. S. Steil, N. Großmann, M. Laux, A. Ruffing, D. Steil, M. Wiesenmayer, S. Mathias, O.L.A. Monti, M. Cinchetti, M. Aeschlimann, Spin-dependent trapping of electrons at spinterfaces. Nat. Phys. **9**, 242–247 (2013)

55. L. Schulz, L. Nuccio, M. Willis, P. Desai, P. Shakya, T. Kreouzis, V.K. Malik, C. Bernhard, F.L. Pratt, N.A. Morley, A. Suter, G.J. Nieuwenhuys, T. Prokscha, E. Morenzoni, W.P. Gillin, A.J. Drew, Engineering spin propagation across a hybrid organic/inorganic interface using a polar layer. Nat. Mater. **10**, 39–44 (2011)

56. K.V. Raman, A.M. Kamerbeek, A. Mukherjee, N. Atodiresei, T.K. Sen, P. Lazić, V. Caciuc, R. Michel, D. Stalke, S.K. Mandal, S. Blügel, M. Münzenberg, J.S. Moodera, Interface-engineered templates for molecular spin memory devices. Nature **493**, 509–513 (2013)

Part II
Self-Assembled Monolayers for Molecular Spintronics

One of the most exciting targets of molecular spintronics field is multifunctional devices where the properties can be accurately controlled and actively changed. Indeed, spin-dependent hybridization could be used in the tailoring of the resistive and magnetoresistive response of spintronic devices by using functional molecules. Exploiting the molecules' chemical versatility, it could be possible to engineer the devices at molecular level, and the spin-dependent broadening and shifting of the hybridized states (and hence the device functionality) would be changed *in situ* and *at will* by external stimuli such as light, temperature, or electric field. In this new direction, self-assembled monolayers (SAMs) appear as highly promising candidates since each part and function of this system can be modulated independently (like a molecular LEGO building unit). Despite being highly promising, they are still scarcely investigated in the literature probably due to the difficulties in device fabrication.

In this second part of the manuscript we will present the work done on the investigation of SAMs-based magnetic tunnel nanojunctions. The aim of this study is to probe the opportunities of these systems for spintronics and set the bases towards the future possibility to tune the SAMs barrier and engineer at molecular level the properties of the device. In Chap. 4 we will start by explaining more in detail the advantages of SAMs for spintronics and we will show some methods used in molecular electronics to contact single molecular layers. Then, we will report on theoretical models used to describe the charge transport through a SAM barrier and finally a state of the art in molecular spintronics will also be introduced. In Chap. 5, we will explain our device geometry and FM electrode choice. We will then present the results of SAMs grafting and develop the whole nanofabrication technique used to realize our devices. Finally, in Chap. 6 we will report the magneto-transport results obtained in our LSMO/SAM/Co nanojunctions. First we will focus on LSMO/C12P/Co MTJs and then we will show results obtained when tuning the molecular chain length from C10P to C18P.

Chapter 4
Introduction to Self-Assembled Monolayers

4.1 Why Self-Assembled Monolayers?

In Chap. 3 we discussed the fundamental role played by the metal/molecule hybridization on the spin properties of the devices. We highlighted how this opens new ways for spin polarization tailoring and the consequent possibility to control the spintronic response of organic devices. Depending on the metal/molecule coupling, the induced interfacial spin polarization can be enhanced or change sign in comparison to the one of the ferromagnetic metal. What is now more interesting is that the hybridization between the ferromagnetic electrode and the molecule induces a polarization on the interfacial molecular states that can be potentially tailored by external inputs as thermal excitation, light or electric field. All these effects are not achievable with inorganic materials, thus unveiling the high potentiality of organics for spintronics.

The aim of this thesis is to contribute to the essential investigation of the interfacial mechanisms in hybrid organic-inorganic spintronic devices and to set the basis towards the future possibility to engineer at the molecular level the properties of these devices. In this scenario, we chose to focus our study on self-assembled monolayers (SAMs) molecules since, while scarcely studied [1, 2], they could be the perfect toy barrier to further test these tailoring properties in molecular magnetic tunnel junctions (MTJs). The main advantage of SAMs compared to inorganics and other organic materials is that they are modular: as shown in Fig. 4.1 they are composed by a head, a body and an anchoring group that can be independently tuned thus allowing an easy engineering of the barrier. SAMs also form an organized layer since molecules "recognize" the surface and distribute in a compact and uniform way over it. In the following we will show some examples on how the tuning of molecular body, head or anchoring group can influence the properties of the system.

Fig. 4.1 Schematic of a
self-assembled monolayer
structure. Molecules are
formed by a head, a body and
an anchoring group that can
be independently changed
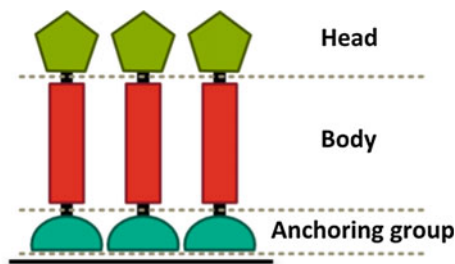
4.1.1 Influence of the Molecular Body

Probably the key role on transport properties is played by the structure of the mole-
cular body. Its choice allows to modify the barrier potential, from fine tuning of its
properties (height, width, etc…) to the addition of new functionalities.

- **Influence on the barrier properties**: As shown in Sect. 2.2.2, a saturated alkane
  chain is insulating and electrically equivalent to a rectangular potential barrier
  (Fig. 4.2a). On the contrary, the insertion of an aromatic ring in the chain introduces
  discrete levels in the barrier that modify its height and can also lead to a resonant
  configuration (Fig. 4.2b). A similar trend has been experimentally observed in fully
  π-conjugated molecules that are electrically more transparent than saturated ones
  [4, 5]. This results in a lower decay coefficient ($\beta \simeq 0.2$–0.6 Å^{-1}) for this kind
  of molecules than the saturated ones ($\beta \simeq 0.6$–1 Å^{-1}) [6]. These differences in β
  values can be observed for example in Fig. 4.3 where molecules with alkyl, acene
  and phenylene groups are compared.
- **Influence on the molecule functionalities**: The conformation of the molecule can
  also play an important role on the transport properties [7]. It can be changed by
  chemically adding different substituents or by providing external stimuli as light
  [8] or a voltage pulse.
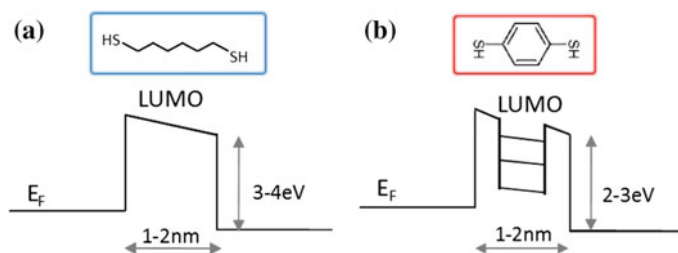
Fig. 4.2 a Alkanedithiol molecule forms a tunnel barrier of 3–4 eV height. The thickness of the
barrier depends on the length of the carbon chain of the molecule. **b** The aromatic ring of a ben-
zenedithiole molecule forms a quantum well inside the tunnel barrier. The barrier height is smaller
than before and the resonant levels correspond to the LUMO levels of the aromatic ring
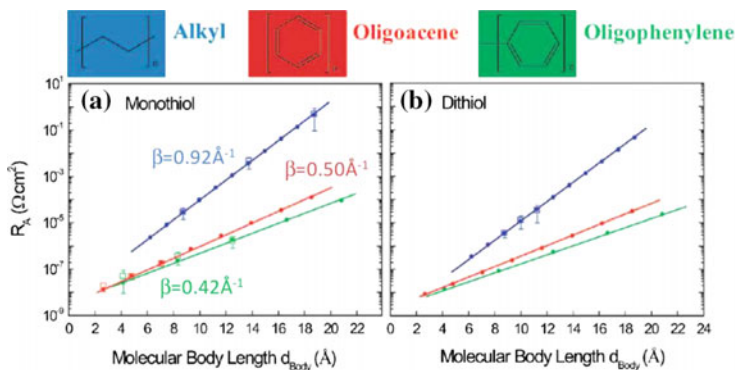
Fig. 4.3 Semilog plot of the resistance area product (RA) as a function of the molecular body length for monothiols (**a**) and dithiols (**b**) molecules. Three different types of molecules have been compared: alkyl (*blue*), oligoacene (*red*) and oligophenylene (*green*) chains in Au–molecule–Au junctions. RA product is lower for π-conjugated molecules due to the smaller HOMO-LUMO gap than in saturated molecules. Reprinted with permission from [3]. Copyright 2008 American Chemical Society

For example, it has been shown in biphenyldiamine molecules that the relative orientation of two aromatic rings can change the conductance of the molecule [9]. As another example, Smaali et al. [10] showed that azobenzenethiophene molecules could change their conformation (cis or trans) by applying a light stimulus (Fig. 4.4a). In a tunnel junction this results in a switch of the device conductance of more than three orders of magnitude as it is shown in Fig. 4.4b. This phenomenon is ascribed to the change of the molecule length and a reorganization of the electronic levels in the two configurations. The molecule consequently has two different states depending on its configuration: a conducting one and an insulating one and it behaves as a molecular switch.
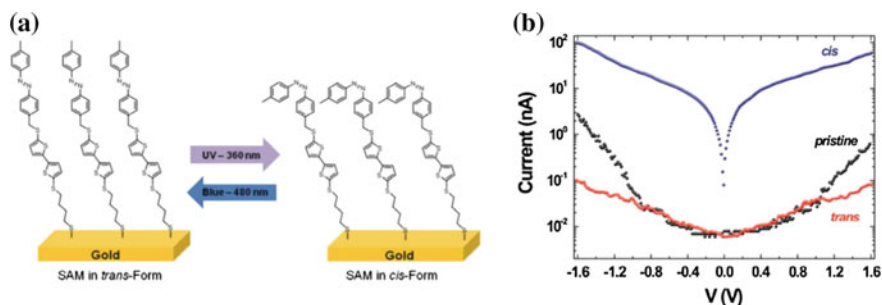
Fig. 4.4 A molecular switcher. **a** Schematic azobenzene-thiophene SAM over a Au surface. Azobenzene molecules change their conformation from *trans* to *cis* isomer with light irradiation. **b** I–V characteristic of the device for the different conformations of the azobenzene group. Reprinted with permission from [10]. Copyright 2010 American Chemical Society

4.1.2 Influence of the Head and Anchoring Group

The head and the anchoring group also play an important role for the transport properties of the junction since they determine the coupling of the molecule with the electrodes.

For example, some studies have been performed in molecular electronics to compare transport through molecules depending on the nature of the contacts [3, 11, 12]. The effect of anchoring groups has been studied for example by Chen et al. [13] on single molecules using alkanes terminated with dithiol (–S), diamine (–NH$_2$), and dicarboxylic-acid (–COOH) groups on Au electrodes. Authors found that the contact resistance (R) is highly sensitive to the type of the anchoring group: R(Au-COOH) $\simeq 100 \cdot$ R(Au-S) and R(Au-COOH) $\simeq 5 \cdot$ R(Au-NH$_2$). This dependence is attributed to a different electronic coupling between the molecule and the electrode and to a different molecular levels alignment with the Fermi energy of the electrode introduced by the anchoring groups.

For what concerns the interface engineering, some limits are imposed in the choice of the anchoring groups giving the specificity of the self-assembly process. For example, thiols (–SH) or amines (–CN) are typically grafted on metals like Au, while carboxylic acids (–CO$_2$H) or silanes (–SiCl$_3$) are grafted on oxides as TiO$_2$ or Al$_2$O$_3$. On the contrary, a priori there is no limit in the top interface engineering since there is no restriction in the choice of the molecular head and every metal can be deposited on its top thus allowing very large possibilities for tuning.

4.1.3 And for Spintronics?

The modularity of SAMs could present great advantages also for the spintronic field. For example, the reorganization of electronic levels observed in molecules such as azobenzenethiophenes [10] by applying an external stimulus, could be exploited in spintronics to tune in situ the FM metal/molecule coupling at the interfaces. Indeed, according to the model discussed in Sect. 3.2.1, the spin polarization of the spinterface is proportional to the coupling Γ and energy shift ΔE of the molecular levels. By tuning ΔE with an external stimulus it would be possible to modulate the spin polarization of the interface and consequently the effects on the magnetoresistance signal of the device.

Another way to tune the interface spin polarization is to change the SAM's head and anchoring group. Accurately choosing and combining their properties it should be possible to customize the interface metal/molecule hybridization. For example, it has been proposed that a selection of the orbitals involved in the tunnel current could be achieved by choosing the anchoring group: thiols would select "s" bands, while –CN group would select "d" bands [14].

In conclusion, we have seen in this section examples of the many tailoring opportunities offered by SAMs and the possibility to combine them by the independent

tuning of the molecular head, body and anchoring group. These properties make us consider this system as a very promising approach for the metal/molecule interfacial studies and tunability, thus envisaging the future possibility to engineer at the molecular level the spintronic properties of these devices.

4.2 How to Contact Self-Assembled Monolayers

Despite the very promising properties presented by SAMs, their spread diffusion in the organic/molecular spintronics field is still extremely limited. One of the main issues that may have prevented their diffusion until now is probably the difficulty to electrically connect them, added to the oxidation problems associated with ferromagnetic electrodes. Indeed most of the techniques usually rely on Au. Making a contact is not a trivial task since molecules are soft and the most conventional ultra-high vacuum based methods are likely to damage the molecules when used to contact soft thin films [15]. Few examples of the most common alternative techniques used to contact SAMs and single molecules will be presented here below. The ones related to spintronics will be discussed more in detail in Chap. 5.

4.2.1 Examples of Contacting Methods

Probably the first technique that has been historically used to contact organic molecules was the one introduced by Mann and Kuhn [16] in 1971 when they used a Hg drop to contact an aliphatic monolayer deposited on Al.

Nowadays, the use of a **liquid metal** as top electrode is largely diffused since it is a soft, fast and easy technique (Fig. 4.5). The most common choice as liquid metal is Hg since it presents a large surface tension that avoids its diffusion through the molecular layer. Despite its practicality, this technique can unfortunately not be used for our purpose since it is not compatible with ferromagnetic materials.

Some years later, in the 80s, a new method to contact molecules started to spread. It consisted in the use of a **STM tip** as top electrode (Fig. 4.6a) allowing to probe a very small number of molecules down to almost single molecule studies. This technique represented a strong improvement thanks to its high sensitivity. However,

Fig. 4.5 Schematic illustration of the liquid metal technique used to contact a SAM
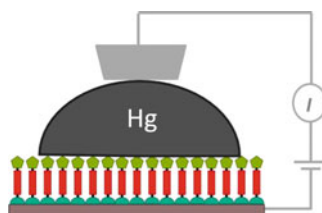
Fig. 4.6 **a** Schematic illustration of the STM technique used to measure a SAM. **b** Schematic illustration of metallic nanoparticle used as top electrode in a SAM junction that is then measured with a STM tip
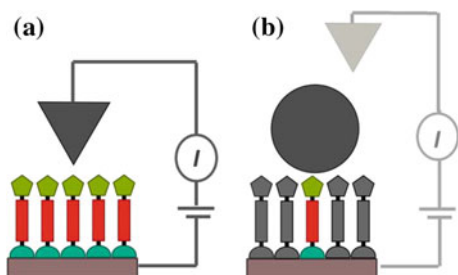
the main drawback of STM experiments is represented by the fact that the electrical 'contact' in STM occurs through the air gap between the molecules and the tip and this makes the estimation of the actual conductance of the molecules difficult.

A solution to this problem has been found for example with the deposition of metal **nanoparticles** over the molecular layer and using them as top electrode. The STM tip is still required to take contact over the nanoparticles (Fig. 4.6b) but this time the metal/molecule contact is direct.

Finally, in the last years many other techniques more or less complicated have been elaborated by the ingenuity of researchers to contact SAMs or single molecules in devices. Examples are: **crossed-wired tunneling junctions** [17], **transfer printing** [18–20], **spin-coating of conductive polymers** [21], **break-junctions** [9, 22–26], **nanopores** [14, 27–30], or **CP-AFM** [31–33]. Some of these techniques are resumed in Fig. 4.7 but more details can be found in good reviews as [15, 34].

4.3 Transport in Self-Assembled Monolayers

In the study of transport properties through self-assembled monolayers, the standard structure is an alkanethiol chain $(CH_3(CH_2)_{n-1}SH)$. This system has been used as test-bed in the literature since it is the simplest one and thus good to be used as a reference. Indeed, properly prepared SAMs form single van der Waals crystals and present a simple classical metal-insulator-metal (M-I-M) tunnel regime when fabricated between metallic contacts due to the large HOMO-LUMO gap of about 8 eV [35, 36]. Tunneling regime is characterized by a weak dependence of the device resistance with temperature.

We are particularly interested in the modelization of this system since we also started our spin transport studies from saturated alkyl-chain based SAMs. First, this allows to validate our system by comparing its electrical characterization with the many results reported in molecular electronics. Second, the tunneling regime allowed to simplify the system and focus the investigation on the metal/molecule interfaces.

A general overview on the transport mechanisms that may apply to molecules has been already presented in Sect. 2.1. Here we will focus on the tunneling regime since it is the one observed in alkyl-chain based SAMs. The main models describing
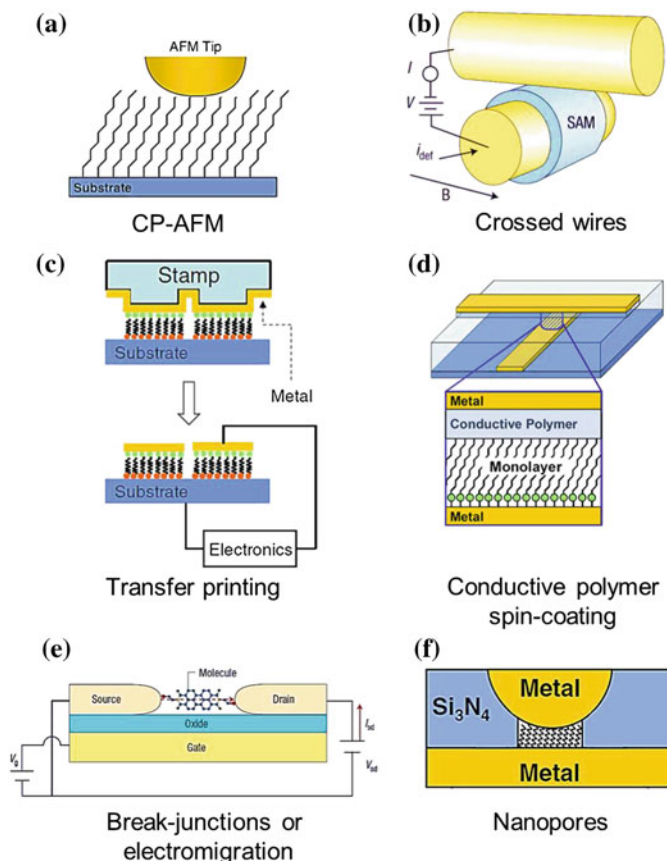
Fig. 4.7 Summary of some of the most popular techniques to contact SAMs. **a** CP-AFM: Contrarily to the STM technique, here a metal-coated AFM tip is placed in direct contact with the monolayer. By controlling the pressures exerted by the tip, one can progress from contact, to deformation of the monolayer, to contact with the substrate. **b** Crossed wires: the SAM is sandwiched between two crossed wires to form the junction. **c** Transfer printing: a metal-coated stamp is brought into mechanical contact with a SAM having a reactive termination group. When the stamp is removed, the pattern is transferred over the SAM since the metal adhesion to the stamp is significantly smaller than the one with the reactive terminal group. **d** Conductive polymer spin-coating: a conductive polymer as PEDOT-PSS is spin-coated over the SAM and acts as top electrode in the junction **e** Break-junction or electromigration: two electrodes are separate by a small gap of ∼1 nm. Molecules are deposited by solution or evaporation and the junction is formed when randomly a molecule grafts between the two electrodes. **f** Nanopores: Electron-beam lithography and a timed reactive-ion etch are used to fabricate a bowl-shaped hole through a suspended Si_3N_4 membrane. The pores have a diameter in the range of 5–10 nm. One first electrode is then deposited by evaporation onto the bowl-shaped side of the sample without filling the hole. Molecules are deposited by solution and finally the device is completed with the top metal evaporation over them. **a**, **c**, **d**, **f** Reprinted from [15], copyright 2008, with permission from Elsevier. **b**, **e** Reprinted by permission from Macmillan Publishers Ltd: Nature Nanotechnology [34], copyright 2006

direct tunneling and their application to molecules will be presented in Sect. 4.3.1. Then, in Sect. 4.3.2 the transition voltage spectroscopy (TVS) will be presented as an alternative tool to extract transport parameters from the analysis of experimental data. Finally, in Sect. 4.4 the dependence of transport properties on the monolayer structure will be discussed.

4.3.1 Introduction to the Main Models of Direct Tunneling

The description of tunneling transport through a molecular barrier is not an easy task. Many effects as the hybridization of the molecular states with the metals or interfacial dipoles play a role on the barrier potential shape making its modelization quite difficult. Nowadays, the precise contribution of all these effects to transport is still unclear and despite different approaches have been proposed in the literature, the satisfactory description of these systems still represents an open challenge.

As we will see below, most of the existing approaches to describe tunneling transport through molecules are based on models borrowed from the field of metallic tunnel junctions and semiconductors inorganic devices. The simplest one is the Simmons model [37] that describes tunnel transport through thin insulating films. However, the adequacy of adapting this model to the description of metal-molecule-metal junctions is controverted. For this reason other approaches incorporate the molecular features right from the start to describe these systems. One example is the coherent tunneling model through a single molecular level.

These two approaches, the one coming from the community of solid state physics (Simmons model) the other coming from chemistry community (single level coherent transport model) will be presented more in detail in the following.

4.3.1.1 Simmons Model

Simmons model was introduced in 1963 to describe the tunnel transport through thin insulating films [37]. This approach adopts the non-interacting free electron approximation and is based on the Wentzel-Kramers-Brillouin (WBK) approximation.

In this model the tunneling current depends on the mean value of the barrier height $\bar{\varphi}$, allowing the simplification of the problem of an arbitrarily shaped potential barrier (Fig. 4.8a) to that of a rectangular one (Fig. 4.8b).

The tunnel current density through a generalized barrier in the tunneling regime is expressed as:

$$J = J_0 \left\{ \bar{\varphi} e^{-A\sqrt{\bar{\varphi}}} - (\bar{\varphi} + eV)\, e^{-A\sqrt{\bar{\varphi}+eV}} \right\} \tag{4.1}$$

where

$$J_0 = \frac{e}{2\pi h(\xi \Delta s)^2} \tag{4.2}$$
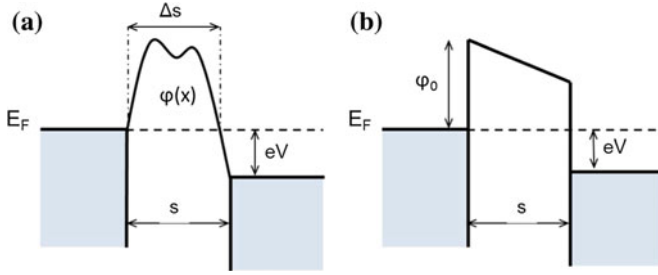
Fig. 4.8 **a** Energy band representation of a metal-insulator-metal junction with a generally shaped potential barrier under a bias V. **b** Simplification of the general potential barrier with a rectangular one under a bias V ($V < \varphi_0/e$)

and

$$A = \frac{4\pi\xi\Delta s\sqrt{2m_e}}{h} \tag{4.3}$$

Δs is the barrier width at the Fermi level of the electrodes, m_e is the free electron mass, V is the applied voltage and h is the Planck constant. Moreover the term ξ is a correction parameter which approaches unity for $V < \bar{\varphi}/e$.

It is possible to simplify the general equation 4.1 to the case of a **rectangular barrier** if we consider $\bar{\varphi} = \varphi_0$, where φ_0 is the height of the rectangular barrier and $\Delta s = s$ is the thickness of the insulating layer.

From Fig. 4.8b one can observe that in the bias regime of $V < \varphi_0/e$, the mean barrier height can be written as $\bar{\varphi} = (\varphi_0 - eV/2)$ and $\xi \simeq 1$.

By substituting this in Eq. 4.1, it becomes:

$$J = \frac{e}{4\pi^2\hbar s^2}\left\{\left(\varphi_0 - \frac{eV}{2}\right)exp\left[-\frac{2(2m)^{1/2}}{\hbar}\left(\varphi_0 - \frac{eV}{2}\right)^{1/2}s\right]\right.$$
$$\left. - \left(\varphi_0 + \frac{eV}{2}\right)exp\left[-\frac{2(2m)^{1/2}}{\hbar}\left(\varphi_0 + \frac{eV}{2}\right)^{1/2}s\right]\right\} \tag{4.4}$$

Approximations

Equation 4.4 can be approximated in two limit cases: when the applied voltage is almost zero (Fig. 4.9a) or more generally when $eV < \varphi_0$ (Fig. 4.9b).

- In the low-voltage range ($V \simeq 0$), as represented in Fig. 4.9a, $\Delta s = s$ and $\bar{\varphi} = \varphi_0$. Equation 4.1 can be thus approximated as shown in [37] as:

$$J \approx \left(\frac{(2m\varphi_0)^{1/2}e^2}{h^2 s}\right)V exp\left[-\frac{2(2m)^{1/2}}{\hbar}(\varphi_0)^{1/2}s\right] \tag{4.5}$$
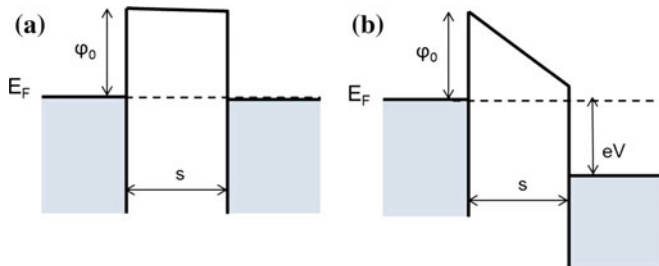
Fig. 4.9 a Energy band representation of a rectangular barrier in the low-voltage range, when the applied bias V $\simeq$ 0. **b** Energy band representation of a rectangular barrier when eV approaches φ_0 value

In this case the tunneling current depends on the barrier width s as $J \propto (1/s)$ $exp(-\beta_0 s)$, where β_0 is the bias-independent decay coefficient:

$$\beta_0 = \frac{2(2m)^{1/2}}{\hbar}(\varphi_0)^{1/2} \tag{4.6}$$

- When the voltage applied increases and eV approaches φ_0 value, always maintaining $V < \varphi_0/e$ (Fig. 4.9b), the first term in Eq. 4.4 becomes dominant on the second one. This equation can hence be approximated as:

$$J \approx \left(\frac{e}{4\pi^2 \hbar s^2}\right)\left(\varphi_0 - \frac{eV}{2}\right)exp\left[-\frac{2(2m)^{1/2}}{\hbar}\left(\varphi_0 - \frac{eV}{2}\right)^{1/2}s\right] \tag{4.7}$$

In this case the current has a quadratic dependence on the barrier width $J \propto (1/s^2)$ $exp(-\beta_v s)$ and β_v, the bias-dependent decay coefficient, is expressed as:

$$\beta_v = \frac{2(2m)^{1/2}}{\hbar}\left(\varphi_0 - \frac{eV}{2}\right)^{1/2} = \beta_0\left(1 - \frac{eV}{2\varphi_0}\right)^{1/2} \tag{4.8}$$

We remark here that β_v decreases as the bias increases, which results from the barrier lowering effect due to the applied bias.

4.3.1.2 Application of Simmons Model to Molecules

To describe the tunneling transport through a molecular layer many approaches start from the Simmons model and try to adapt it to a molecular system. Nevertheless, the adaptation of inorganic models to organic ones is not obvious since the electronic structure of a molecule and an inorganic material are completely different: the first presents discrete levels while the second a continuum of states.

Some adaptations of Simmons model to molecular systems will be presented here below.

1st approach: One first modification to the Simmons model was proposed by the group of M. Reed [38]. In their work, authors performed studies on alkanethiols of different length using the nanopore technique (Fig. 4.10a). This kind of device allowed I(V, T) measurements and the current found was rather insensitive to the temperature thus concluding that the conduction mechanism through alkanethiols was tunneling. Once it was established that coherent tunneling was the dominant transport mechanism, the transport was interpreted by authors in terms of the classical tunneling model through a thin insulating film provided by Simmons with some small adaptations.

An extra fit parameter α was added in order to obtain a fit to the measured data as reported in Fig. 4.10b. Equations (4.4)–(4.8) can thus be rewritten exactly in the same way with just the substitution of:

$$m \rightarrow m\alpha^2 \tag{4.9}$$

The added parameter α is an unitless adjustable parameter that is of the order of 1 for a rectangular barrier and free electron mass (Simmons model). Despite its physical meaning being still under debate, it can be used as a fitting parameter to account for the possibility of non-rectangular barriers or an effective mass, m^*, different from the free electron mass.
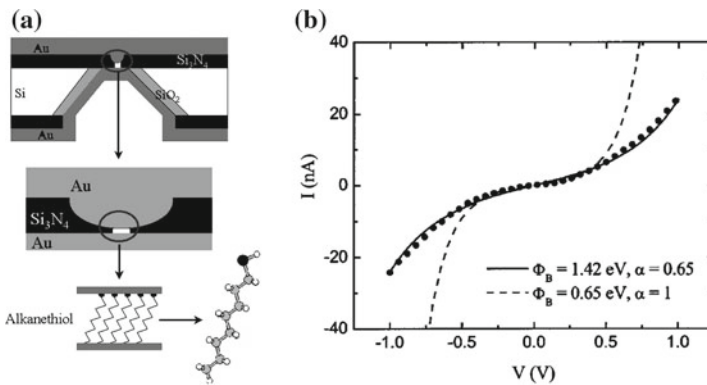
Fig. 4.10   a Schematic and zoom of the nanometer-scale device fabricate by nanopore technique. Authors used this device to perform studies on Au-alkanethiol-Au nanojunctions. **b** I(V) character-istic of a measured Au-C12-Au junction (*circles*) and comparison with fits using different models. *Solid curve* corresponds to the fit performed with the model proposed by authors using the opti-mum fitting parameters: $\varphi_0 = 1.42\,\mathrm{eV}$ and $\alpha = 0.65$. *Dashed curve* is the one obtained using not modified Simmons model ($\alpha = 1$) for a rectangular barrier with $\varphi_0 = 0.65\,\mathrm{eV}$. Reprinted figure with permission from [38]. Copyright 2003 by the American Physical Society

For example, a dodecanethiol (C12) I–V curve is shown in Fig. 4.10b. The fit curve corresponding to a rectangular barrier and $\alpha = 1$ (classical Simmons model) is represented in dotted line and, as one can see, it describes the experimental data only at low bias voltage. On the contrary, the fit curve obtained by using modified Eq. 4.4 and adjusting the parameters φ_0 and α is represented in black line. The best parameters obtained with a nonlinear least-square fitting in this case were $\varphi_0 = 1.42 \pm 0.04$ eV and $\alpha = 0.65 \pm 0.01$. The fitting curve now describes quite well the system, even if a better approximation is still obtained at low bias voltage.

2nd approach: Another modification to Simmons model was proposed by Akkerman et al. [39]. Authors started from the idea that, despite Simmons model is commonly used to describe SAMs systems, there are some points that are not completely satisfactory.

First of all, the attempt to fit the results with a rectangular barrier fails to describe the high-bias regime. This conclusion has been drawn in several analyses of the transport through alkanethiol [40, 41] and this is the reason why α was used as an adjustable parameter in the first place (Fig. 4.10b).

Second, the value obtained for the barrier height is certainly small compared to the expectations. φ_0 represents the energy difference between the Fermi level of the electrodes and the nearest molecular energy level in the molecule. For a system formed by Au contacts and alkanes it is expected to lay between 4 and 5 eV [42].

As a possible solution, authors showed [39] that the description of the transport through SAMs of alkenethiols can be improved by including the effect of the image potential in the Simmons model. In this way it is possible to describe the transport in the experiments up to 1 V by using a single effective mass and a barrier height.

Incorporating the image force clearly reduces the height and width of the potential barrier as shown in Fig. 4.11a. The image potential V_i at a distance x from the Au electrode was approximated as [37]:

$$V_i = -1.15\lambda \frac{s^2}{x(s-x)} \tag{4.10}$$

where

$$\lambda = \frac{e^2 \ln 2}{8\pi\varepsilon\varepsilon_r s} \tag{4.11}$$

Here ε is the vacuum permittivity and ε_r is the relative dielectric constant of the insulating monolayer. In general, the smaller the value of ε_r, the lower the tunnel resistivity. Incorporating the image potential in the expression of the potential barrier height at a position x one obtains:

$$\varphi(x) = \varphi_0 - eV\frac{x}{s} - 1.15\lambda \frac{s^2}{x(s-x)} \tag{4.12}$$
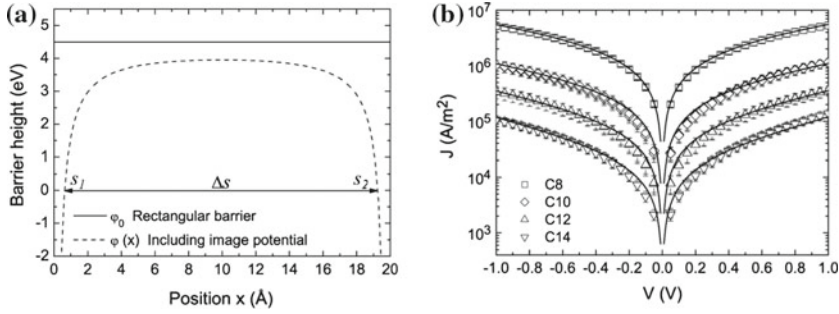
Fig. 4.11 **a** Representation of the effect of the image force on a rectangular potential barrier. The rectangular barrier of 4.5 eV (*solid line*) is lowered and rounded at the corners due to the image force (*dashed line*). The barrier width Δs is also reduced in comparison to the one of the rectangular barrier. **b** Current density J plotted versus the applied voltage V for four different molecule length (from C8 to C14). In *solid lines* are reported fittings performed using Simmons model and including the image potential with a dielectric constant $\varepsilon_r = 2.1$. Figure reprinted with permission from [39]. Copyright (2007) National Academy of Sciences, USA

and the mean value can be written as:

$$\bar{\varphi} = \varphi_0 - eV\frac{s_2 - s_1}{2s} - \left[1.15\lambda\frac{s}{s_2 - s_1}\right] \times \ln\left[\frac{s_2(s - s_1)}{s_1(s - s_2)}\right] \tag{4.13}$$

where s_1 is the distance between the potential barrier at the Fermi level of the contacts and the Au electrode at $x = 0$, and s_2 is the distance from the Au electrode to the potential barrier at the top electrode (see Fig. 4.11). The width of the barrier Δs at the Fermi level of the Au contact is given by $\Delta s = s_2 - s_1$.

To calculate the tunnel current density through the system authors considered the Simmons Equation 4.1:

$$J = J_0(\bar{\varphi}e^{-A\sqrt{\bar{\varphi}}} - (\bar{\varphi} + eV)e^{-A\sqrt{\bar{\varphi}+eV}}) \tag{4.14}$$

where now $\bar{\varphi}$ is the mean value of the barrier height as calculated in Eq. 4.13.

To apply this model it is first necessary to know the dielectric constant ε_r. By accurate impedance measurements, authors estimated $\varepsilon_r \approx 2.1$ for an alkanedithiol monolayer. Then it is possible to calculate the strength of the image potential at position x in the potential barrier by using Eq. 4.10. As one can see in Fig. 4.11a, the resulting potential barrier is rounded at the corners and the total area under it is largely reduced compared to the initial rectangular one. In total, these effects strongly enhance the probability for a charge carrier to tunnel through the barrier.

The two fit parameters that are used for the final modelization are: φ_0 that corresponds to the initial rectangular potential barrier height without image force incorporated, and m_e^* that is the electron effective mass. In these measurements the authors obtained barrier heights φ_0 ranging from 5.59 eV for C8 to 3.62 eV for

C14. Moreover, independently on the molecular length, the data measured were well described by using only one unique electron effective mass of $m_e^* = 0.28 m_e$ as shown in Fig. 4.11b.

In this way it was possible to simultaneously describe both the low (<0.3 V) and high (> 0.3 V) bias regime with the Simmons model, without the necessity to introduce the "artificial" parameter α.

4.3.1.3 Single Level Coherent Transport Model

Despite the previous adaptations of Simmons model being quite popular in molecular electronics, the use for molecules of a model developed for inorganic materials is quite questionable since molecules present discrete levels instead of a continuum of states and this produces hybridization and coupling effects that are not taken into account on the potential barrier. One other approach coming from the chemistry community is to use models that incorporate the molecular features from the beginning.

As described in Sect. 2.2, the hybridization of the molecular orbitals and the metallic states leads to a broadening of the molecular levels that depends on the strength of the metal-molecule coupling. In principle, different molecular orbitals can participate in the electron transport simultaneously. However, there are many situations where one level (HOMO or LUMO) lies closer to the Fermi level of the metal and therefore dominates the transport in a certain voltage range (Fig. 4.12). This situation can be described for example with the single-level resonant tunneling model.

As shown in Fig. 4.12, the level position is denoted by ε_0, measured with respect to the Fermi energy of the electrodes. The position of this level depends on the voltage applied across the junction and on the way the voltage drops at the interfaces. It is important to remark here that ε_0 is the equivalent of φ_0 in the Simmons model. We use these different notations to respect the conventions usually adopted from chemistry and solid state communities and avoid confusion when consulting the literature, but it is important to remind that the physical meaning is the same.
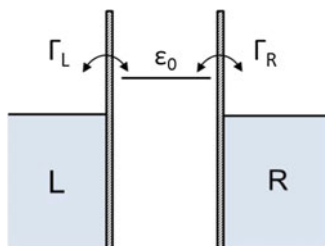
Fig. 4.12 Level scheme in a metal-molecule-metal junction in the simple case where transport is dominate from a single level in the molecule at an energy ε_0. While molecular levels are discrete, metal electrodes posses a continuum of states that is filled up to the Fermi energy. The molecular coupling with the metal at the interfaces is represented by Γ_L and Γ_R. Figure adapted from [43]

The other key parameters of this model are the scattering rates Γ_L, Γ_R which take into account the strength of the coupling to the metal electrodes. They have dimension of energy and they determine the lifetime or broadening of the resonant level (see Sect. 3.2.1).

Following the Landauer approach [44], the I–V characteristic can be written as:

$$I(V) = \frac{2e}{h} \int_{-\infty}^{\infty} dE\, T(E, V)[f(E - eV/2) - f(E + eV/2)] \quad (4.15)$$

where the factor 2 is due to the symmetry of the problem, $f(E)$ is the Fermi function and $T(E, V)$ is the energy and voltage dependent transmission coefficient given by the Breit-Wigner formula:

$$T(E, V) = \frac{4\Gamma_L\Gamma_R}{[E - \varepsilon_0(V)]^2 + [\Gamma_L + \Gamma_R]^2} \quad (4.16)$$

Here the scattering rates are assumed to be energy and bias independent. This is usually a good approximation for noble metals like gold with a rather flat DOS around the Fermi energy.

In the zero temperature limit, the integral of Eq. 4.15 can be resolved analytically and the current can thus be written as:

$$I(V) = \frac{2e}{h} \frac{4\Gamma_L\Gamma_R}{\Gamma} \left[\arctan\left(\frac{eV/2 - \varepsilon_0}{\Gamma}\right) + \arctan\left(\frac{eV/2 + \varepsilon_0}{\Gamma}\right) \right] \quad (4.17)$$

where $\Gamma \equiv \Gamma_L + \Gamma_R$.

A typical curve described by Eq. 4.17 is shown in Fig. 4.13a. I(V) curve has been numerically calculated assuming a level position of $\varepsilon_0 = 1$ eV and equals values of $\Gamma_{L,R}$ at both electrodes. From this picture one can see that three different regions can be distinguished, corresponding to the situations represented in Fig. 4.14.

At low bias the current is low and the situation corresponds to Fig. 4.14a ($eV \ll |\varepsilon_0|$). The second region corresponds to the resonant condition (Fig. 4.14b) when the level is aligned with the chemical potential of one of the electrodes and $eV/2 = \varepsilon_0$. This leads to a change of slope in the I–V curve that can be seen in the conductance plot in Fig. 4.13b as the two peaks at $eV = 2\varepsilon_0$. Finally, when the bias is larger than $2|\varepsilon_0| + \Gamma$ (Fig. 4.14c), the current reaches the value $I_{sat} = (2e/h)\, 4\pi\Gamma_L\Gamma_R/\Gamma$.

4.3.2 Transition Voltage Spectroscopy (TVS)

In the previous section the difficulty to describe the tunneling mechanism in a molecular system was highlighted. Despite different models have been developed until now, an unique one able to satisfactory describe the whole system is still missing.

Alternatively, another approach that is not based on the I(V) curves fitting also exist to evaluate some of the characteristic parameters of a molecular junction, as its
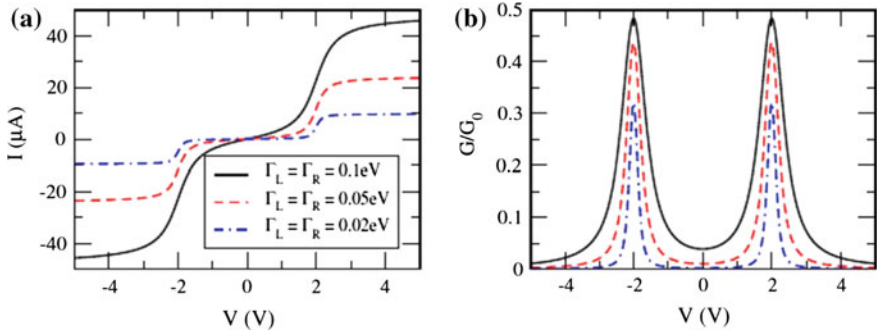
Fig. 4.13 a Typical I(V) characteristic in the single level coherent transport model calculated considering a level position $\varepsilon_0 = 1$ eV and at room temperature ($k_B T = 0.025$ eV). Different curves are represented, corresponding to different scattering rates that are assumed to be symmetric at both interfaces. **b** Conductance $G = dI/dV$ calculated respectively for the different I(V) of figure (**a**) and normalized by $G_0 = 2e^2/h$. Figure reprinted with permission from [43], copyright 2010 by World Scientific Publishing Co. Pte. Ltd
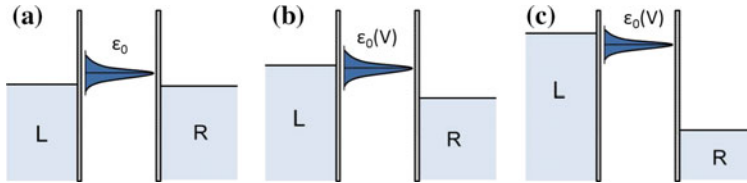
Fig. 4.14 Level alignment for different values of applied voltage in the single level coherent transport model for symmetric coupling. **a** Low bias region, when $eV \ll |\varepsilon_0|$. **b** Resonant situation, when the level is aligned with the chemical potential of one of the electrodes and $eV/2 = \varepsilon_0$. **c** High bias region where the current saturates. Figure adapted from [43]

barrier height φ_0 (=the level position ε_0 in the language of chemistry community). This approach consists in the transition voltage spectroscopy (TVS).

During the last years the TVS technique has become a very popular tool in molecular electronics since it allows to calculate in a fast and easy way φ_0: the energy shift between the Fermi level of the electrode and the molecular orbital (HOMO or LUMO). This method was firstly proposed by Beebe et al. [45] where they stated that the position of the nearest molecular level in a two-terminal device could be directly derived from I–V measurements and corresponded to the minimum of the Fowler-Nordheim (FN) plot ($\ln(I/V^2)$ versus $1/V$) as shown in Fig. 4.15. Author's interpretation of FN curve is based on the Simmons model. As it is schematically represented in the inset, the region (a) of the curve corresponds to a regime where the applied bias is higher than the barrier height ($eV > \varphi_0$). This region is called Fowler-Nordheim tunneling regime: the barrier becomes triangular and $I \propto V^2 \exp(-A/V)$, where A is a positive constant.
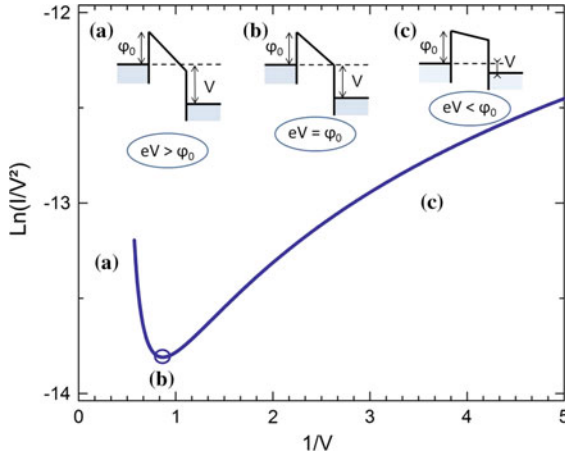
Fig. 4.15 Example of a typical Fowler-Nordheim curve obtained from an I–V characteristic calculated for a symmetric junction and a Lorentzian transmission function with $\varepsilon_0 = 1\,\text{eV}$ and $\Gamma = 0.1\,\text{eV}$. On the *top* of the graph are represented the energy band schemes for the different regions of the curve. **a** High bias regime where $eV > \varphi_0$. The potential barrier is largely deformed and becomes triangular. **b** Minimum point in the Fowler-Nordheim curve that corresponds to the situation where $eV = \varphi_0$. **c** Low bias region when $eV < \varphi_0$, the barrier is trapezoidal and not largely deformed

On the contrary, region (c) corresponds to a direct tunneling regime where the applied bias is low ($eV < \varphi_0$) and the barrier here is trapezoidal. According to Simmons model, in this case the relation between bias and current is linear ($I \propto V$).

Between these two limits, there is the minimum (b) called "V_t" that corresponds to the voltage transition between the direct tunneling regime and the Fowler-Nordheim conduction. As shown in the picture, in this case the applied bias compensates exactly the barrier height φ_0 and it is possible to write a direct relation between the transition voltage and the barrier height: $eV_t = \varphi_0$.

After the first interpretation based on Simmons model, in the following years TVS has been reinterpreted using for example a coherent transport model based on a single level [46] or ab-initio calculations [47] to refine it and take into account the asymmetries in the coupling of the molecule to the two electrodes. This ends in a relation between the bias transition and the barrier height as $eV_t = \alpha\,\varphi_0$ where α (not to be confused with the correction parameter in Reed's approach) is a parameter that takes into account the symmetry of the system with values in general between $0.8 < \alpha < 2$. In the case of a simple symmetric structure $\alpha = 2$.

Finally, I. Bâldea pointed out that the transition voltages $V_{t\pm}$ for both bias polarities ($V \gtrless 0$) should be used to properly determine the energy level ε_0 ($=\varphi_0$) of the participating molecular orbital and the bias asymmetry γ in molecular junctions [48, 49] as represented in Fig. 4.16. The formulas found by the author to estimate ε_0 and γ as a function exclusively of $V_{t\pm}$ are:
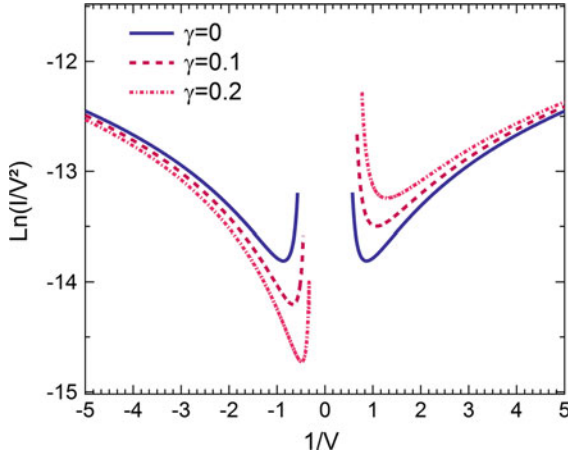
Fig. 4.16 Effect of junction symmetry ($\gamma = 0$) and asymmetry ($\gamma \neq 0$) on Forwler-Nordheim curves. I–V characteristics calculated for symmetric ($\gamma = 0$) and asymmetric ($\gamma = 0.1$, $\gamma = 0.2$) junctions with a Lorentzian transmission function where $\varepsilon_0 = 1\,\text{eV}$ and $\Gamma = 0.1\,\text{eV}$

$$|\varepsilon_0| = 2\,\frac{e\,|V_{t^+}V_{t^-}|}{\sqrt{V_{t^+}^2 + 10|V_{t^+}V_{t^-}|/3 + V_{t^-}^2}} \tag{4.18}$$

$$\gamma = \frac{sign\,\varepsilon_0}{2}\,\frac{V_{t^+} + V_{t^-}}{\sqrt{V_{t^+}^2 + 10\,|V_{t^+}V_{t^-}|/3 + V_{t^-}^2}} \tag{4.19}$$

One main limitation to the application of TVS method is represented by the difficulty for molecular devices to reach without damages the often high voltage (V_t) required to achieve resonant tunnel and estimate ε_0 from FN plot.

In this regard, one improvement was suggested by Markussen et al. [50] who proposed a method to determine the molecular level position at a voltage lower than the resonant one. This could be achieved by plotting a generalized Fowler-Nordheim curve as $\ln(I/V^\kappa)$ versus $1/V$ with $1 < \kappa \leq 2$ and finding the minimum $V_t(\kappa)$ of this plot.

Equations 4.18 and 4.19 can be thus generalized as [48]:

$$|\varepsilon_0| = \frac{\kappa(\kappa + 1)}{\kappa^2 - 1}\,\frac{e\,|V_{t^+}(\kappa)V_{t^-}(\kappa)|}{\sqrt{V_{t^+}^2(\kappa) + 2\frac{\kappa^2+1}{\kappa^2-1}|V_{t^+}(\kappa)V_{t^-}(\kappa)| + V_{t^-}^2(\kappa)}} \tag{4.20}$$

$$\gamma = \frac{sign\,\varepsilon_0}{2}\,\frac{V_{t^+}(\kappa) + V_{t^-}(\kappa)}{\sqrt{V_{t^+}^2(\kappa) + 2\frac{\kappa^2+1}{\kappa^2-1}|V_{t^+}(\kappa)V_{t^-}(\kappa)| + V_{t^-}^2(\kappa)}} \tag{4.21}$$
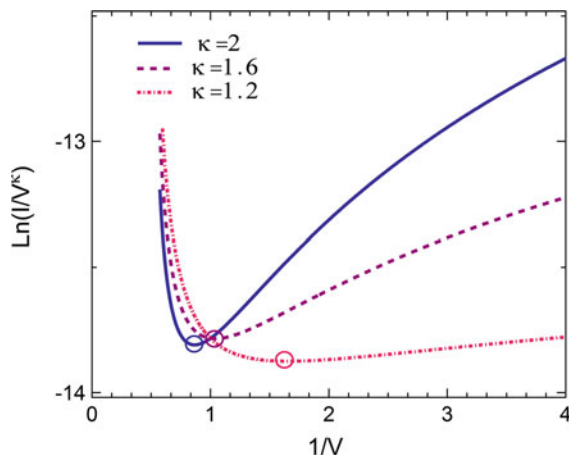
Fig. 4.17 Comparison of FN-plots for a same I–V characteristic plotted with different values of the exponent κ. I–V curve is calculated for a symmetric junction and a Lorentzian transmission function with $\varepsilon_0 = 1\,\text{eV}$ and $\Gamma = 0.1\,\text{eV}$. For decreasing κ values $V_t(\kappa)$ also decreases, while the error on its estimation becomes larger

The behaviour of $V_t(\kappa)$ in the FN-plot for different values of exponent κ is shown in Fig. 4.17. As one can see, $V_t(\kappa)$ is shifted towards lower voltages for smaller κ values. Despite lower transition voltages $V_t(\kappa)$ allow easier measurements in experiments, as one can observe in the curve, the parameters calculation is more affected by the imprecision on the minimum position.

4.4 Application to Devices: The Alkyl-Chain Case

In Sect. 4.3 we discussed standard solid state physics and molecular models to describe the direct tunneling transport through SAMs based systems. Here we will see how these models have been applied to the description of real devices and we will focus on the canonic case of alkyl-chain SAMs.

4.4.1 Where Does the Electron Go?

The first consideration to do before applying the transport models to a real device is about the real path that electrons travel when tunneling through a molecular layer. In this regard, it is generally assumed that the dominant charge transport mechanism in alkanethiol SAMs is the "through-bond" (or *intramolecular*) tunneling, in which the current follows the σ-bond overlaps along the backbone of the alkyl chain (Fig. 4.18a).
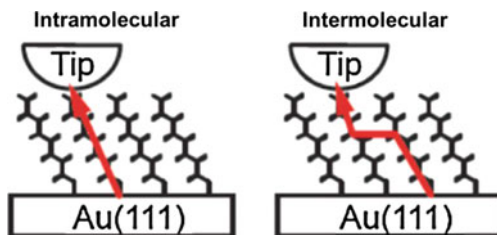
However, in an ensemble of molecules a contribution to transport is also given by the *intermolecular* coupling through van der Waals interactions. This can provide chain-to-chain tunneling (or "through-space" tunneling) which involves lateral charge "hopping" between adjacent chains as it is schematically represented in Fig. 4.18b. It is clear from this that the estimation of the "effective barrier thickness" is not evident.

Different studies have been performed in order to investigate the separate intra- and intermolecular contribution to tunneling transport.

For example, Slowinski et al. [52, 53] demonstrated that intramolecular tunneling is the main transport contribution by measuring the current through an alkanethiol SAM as a function of the monolayer thickness. To do that, they changed the barrier thickness by separately varying: (i) the number of carbon atoms in the alkane chain and thus the monolayer length; (ii) the tilt angle of the molecules with respect to the surface by increasing the load of the Hg top electrode.

In the first scenario, authors found that decreasing the molecular chain length resulted in an exponential increase of the tunneling current with a decay coefficient $\beta = 0.96$ Å^{-1}. In the second scenario, the tunneling current increased with the molecules tilt, but this value was much weaker than the previous one: $\beta = 0.12$ Å^{-1}. This proves that current predominantly follows the backbone of the molecule (intramolecular transport) with a small chain-to-chain contribution.

For what concerns the intermolecular contribution, studies generally concord that conduction of alkanethiol junctions is higher for more tilted configurations and this effect is more pronounced the longer is the chain length [54, 55]. This phenomenon is explained as an increase of the intermolecular contribution and, in some case [54], by the concurrent change of the effective interface dipole that brings HOMO resonance closer to the Fermi energy thus enhancing the conduction with molecule tilt.

4.4.1.1 Current Dependence on Molecule Length

The application of solid state physic models to real devices usually implies the study of transport dependence with the molecular chain length in order to extract the decay coefficient β. On the contrary, the application of molecular models is normally based on TVS analysis to extract the molecular level position ε_0. In the following we will see some examples starting from the estimation of β value. Results reported in the literature are summarized and compared in Table 4.1.

Many studies have been performed in order to characterize the transport dependence on molecular chain length and a figure of merit in this regard is the decay coefficient β. Lower β values mean less attenuation of the current per unit distance and consequently a more efficient tunneling. This parameter can be analytically estimate by Eq. 4.6 where the free electron mass m is substituted with $m\alpha^2$. Otherwise, it can be directly calculated by data slope when the current or resistance of the junction is plotted as a logarithmic function of the molecular length.

The current density J through a molecular tunneling barrier decreases exponentially with increasing molecular length as $J \propto \exp(-\beta d)$, where d is the length of the molecule in Å and β is the decay coefficient expressed in Å^{-1}. When the resistance of the molecule (R_{mol}) is plotted versus the number of the carbon atoms (N), the relation becomes $R_{mol} = R_0 \exp(\beta_N N)$, with R_0 the contact resistance and β_N the decay coefficient expressed in C^{-1}.

A conversion of β expressed in C^{-1} to Å^{-1} is not evident. Normally the carbon-to-carbon distance is used for this conversion ($d_{C-C} = 1.25$ Å), however the different intra- and intermolecular transport contributions, that could vary the carriers path, should be taken into account to obtain an accurate value.

One example of transport study through three different alkanethiol lengths (C8, C12 and C16) [38] is reported in Fig. 4.19. Here the tunneling current densities multiplied by molecular length (Jd at low bias and Jd^2 at high bias) are plotted versus the chain length.

As one can see, the tunneling current decreases exponentially with the molecular chain length. Moreover, the parameter β is found to be almost independent on bias in low bias range ($V \lesssim 0.5\,\text{V}$) and in this case its average value is $\beta \approx 0.77\text{Å}^{-1}$. Many other results are reported in the literature [31, 38, 53, 56–58] and the current is found to decrease exponentially with increasing molecule chain length in all of them. For simplicity, a comparison of the measured decay coefficient β for alkane-based molecules is reported in Table 4.1.
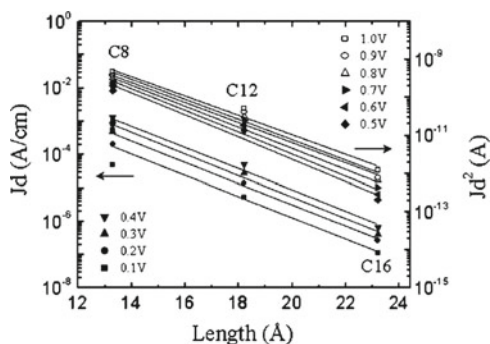
Fig. 4.19 Semi-logarithmic plot of the tunneling current density multiplied by the molecular length at low bias (Jd) and high bias (Jd^2) as a function of the chain length in alkanethiol molecules. Tunneling current is exponentially decreasing with the increase of the molecular length. Reprinted figure with permission from [38]. Copyright 2003 by the American Physical Society

Table 4.1 Summary and comparison of β, β_N and φ_0 characteristic parameters reported in the literature by different research groups for alkane-based molecules

Junction	$N_{Carbons}$	Technique	β (Å^{-1})	β_N (C^{-1})	φ_0 (eV)	N_{mol}	Reference
Au-S/CH$_3$-Au	9–16	STM	1.2	1.5		1	[59]
Au-S/S-Au	6, 8, 10	STM	0.87	1.09		1	[13]
Au-S/S-Au	6, 8, 9	STM	0.41	0.51		1	[60]
Au-S/S-Au	6, 8	STM	0.79	0.99		1	[61]
Au-S/S-Au	6, 8, 10	STM	0.8 ± 0.08	1.04 ± 0.05	5 ± 2	1	[23]
Au-NH$_3$/NH$_3$-Au	2-8	STM	0.69	0.86		1	[9]
Au-S/S-Au	8, 10, 12	Nanopart. AFM	0.46 ± 0.02	0.57	1.3-1.5	1	[62]
Au-S/S-Au	8, 10, 12	Nanopart. AFM	0.76	0.95		1	[63]
Au-S/CH$_3$-Au	4–8	Theory	0.76	0.95	1.3–3.4	1	[64]
Au-S/CH$_3$-Au	8	Theory	0.79	0.99		1	[42]
Au-S/CH$_3$-Au	4, 8, 12	Theory	0.76	0.95 ± 0.01			[65]
Au-S/CH$_3$-Au/Au-CH$_3$/S-Au	6, 10, 12	Nanopart. bridge	0.70	0.87		10^2	[66]
Au-S/CH$_3$-Au	6, 8, 10, 12	CP-AFM	0.81	1.01		10^3	[31]
Au-S/CH$_3$-Au	4–10, 12	CP-AFM	1.1	1.19	2.2	10^2–10^3	[33]
Au-S/CH$_3$-Au	12, 14, 16, 18	CP-AFM	1.07	1.16	2.2	10^2–10^3	[33]
Au-S/CH$_3$-Pt	8–10	CP-AFM	0.94	1.197 ± 0.003		10^2–10^3	[67]
Au-S/CH$_3$-Pt	9–12	CP-AFM	0.93	1.187 ± 0.007		10^2–10^3	[67]
Au-S/CH$_3$-Au	8–10, 12–14	CP-AFM	0.64	0.8 ± 0.2	2.3	10^2–10^3	[68]
Au-S/CH$_3$-Au (Au, Ag, Pt)	4, 6, 8	CP-AFM	0.88	1.16	0.73	10^2–10^3	[69]
Au-S/S-Au (Au, Ag, Pt)	4, 6, 8	CP-AFM	0.88	1.16	0.73	10^2–10^3	[69]
Au-S/CH$_3$-Pt	16	Tuning fork AFM	1.37 ± 0.03	1.71	1.8		[70]
Au-S/CH$_3$-Au	8, 12, 16	Nanopores	0.79 ± 0.01	0.83	1.4	10^3	[38]

(continued)

Table 4.1 (continued)

Junction	$N_{Carbons}$	Technique	β (Å^{-1})	β_N (C^{-1})	φ_0 (eV)	N_{mol}	Reference
Au-S/CH₃-Au	8, 12, 16	Nanopores	0.86 ± 0.02	*1.08*		10^4	[71]
Au-S/CH₃-Au	6, 12, 16	Thermally evap.	*0.86*	1.08		10^7	[72]
Au-S/S-Hg	9–12, 15, 16, 18	Hg-junction	0.85	1.06		10^{11}	[73]
Au-S/S-Hg	16, 18, 20, 22, 24	Hg-junction	*0.81*	1.01		10^{11}	[73]
Au-S/S-Hg	20, 24, 28	Hg-junction	*0.68*	0.85		10^{11}	[74]
Hg-S/CH₃-SiO₂/p-Si	4, 6, 8, 10, 12	Hg-junction	087 ± 0.1	*1.09*	2 ± 0.2	10^{12}	[57]
Hg-S/CH₃-p-Si	4, 6, 8, 10	Hg-junction	0.55 ± 0.06	*0.69*	0.74–0.87	10^{12}	[57]
Hg-S/CH₃-SiO$_x$/p-Si	6, 8, 10, 12	Hg-junction	*0.50*	0.63 ± 0.1	0.46 ± 0.05	10^{12}	[58]
Al/Al₂O₃-PO₃H₂/CH₃-Hg	8, 10, 12	Hg-junction	*1.07*	1.34 ± 0.004		10^{11}	[75]
Al/Al₂O₃-PO₃H₂/CH₃-Hg	12, 14, 16	Hg-junction	*0.61*	0.77 ± 0.05		10^{11}	[75]
p⁺⁺-Si-C/C-Hg	14, 16, 18	Hg-junction	0.84 ± 0.05	*1.05*	2.3 ± 0.3	10^{11}	[76]
Ag-monothiol₁/monothiol₂-Hg		Hg-junction	0.87 ± 0.1	*1.09*	2.1	10^{11}	[40]
Hg-monothiol₁/monothiol₂-Hg		Hg-junction	0.71 ± 0.08	0.89 ± 0.1		10^{11}	[77]
Hg-monothiol₁/monothiol₂-Ag		Hg-junction	*0.87*	*1.09*	4–4.8	10^{11}	[41]
Hg-S/CH₃-Hg	8, 10, 12, 14, 16, 18	Electrochemical	0.91 ± 0.08	1.14		10^{11}	[53]
Au-S/CH₃-Au	6–10	Electrochemical	0.97 ± 0.04	1.21 ± 0.05		10^{11}	[78]
Au-S/CH₃-Ferrocene	8–11, 16	Electrochemical	0.85	1.1		10^{11}	[79]
Au-S/CH₃-PmPV	8, 10, 12, 14, 16	Large area junct.	*0.90*	1.13		10^{11}–10^{12}	[80]
Au-S/SH-PEDOT	8, 10, 12, 14	Large area junct.	0.66 ± 0.06	*0.83*		10^8–10^{10}	[21]
Al₂O₃-O-CO/CH₃-Au	17–22	PALO	0.68	0.85		10^{12}	[81]
LSMO-PO₃H₂/CH₃-Co	10–18	Nanoindentation	0.90	1.13	(This work)	10^3–10^4	[82]

Data are collected for different molecular junctions and, for a better comparison, when not reported by authors β values are transformed from C^{-1} to Å^{-1} and vice versa considering a distance $d_{C-C} = 1.25$ Å^{-1}. Calculated β are shown in italics

As one can see, no clear correlation emerges between the different values of β obtained from similar molecular junctions and the different experimental conditions.

The value of the decay factor β is usually found in the range between 0.6 to 1 Å^{-1} even if there are also a number of reports with lower values down to 0.5 Å^{-1} [31, 32, 38, 40, 57, 58, 62, 68, 83, 84] depending on the measurement technique, contact area, binding group, or electrodes.

Additionally, differences in the β value have been reported depending on the transport mechanism involving holes or electron tunneling in the junction. For example, in identical experiments on junctions with Hg and Si contacts, lower β values (0.6–0.7 Å^{-1}) [57, 83] were found with p-Si than with n-Si ($\beta \sim 1.0$ Å^{-1}). This could be explained with a transport at low bias that would involve HOMO level for p-Si junctions and LUMO level for the n-Si ones.

Moreover, it has been also highlighted that the structure and the quality of the monolayer has an influence on its transport characteristics. For example, Levine et al. [75] investigated the dependance of SAMs conductivity with the density of the monolayer. To do that they studied different alkyl-phosphonate chain lengths on Al-AlOx substrates and they highlighted how SAMs with longer alkyl chains (>C12) formed denser and more organized monolayers than SAMs with shorter chains (<C12). They also remarked that junctions with scarcely packed "short" monolayers attenuated the current relatively more efficiently than those with densely packed "long" ones. This is reflected in a higher β value for short molecules ($\beta \simeq 1.34$ C^{-1}) than for longer ones ($\beta \simeq 0.77$ C^{-1}). The worst conductivity in short monolayers is ascribed by the authors to the low density and bad organization that results in an increasing of the intermolecular distances with the consequent significantly lower intermolecular interactions.

Authors also found that "long" monolayer junctions showed strong bias variation of the length decay coefficient β, while in "short" monolayers junctions β is nearly independent on bias.

Finally, in a study reported by Wang et al. [85], authors proposed to separate the contributions of the molecule head, body and anchoring group in the β coefficient in order to refine the system description. With this aim, they suggested a multibarrier tunneling model (MBT) where the metal-molecule-metal junction is divided into three individual barriers: a molecular-chain body and metal-molecule contacts on either side of the molecule as shown in Fig. 4.20a. Using the MTB model they could derive and distinguish the decay coefficients for contact barriers (β_1, β_2) and the contact-dependent and contact-independent ones (β_0, β_{body}). A schematic of this is represented in Fig. 4.20b. The decay coefficient calculated by Eq. 4.6 is thus the average of the different contributions and it can be expressed as:

$$\beta_0 = \frac{\beta_1 d_1 + \beta_{body} d_{body} + \beta_2 d_2}{d_1 + d_{body} + d_2} \tag{4.22}$$

where $d = d_1 + d_{body} + d_2$ is the total barrier thickness.

By comparing measurements on alkanemonothiole and alkanedithiole molecules in Au/SAM/Au devices, authors could estimate the value of β_{body} for an alkane
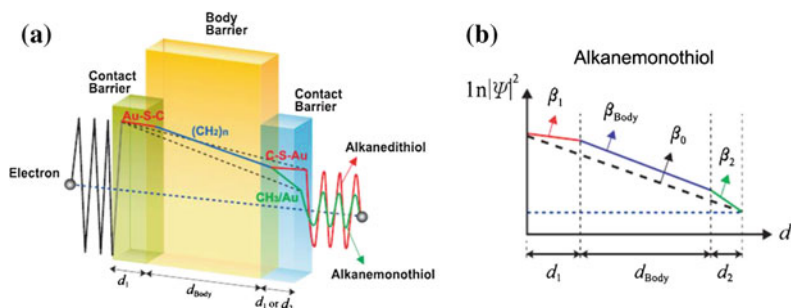
Fig. 4.20 a Schematic representation of the multibarrier tunneling model (MTB). The molecular barrier is divided in three parts: the two at the extremities correspond to the metal-molecule contacts and the one in the middle corresponds to the molecular body. Each part has a different decay coefficient of the current through the barrier. **b** Representation of the different decay coefficients for the different parts of an alkanemonothiol molecule: anchoring group (β_1), body (β_{body}) and head (β_2), as a function of the barrier thickness. In *dotted line* is represented β_0, calculated as Eq. 4.22 that is an average of the different decay coefficient contributions in the barrier. Reprinted figure with permission from [85]. Copyright 2007 by the American Physical Society

chain to $\beta_{body} \approx 0.92\,\text{Å}^{-1}$. This value is independent on contacts and, in principle, it could be used to directly compare experiments on alkane chain based SAMs with different environment at the interfaces. It must be also observed that β_0 value converges to β_{body} for a very long molecule. Moreover, values of β_1 and β_2 also become quite negligible if the contact resistances are either very similar or very small in comparison to the electrical insulating properties of the molecules [32, 40, 57, 58, 77]. It has been highlighted that in alkanethiol and dithiol junctions where molecules are chemisorbed on Au, Hg or Si, the current is almost independent for different contacts and/or electrodes [5].

4.4.1.2 TVS Analysis on Alkanethiol Junctions

Different characterizations of alkanethiols molecules using TVS technique also exist in the literature and some of them are collected in Table 4.2. For example, Beebe et al. [86] compared V_t values in alkanethiol based junctions measured by CP-AFM and crossed-wire tunnel junctions. In this work authors found a transition voltage value around $V_t = 1.22$ V for saturated alkane chains which was independent on the molecular length. This independence was ascribed [87] to the large HOMO-LUMO gap of saturated molecules that is almost constant for different chain lengths. Moreover, V_t value was also found to be independent on the junction area. However, this consideration may not be true if this type of analysis was performed in junctions where metal contacts were deposited by evaporation, as the metal evaporation step likely perturbs the physical structure of the molecules [88] and therefore the electronic structure of the resulting junction [89].

Other works have been also performed on thiol and dithiol alkyl chains and in general the voltage transition measured in different systems is commonly found between 1.2 and 1.9 V [90–93].

Table 4.2 Summary and comparison of some V_t values reported in the literature by different research groups for alkane-based molecules

Junction	Contacting technique	V_t (V)	Reference
Au/alkanethiol/Au	CP-AFM, crossed-wire	1.22	Beebe et al. [86]
Au/alkanedithiol/Au	Electromigration	1.9 ± 0.1	Song et al. [90]
Au/alkanedithiol/Au	Break-junction	1.07–1.42	Guo et al. [91]
Au(NPs)/alkanethiol/Pt	CP-AFM	1.3	Clement et al. [92]
Au/alakanedithiol(DC8)/PEDOT	Soft electrode (polymer)	1.9	Wang et al. [93]
Au/alakanedithiol(DC12)/PEDOT	Soft electrode (polymer)	1.10	Wang et al. [93]
"Unoxidized" interface/alkanethiol	CP-AFM	0.9–1.4	Ricoeur et al. [49]
"Oxidized" interface/alkanethiol	eGaIn, Hg, metal	0.1–0.6	Ricoeur et al. [49]

Finally, another interesting work was reported by Ricoeur et al. [49] where various molecular junctions made by alkyl chains grafted on unoxidized and oxidized electrodes were investigated. In the case of unoxidized electrode/molecule interfaces, authors reported a value for the transition voltage between 0.9 and 1.4 V. Based on some previous works [76, 94] they assumed that the electron transport properties were controlled by the LUMO level. They could explain the discrepancy between the LUMO position estimated by TVS technique ($\varepsilon_0/e \lesssim 2V_t$) and the value estimated by techniques as the inverse photoemission spectroscopy (IPES) ($\varepsilon_0 \simeq 3.35$ eV) with the broadening of the molecular level. This can be understood looking at Fig. 4.21a: TVS is supposed to probe just the tail of the LUMO density of states which is much
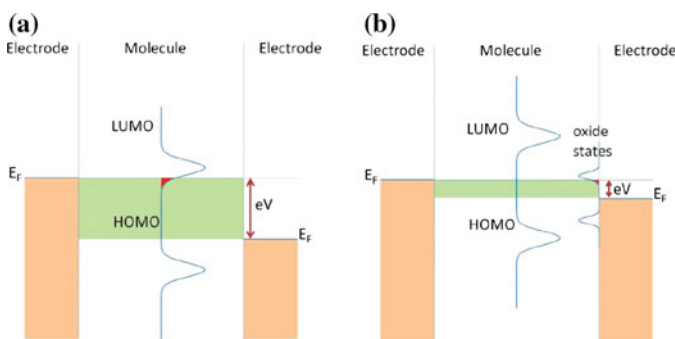
Fig. 4.21 Schematic representation of the energy level alignment corresponding to the V_t bias in the TVS curve **a** in the case of a junction with no oxide; **b** in the case of a junction with an oxide at one interface. Electrodes are represented by the continuum of states up to Fermi energy, molecule by the HOMO and LUMO level and the oxide by some energy levels close to the Fermi energy of the oxidized electrode. Reprinted with permission from [49]. Copyright 2012 American Chemical Society

lower than the edge at 3.35 eV probed by IPES technique. On the contrary, in the case of oxidized interfaces (monolayers formed on slightly oxidized Si) lower transition voltages were found: $V_t = 0.1$–0.6 V. This result was explained by the presence of some surface states at the interface with an energy lower than the HOMO/LUMO levels of the molecules, as represented in Fig. 4.21b. TVS method has been thus delineated also as an useful tool to assess the quality of the molecule/electrode interfaces in molecular junctions.

In conclusion, despite the clear physical interpretation of transition voltage is still under debate [50, 95–98], TVS appears to be a very useful tool to roughly estimate in an empirical way the height of the barrier potential and allow comparison between the largely characterized alkylthiol systems.

4.5 State of the Art on SAMs-Based Magnetic Tunnel Junctions for Spintronics

After having discussed the large characterization of SAMs devices in molecular electronics, we will focus here on their use for spintronics and we will review some of the main efforts done until now to merge these two fields.

From theory: For example, one study compared transport properties of octane and tricene molecules between Ni electrodes and predicted that in the case of transport through molecular states extending throughout the entire molecule (tricene), a much larger magnetoresistance ratio can be achieved (up to 600 %). These effects are due to some hybridization phenomena that reduced π-bonded molecules to an unique molecule connected between two ferromagnetic electrodes [99].

Other theoretical works investigated the metal/molecule interfacial properties of single molecule devices, confirming through simulations the tailoring possibilities of TMR signal depending on the interface hybridization. For example Mandal et al. [100] used a single-particle Green's function approach to investigated the properties of a Ni/1,4-diethynylbenzene/Ni junction as a function of the interfacial distance between the metal and the molecule. In this work authors found that a small change of the interfacial distance by 3 % changes the number of the participating eigenchannels for the antiparallel configuration as well as their orbital characteristics and leads to an alteration of the TMR sign from a positive to a negative value. It was also calculated that, as predicted by the model presented in Sect. 3.2.1, the spin polarization induced on a non magnetic molecule by the hybridization with the magnetic electrodes plays a crucial role on the TMR effects. For example, it was found that in a system with a weaker molecule-electrode interaction, stronger spintronic effects of the spin injection and tunneling magnetoresistance should be observed [101].

The orientation of the molecule with respect to the substrate can also play a role on the magneto-transport properties. In another work investigating a benzene molecule on a Fe(100) surface it was found that the interfacial magnetic properties and spin polarization of this system were controlled by the hybridization between the d orbitals
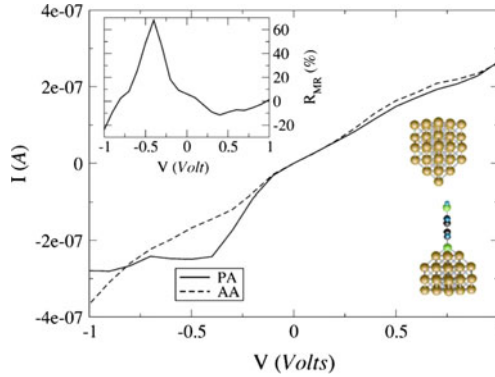
Fig. 4.22 *Right inset* Schematic representation of the considered system: a benzene-thiole-thiolate molecule attached on a Ni [001] surface and probed by a Ni STM tip. In the picture is represented the calculated IV characteristics for such a device in the parallel and antiparallel alignment of the electrode. Around –0.5 V the PA current drastically increases due to a resonant transport. This results in a large positive peak in the MR reaching 70 % (*top inset*). Reprinted with permission from [108]. Copyright 2007, AIP Publishing LLC

of Fe and the *p* orbitals of the molecule. In particular, a spin polarization reversal was observed when molecules change from a perpendicular to a planar position with respect to the surface [102].

Other works also predicted a change of TMR properties by slightly changing the interfacial coupling between the molecule and the metal [103–106]. The role played by external bias voltage on the TMR effect has been also investigated [107]. For example, Rocha et al. [108] performed ab-initio electronic transport calculations for benzene-thiolate molecules chemically attached to a Ni(001) surface terminated by a thiol group and probed by a Ni scanning tunneling microscope tip. With this geometry they demonstrated that the spin current and the magnetoresistance could be drastically changed with bias as the result of a resonance between a spin-polarized surface state of the substrate and the *d*-shell band edge of the tip. In Fig. 4.22 is reported the calculated IV characteristic for such a junction, while in the inset is shown the MR dependence as a function of bias. As one can see, a large positive peak in MR reaching 70 % is predicted for V abound –0.5 V and a negative MR signal can also be observed when tuning the bias.

From experiments: Despite different theoretical works exist predicting the effect of molecular spintronic junctions, very few experimental works have been reported until now probably due to the high technological difficulty to fabricate the device. In addition to the challenge of properly contacting a single molecular layer avoiding any short-circuit, when working with spintronics one also have to face with the ferromagnetic electrodes compatibility issues with wet chemistry and air stability, since most of them get oxidized. Very complicated fabrication techniques are thus required for spintronics SAMs-based devices to avoid all these problems.

One approach adopted to avoid the problem to contact few molecules has been to use magnetic nanoparticles (NPs) self-assemblies deposited between two microscopic contacts. In this system the stabilizing organic ligand surrounding the NPs acts as a tunnel barrier and TMR signal can be measured [109]. For example, Wang et al. [110] fabricated junctions of superparamagnetic Fe_3O_4 NPs self-assembled with alkane molecules of different lengths (C4, C8, C12, C18) as spacer (Fig. 4.23a). In this kind of device authors recorded a MR signal up to 21 % at room temperature (Fig. 4.23b) and this effect was observed to be nearly independent on the molecular length. The resistivity dependence on the molecular length is also reported in Fig. 4.23c. The β value extrapolated for these devices was ~0.2Å^{-1} that is much lower compared to the values reported on Au nanoparticles coated with alkanethiols or Au-alkanethiols-Au junctions (Table 4.1). This difference was ascribed by the authors to a stronger strength in Fe_3O_4–COO^- bonds than in Au–S bonds.

A work on a similar system was also reported by Dugay et al. [111] on Fe NPs surrounded by two types of organic barriers: hexadecylamine (sample I) and a mixture of hexadecylamine/palmitic acid (sample II). The observed MR curves were composed by two different contributions: one at high magnetic field characterized by a linear decrease of the resistance, and the other at low magnetic field (<0.5 T) considered as the real TMR contribution. In the case of sample I TMR persisted up to room temperature with an amplitude of 0.3 %, while it disappeared in the case of sample II.
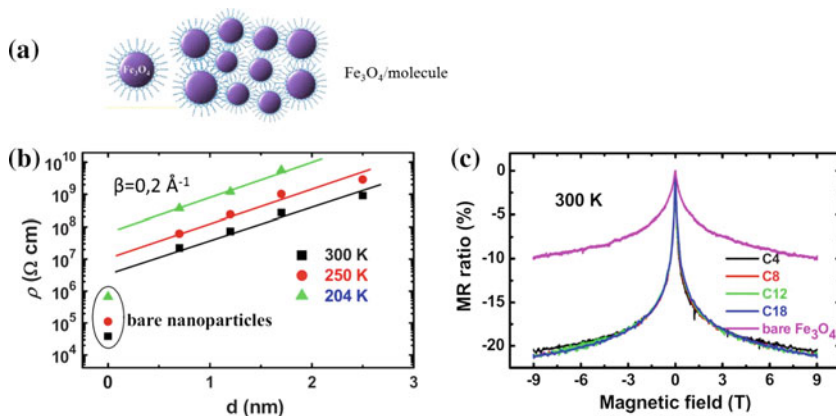
Fig. 4.23 **a** Schematic representation of Fe_3O_4 NPs self-assembled with alkane molecules that act as a tunnel barrier. **b** Resistivity at different temperatures for junctions formed as (**a**) with alkane molecules of different length. The decay coefficient $\beta = 0.2\ \text{Å}^{-1}$ is smaller than the one normally found in Au-alkanethiols-Au system and it is attributed to a stronger strength in Fe_3O_4–COO^- bonds than that in Au–S bonds. **c** MR signal measured at room temperature for junctions with different lengths of the alkane chain. One has to note that this is a high-field MR effect. No difference is observed in the signal for the different molecular lengths. Reprinted with permission from [110]. Copyright 2011, AIP Publishing LLC
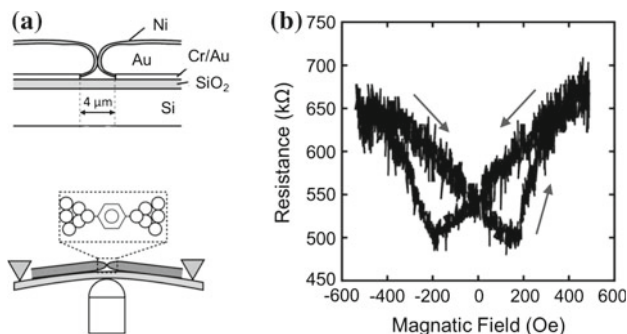
Fig. 4.24 **a** Schematic representation and zoom of an Au break junction coated with Ni which forms a Ni/benzene-1,4-dithiol (BDT)/Ni device. **b** MR signal measured in this device at room temperature. Nevertheless, an AMR signal of the same amplitude was also measured in this system (not shown here) and it could also account for the MR loop shown in (**b**). Figure reprinted from [112]

Another approach to realize molecular spintronic devices is the fabrication of break junctions with ferromagnetic electrodes. This presents the additional difficulty that experiments must be carried out under protect atmosphere to avoid electrodes oxidation. One example is the one reported by Yamada et al. [112] on Ni/benzene-1,4-dithiol (BDT)/Ni junctions (Fig. 4.24a) where –30 % MR signal was recorded as shown in Fig. 4.24b. Nevertheless, it is not clear if this signal is real MR or if it could be ascribed to anisotropic effects of the Ni atomic junction since the AMR signal measured had the same intensity than the observed MR.

Another example is the one reported by Pasupathy et al. [113] on Ni/C$_{60}$/Ni break-junctions where a negative MR signal could be measured.

Finally, other few examples exist on magnetic tunnel junctions with SAMs used as tunnel barrier. In these works authors used the nanopore technique to fabricate nanometric junctions and limit the short-circuits formation problem during top electrode deposition.

One first study was reported by Petta et al. in 2004 [1]. It concerned the investigation of magnetotransport properties in Ni/octanethiol/Ni devices where the diameter of the nanopores was 5–10 nm. Magnetoresistance effects could be observed at low temperature as reported in Fig. 4.25 but the curves were highly degraded. One possible reason invoked by authors is the presence of defects inside the monolayer that involve resonant effects on the magnetoresistance [114, 115]. In Fig. 4.25 is also reported the junction magnetoresistance (JMR) dependence with bias voltage. As one can note the magnitude of JMR strongly depends on V. In general the JMR decreases when bias increases: it is reduced to less than 2 % for $|V| > 40$ mV and in some case it can also change sign. The magnetoresistance is also strongly temperature dependent as shown in Fig. 4.25f.

One second work was presented by W. Wang and C. Richter [2] on the magnetotransport properties of Co/octanethiol/Ni magnetic tunnel junctions fabricated
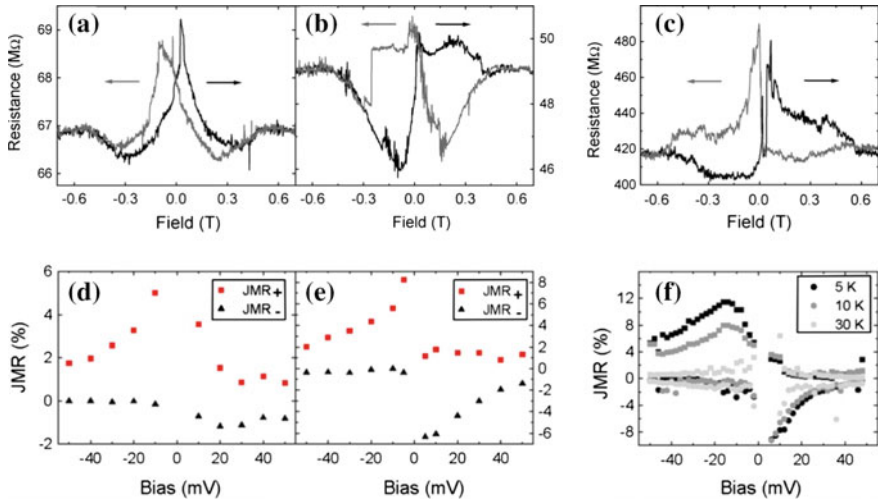
Fig. 4.25 **a**, **b**, **c** Resistance behaviour for three different Ni/octanethiol/Ni junctions as a function of magnetic field applied in the plane of the junction. Measurement are taken at 4.2 K with a bias of 10 mV for sample (**a**) and (**b**) and 5 mV for sample (**c**). Devices are fabricated using nanopore technique. **d**, **e**, **f** Junction magnetoresistance (JMR) behaviour as a function of the applied bias voltage for three different Ni/octanethiol/Ni samples measured at T = 4.2 K. JMR_+ and JMR_- are calculated as: $JMR_+ = (R_{max} - R_P)/R_P$ and $JMR_- = (R_{min} - R_P)/R_P$. **f** JMR_+ (*squares*) and JMR_- (*circles*) dependence on bias is also represented for different temperatures of 5, 10 and 30 K. Reprinted figure with permission from [1]. Copyright 2004 by the American Physical Society
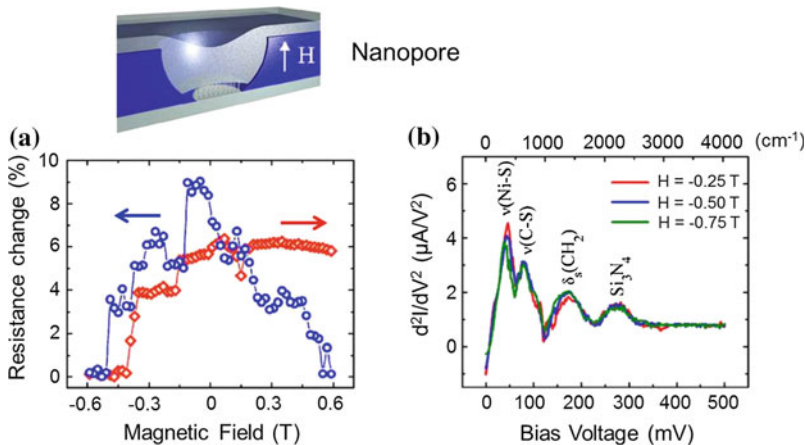
Fig. 4.26 *Top* Schematic representation of the Ni/octanethiol/Co device fabricated by nanopore technique. **a** Plot of the junction resistance change as a function of magnetic field applied perpendicular in a Ni/octanethiol/Co tunnel junction. The arrows denote the field sweeping direction. Measurements are taken at 2 K and with an applied bias of 10 mV. **b** Spin-polarized IETS measurement of the junction under an applied field of –25 T, –0.5 T and –0.75 T. The peaks that appear correspond to the excitation of different vibrational mode in the molecular junction. Figure reprinted from [2]

using the nanopore technique. As reported in Fig. 4.26a, a magnetoresistance effect
was observed at low temperature with a magnetic field applied perpendicular to the
junction. Moreover, authors also performed inelastic electron tunnel spectroscopy
(IETS) measurements in order to provide unambiguous experimental evidence of
the existence of molecules in the fabricated devices. As we will see in Sect. 6.2,
IETS techniques allows to relate electric measurements on the junctions to the exci-
tation of molecular vibrations inside the barrier. These can be identified as peaks
in the d^2I/dV^2 plot as shown in Fig. 4.26b. Nevertheless, a debate arose about the
shift of the IETS peaks measured by authors in comparison to the vibrational values
previously tabulated in the literature [116, 117]. This difference was then partially
explained by Yu et al. [89] with the presence of metallic atoms inside the barrier that
perturbed the molecular vibrations.

Finally, some other studies [118–120] concerning Langmuir-Blodgett films also
tried to measure spin polarization in Self-Assembled Monolayers but they did not
show more convincing magnetoresistance results.

In conclusion, we have seen in this section how molecular spintronic devices
based on self-assembled monolayers are a very promising opportunity for tailoring,
as predicted by theoretical work, but the technological issues strongly limited until
now their development in devices. In this scenario, a better understanding of the
growth of SAMs on magnetic surfaces and improved procedures for the deposition
of top contacts are essential to improve the device yield and increase the MR signal.

References

1. J.R. Petta, S.K. Slater, D.C. Ralph, Spin-dependent transport in molecular tunnel junctions. Phys. Rev. Lett. **93**, 136601 (2004)
2. W. Wang, C.A. Richter, Spin-polarized inelastic electron tunneling spectroscopy of a molecular magnetic tunnel junction. Appl. Phys. Lett. **89**, 153105 (2006)
3. G. Wang, T.-W. Kim, Y.H. Jang, T. Lee, Effects of metal—molecule contact and molecular structure on molecular electronic conduction in nonresonant tunneling regime: alkyl versus conjugated molecules. J. Phys. Chem. C **112**(33), 13010–13016 (2008)
4. S. Ho Choi, B. Kim, C.D. Frisbie, Electrical resistance of long conjugated molecular wires. Science **320**, 1482–1486 (2008)
5. A. Salomon, D. Cahen, S. Lindsay, J. Tomfohr, V. Engelkes, C. Frisbie, Comparison of electronic transport measurements on organic molecules. Adv. Mater. **15**, 1881–1890 (2003)
6. M. Magoga, C. Joachim, Conductance and transparence of long molecular wires. Phys. Rev. B **56**, 4722–4729 (1997)
7. A. Mishchenko, D. Vonlanthen, V. Meded, M. Bürkle, C. Li, I.V. Pobelov, A. Bagrets, J.K. Viljas, F. Pauly, F. Evers, M. Mayor, T. Wandlowski, Influence of conformation on conductance of biphenyl-dithiol single-molecule contacts. Nano Lett. **10**, 156–163 (2010)
8. B.L. Feringa, N.P.M. Huck, A.M. Schoevaars, Chiroptical molecular switches. Adv. Mater. **8**, 681–684 (1996)
9. L. Venkataraman, J.E. Klare, C. Nuckolls, M.S. Hybertsen, M.L. Steigerwald, Dependence of single-molecule junction conductance on molecular conformation. Nature **442**, 904–7 (2006)
10. K. Smaali, S. Lenfant, S. Karpe, M. Oçafrain, P. Blanchard, D. Deresmes, S. Godey, A. Rochefort, J. Roncali, D. Vuillaume, High on-off conductance switching ratio in optically-driven self-assembled conjugated molecular systems. ACS Nano **4**, 2411–2421 (2010)

11. L.A. Zotti, T. Kirchner, J.-C. Cuevas, F. Pauly, T. Huhn, E. Scheer, A. Erbe, Revealing the role of anchoring groups in the electrical conduction through single-molecule junctions. Small **6**, 1529–1535 (2010)

12. W. Hong, D.Z. Manrique, P. Moreno-García, M. Gulcur, A. Mishchenko, C.J. Lambert, M.R. Bryce, T. Wandlowski, Single molecular conductance of tolanes: experimental and theoretical study on the junction evolution dependent on the anchoring group. J. Am. Chem. Soc. **134**, 2292–2304 (2012)

13. F. Chen, X. Li, J. Hihath, Z. Huang, N. Tao, Effect of anchoring groups on single-molecule conductance: comparative study of thiol-, amine-, and carboxylic-acid-terminated molecules. J. Am. Chem. Soc. **128**, 15874–81 (2006)

14. J. Chen, L. Calvet, M. Reed, D. Carr, D. Grubisha, D. Bennett, Electronic transport through metal-1,4-phenylene diisocyanide-metal junctions. Chem. Phys. Lett. **313**, 741–748 (1999)

15. H. Haick, D. Cahen, Making contact: connecting molecules electrically to the macroscopic world. Prog. Surf. Sci. **83**, 217–261 (2008)

16. B. Mann, H. Kuhn, Tunneling through fatty acid salt monolayers. J. Appl. Phys. **42**, 4398–4405 (1971)

17. J.G. Kushmerick, Metal-molecule contacts. Mater. Today **8**, 26–30 (2005)

18. Y.-L. Loo, R.L. Willett, K.W. Baldwin, J.A. Rogers, Interfacial chemistries for nanoscale transfer printing. J. Am. Chem. Soc. **124**, 7654–7655 (2002)

19. Y.-L. Loo, D.V. Lang, J.A. Rogers, J.W.P. Hsu, B. Laboratories, L. Technologies, M. Hill, Electrical contacts to molecular layers by nanotransfer printing. Nano Lett. **3**, 913–917 (2003)

20. J.W. Hsu, Soft lithography contacts to organics. Mater. Today **8**, 42–54 (2005)

21. H.B. Akkerman, P.W.M. Blom, D.M. de Leeuw, B. de Boer, Towards molecular electronics with large-area molecular junctions. Nature **441**, 69–72 (2006)

22. A.S. Blum, J.G. Kushmerick, D.P. Long, C.H. Patterson, J.C. Yang, J.C. Henderson, Y. Yao, J.M. Tour, R. Shashidhar, B.R. Ratna, Molecularly inherent voltage-controlled conductance switching. Nat. Mater. **4**, 167–72 (2005)

23. B. Xu, N.J. Tao, Measurement of single-molecule resistance by repeated formation of molecular junctions. Science **301**, 1221–3 (2003)

24. B.Q. Xu, X.L. Li, X.Y. Xiao, H. Sakaguchi, N.J. Tao, Electromechanical and conductance switching properties of single oligothiophene molecules. Nano Lett. **5**, 1491–5 (2005)

25. M.T. Gonzalez, S. Wu, R. Huber, S.J. van der Molen, C. Schönenberger, M. Calame, Electrical conductance of molecular junctions by a robust statistical analysis. Nano Lett. **6**, 2238–42 (2006)

26. X. Xiao, B. Xu, N.J. Tao, Measurement of single molecule conductance: benzenedithiol and benzenedimethanethiol. Nano Lett. **4**, 267–271 (2004)

27. C. Zhou, M.R. Deshpande, M.A. Reed, L. Jones, J.M. Tour, Nanoscale metal/self-assembled monolayer/metal heterostructures. Appl. Phys. Lett. **71**, 611 (1997)

28. J. Chen, W. Wang, M.A. Reed, A.M. Rawlett, D.W. Price, J.M. Tour, Room-temperature negative differential resistance in nanoscale molecular junctions. Appl. Phys. Lett. **77**, 1224 (2000)

29. M.A. Reed, J. Chen, A.M. Rawlett, D.W. Price, J.M. Tour, Molecular random access memory cell. Appl. Phys. Lett. **78**(23), 3735 (2001)

30. J. Chen, M.A. Reed, A.M. Rawlett, J.M. Tour, Large on-off ratios and negative differential resistance in a molecular electronic device. Science **286**, 1550–1552 (1999)

31. J.M. Beebe, V.B. Engelkes, L.L. Miller, C.D. Frisbie, Contact resistance in metal-molecule-metal junctions based on aliphatic SAMs: effects of surface linker and metal work function. J. Am. Chem. Soc. **124**, 11268–11269 (2002)

32. D.J. Wold, C.D. Frisbie, Formation of metal-molecule-metal tunnel junctions: microcontacts to alkanethiol monolayers with a conducting AFM tip. J. Am. Chem. Soc. **122**, 2970–2971 (2000)

33. D.J. Wold, C.D. Frisbie, Fabrication and characterization of metal-molecule-metal junctions by conducting probe atomic force microscopy. J. Am. Chem. Soc. **123**, 5549–56 (2001)

34. N.J. Tao, Electron transport in molecular junctions. Nat. Nanotechnol. **1**, 173–81 (2006)

35. C. Boulas, J. Davidovits, F. Rondelez, D. Vuillaume, Suppression of charge carrier tunneling through organic self-assembled monolayers. Phys. Rev. Lett. **76**, 4797–4800 (1996)
36. M. Fujihira, H. Inokuchi, Photoemission from polyethylene. Chem. Phys. Lett. **17**, 554–556 (1972)
37. J.G. Simmons, Generalized formula for the electric tunnel effect between similar electrodes separated by a thin insulating film. J. Appl. Phys. **34**, 1793 (1963)
38. W. Wang, T. Lee, M.A. Reed, Mechanism of electron conduction in self-assembled alkanethiol monolayer devices. Phys. Rev. B **68**, 35416 (2003)
39. H.B. Akkerman, R.C.G. Naber, B. Jongbloed, P.A. van Hal, P.W.M. Blom, D.M. de Leeuw, B. de Boer, P.A. van Hal, D.M. de Leeuw, B. de Boer, Electron tunneling through alkanedithiol self-assembled monolayers in large-area molecular junctions. Proc. Natl. Acad. Sci. USA **104**,11161–11166 (2007)
40. R.E. Holmlin, R. Haag, M.L. Chabinyc, R.F. Ismagilov, A.E. Cohen, A. Terfort, M.A. Rampi, G.M. Whitesides, Electron transport through thin organic films in metal–insulator–metal junctions based on self-assembled monolayers. J. Am. Chem. Soc. **123**, 5075–5085 (2001)
41. M.A. Rampi, G.M. Whitesides, A versatile experimental approach for understanding electron transport through organic materials. Chem. Phys. **281**, 373–391 (2002)
42. J. Tomfohr, O. Sankey, Complex band structure, decay lengths, and Fermi level alignment in simple molecular electronic systems. Phys. Rev. B **65**, 245105 (2002)
43. J.C. Cuevas, E. Scheer, Molecular Electronics: An introduction to Theory and Experiment. World Scientific Plublishing Co, Singapore (2010)
44. R. Landauer, Spatial variation of currents and fields due to localized scatterers in metallic conduction. IBM J. Res. Dev. **1**, 223–231 (1957)
45. J. Beebe, B. Kim, J. Gadzuk, C.D. Frisbie, J. Kushmerick, Transition from direct tunneling to field emission in metal-molecule-metal junctions. Phys. Rev. Lett. **97**, 026801 (2006)
46. E.H. Huisman, C.M. Guédon, B.J. van Wees, S.J. van der Molen, C.M. Gue, B.J.V. Wees, Interpretation of transition voltage spectroscopy. Nano Lett. **9**, 3909–13 (2009)
47. J. Chen, T. Markussen, K.S. Thygesen, Quantifying transition voltage spectroscopy of molecular junctions: ab initio calculations. Phys. Rev. B **82**, 121412 (2010)
48. I. Baldea, Ambipolar transition voltage spectroscopy: analytical results and experimental agreement. Phys. Rev. B **85**(3), 035442 (2012)
49. G. Ricoeur, S. Lenfant, D. Guérin, D. Vuillaume, Molecule/electrode interface energetics in molecular junction: a transition voltage spectroscopy study. J. Phys. Chem. C **116**, 20722–20730 (2012)
50. T. Markussen, J. Chen, K.S. Thygesen, Improving transition voltage spectroscopy of molecular junctions. Phys. Rev. B **83**, 155407 (2011)
51. N. Okabayashi, M. Paulsson, H. Ueba, Y. Konda, T. Komeda, Inelastic tunneling spectroscopy of alkanethiol molecules: high-resolution spectroscopy and theoretical simulations. Phys. Rev. Lett. **104**, 077801 (2010)
52. K. Slowinski, R.V.C. Ii, R. Bilewicz, M. Majda, Evidence for inefficient chain-to-chain coupling in electron tunneling through liquid alkanethiol monolayer films on mercury. J. Am. Chem. Soc. **118**(19), 4709–4710 (1996)
53. K. Slowinski, R.V. Chamberlain, C.J. Miller, R.V. June, V. Re, M. Recei, V. September, Through-bond and chain-to-chain coupling. two pathways in electron tunneling through liquid alkanethiol monolayers on mercury electrodes. J. Am. Chem. Soc. **119**(49), 11910–11919 (1997)
54. T. Frederiksen, C. Munuera, C. Ocal, M. Brandbyge, M. Paulsson, D. Sanchez-Portal, A. Arnau, Exploring the tilt-angle dependence of electron tunneling across molecular junctions of self-assembled alkanethiols. ACS Nano **3**, 2073–80 (2009)
55. H. Song, H. Lee, T. Lee, Intermolecular chain-to-chain tunneling in metal-alkanethiol-metal junctions. J. Am. Chem. Soc. **129**, 3806–7 (2007)
56. X. Cui, A. Primak, X. Zarate, J. Tomfohr, O. Sankey, A. Moore, T. Moore, D. Gust, G. Harris, S. Lindsay, Reproducible measurement of single-molecule conductivity. Science **294**, 571–4 (2001)

57. Y. Selzer, A. Salomon, D. Cahen, Effect of molecule-metal electronic coupling on through-bond hole tunneling across metal-organic monolayer-semiconductor junctions. J. Am. Chem. Soc. **124**, 2886–7 (2002)

58. Y.-J. Liu, H.-Z. Yu, Alkyl monolayer-passivated metal-semiconductor diodes: molecular tunability and electron transport. Chemphyschem **3**, 799–802 (2002)

59. L.A. Bumm, J.J. Arnold, T.D. Dunbar, D.L. Allara, P.S. Weiss, U.V. Park, V. Pennsyl, Electron transfer through organic molecules. J. Phys. Chem. B **103**, 8122–8127 (1999)

60. W. Haiss, R.J. Nichols, H.V. Zalinge, S.J. Higgins, D. Bethell, D.J. Schiffrin, Measurement of single molecule conductivity using the spontaneous formation of molecular wires Wolfgang. Phys. Chem. Chem. Phys. **6**, 4330–4337 (2004)

61. M. Suzuki, S. Fujii, M. Fujihira, Measurements of currents through single molecules of alkanedithiols by repeated formation of break junction in scanning tunneling microscopy under ultrahigh vacuum. Jpn. J. Appl. Phys. **45**, 2041–2044 (2006)

62. X. Cui, A. Primak, X. Zarate, J. Tomfohr, O.F. Sankey, A.L. Moore, T.A. Moore, D. Gust, L.A. Nagahara, S.M. Lindsay, Changes in the electronic properties of a molecule when it is wired into a circuit. J. Phys. Chem. B **106**, 8609–8614 (2002)

63. T. Morita, S. Lindsay, Determination of single molecule conductances of alkanedithiols by conducting-atomic force microscopy with large gold nanoparticles. J. Am. Chem. Soc. **129**, 7262–3 (2007)

64. C.-C. Kaun, H. Guo, Resistance of alkanethiol molecular wires. Nano Lett. **3**(11), 1521–1525 (2003)

65. S. Piccinin, A. Selloni, S. Scandolo, R. Car, G. Scoles, Electronic properties of metal-molecule-metal systems at zero bias: a periodic density functional study. J. Chem. Phys. **119**(13), 6729 (2003)

66. C. Chu, J.-S. Na, G.N. Parsons, Conductivity in alkylamine/gold and alkanethiol/gold molecular junctions measured in molecule/nanoparticle/molecule bridges and conducting probe structures. J. Am. Chem. Soc. **129**, 2287–96 (2007)

67. D. Scaini, M. Castronovo, L. Casalis, G. Scoles, Electron transfer mediating properties of hydrocarbons as a function of chain length: a differential scanning conductive tip atomic force microscopy investigation. ACS Nano **2**(3), 507–515 (2008)

68. X. Cui, X. Zarate, J. Tomfohr, O.F. Sankey, A. Primak, A.L. Moore, T.A. Moore, D. Gust, G. Harris, S.M. Lindsay, Making electrical contacts to molecular monolayers. Nanotechnology **13**, 5–14 (2002)

69. V.B. Engelkes, J.M. Beebe, C.D. Frisbie, Length-dependent transport in molecular junctions based on SAMs of alkanethiols and alkanedithiols: effect of metal work function and applied bias on tunneling efficiency and contact resistance. J. Am. Chem. Soc. **126**, 14287–96 (2004)

70. F.-R.F. Fan, J. Yang, L. Cai, D.W. Price, S.M. Dirk, D.V. Kosynkin, Y. Yao, A.M. Rawlett, J.M. Tour, A.J. Bard, Charge transport through self-assembled monolayers of compounds of interest in molecular electronics. J. Am. Chem. Soc. **124**, 5550–60 (2002)

71. H. Song, T. Lee, N.-J. Choi, H. Lee, A statistical method for determining intrinsic electronic transport properties of self-assembled alkanethiol monolayer devices. Appl. Phys. Lett. **91**(25), 253116 (2007)

72. T.-W. Kim, G. Wang, H. Lee, T. Lee, Statistical analysis of electronic properties of alkanethiols in metal-molecule-metal junctions. Nanotechnology **18**, 315204 (2007)

73. R.L. York, P.T. Nguyen, K. Slowinski, Long-range electron transfer through monolayers and bilayers of alkanethiols in electrochemically controlled Hg – Hg tunneling junctions. J. Am. Chem. Soc. **125**, 5948–5953 (2003)

74. E.A. Weiss, R.C. Chiechi, G.K. Kaufman, J.K. Kriebel, Z. Li, M. Duati, M.A. Rampi, G.M. Whitesides, Influence of defects on the electrical characteristics of mercury-drop junctions: self-assembled monolayers of n-alkanethiolates on rough and smooth silver. J. Am. Chem. Soc. **129**, 4336–49 (2007)

75. I. Levine, S.M. Weber, Y. Feldman, T. Bendikov, H. Cohen, D. Cahen, A. Vilan, Molecular length, monolayer density, and charge transport: lessons from Al-AlOx/alkyl-phosphonate/Hg junctions. Langmuir **28**, 404–15 (2012)

76. O. Yaffe, Y. Qi, L. Scheres, S.R. Puniredd, L. Segev, T. Ely, H. Haick, H. Zuilhof, A. Vilan, L. Kronik, A. Kahn, D. Cahen, Charge transport across metal/molecular (alkyl) monolayer-Si junctions is dominated by the LUMO level. Phys. Rev. B **85**, 045433 (2012)

77. K. Slowinski, H.K.Y. Fong, M. Majda, R.V. May, Mercury—mercury tunneling junctions. 1. Electron tunneling across symmetric and asymmetric alkanethiolate bilayers. J. Am. Chem. Soc. **121**(31), 7257–7261 (1999)

78. J.F. Smalley, S.W. Feldberg, C.E.D. Chidsey, M.R. Linford, M.D. Newton, Y.-P. Liu, The kinetics of electron transfer through ferrocene-terminated alkanethiol monolayers on gold. J. Phys. Chem. **99**, 13141–13149 (1995)

79. K. Weber, L. Hockett, S. Creager, Long-range electronic coupling between ferrocene and gold in alkanethiolate-based monolayers on electrodes. J. Phys. Chem. B **101**, 8286–8291 (1997)

80. F. Milani, C. Grave, V. Ferri, P. Samorì, M.A. Rampi, Ultrathin pi-conjugated polymer films for simple fabrication of large-area molecular junctions. Chemphyschem **8**, 515–8 (2007)

81. K.T. Shimizu, J.D. Fabbri, J.J. Jelincic, N.A. Melosh, Soft deposition of large-area metal contacts for molecular electronics. Adv. Mater. **18**, 1499–1504 (2006)

82. M. Galbiati, C. Barraud, S. Tatay, K. Bouzehouane, C. Deranlot, E. Jacquet, A. Fert, P. Seneor, R. Mattana, F. Petroff, Unveiling self-assembled monolayers' potential for molecular spintronics: spin transport at high voltage. Adv. Mater. **24**(48), 6429–6432 (2012)

83. Y. Selzer, A. Salomon, D. Cahen, The importance of chemical bonding to the contact for tunneling through alkyl chains. J. Phys. Chem. B **106**, 10432–10439 (2002)

84. Y. Gu, B. Akhremitchev, G.C. Walker, D.H. Waldeck, Structural characterization and electron tunneling at n-Si/SiO$_2$/SAM/liquid interface. J. Phys. Chem. B **103**, 5220–5226 (1999)

85. G. Wang, T.-W. Kim, H. Lee, T. Lee, Influence of metal-molecule contacts on decay coefficients and specific contact resistances in molecular junctions. Phys. Rev. B **76**, 205320 (2007)

86. J.M. Beebe, B. Kim, C.D. Frisbie, J.G. Kushmerick, Measuring relative barrier heights in transition voltage spectroscopy. ACS Nano **2**(5), 827–832 (2008)

87. M.L. Trouwborst, C.A. Martin, R.H.M. Smit, C.M. Guédon, T.A. Baart, S.J. van der Molen, J.M. van Ruitenbeek, Transition voltage spectroscopy and the nature of vacuum tunneling. Nano Lett. **11**, 614–617 (2011)

88. A.V. Walker, T.B. Tighe, J. Stapleton, B.C. Haynie, S. Upilli, D.L. Allara, N. Winograd, Interaction of vapor-deposited Ti and Au with molecular wires. Appl. Phys. Lett. **84**(20), 4008 (2004)

89. L.H. Yu, C.D. Zangmeister, J.G. Kushmerick, Origin of discrepancies in inelastic electron tunneling spectra of molecular junctions. Phys. Rev. Lett. **98**, 206803 (2007)

90. H. Song, Y. Kim, H. Jeong, M.A. Reed, T. Lee, Coherent tunneling transport in molecular junctions. J. Phys. Chem. C **114**, 20431–20435 (2010)

91. S. Guo, J. Hihath, I. Díez-Pérez, N. Tao, Measurement and statistical analysis of single-molecule current-voltage characteristics, transition voltage spectroscopy, and tunneling barrier height. J. Am. Chem. Soc. **133**, 19189–97 (2011)

92. N. Clément, G. Patriarche, K. Smaali, F. Vaurette, K. Nishiguchi, D. Troadec, A. Fujiwara, D. Vuillaume, Large array of sub-10-nm single-grain Au nanodots for use in nanotechnology. Small **7**, 2607–13 (2011)

93. G. Wang, Y. Kim, S.-I. Na, Y.H. Kahng, J. Ku, S. Park, Y.H. Jang, D.-Y. Kim, T. Lee, Investigation of the transition voltage spectra of molecular junctions considering frontier molecular orbitals and the asymmetric coupling effect. J. Phys. Chem. C **115**, 17979–17985 (2011)

94. Y. Qi, O. Yaffe, E. Tirosh, A. Vilan, D. Cahen, A. Kahn, Filled and empty states of alkanethiol monolayer on Au (111): Fermi level asymmetry and implications for electron transport. Chem. Phys. Lett. **511**, 344–347 (2011)

95. M. Araidai, M. Tsukada, Theoretical calculations of electron transport in molecular junctions: Inflection behavior in Fowler-Nordheim plot and its origin. Phys. Rev. B **81**, 235114 (2010)

96. F. Mirjani, J.M. Thijssen, S.J. van der Molen, Advantages and limitations of transition voltage spectroscopy: a theoretical analysis. Phys. Rev. B **84**, 115402 (2011)

97. A. Vilan, D. Cahen, E. Kraisler, Rethinking transition voltage spectroscopy within a generic Taylor expansion view. ACS Nano **7**, 695–706 (2013)

98. I. Baldea, Transition voltage spectroscopy in vacuum break junction: possible role of surface states. EPL (Europhys. Lett.) **98**, 17010 (2012)

99. A.R. Rocha, V.M. García-Suárez, S.W. Bailey, C.J. Lambert, J. Ferrer, S. Sanvito, Towards molecular spintronics. Nat. Mater. **4**, 335–339 (2005)

100. S. Mandal, R. Pati, What determines the sign reversal of magnetoresistance in a molecular tunnel junction? ACS Nano **6**, 3580–3588 (2012)

101. H. Kondo, T. Ohno, Spintronic transport of a non-magnetic molecule between magnetic electrodes. Appl. Phys. Lett. **103**(23), 233115 (2013)

102. S. Goumri-Said, M.B. Kanoun, A.A. Manchon, U. Schwingenschlögl, Spin-polarization reversal at the interface between benzene and Fe(100). J. Appl. Phys. **113**, 013905 (2013)

103. S.H. Liang, D.P. Liu, L.L. Tao, X.F. Han, H. Guo, Organic magnetic tunnel junctions: the role of metal-molecule interface. Phys. Rev. B **86**(22), 224419 (2012)

104. N. Gorjizadeh, S.Y. Quek, Interface effects on tunneling magnetoresistance in organic spintronics with flexible amine-Au links. Nanotechnology **24**, 415201 (2013)

105. X. Wang, Z. Zhu, A. Manchon, U. Schwingenschlögl, Peculiarities of spin polarization inversion at a thiophene/cobalt interface. Appl. Phys. Lett. **102**, 111604–111644 (2013)

106. K. Ulman, S. Narasimhan, A. Delin, Tuning spin transport properties and molecular magnetoresistance through contact geometry. J. Chem. Phys. **140**, 044716 (2014)

107. Z. Ning, Y. Zhu, J. Wang, H. Guo, Quantitative analysis of nonequilibrium spin injection into molecular tunnel junctions. Phys. Rev. Lett. **100**(5), 56803 (2008)

108. A.R. Rocha, S. Sanvito, Resonant magnetoresistance in organic spin valves. J. Appl. Phys. **101**(9), 09B102 (2007)

109. C.T. Black, C.B. Murray, R.L. Sandstrom, S. Sun, Spin-dependent tunneling in self-assembled cobalt-nanocrystal superlattices. Science **290**, 1131–4 (2000)

110. S. Wang, F.J. Yue, J. Shi, Y.J. Shi, A. Hu, Y.W. Du, D. Wu, Room-temperature spin-dependent tunneling through molecules. Appl. Phys. Lett. **98**, 172501 (2011)

111. J. Dugay, R.P. Tan, A. Meffre, T. Blon, L.-M. Lacroix, J. Carrey, P.F. Fazzini, S. Lachaize, B. Chaudret, M. Respaud, Room-temperature tunnel magnetoresistance in self-assembled chemically synthesized metallic iron nanoparticles. Nano Lett. **11**(12), 5128–5134 (2011)

112. R. Yamada, M. Noguchi, H. Tada, Magnetoresistance of single molecular junctions measured by a mechanically controllable break junction method. Appl. Phys. Lett. **98**, 053110 (2011)

113. A.N. Pasupathy, R.C. Bialczak, J. Martinek, J.E. Grose, L.A.K. Donev, P.L. McEuen, D.C. Ralph, The Kondo effect in the presence of ferromagnetism. Science **306**, 86–89 (2004)

114. E.Y. Tsymbal, A. Sokolov, I.F. Sabirianov, B. Doudin, Resonant inversion of tunneling magnetoresistance. Phys. Rev. Lett. **90**(18), 186602 (2003)

115. J. Zhang, R.M. White, Voltage dependence of magnetoresistance in spin dependent tunneling junctions. J. Appl. Phys. **83**, 6512 (1998)

116. W. Wang, T. Lee, I. Kretzschmar, M.A. Reed, Inelastic electron tunneling spectroscopy of an alkanedithiol self-assembled monolayer. Nano Lett. **4**, 643–646 (2004)

117. J.G. Kushmerick, J. Lazorcik, C.H. Patterson, R. Shashidhar, D.S. Seferos, G.C. Bazan, Vibronic contributions to charge transport across molecular junctions. Nano Lett. **4**, 639–642 (2004)

118. Y. Ando, J. Murai, T. Miyashita, T. Miyazaki, Spin dependent tunneling in 80NiFe/LB lm with ferrocene and tris(bipyridine)ruthenium derivatives/Co junctions. Thin Solid Films **331**, 158–164 (1998)

119. T.X. Wang, H.X. Wei, Z.M. Zeng, X.F. Han, Z.M. Hong, G.Q. Shi, Magnetic/nonmagnetic/magnetic tunnel junction based on hybrid organic Langmuir-Blodgett-films. Appl. Phys. Lett. **88**(24), 242505 (2006)

120. J.-C. Tai, J.-C. Huang, Y.-M. Chang, K.-S. Li, W.-C. Chiang, M.-T. Lin, Applying large-area molecular technology to improve magnetoresistive performance of hybrid molecular spin valves. Appl. Phys. Express **5**(6), 63006 (2012)

Chapter 5
SAMs Based Device Fabrication and Characterization

Despite the high potentiality of SAMs for spintronics highlighted in the previous chapter, not many results exist at the moment in the literature. This lack of results is mainly due to the difficulty to fabricate the devices. As we saw, the two main technological problems consist in the ferromagnetic electrodes compatibility issues with wet chemistry and the short-circuit formation during top electrode deposition. A part of this thesis has been committed to overcome these technological problems. In this chapter we will explain the steps that led us to the development of SAMs-based magnetic tunnel nanojunctions.

In Sect. 5.1 we will present the two possible geometries for the device fabrication: the lateral one and the vertical one. After having compared the relative problems and advantages of each configuration, we will focus on the vertical geometry that is the one that we chose for our devices. In Sect. 5.2 we will discuss the choice of LSMO ferromagnetic material as bottom electrode to avoid the oxidation problem. In Sect. 5.3 we will present the SAMs grafting and characterization. Finally, in Sect. 5.4 we will present the fabrication process of the final device where we use a nanoindentation lithography technique to fabricate LSMO/SAM/Co vertical nanojunctions.

5.1 Choice of Device Geometry

As presented in Sect. 4.2, many techniques have been developed to contact monolayers. Nevertheless, in spintronics the contacting problem becomes even more difficult since new constraints are introduced by the use of ferromagnetic electrodes. The biggest issue is that most ferromagnetic metals are not compatible with air since they get oxidized.Not all the previous techniques can thus be used and usually more elaborated processes are required to avoid the oxidation problem.
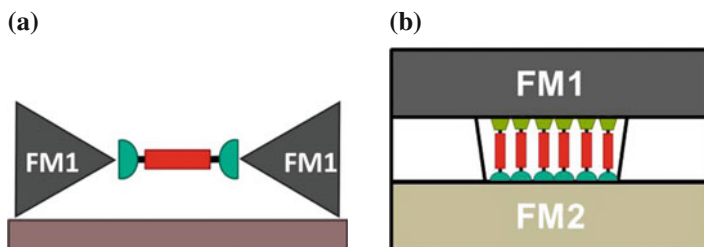
Fig. 5.1 Schematic illustration of **a** a lateral nano-device **b** a vertical nano-device
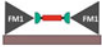
Spintronic devices connecting SAMs or single molecule can hence be grouped in two different geometries: the lateral and the vertical one.

Lateral geometry: In this geometry the device is first totally fabricated and afterwards the molecules are deposited. The deposition can be provided by solution or evaporation with the hope that a single molecule will randomly graft or place itself between the two electrodes detached by 1 or few nanometers (Fig. 5.1a). One third electrode, acting as a gate, can be eventually added to the device.

The most common devices that use this configuration are the ones fabricated by break-junctions or electromigration [1, 2].

Vertical geometry: In this geometry the monolayer is directly grown on the bottom electrode and then it is covered with the top ferromagnetic electrode normally deposed by evaporation. One major problem of this configuration is that it is not possible to use it on large contact areas since the thickness of the molecular barrier is in the nm range. The probability to have some metal atom diffusion into the barrier is inversely proportional to the area. Hence, for large area devices the probability to short circuit the system is extremely high with such a thin barrier. For this reason it is compulsory to use nanocontacts, thus controlling and localizing the zone where the SAM will be grown to a surface of some tens of nm^2 (Fig. 5.1b). Examples of this configuration are nanopores [3, 4] and nanocontacts. These last are made using the nanoindentation technique [5] and they are the ones that we developed for our devices (see Sect. 5.4). This choice was made since the most interesting advantage of vertical geometry is that it is possible to independently choose the ferromagnetic electrodes, thus allowing to separately tune the different interfaces.

In Table 5.1 are schematically resumed and compared the different advantages of both geometries.

Table 5.1 Table resuming and comparing the main problems ($\times$) and advantages ($\checkmark$) for vertical and lateral geometries in spintronic devices

| Lateral structure	Vertical structure
$\times$ Difficult to fabricate with FM	$\times$ Oxidation of bottom electrode (top OK)
$\times$ Oxidation of FM electrodes	$\checkmark$ Possibility to use FM oxides
$\checkmark$ Gate	$\times$ No gate
$\checkmark$ Probe single molecule	$\times$ Probe several molecules
$\checkmark$ No metal diffusion	$\times$ Metal diffusion
$\times$ No clear magnetic configuration	$\checkmark$ Control of magnetic configuration
$\times$ Electrodes necessarily identical	$\checkmark$ Independent choice of FM electrodes
	$\checkmark$ Study of different interfaces

Sentences written in orange mean that the problem is significantly reduced by the fabrication of a nanocontact where the surface of the junction is reduced to the nanometric size

5.2 Choice of the Bottom Electrode

As already said, a major concern when grafting molecules over ferromagnetic metals (Co, Ni, Fe, etc…) is that they can get easily oxidized in contact with molecules or solutions and especially air. This is a strong limitation since it makes the device fabrication process much more difficult and it obliges to continuously work under a controlled atmosphere such as inside a glove box. For this reason, we decided to use $La_{0.7}Sr_{0.3}MnO_3$ (LSMO) as bottom electrode. LSMO is a half-metallic manganite oxide of the perovskite family. The structure of one unit cell of LSMO is represented in Fig. 5.2. This material is largely used in organic spintronics for its advantageous properties: it is air stable, compatible with molecules grafted in solution and it also presents a high spin polarization (nearly 100 %) making it very useful as spin analyser in magnetic tunnel junctions.

Fig. 5.2 Schematic representation of the $La_{0.7}Sr_{0.3}MnO_3$ unit cell
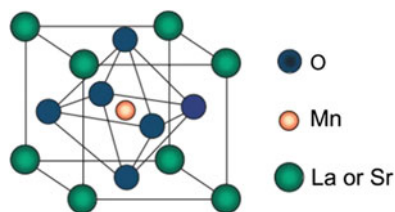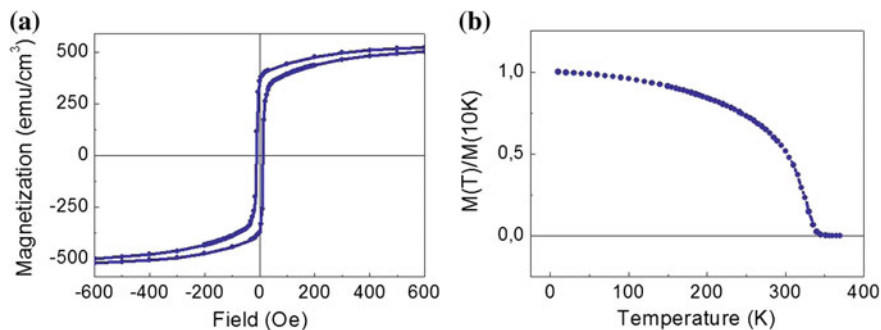
Fig. 5.3 **a** Magnetization versus field measurement at 4 K for a bare LSMO surface. The coercive field of LSMO is ~10 Oe. **b** Measurement of the magnetic moment of LSMO as a function of temperature. The Curie temperature of LSMO is around 340 K

LSMO layers are deposited in our laboratory by Pulsed Laser Deposition (PLD). In this technique a high-power pulsed laser beam is focused inside a vacuum chamber to strike a target that already presents the stoichiometric composition of the material that must be deposited. This material is vaporized from the target in a plasma plume and it deposits on a substrate, atomic layer by atomic layer.

We use a pulsed KrF excimer laser with $\lambda = 248$ nm and a frequency of 2 Hz to deposit LSMO on double polished 10 mm^2 × 0.5 mm (100) SrTiO$_3$ (STO) substrates. LSMO thin films are deposited at 800 °C under a 1.5×10^{-1} mbar O$_2$ atmosphere and the final thickness is 25 nm, as determined by spectroscopic ellipsometry and X-Ray reflectometry.

The AFM topography image of the surface reveals a roughness of about 0.6 nm over 3 μm^2. The terraces are 500–1000 nm width with 1 u.c. height and a roughness <0.3 nm within terraces. The resistivity reported for the LSMO layers growth under these conditions is about 10 mΩ· cm at room temperature.

LSMO magnetic properties have been checked by standard magnetometry, in Fig. 5.3a the hysteresis cycle recorded at 4 K is shown. The LSMO magnetization behaviour with temperature is shown in Fig. 5.3b. The coercive field of LSMO is ~10 Oe, while its Curie temperature is T$_c$ ∽ 340 K.

5.3 Self-Assembled Monolayers Grafting Over LSMO

Once the bottom electrode had been chosen, the following problem was how to graft molecules over it. As it has been presented in Sect. 4.1, SAMs are formed by an anchoring group that is specific for the surface where the molecule must be grafted. This meant that it was necessary to find an anchoring group that was compatible with the LSMO manganite.

5.3.1 Grafting Protocol for SAMs Over LSMO

A lot of work has been done in the laboratory in order to graft SAMs over LSMO. When this work started, no previous work was reported in the literature about LSMO surface functionalization, but just a few results on SAMs grafting over LSMO nanoparticles [6, 7]. After having tested different combinations of common organic solvents (hexane, chloroform, toluene, acetone, ethanol, and tetrahydrofuran) and anchoring groups (such as: -carboxylic acids (–COOH), -phosphonic acids (–$PO(OH)_2$), -silanes (–$Si(OCH_3)_3$, –$SiCl_3$), -amino (–NH_2), and -thiols (–SH)), we chose to focus on phosphonic acids –$PO(OH)_2$ since they are the ones that gave the best results [8]. The structure of the molecules is represented in Fig. 5.4.

The first molecules we characterized are dodecyl-phosphonic acids (C12P) that present a phosphonic anchoring group and an alkyl chain formed by 11 carbon atoms (–CH_2–)$_{11}$. The head of the molecules consists on a methyl group (–CH_3). C18P molecules, which present the same structure but with 17 carbon atoms in the alkyl chain, have been also characterized. For simplicity in the following we will refer to C12P but the grafting protocol of the two molecules is exactly the same.

C12P are deposited by solution under normal atmosphere and at room temperature. First of all, we realized that it is important that the LSMO surface is clean. For this reason substrates are sonicated for 5 min cycles in acetone, trichloroethylene, 2-propanol, and water and are dried under a nitrogen stream. Next they are treated with an oxygen plasma to further clean the surface. Finally, SAMs are prepared by immersion of the LSMO substrates into 2 mL of a freshly filtered 0.05 mM solution of C12P in ethanol. Samples are left under immersion for 2 days, then removed from the solution and finally rinsed with ethanol.

In order to verify the grafting and determine the structure of the monolayer over the LSMO surface, characterization is performed by water contact angle, AFM, ellipsometry and other spectroscopic techniques such as Infrared reflection spectroscopy (IRRAS), X-ray photoelectron spectroscopy (XPS) and X-ray absorption spectroscopy (XAS). This allowed to estimate the final structure of C12P over LSMO: molecules organize themselves in a compact layer of approximately 1.3 nm thick with a tilt angle of 43°, as represented in Fig. 5.5.
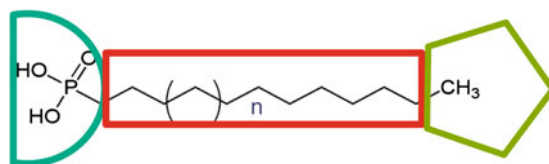
Fig. 5.4 Structure of an alkyl-phosphonic acid molecule. In the picture are highlighted in *blue* the phosphonic anchoring group (–$PO(OH)_2$), in *red* the body of the molecule formed by the carbon alkyl chain and, in *green*, the head of the molecule that is just the end of the chain (–CH_3)

Fig. 5.5 Estimated structure of dodecyl-phosphonic acids (C12P) SAMs over an LSMO surface. Molecules organize themselves in a compact layer with a thickness of 1.3 nm and a tilt angle of 43°. Reprinted with permission from [8]. Copyright 2012 American Chemical Society
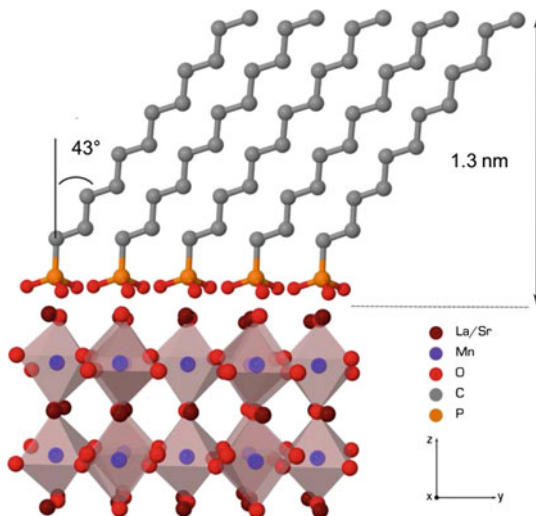
## 5.3.2 Characterization of SAMs Grafted Over LSMO

The methods used to characterize C12P grafted over LSMO will be presented in this section. Since the chemical characterization of the monolayer over the surface already started before the beginning of my PhD and its detailed discussion exceeds the aim of this work, here will be reported just the main results. On the contrary, a more accurate discussion will be provided on the physical characterization of the samples by Ultraviolet Photoelectron Spectroscopy (UPS) (performed in collaboration with the University of Kaiserslautern) and X-ray magnetic circular dichroism (XMCD) performed, during my thesis, in Soleil Synchrotron.

Contact Angle

This technique is largely used to get a fast estimation on the quality of the SAMs. Alkyl chain head (–CH$_3$) is hydrophobic, hence by quantifying the wettability of the functionalized surface it is possible to verify the quality of the monolayer. The principle of this technique is shown in Fig. 5.6.

A deionized water drop is deposited on the functionalized surface and the angle between the tangent to the drop and the surface is measured. Since for alkylic functionalized substrates the surface is expected to be hydrophobic, a high contact angle (normally $>100°$) is proof of a good quality monolayer.

To perform this experiment $\sim$12 μL water droplets were deposited on the sample with a micropipette and static water contact angles were measured on the left and right sides of the drop using a Kraüs goniometer. At least three consecutive drops were deposited on each substrate and averaged for the reported contact angles. Measurements on bare LSMO samples and C12P functionalized one have been performed in order to compare. A contact angle of about 70° was found for bare LSMO
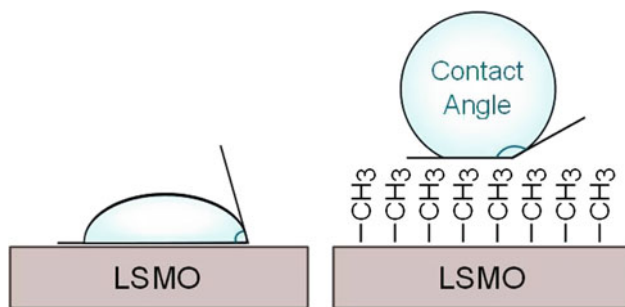
Fig. 5.6 Schematic representation of a contact angle measurement. *Left* a bare LSMO surface gives a contact angle of ∼70°. *Right* An alkylic functionalized surface is expected to be hydrophobic. Contact angle is 108° for C12P functionalized surfaces and 112° for C18P functionalized ones. For a bare LSMO surface treated by plasma contact angle is <30° and after immersion in pure ethanol it is ∼70°

immersed in pure ethanol, while an angle of 108° was measured for those immersed in C12P solution. This is a first proof of the molecular grafting over the surface. Moreover, samples with C18P SAMs have been also measured and in this case the contact angle was 112°.

Atomic Force Microscopy (AFM)

AFM imaging of a functionalized surface can also give information about the quality of the monolayer. It is important to check if the molecules are uniformly distributed to form a compact layer with no island growth over the surface.

A tapping AFM image of a functionalized sample is reported in Fig. 5.7. From the picture it is possible to see that the molecules uniformly cover the surface with no island growth and that the atomic steps of LSMO are still clearly visible.

Fig. 5.7 AFM image of the LSMO surface after functionalization with C12P solution. Molecules uniformly cover the surface with no island growth. Atomic steps of LSMO are still visible. Reprinted with permission from [8]. Copyright 2012 American Chemical Society
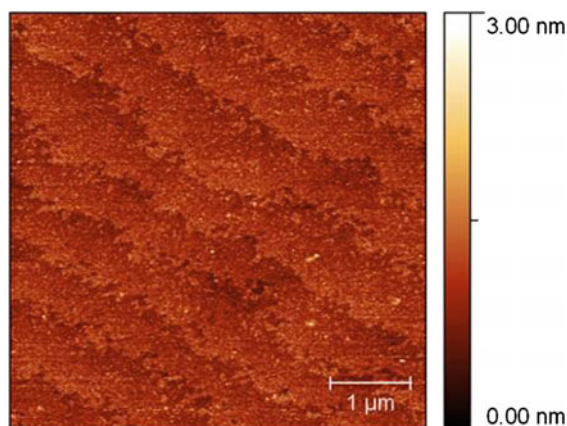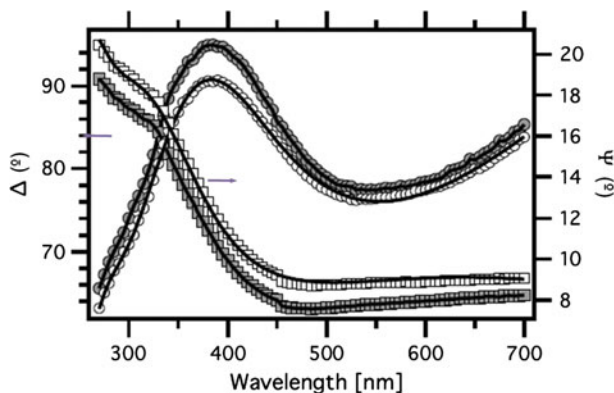
Fig. 5.8 Amplitude ratio (Ψ) and phase shift (Δ) spectra measured for bare LSMO and C12P LSMO functionalized samples. Spectra are fitted using a Cauchy/triple-amorphous model that allows to estimate the thickness of the monolayer to be ~12.8 Å

Ellipsometry

This technique allows to estimate the thickness of a monolayer. The principle of ellipsometry is to measure the change in light polarization upon reflection over the sample. The polarization change is quantified by the amplitude ratio (Ψ) and the phase shift (Δ) that in turn depend on the sample properties, thickness and refractive index.

In Fig. 5.8 are shown the amplitude ratio and the phase shift spectra measured for bare LSMO and C12P LSMO functionalized samples. Comparing the two spectra and modelizing the measured signals using a Cauchy/triple-amorphous model, it is possible to estimate the thickness of the monolayer to be 12.8 Å. The comparison with the theoretical SAM thickness of 17.5 Å also allows to estimate the chain tilt between the alkyl chain axis and the surface normal to be 43°.

C18P LSMO functionalized samples were also measured with this technique. In this case the monolayer thickness was found to be 22.7 Å and the estimated tilt angle from the surface normal was 27°. This is in agreement with results reported in the literature where longer alkyl chain SAMs form higher packed and less tilted monolayers in comparison to shorter ones [9].

Infrared Reflection Spectroscopy

Functionalized substrates with C12P and C18P molecules have been also characterized by infrared reflection spectroscopy (IRRAS). The Fourier transform infrared spectra for these two samples is shown in Fig. 5.9. We were able to analyze only the aliphatic region between 3100 and 2700 cm^{-1} since the analysis of the signals associated with the P–O–(H) was hampered by the strong absorption of both LSMO and STO between 1400 and 600 cm^{-1}.

Fig. 5.9 Fourier transform IRRAS spectra for C12P and C18P LSMO functionalized samples
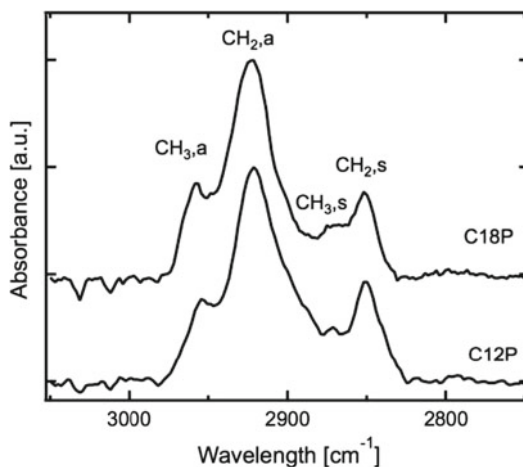
According to IRRAS selection rules, the fact that CH_2/CH_3 intensity ratio is proportionally higher than those observed in bulk C12P and C18P spectra indicates that alkylic chains are ordered and stand vertically [10].

X-Ray Photoelectron Spectroscopy

Next, C12P SAMs were characterized by X-ray photoelectron spectroscopy (XPS) in collaboration with P. Jegou (CEA Saclay). This technique is useful to gain chemical information about the monolayer. XPS spectra are obtained by irradiating a material with a X-ray beam while simultaneously measuring the kinetic energy and number of electrons that escape from the top 0–10 nm of the analysed surface.

In our experiment, XPS spectra clearly showed the presence of peaks coming from all the expected elements. This confirms once more the actual grafting of SAMs over the LSMO surface.

The P2s and P2p peak associated with the phosphonic acid group are partially masked by the Sr3d peak. The high-resolution O1s core level spectrum shown in Fig. 5.10a could be deconvoluted into three peaks and assigned to different oxygen species [11–14]. Peak at 533.1 eV corresponds to –P–O–H groups, adsorbed water, and loosely bond oxygen species. Peak at 531.4 eV corresponds to surface hydroxides, –P–O–, and/or –P=O and, finally, peak at 529.0 eV corresponds to bulk LSMO oxygen.

The comparison of obtained peak ratio (1.0/0.9/0.6) with that obtained in the case of bare LSMO substrates (1.0/0.4/0.8) suggests that the presence of unbound –P–O–H groups is not significant and phosphonic acid groups are mainly bound to the surface in a bidentate and/or tridentate mode, as shown in Fig. 5.10b.

Ultraviolet Photoelectron Spectroscopy (UPS)

This experiment was performed in collaboration with the university of Kaiserslautern in order to gain information about the energy level alignment of SAMs grafted
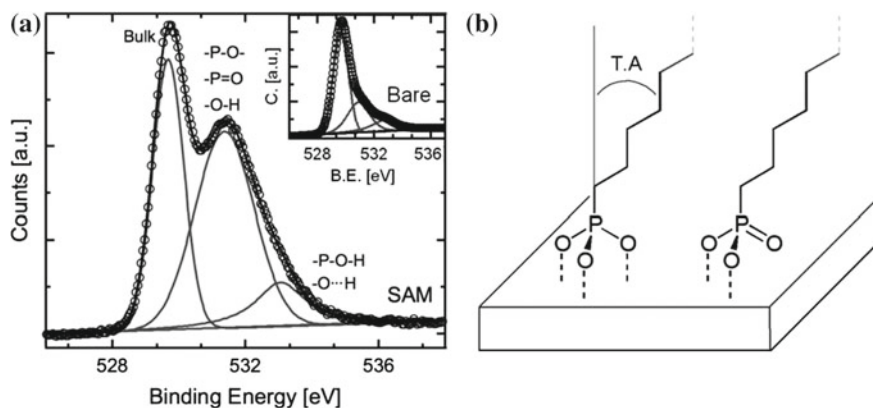
**Fig. 5.10** **a** XPS O1s core level spectrum of a C12P functionalized LSMO sample and of a bare LSMO (*inset*). **b** Schematic representation of alkylphosphonic acid SAMs bonded to the surface in a tridentate (*left*) and bidentate (*right*) mode. Reprinted with permission from [8]. Copyright 2012 American Chemical Society

Fig. 5.11 UPS spectra recorded for LSMO/C12P, LSMO/C18P and bare LSMO samples measured at 120 K. On the *left* side of the spectra: low energy cutoff. On the *right* part of the spectra: peaks corresponding to the HOMO (-6.5 eV) and HOMO-1 (-9.5 eV) levels of the molecules grafted over the surface, while these peaks are not visible for bare LSMO
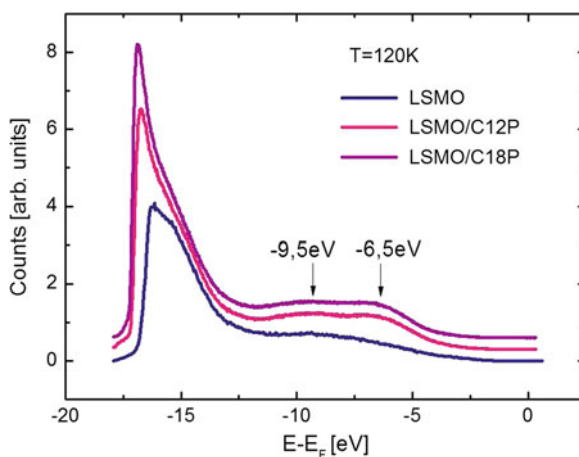
on the LSMO surface. This technique is based on the measurement of the kinetic energy spectra of photoelectrons emitted by molecules after having absorbed the ultraviolet photons. In our experiment, UPS was performed using an Omicron HIS 13 vacuum ultraviolet lamp, which operated at the HeI line (hν = 21.2 eV) at 45° normal to the sample. In Fig. 5.11 are reported the UPS spectra measured at 120 K for LSMO/C12P, LSMO/C18P and bare LSMO samples as a function of the energy $E - E_F$, where E_F was chosen according to the Fermy energy of Cobalt since it is similar to the one of LSMO. In the left side of the spectra the low-energy cutoff reflects the position of the vacuum level. The work function of the sample can be calculated as $\Phi = (21.2 - E_{cutoff})$ eV. In the right side of the spectra two peaks can be distinguished in the case of the SAM functionalized samples. These peaks
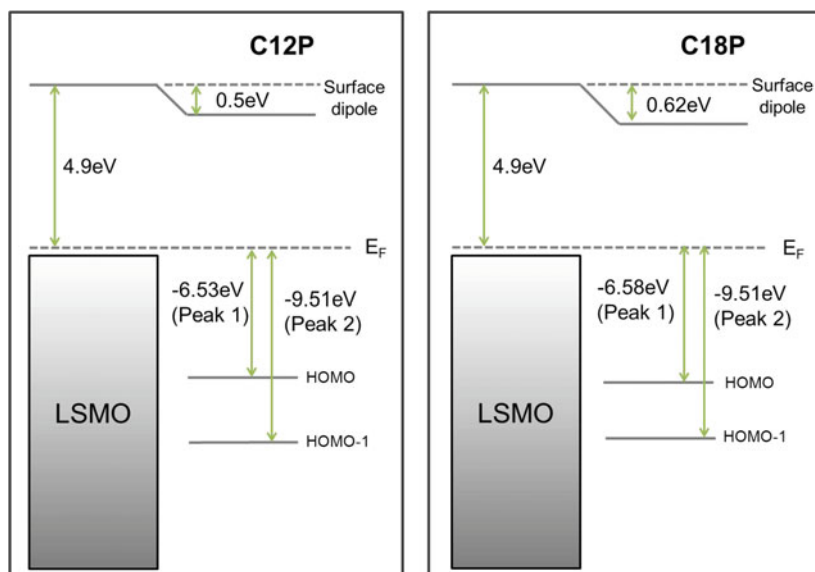
Fig. 5.12 Schematic representation of the energy levels position for LSMO/C12P (*left*) and LSMO/C18P (*right*) samples that can be extrapolated from the UPS spectra. The level position results to be independent on the thickness of the monolayer

are not visible for bare LSMO and they can be attributed to the molecules. Peak at -6.5 eV corresponds to the highest occupied molecular level (HOMO), while peak at -9.5 eV corresponds to the HOMO-1 level. To extract their exact position the background was subtracted from the spectra and peaks were fitted with Gauss peaks.

All the informations extrapolated from these UPS spectra are schematically summarized in Fig. 5.12, where the energy level alignment for LSMO/C12P and LSMO/C18P functionalized samples are represented. As can be seen, the HOMO and HOMO-1 levels position are almost independent on the molecular thickness since they are around -6.55 eV and -9.5 eV in both case for C12P and C18P functionalized samples. The slight shift towards higher binding energies from one sample to the other is not significant and it can be ascribed to the artificial subtraction of the background. In conclusion, the modification of the surface properties with the SAM is confirmed once more by this experiment.

X-Ray Absorption Spectroscopy (XAS) and X-Ray Magnetic Circular Dichroism (XMCD)

XMCD is a powerful technique that allows to study the electronic and magnetic structure of thin films, providing information that is often difficult to obtain by other techniques. Indeed, XAS being element specific and surface sensitive is an useful technique to probe the influence of SAM grafting over the electronic and magnetic properties of LSMO.

XMCD measurements are based on the determination of differences in the absorption cross-section of a material for a left and a right circularly polarized x-ray. It can be calculated by the difference between the x-ray absorption spectra (XAS) taken with left and right circularly polarized light in the presence of a magnetic field.

This technique posses some unique attributes that distinguish it from other common magnetic characterization methods. Most importantly, this method is element-specific and, in addition, it allows direct and independent extraction of the spin and orbital moments of a magnetic element.

Using XMCD we wanted to investigate the influence of alkylphosphonic acid SAMs grafting on the electronic and magnetic properties of the LSMO surface. In this purpose, experiments have been performed at the Deimos beamline of Soleil Synchrotron in Gif sur Yvette (France).

LSMO is a mixed-valence manganite and its electronic and magnetic properties depend on the proportion of Mn^{3+} and Mn^{4+} ions which is linked to the La/Sr ratio. To study the influence of the grafting on the LSMO properties, we measured XAS and XMCD spectra at the manganese $L_{2,3}$ edges in total electron yield (TEY) mode and normal incidence at 4.2 K and 3 T.

In order to discriminate the effect of SAMs grafting from the effects due to the surface treatment during the device preparation, three different sets of samples were analysed. In the first set we directly compared bare LSMO to a functionalized LSMO/C12P sample, none of them subjected to any plasma treatment. In the second set we investigated the effect of solvents and thus we compared bare LSMO to LSMO which had been immersed in neat ethanol. Finally, in one third set of samples the effect of O_2 plasma was also studied comparing bare LSMO and LSMO/C12P samples with plasma treatment to the ones that had not been exposed to any plasma. Since surface properties can slightly change from one LSMO substrate to the other, one single LSMO substrate was used and divided for each set of samples in order to allow a direct comparison of the results.

Effect of SAMs grafting on LSMO magnetic properties The XAS and XMCD spectra recorded with left (σ^-) and right (σ^+) circularly polarized x-ray for the first set of samples are shown in Fig. 5.13a (bare LSMO) and in Fig. 5.13b (LSMO/C12P with no plasma treatment). The superposition of the isotropic XAS spectra for the two samples is also shown in Fig. 5.13c to allow an easier comparison. XMCD spectra are numerically calculated as ($\sigma^- - \sigma^+$) and their percentage is determined by the ratio between the intensity of the XMCD peak and the intensity of the major peak in the isotropic XAS spectra. This value gives a qualitative idea on the magnetic moment variation of the surface with grafting.

The different peaks in the XAS spectra of Mn L_3 edge can be identified by comparison with results reported in the literature [15]. *Peak a* ($\sim$643.4 eV for bare LSMO) corresponds to a mix contribution of Mn^{3+} and Mn^{4+} ions [16, 17]. We unfortunately did not have reference samples during the experiment in order to extrapolate the exact Mn^{3+}/Mn^{4+} ratio. *Peak b* (641.6 eV) represents the contribution of Mn^{4+} ions and *peak c* (640.9 eV) is principally due to Mn^{2+} ions, even if a small contribution of Mn^{3+} is also possible.
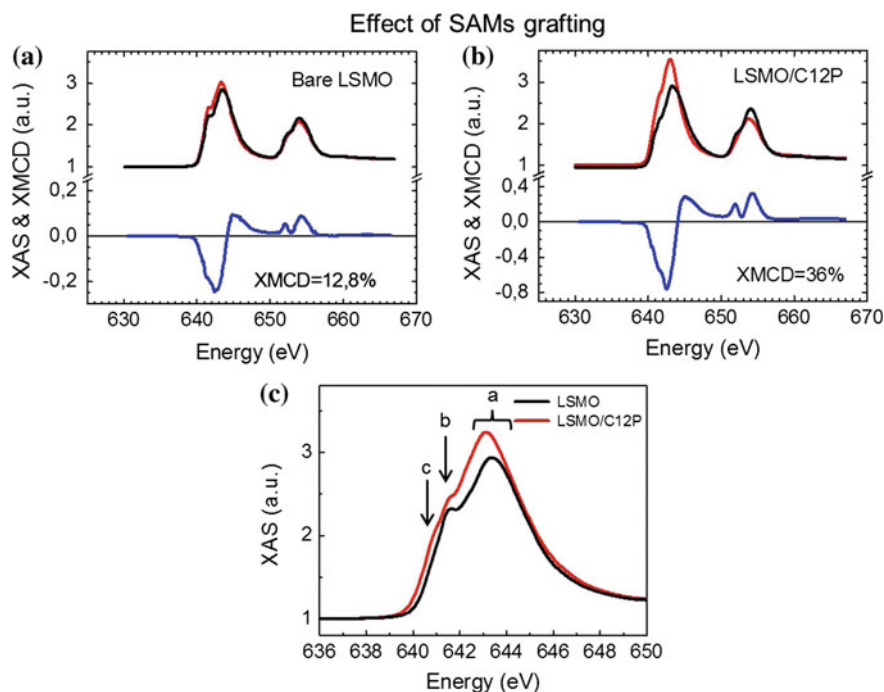
Fig. 5.13 **a** XAS spectra recorded with left (σ^-, *black*) and right (σ^+, *red*) circularly polarized x-ray for a bare LSMO surface not subjected to any plasma treatment. In *blue*, XMCD curve calculated as ($\sigma^- - \sigma^+$) and its percentage is calculated as the ratio between the intensity of the peak in XMCD curve and the intensity of the major peak (around 643.4 eV) of the isotropic XAS curve (translated to 0). **b** Same thing but for a functionalized LSMO/C12P sample not subjected to any plasma treatment. **c** Comparison of the isotropic XAS spectra at the Mn L_3 edge for bare LSMO (*black*) and LSMO/C12P (*red*). Isotropic spectra are calculated as ($\sigma^- + \sigma^+$)/2. *Peak a* is shifted towards lower energies and *peak c* appears thus meaning a partial reduction of surface Mn ions with the molecular grafting

From Fig. 5.13c one can observe that in the case of LSMO/C12P sample, *peak a* is shifted towards lower energies in comparison to the one of bare LSMO (from 643.4 eV to 643.1 eV). This corresponds to an increase of the Mn^{3+}/Mn^{4+} ratio. Moreover, in the case of the functionalized sample *peak c* slightly emerges while it is almost absent for bare LSMO. This means an increase of Mn^{2+} ions for LSMO/SAM sample.

To summarize, all these results clearly suggest that Mn centers are partially reduced by SAMs grafting. This could be probably due to the polarity of the phosphonic anchoring group. The fact that Mn ions are reduced is also reflected on the magnetic properties of the functionalized LSMO surface with an increase of its magnetic moment for the LSMO/SAM sample, as one can see by the comparison of the XMCD ratio in Fig. 5.13a, b.

In order to be sure that this modification came from the grafting of the molecules and not from the surface treatments, we also studied the effect of solvent and plasma.

Effect of solvent immersion It is important to rule out the effect of the solvent used to graft molecules on LSMO in order to be sure that surface reduction is due to molecules and not to the preparation process. In this regard, XAS and XMCD spectra for bare LSMO and LSMO which had been immersed in neat ethanol are shown respectively in Figs. 5.14a, b. Their isotopic XAS spectra are also compared in Fig. 5.14c. As one can see, curves match except for *peak c* that looks more marked in the sample that has been immersed into ethanol. This suggests that the increase of Mn^{2+} ions could be an effect just caused by ethanol over the surface, while it confirms that the shift of *peak a* towards lower energies with the consequent increase of Mn^{3+}/Mn^{4+} ratio is clearly due to molecules and not to the grafting process.

Nevertheless, *peak c* is small, in particular for XMCD spectra, suggesting that Mn^{2+} concentration is very low compared to that of Mn^{3+}/Mn^{4+} ions ratio.
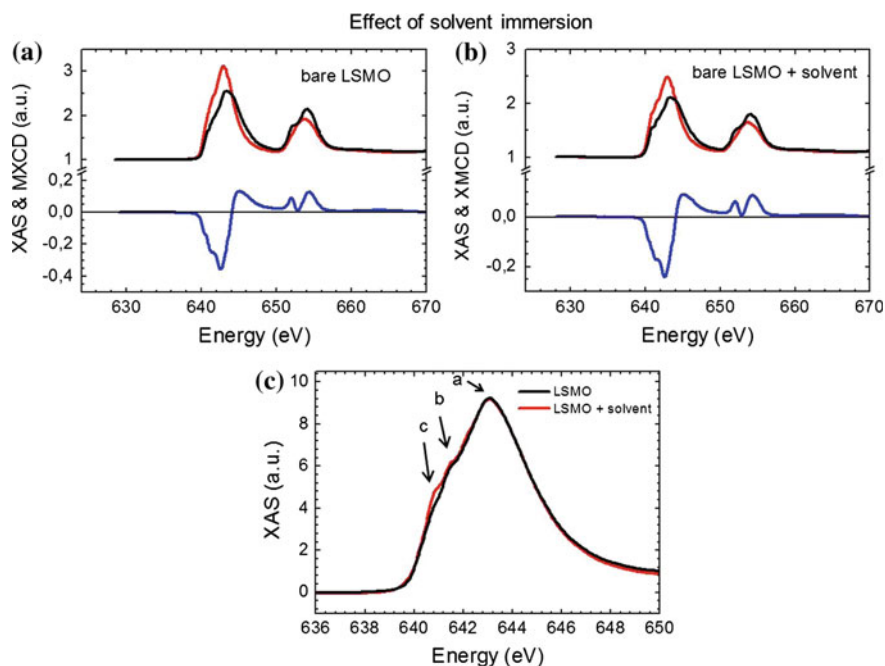
Fig. 5.14 **a** XAS spectra recorded with left (σ^-, *black*) and right (σ^+, *red*) circularly polarized x-ray for a bare LSMO surface. In blue, XMCD curve calculated as ($\sigma^- - \sigma^+$). **b** Same thing but for an LSMO substrate that has been immersed in neat ethanol. **c** Comparison of the isotropic XAS spectra at the Mn L_3 edge for bare LSMO (*black*) and bare LSMO immersed in ethanol (*red*). Isotropic spectra are calculated as ($\sigma^- + \sigma^+$)/2. Curves perfectly recover but *peak c* looks more marked in the sample immersed in ethanol thus suggesting an increase of Mn^{2+} ions

Effect of plasma treatment
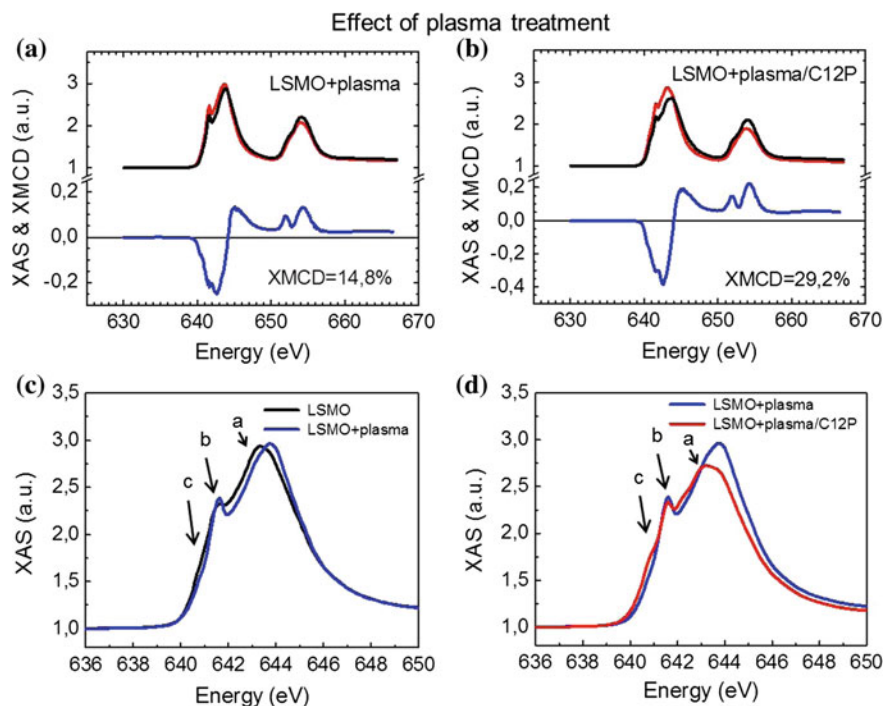
Fig. 5.15 a XAS spectra recorded with left (σ^-, *black*) and right (σ^+, *red*) circularly polarized x-ray for a bare LSMO sample subjected to an O_2 plasma treatment to clean the surface. In *blue*, XMCD curve calculated as ($\sigma^- - \sigma^+$), its percentage is calculated as the ratio between the intensity of the peak in XMCD curve and the intensity of the major peak (around 643.4 eV) of the isotrope XAS curve (translated to 0). **b** Same thing but for a functionalizd LSMO/C12P sample also subjected to the same plasma treatment. **c** Comparison of the isotropic XAS spectra at the Mn L_3 edge for a bare LSMO sample before molecule grafting with (*blue*) and without (*black*) plasma treatment. As expected plasma oxidizes the surface and increases the Mn^{4+}/Mn^{3+} ratio. **d** Comparison of the isotropic XAS spectra at the Mn L_3 edge for bare LSMO (*blue*) and LSMO/SAM (*red*) samples, both subjected to the plasma treatment. Mn centers are reduced by molecule grafting, the Mn^{4+}/Mn^{3+} ions ratio decreases and Mn^{2+} ions increase

Effect of plasma treatment A final test to verify the influence of O_2 plasma treatment, used during the nanodevice fabrication process to enlarge the nanohole before SAMs grafting (see Sect. 5.4.2.2), was carried out. In Fig. 5.15a,b are reported XAS and XMCD spectra recorded for bare LSMO and LSMO/SAMs, both subjected to a plasma treatment. In Fig. 5.15c the effect of plasma on the LSMO surface is highlighted by comparing the isotropic XAS spectra of bare LSMO with and without plasma treatment. From this picture one can clearly see that, as expected, the effect of plasma is to oxidize the surface thus increasing the Mn^{4+}/Mn^{3+} ratio: *peak a* is shifted towards higher energies and *peak b* becomes very marked.

In Fig. 5.15d the isotrope XAS spectra for bare LSMO and LSMO/SAM samples both subjected to O_2 plasma are also compared in order to confirm the effect of

molecules grafting even under these conditions. Again, one can observe that *peak a* is shifted towards lower energies for the functionalized sample and *peak c* appears in comparison to the bare LSMO + plasma one. Once more this confirms that the grafting of SAMs over the surface reduces the Mn ions and increases the magnetic moment of the surface.

In conclusion, these results suggest that hybridization between molecules and LSMO magnetic oxide substrates induces a modification of the electronic structure of the interface with a reduction of the Mn ions and a consequent increase of the magnetic moment of the functionalized surface.

## 5.4 Fabrication of the Nanojunctions

After having characterized and verified the effective grafting of molecules over the LSMO surface, it was possible to proceed with the fabrication of LSMO/SAM/Co nanojunctions.

One of the major problems in the fabrication of spintronic devices with SAMs is the high possibility of short-circuit formation during the top electrode deposition. This is because the molecular layer is soft and very thin ($\sim$1.3 nm), hence the probability to have some metal atoms that diffuse into the barrier during the Co deposition is very high. One way to significantly decrease this probability is to reduce the size of the junction to some tens of nm. Moreover, the reduced size of the junction also allows to test the properties of the device at a "local" scale. This is important for a better understanding of its physical properties, since the heterogeneities of a larger contact can introduce some additional effects that make the understanding of the transport mechanisms much more difficult.

Nanocontacts have been fabricated using the nanoindentation lithography technique that was developed some years ago in the laboratory [5] and has been adapted to SAMs based MTJs during my thesis. This method consists in the notching of a nanohole into an electrical insulator layer by using a conduction tip AFM (CP-AFM) to define the nanometric size of the device. The subsequent layers that form the nanojunction are then deposited in the nanohole to complete the device. The main fabrication steps to produce a LSMO/SAM/Co nanocontact are summarized in Fig. 5.16. All these steps will be explained in detail in the following.

5.4.1 First Step: Optical Lithography

After the deposition of the LSMO bottom electrode on a STO substrate and before the molecular grafting, the first step in the device fabrication process is to use classical optical lithography to define the micrometric zones over the sample where the nanojunctions will be realized by nanoindentation.
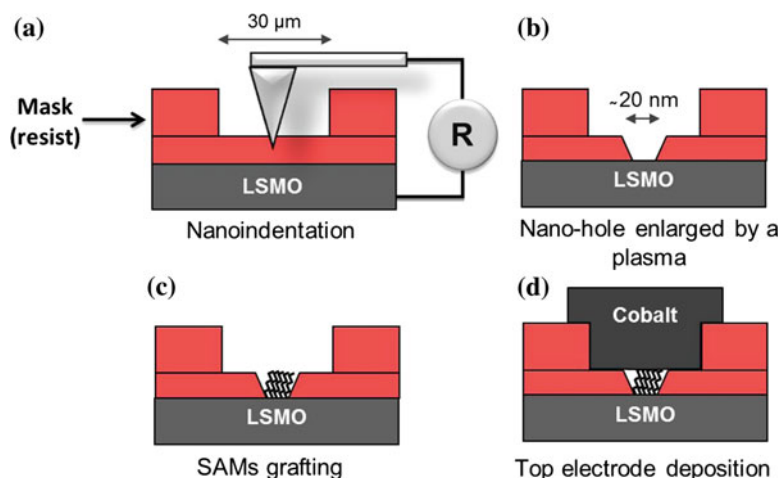
Fig. 5.16 Schematic of the main steps of the device fabrication. **a** A nanohole is notched into a resist that has been previously spin-coated over the LSMO surface, using the nanoindentation lithography technique. **b** The nanohole is enlarged by an O_2 plasma to a final diameter of 10–50 nm. **c** Sample is immersed in a SAM solution to graft the molecules in the nanohole. **d** The device is completed with the Co top electrode deposition by sputtering

To define these zone, the LSMO surface is first cleaned by sonication for 5 min cycles in acetone, trichloroethylene, 2-propanol and water and is dried under a stream of nitrogen. Then, a first layer of a thin resist (around 40 nm) is spin-coated over the whole surface and it is covered by a second layer of a thicker resist (1.4 μm) (Fig. 5.17a). 16 squares of $30 \times 30 \, \mu m^2$ are thus opened in the thick resist by optical lithography (Fig. 5.17b) and they define the zones where the nanoholes will be notched.

Thin resist (diluted Microposit S1805 of Rohm and Haas, thickness 40 nm). This is the first resist layer that is spin-coated over the LSMO surface. The spin-coating parameters are 5500 rpm for 30 s. Once that the resist is deposited, the sample is heated on an hot plate up to 170 °C in order to make it insensible to subsequent photolithographic processes.

Thick resist (Microposit S1813, thickness 1.4 μm). This layer is deposited over the thin resist. The spin-coating parameters are 6000 rpm for 30 s. The resist is heated for 1 min at 90 °C over a hot plate to evaporate the solvent. Sample is then exposed to UV light through a lithography mask in order to define the thin resist zones where the nanoindentation will be done. The thick resist is developed by immersion into a solution of 50:50 Microposit Concentrate and deionized water. Finally, it is heated up to 200 °C on a hot plate in order to evaporate all the solvent, cross-link it and make it hard.
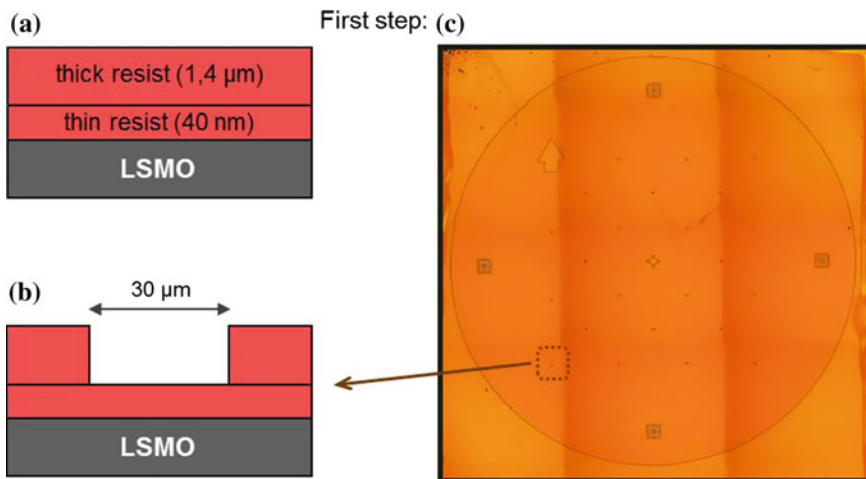
Fig. 5.17 Schematic of the optical lithography steps. **a** A thin resist of 40 nm is spin-coated over the LSMO surface and a thick resist (1.4 μm) is spin-coated over it. **b** Optical lithography is used to open 30×30 μm^2 holes into the thick resist and define the zones that will be subsequently nanoindented. **c** Microscope image of a $(10 \times 10$ mm^2 lithographed sample. 16 square of 30×30 μm^2 are opened over the surface and reference marks are also patterned. (Vertical color change in the image is due to the fact that microscope took pictures on single zones to obtain a better resolution and then built them together to obtain the final image). Au surface has been taken for demonstration since LSMO is transparent and the lithography pattern is harder to see

A photo of one lithographed sample is reported in Fig. 5.17c. In the picture it is possible to identify the 30×30 μm^2 evenly spaced squares. A arrow and crosses are also patterned as visual references on the sample.

5.4.2 Second Step: Nanoindentation Lithography

The second step in the device fabrication is the nanoindentation lithography technique where, using a CP-AFM, a nanohole is notched in the thin resist squares defined in the thick resist by optical lithography.

Nanoindentation technique was firstly developed in the laboratory some years ago for the fabrication of $Co/Al_2O_3/Co$ magnetic tunnel nanojunctions [5]. Since then, thanks to its high versatility, it has been also applied for the development of different kind of studies such as: spin torque transfer through GMR nanocontacts [18], multiferroic tunnel junctions [19], transport in nanowires [20] and to connect single nano-particles [21]. For organic spintronics it has been already used to investigate the local transport properties in organic-semiconductors based magnetic tunnel junctions [22].

In order to fabricate our devices, further modifications were made to the process to make it compatible with the grafting of Self-Assembled Monolayers, as it will be explained in Sect. 5.4.2.2.

The possibility to adapt this technique to the different necessities of the studied molecules reveals its potential. Indeed it could be possibly used for the integration and study in devices of many other molecular objects, such as single molecular magnets or spin crossover molecules.

The principle of nanoindentation lithography and its application to our devices will be detailed in the following.

5.4.2.1 Nanoindentation Principles

Nanoindentation lithography is based on the use of a CP-AFM to notch a nanohole into an insulating layer deposited over a conductive surface. This can be done thanks to the real time control of the tunnel current circulating between the tip and the conductive layer. One of the major advantage of this technique is that the exact thickness and mechanical properties of the insulator are not critical, as the indentation depth is monitored in real time through the tip-sample resistance. Therefore, this technique allows to stop the indentation with great precision and to prevent the deterioration of the underlying layers.

Our CP-AFM is based on an AFM (Bruker EnviroScope/Nanoscope V) coupled with a high performance current measurement module (called Resiscope) developed by F. Houzè Team (LGEP) to perform local resistance measurements from $100\,\Omega$ to $\sim 10^{12}\,\Omega$. Tips used are standard silicon nitride (Si_3N_4) tips coated by Bore-doped polycristalline diamond, with a nominal spring constant of 40 N/m and a resonant frequency of 300 kHz. The macroscopic radius of the tip is about 100 nm but the diamond crystallites induce a nanoroughness that leads to a local radius of less than 10 nm.

The wide range of resistance that can be measured by the resiscope gives a high sensitivity on the indentation depth. In this way, it is possible to stop the tip with sub-nanometric precision and accurately choose the thickness of the insulator barrier that must be leaved. The different steps of the indentation process are shown in Fig. 5.18.

In this example we consider the simplest general structure: a conductive layer (for us LSMO) covered by an insulating one (for us the thin resist S1805). The sample is electrically connected on a corner to the resiscope circuit and the tunnel current that flows between the tip and the sample is measured in real time while the tip approaches the conductive layer. The cantilever deflection and the tip-sample resistance as a function of the displacement of the piezoelectric crystal (z) are represented in Fig. 5.18. The process is divided in three different steps:

1. The tip is not yet in contact with the sample. Thus the cantilever deflection is zero and the system is completely insulating with the measured resistance that saturates to the high limit of the equipment ($R \sim 10^{12}\,\Omega$).
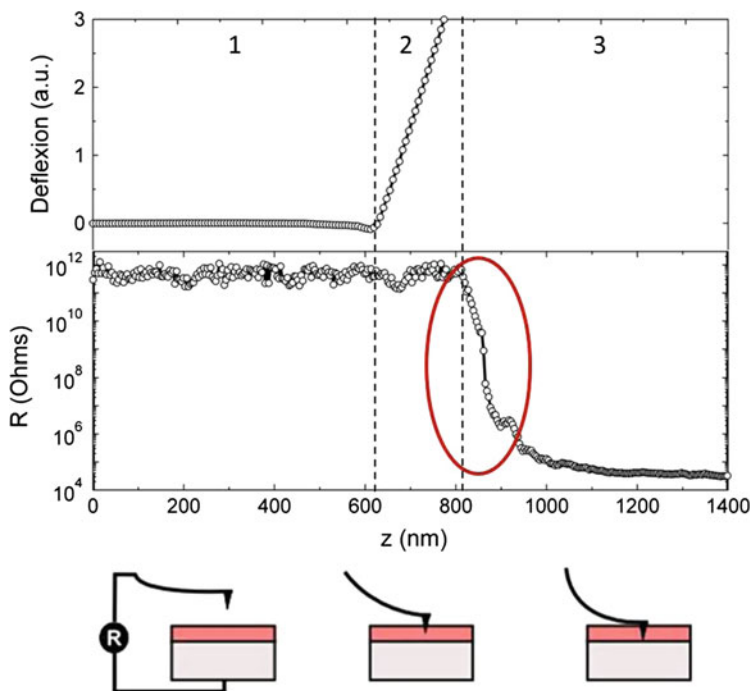
Fig. 5.18 Different steps of the nanoindentation process. The resistance between the tip and a conductive substrate is measured in real-time to stop the tip with subnanometric precision while notching a nanohole. In the graph: cantilever deflection (*top*) and tip-sample measured resistance (*bottom*) as a function of the piezoelectric ceramic displacement (sample is moving up towards the tip). The corresponding steps of the nanoindentation process are schematically represented at the *bottom*. *1* Tip is not yet in contact with the sample. The deflection of the cantilever is zero and the measured resistance is in the high limit of the Resiscope module ($R \sim 10^{12}$). *2* The tip starts to notch a nanohole into the insulating layer. The cantilever deflection increases while the insulating barrier is still too thick and the measured resistance is still $R \sim 10^{12}$. *3* When the tip continues to move towards the conduction layer, the insulating barrier becomes thin enough and a tunnel current starts to flow from the tip to the sample. A decrease of several orders of magnitude of the measured resistance is detected for just few nanometers change in the thickness of the insulating barrier. In this way it is possible to stop the AFM tip with subnanometric precision while indenting

2. The tip touches the sample and starts to penetrate into the thin resist. The deflection of the cantilever now increases exponentially, while the resistance measured from the system does not change since the thickness of the insulating layer is still too high and avoids the flow of any current through it.
3. The tip continues to penetrate into the thin resist, until an electrical contact with the underlying conductive layer is formed. This is the key step of the indentation process. While the cantilever deflection continues to increase, the thickness of the insulating layer starts to be small enough to allow an increasing tunnel current to flow from the tip to the sample. This corresponds to an abrupt decrease of 7

Fig. 5.19 *Top* topographic AFM image of a set of indented nanoholes made with increasing thresholds. *Bottom* Height profile of the indented nanoholes for different threshold resistance at which the indentation is stopped. Just few nm of the thin resist are left after indentation
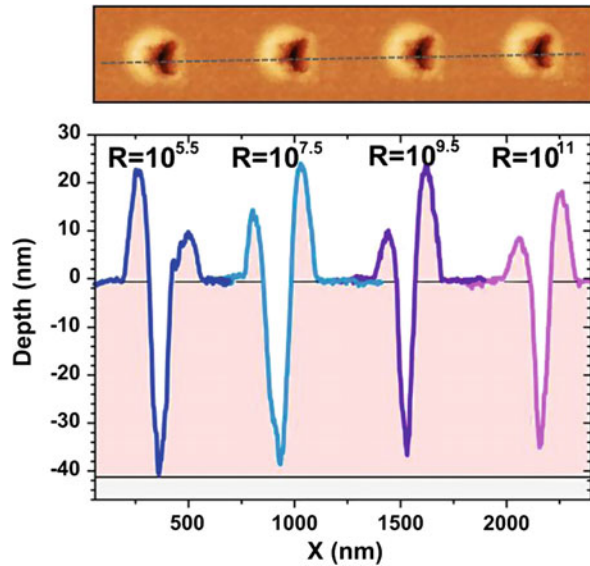

orders of magnitude in the measured resistance (from $\sim 10^{12}\,\Omega$ to $10^5\,\Omega$) for ~ 100 nm displacement of the piezoelectric crystal. This large decrease determines the sensitivity of the technique and allows to stop the process in the desired position by setting a threshold value of the resistance at which tip is retracted.

A preliminary calibration has been performed in order to correlate the measured value of the resistance with the final thickness of the insulating barrier. The profile of four nanoholes corresponding to four different resistance thresholds is reported in Fig. 5.19. On the right is presented a nanohole made using the maximum threshold possible, this is when a tunnel current starts to be detected. For decreasing resistance thresholds, the thickness of the remaining barrier is also decreased, until the electrical contact with the LSMO layer is reached at $R = 10^{5.5}$. It is important to notice that a variation of few nm in the barrier thickness corresponds to a variation of about 2 orders of magnitude in the measured resistance, allowing to tune the barrier thickness with subnanometric precision.

5.4.2.2 Nanoindentation Applied to Self-Assembled Monolayers Based Magnetic Tunnel Junctions

In this section it will be described how this technique has been adapted to the fabrication of SAMs based magnetic tunnel junctions.

Contrarily to the fabrication process of organic semiconductors MTJs, in our case the nanohole cannot be notched directly into the organic layer since SAMs are too thin and they would be destroyed by the indentation process. To avoid this problem
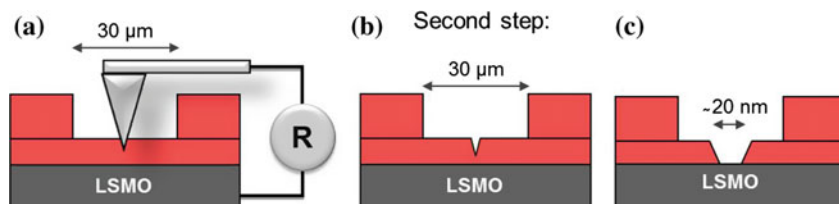
Fig. 5.20 Schematic of the nanoindentation steps: **a** A nanohole is notched into the thin resist in each $30 \times 30\ \mu m^2$ squares opened by optical lithography. **b** Nanohole notched into the thin resist. Few nanometers of resist are left over LSMO surface. **c** Nanohole is enlarged by an oxygen plasma to expose LSMO. The final size of the nanohole is $\sim 20 \times 20\ nm^2$

we adopted an inverse approach: first the hole is defined into the resist, then it is enlarged by an oxygen plasma to take the contact on the underlying LSMO and only in a second time molecules are deposited.

Nanoindentation When the nanohole is notched into the resist we set the threshold resistance value in order to leave just few nanometers of the insulating resist (Fig. 5.20a, b). It is important to avoid the mechanical contact between the AFM tip and the LSMO layer since the diamond tip could slightly scratch the LSMO surface thus varying its properties and inhibiting the molecular monolayer assembly.

Plasma After that one nanohole has been indented in every $30 \times 30\ \mu m^2$ zone defined by lithography, the sample is exposed to a 6 W oxygen plasma (5:1, O_2:Ar composition) for 2 min (6 W in our system corresponds to a power of 0.07 W/cm^2). This plasma removes about 10 nm of resist in order to enlarge the hole and open the contact on the underlaying LSMO surface (Fig. 5.20c).

An accurate calibration of the plasma time has been also performed in order to optimize the etching conditions. If a lot of resist is removed, the final hole would be too large with a high probability to have short-circuit formation in the nanocontact. On the contrary, if the plasma time is too short the removed resist would be not enough and some resist could "flow" a little bit and cause the hole obstruction.

Despite the calibration, it is not possible to exactly control the size of a nanohole since it completely depends on the edge shape of the AFM tip used to perform the indentation and some elastic constraints or relaxations in the resist could also play a role. Anyway, high statistics of AFM tapping images taken on hundreds of nanoholes confirm that after 2 min of 6 W oxygen plasma the section of the nanohole does not exceed some tens of nanometers. In Fig. 5.21 is provided the profile of a nanohole before and after the plasma treatment and it can be clearly distinguished the "plateau" opened on the LSMO surface after the O_2 plasma.

In conclusion, with this technique it is possible to fabricate junctions with a final area in the few 100 nm^2 range so that, with a density of 1.86 Å$^2 \cdot$molecule^{-1}, roughly 10^4 molecules are electrically connected in parallel.

Fig. 5.21 Comparison of a
nanohole profile before
(*gray*) and after (*blue*) the
oxygen plasma treatment at
6 W for 2 min
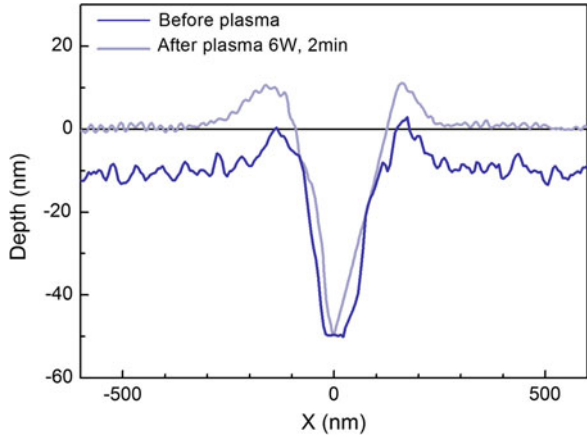
5.4.3 Third Step: Self-Assembled Monolayer Deposition

The third step in the fabrication process of the nanodevice is the deposition of the
molecular barrier (Fig. 5.22). We have seen in the previous section that the nanohole
has been opened using the oxygen plasma. The underlying LSMO surface is now
exposed and clean at the bottom of the nanohole, ready for the molecular grafting.
The process used to deposit SAMs is the one described in Sect. 5.3. After plasma,
samples are immediately immersed into the SAMs solution in order to avoid any
surface contamination that could prevent the formation of a good quality monolayer.
Samples are left for two days in the solution and then removed and rinsed with neat
ethanol to carry away the ungrafted molecules.

Influence of the solvent on the photoresist An important test to do was to verify
the effect of ethanol on the photoresist to be sure that after the immersion in the
solvent the resist is not flowing. Despite the photoresist was heated up to 200 °C to
cross-link it and make it resistant to the solvent, its stability is not a trivial issue at
the nanometric scale. Preliminary tests on short-circuit samples show that for small
nanoindentation holes (<15 nm diameter) the immersion in ethanol can cause some
resist flow that, even if small, could obstruct the nanoholes. In this regard, accurate

Fig. 5.22 Schematic of the
SAM grafting at the bottom
of the nanohole
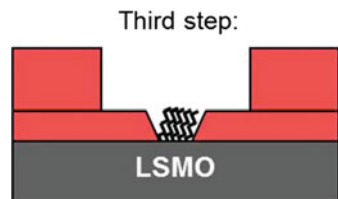
tests were performed to verify that in "normal size" conditions ($\geqslant 20$ nm diameter) the holes are not blocked after immersion in ethanol.

Experiments were performed taking a test sample where half of the squares had been indented. The usual fabrication process was followed but sample was immersed in neat ethanol for 2 days instead of SAMs solution. In this way direct top/bottom electrode contact is obtained when the device is completed since there is no barrier. The electrical measurement of the contacts revealed that the indented squares were short-circuited, confirming the fact that in these conditions the resist did not flow closing the nanoholes. To be sure that the test is trustful we also verify that not indented contacts are insulating, thus excluding that short-circuits were just due to defects on the thin resist.

5.4.4 Fourth Step: Top Electrode Deposition and Sample Bonding

After SAMs grafting, the device is completed with deposition of the top electrode Co/Au bilayer by sputtering (Fig. 5.23a). Silver paint is manually added on the top of each contact and used as a mask while the short circuits between contacts are removed by ion beam etching (Fig. 5.23c). Sample is finally bonded into a chip to perform the transport measurements.

5.4.4.1 Top Electrode Deposition by Sputtering

After the grafting of the molecular barrier, the sample is immediately transferred in the sputtering machine (Plassys MP900S) for the top electrode deposition. Sputtering technique uses a plasma to extract the atoms from a material target and deposit them
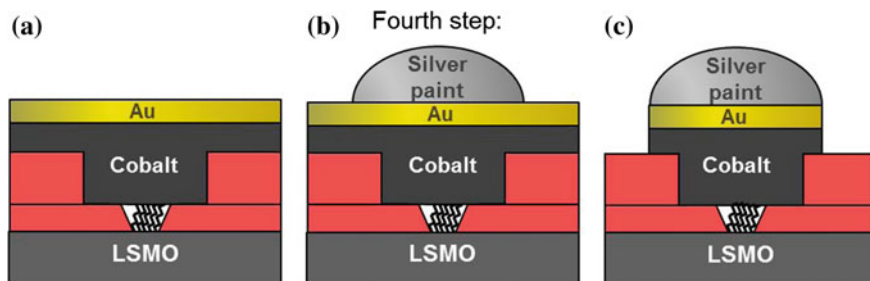
Fig. 5.23 Schematic representation of the last steps of the device fabrication. **a** The top electrode of Co (20 nm) is deposited by sputtering and is covered by an Au layer (80 nm) to protect it from oxidation. **b** A drop of silver paint is deposited over each contact to protect the electrode from etching. **c** Unprotected Co/Au is etched by IBE to remove the short-circuits between one contact to the other. The device is now completed

over the sample. To do that, a vector gas, generally Ar, is injected into the vacuum chamber (5×10^{-8} mbar of residual pressure in our system). The target is negatively polarized while the sample is positively polarized. A difference of potential is created and this electric field ionizes the gas and accelerates the Ar^+ ions on the material target. The surface atoms are so extracted and deposited on the upstanding sample. This deposition technique is quite energetic and the probability to have atom diffusion through the molecular barrier is supported by the energy of the incident atoms with the subsequent creation of short-circuits. Nevertheless, the nanometric size of our junction dramatically reduces the probability to have some atoms that diffuse to the bottom of the nanohole, while on the rest of the sample the resist insulator layer of 40 nm is thick enough to prevent short-circuit formation.

Using this technique Co (20 nm) is deposited and is covered with an Au layer (80 nm) in order to protect Co by oxidation when the sample is exposed to air (Fig. 5.23a).

5.4.4.2 Ion Beam Etching (IBE)

With the sputtering deposition the tunnel junction is completed. Since Co (20 nm)/Au (80 nm) layer has been deposited on the whole surface, an etching process is necessary to remove lateral short-circuits between nanocontacts. First of all, a small drop of silver paint is deposited by hand on each indented square as represented in Fig. 5.23b. Then, the sample is heated until all the paint solvent is removed. Silver paint acts as a mask and protects the underlying Co/Au electrode during the following ion beam etching (IBE). During IBE, Ar ions are accelerated by a grid and neutralized before to arrive on the surface. The etching is real time controlled by a mass spectrometer (SIMS) that allows to check one or more etched materials at the same time.

In Fig. 5.24 is represented a typical curve of the Co/Au etching provided by the mass spectrometer in function of time. When etching starts, the Au atoms are firstly removed from the surface thus the Au signal is maximum. In Fig. 5.24 it can be seen that the Co signal is present even for the first few seconds of the process. This signal probably corresponds to Co coming from the borders of the sample. The bulk Co signal appears after about 4 min, when all the Au layer is removed and the Co is now completely exposed. The process is stopped when no more Co signal is detected: all the Co layer has been removed and the resist is now exposed. The etching rate of the resist under these conditions is much slower than the one of the metals and the few seconds of exposition after Co do not affect at all its insulating function.

With IBE process nanocontacts are no more laterally connected one to the other and they are ready to be measured (Fig. 5.23c).

5.4.4.3 Sample Bonding

The final step is to bond the completed device into a chip to be able to measure it into the cryostat. This step is done using a ball-bonding machine. Au wires of

Fig. 5.24 Real-time measurement of a Co(20 nm)/Au(80 nm) bilayer etching. The peak for Co signal at the beginning is systematically observed but it does not correspond to a real etching of the Co layer. After 400 s the signal of Co disappears and the thick resist starts to be etched
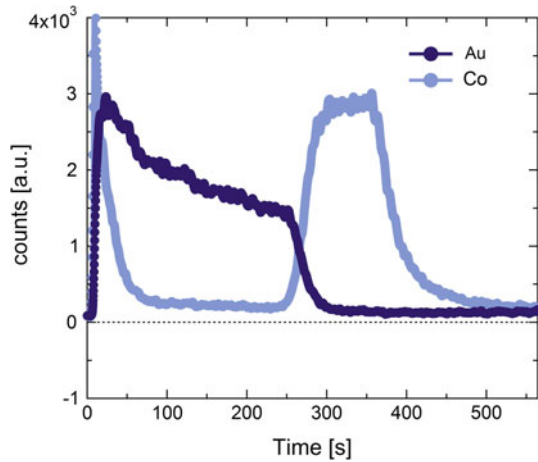
Fig. 5.25 Photo of the final device (5 × 5 mm), bonded into a chip and ready to be measured into the cryostat
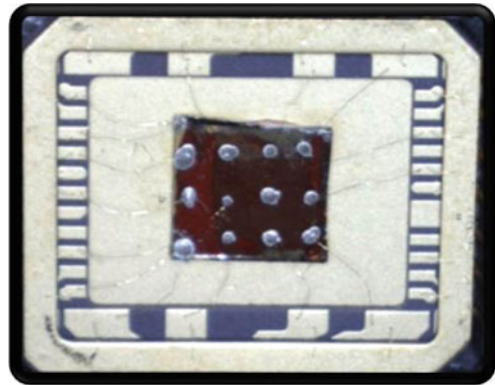
20 μm diameter are manually connected from the chip contacts to the silver paint top contacts. Silver paint drops are manually deposited over each contact to fix the Au wire and provide the electrical contact. Resist is also scratched on the corners of the sample in order to take a contact on the LSMO bottom electrode. A picture of the final device is provided in Fig. 5.25.

References

1. A.N. Pasupathy, R.C. Bialczak, J. Martinek, J.E. Grose, L.A.K. Donev, P.L. McEuen, D.C. Ralph, The Kondo effect in the presence of ferromagnetism. Science **306**, 86–89 (2004)
2. R. Yamada, M. Noguchi, H. Tada, Magnetoresistance of single molecular junctions measured by a mechanically controllable break junction method. Appl. Phys. Lett. **98**, 053110 (2011)
3. J.R. Petta, S.K. Slater, D.C. Ralph, Spin-dependent transport in molecular tunnel junctions. Phys. Rev. Lett. **93**, 136601 (2004)

4. W. Wang, C.A. Richter, Spin-polarized inelastic electron tunneling spectroscopy of a molecular magnetic tunnel junction. Appl. Phys. Lett. **89**, 153105 (2006)

5. K. Bouzehouane, S. Fusil, M. Bibes, J. Carrey, T. Blon, M. Le Dû, P. Seneor, V. Cros, L. Vila, Nanolithography based on real-time electrically controlled indentation with an atomic force microscope for nanocontact elaboration. Nano Lett. **3**, 1599–1602 (2003)

6. Y. Tian, D. Chen, X. Jiao, Nearly freestanding in water: preparation and magnetic properties. Chem. Mater. **18**, 6088–6090 (2006)

7. R. Rajagopal, J. Mona, S.N. Kale, T. Bala, R. Pasricha, P. Poddar, M. Sastry, B.L.V. Prasad, D.C. Kundaliya, S.B. Ogale, $La_{0.7}Sr_{0.3}MnO_3$ nanoparticles coated with fatty amine. Appl. Phys. Lett. **89**, 023107 (2006)

8. S. Tatay, C. Barraud, M. Galbiati, P. Seneor, R. Mattana, K. Bouzehouane, C. Deranlot, E. Jacquet, A. Forment-Aliaga, P. Jegou, A. Fert, F. Petroff, Self-assembled monolayer-functionalized half-metallic manganite for molecular spintronics. ACS Nano **6**, 8753–8757 (2012)

9. D.M. Spori, N.V. Venkataraman, S.G.P. Tosatti, F. Durmaz, N.D. Spencer, S. Zürcher, Influence of alkyl chain length on phosphate self-assembled monolayers. Langmuir **23**, 8053–8060 (2007)

10. N. Tillman, A. Ulman, J.S. Schildkraut, T.L. Penner, Incorporation of phenoxy groups in self-assembled monolayers of trichlorosilane derivatives: effects on film. J. Am. Chem. Soc. **110**(18), 6136–6144 (1988)

11. J.-J. Liang, H.-S. Weng, Catalytic properties of $La_{1-x}Sr_xBO_3$ (B=Mn, Fe Co, Ni) for toluene oxidation. Ind. Eng. Chem. Res. **32**, 2563–2572 (1993)

12. W. Rao, J. Yu, The structural and morphology of $(La_{0.7}Sr_{0.3})MnO_3$ thin films prepared by pulsed laser deposition. Adv. Mater. Res. **150–151**, 908–911 (2011)

13. M. Textor, L. Ruiz, R. Hofer, A. Rossi, K. Feldman, N.D. Spencer, Structural chemistry of self-assembled monolayers of octadecylphosphoric acid on tantalum oxide surfaces. Langmuir **16**, 3257–3271 (2000)

14. G. Zorn, I. Gotman, E.Y. Gutmanas, R. Adadi, G. Salitra, C.N. Sukenik, Surface modification of Ti45Nb alloy with an alkylphosphonic acid self-assembled monolayer. Chem. Mater. **17**, 4218–4226 (2005)

15. F. Li, Y. Zhan, T.-H. Lee, X. Liu, A. Chikamatsu, T.-F. Guo, H.-J. Lin, J.C.A. Huang, M. Fahlman, Modified surface electronic and magnetic properties of $La_{0.6}Sr_{0.4}MnO_3$ thin films for spintronics applications. J. Phys. Chem. C **115**, 16947–16953 (2011)

16. T. Burnus, Z. Hu, H. Hsieh, V. Joly, P. Joy, M. Haverkort, H. Wu, A. Tanaka, H.-J. Lin, C. Chen, L. Tjeng, Local electronic structure and magnetic properties of $LaMn_{0.5}Co_{0.5}O_3$ studied by x-ray absorption and magnetic circular dichroism spectroscopy. Phys. Rev. B **77**, 125124 (2008)

17. R. Sahu, Z. Hu, M. Rao, S. Manoharan, T. Schmidt, B. Richter, M. Knupfer, M. Golden, J. Fink, C. Schneider, X-ray absorption spectra at the Ru and Mn $L_{2,3}$ edges and long-range ferromagnetism in $SrRu_{1-x}Mn_xO_3$ solid solutions ($0 \leqslant x \leqslant 0.5$). Phys. Rev. B **66**, 144415 (2002)

18. A. Ruotolo, V. Cros, B. Georges, A. Dussaux, J. Grollier, C. Deranlot, R. Guillemet, K. Bouzehouane, S. Fusil, A. Fert, Phase-locking of magnetic vortices mediated by antivortices. Nat. Nanotechnol. **4**, 528–532 (2009)

19. V. Garcia, M. Bibes, L. Bocher, S. Valencia, F. Kronast, A. Crassous, X. Moya, S. Enouz-Vedrenne, A. Gloter, D. Imhoff, C. Deranlot, N.D. Mathur, S. Fusil, K. Bouzehouane, A. Barthélémy, Ferroelectric control of spin polarization. Science **327**, 1106–1110 (2010)

20. S. Fusil, L. Piraux, S. Mátéfi-Tempfli, M. Mátéfi-Tempfli, S. Michotte, C.K. Saul, L.G. Pereira, K. Bouzehouane, V. Cros, C. Deranlot, J.-M. George, Nanolithography based contacting method for electrical measurements on single template synthesized nanowires. Nanotechnology **16**, 2936–2940 (2005)

21. A. Bernand-Mantel, P. Seneor, K. Bouzehouane, S. Fusil, C. Deranlot, F. Petroff, A. Fert, Anisotropic magneto-Coulomb effects and magnetic single-electron-transistor action in a single nanoparticle. Nat. Phys. **5**, 920–924 (2009)

22. C. Barraud, P. Seneor, R. Mattana, S. Fusil, K. Bouzehouane, C. Deranlot, P. Graziosi, L. Hueso, I. Bergenti, V. Dediu, F. Petroff, A. Fert, Unravelling the role of the interface for spin injection into organic semiconductors. Nat. Phys. **6**, 615–620 (2010)

Chapter 6
# Magneto-Transport Results in SAM Based MTJs

This chapter is dedicated to the description of the magneto-transport results obtained in LSMO/SAM/Co magnetic tunnel nanojunctions fabricated by nanoindentation lithography technique as described in Sect. 5.4.

We started by focusing on the study of LSMO/C12P/Co MTJs. This is because C12P is a medium size alkyl chain: long enough to avoid short-circuits in the junction but short enough to give a device resistance in the order of few tens of MΩ and thus easier to measure. Next, we started to tune the molecule thickness from C10P to C18P (from 10 carbon atoms in the alkyl chain to 18). This allowed on one hand to validate our system by comparing the exponential increase of the junction resistance to the one reported in the literature (see Sect. 4.4) and, on the other hand, it represents the first step towards the barrier tailoring at the molecular level.

6.1 Experimental Set-Up

Experiments have been performed in an Oxford Instruments cryostat equipped with a superconducting coil able to generate a magnetic field up to 7 T. Since the resistance of the contacts is quite high (in the MΩ range), we applied a bias on the sample and measured the current through the junction. The DC source used to apply the voltage is a Yokogawa 7651. The current is amplified at the exit of the sample by a DLPCA-200 amplifier in order to reduce the signal to noise ratio. Current is then converted to voltage and finally measured by a nanovoltmeter (Keithley 2182a). The actual limit of measurement of this set-up is hundreds of fA.

Along my PhD the equipment has been progressively improved in order to perform simultaneous measurements of DC and AC signals applied to the sample. Measurement of AC signal is very useful to directly measure the first or second derivative of current and gain accurate information on the fine structure of the junction, as we will see in the next section where inelastic electron tunneling spectroscopy technique (IETS) will be presented. With this aim, a small AC signal (1–10 mV) at a frequency ω (∼4 Hz) is generated by an AC source (SRS DS360) and added to the DC one. It is

(a)

(b)
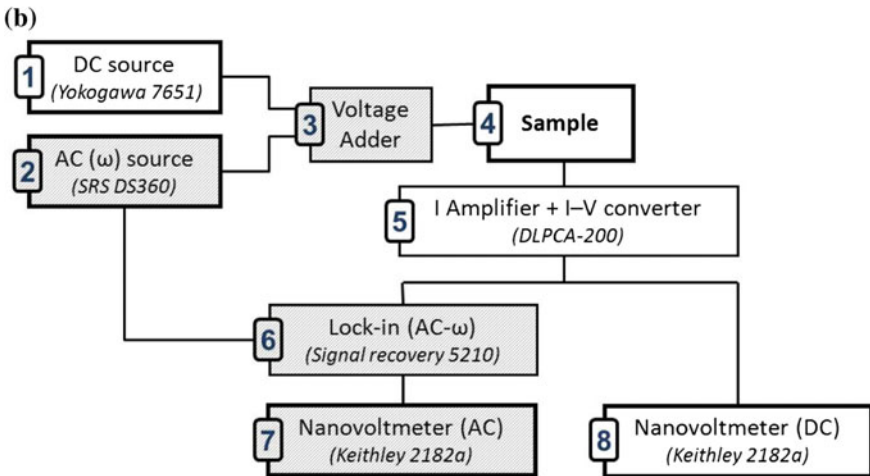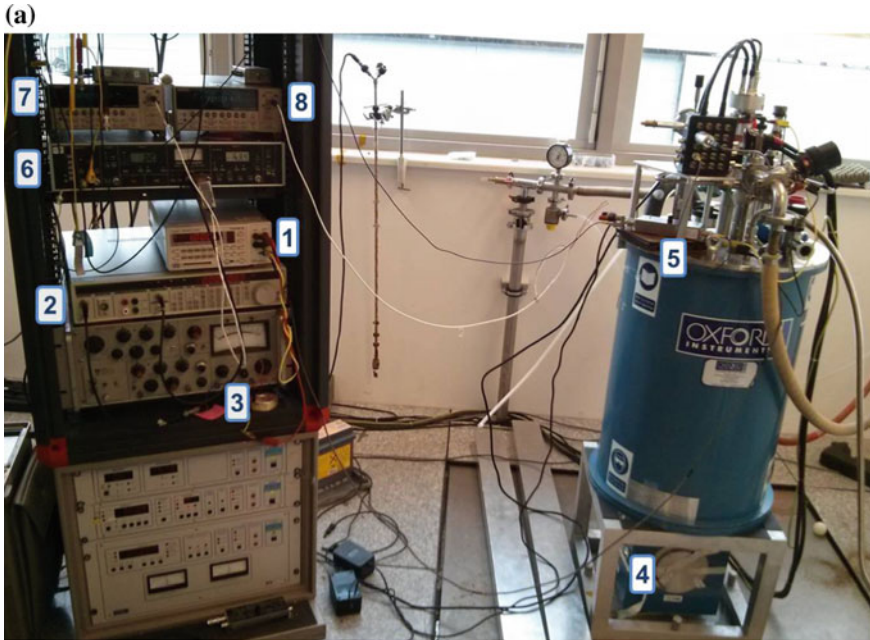
Fig. 6.1 **a** Photo of the equipment used to perform magneto-transport measurements on the devices. Sample is situated inside a cryostat equipped with a superconducting coil able to generate a magnetic field up to 7 T. **b** Schematic representation of the set-up used to measure. In *gray* are highlighted instruments added in a second time and used to directly measure the first and second derivative of current

then detected at the exit of the sample by a lock-in and finally measured by another nanovoltmeter Keithley 2182a.

The schematic of this set-up is represented In Fig. 6.1b and the parts that have been added in order to perform the simultaneous DC and AC signal measurement are shown in gray. A photo of the equipment is also provided in Fig. 6.1a.

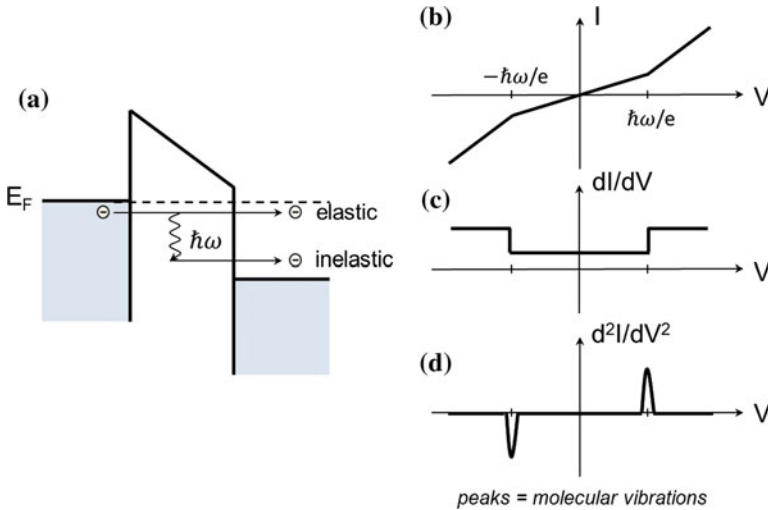## 6.2 Inelastic Electron Tunneling Spectroscopy

Inelastic Electron Tunneling Spectroscopy (IETS) is a powerful spectroscopic tool that relates feature in the d^2I/dV^2 signal to the vibrational excitations of the molecules contained into the barrier.

This possibility was discovered in 1966 by Jaklevic and Lambe at Ford Motor Co. [1]. While studying the tunnelling effect of metal-oxide-metal junctions, authors found anomalous peaks in the d^2I/dV^2 versus V characteristic that they could relate to the presence of organic impurities in their device [1, 2]. In the following years IETS was developed as a powerful tool for various applications such as chemical identification, bonding investigation, trace substance detection, etc. In the last years this technique has been also increasingly used in molecular electronics as a premier analytical tool in the understanding of nanoscale and molecular junctions.

One of the main advantages of this technique compared to IR or Raman spectroscopy is its sensitivity. While IR and Raman require 10^3 or more molecules to provide a spectrum, IETS can provide good spectra with a single molecule since the interaction of the electron with molecular vibrations is much stronger than that of photon. Moreover, despite IETS is more sensitive to vibrations parallel to the current direction, this technique is not subjected to rigorous selection rules and both IR and Raman-active vibrational modes can be detected in this way. Finally, the most interesting advantage for molecular devices is that molecules can be characterized directly in the junction, thus giving information on the real and specific characteristics of each device. For this reason the vibrational spectra can be used as a fingerprint to identify the molecular species confined inside the junction [3, 4].

IETS Principle

In order to better understand the principles behind IETS technique, in Fig. 6.2a is reported the schematic diagram of a metal-insulating-metal tunnel junction. When a bias is applied on one of the two electrodes, a difference of potential is created and electrons from an occupied state, in the case of the picture in the left electrode, can tunnel into an empty state of the right one. If the electron has the same energy before and after tunneling the process is elastic. On the contrary, if there is a vibrational mode with a frequency ω inside the barrier, an electron with enough energy (eV $\geq$ $\hbar\omega$) could excite the vibrational mode and then tunnel into another empty state of the right electrode. In this case the process is inelastic: an inelastic channel is opened for the electron and its overall tunneling probability is increased. When measuring the

(b)

(a)

$-\hbar\omega/e$

E_F ⊖ - - - - - - → ⊖ elastic   **(c)**

$\hbar\omega$

→ ⊖ inelastic

$\hbar\omega/e$

V

dI/dV

V

d²I/dV²

(d)

V

peaks = molecular vibrations

Fig. 6.2 a Schematic of a metal-insulator-metal tunnel junction. If electrons tunnel through the barrier without losing energy the process is called elastic, while if some energy is lost the process is inelastic. Electrons that relax can excite a molecular vibration in the barrier at an energy $E = \hbar\omega$. This can be detected as a change of the slope in the I(V) characteristic at $V = \pm\hbar\omega/e$ (**a**), as a step in the dI/dV(V) characteristic (**b**) and as a peak in the d²I/dV²(V) curve (**c**)

I(V) characteristic of a junction, as shown in Fig. 6.2b, the opening of an inelastic channel results in a change of the slope for the specific bias value. This slope change corresponds to a step in the dI/dV plot (Fig. 6.2c) and to a peak in the d^2I/dV^2 plot (Fig. 6.2d). These peaks are the ones that are detected by IETS and are related to the vibrational modes excited into the molecular barrier.

Experimental Set-Up

In general, only a small fraction of electrons tunnel inelastically and the signal corresponding to molecular vibrations is very small. For this reason when I(V) characteristics are numerically derived, noise is often too high to detect any peak corresponding to a vibrational mode. One more sophisticated but much efficient method is to directly measure the second derivative of current using a "lock-in" detection technique. The schematic representation of the setup is the one presented in Fig. 6.1b. The IETS signal is measured by an AC modulation method. A small sinusoidal signal at a frequency ω is generated by the AC source and added to the DC voltage applied across the junction. The current response of the device is measured and the AC signal is detected at the frequency ω or 2ω by a "lock-in" and measured by a nanovoltmeter. The signal detected at ω is directly proportional to the first derivative of current, while the signal detected at 2ω is proportional to the second derivative one. This can be seen mathematically if we consider the Taylor expansion of the current around the applied bias [5]:

$$I\left(V_d + V_a \cos \omega t\right) = I\left(V_d\right) + \left.\frac{dI}{dV}\right|_{V_d} V_a \cos \omega t \ + \frac{1}{2} \left.\frac{d^2 I}{dV^2}\right|_{V_d} V_a{}^2 \cos^2 \omega t \ + \cdots$$

$$= I\left(V_d\right) + \left.\frac{dI}{dV}\right|_{V_d} V_a \cos \omega t \ + \frac{1}{4} \left.\frac{d^2 I}{dV^2}\right|_{V_d} V_a{}^2 \left(1 + \cos 2\omega t\right) + \cdots$$

$$\tag{6.1}$$

where V_d is the DC voltage applied to the junction and V_a is the AC modulation at a frequency ω. As one can note in the second term of the development, the signal detected at a frequency of 2ω is proportional to $d^2 I / dV^2$ and thus IETS can be directly measured.

6.3 Magneto-Transport Results on LSMO/C12P/Co Nanojunctions

In order to study transport through dodecylphosphonic acid (C12P) SAMs, a total of 74 LSMO/C12P/Co junctions have been characterized. About 30 % of them were measurable with resistances in the MΩ range and below. Among the measurable contacts, 2/5 presented a resistance in the kΩ range and a behaviour in temperature comparable to the one of a short-circuit sample. In average contacts showed resistances in the order of 10 MΩ with markedly nonlinear I(V) curves and 2/3 of them also presented clear tunnel magnetoresistance (TMR) signal, all with a positive sign and ranging from 20 to 50 % of TMR ratio.

6.3.1 Electrical Characterization of the Nano-Junctions

We started our studies by the electrical characterization of the nanojunctions in order to verify the tunnel behaviour of current through the molecular barrier. In Fig. 6.3a is represented the I(V) characteristic recorded for a nano-junction. Positive bias in these measurements corresponds to electrons injected from the Co contact (top electrode) into the molecules. Nonlinear I(V) curves are indicative of carriers tunnelling through the insulating SAMs barrier and the curves are similar to the ones reported on alkane SAMs presented in Sect. 4.3.1.

Moreover, we also investigated the resistance dependence on temperature in order to definitely confirm that the transport regime that we observed was tunnelling. Even if the junction resistance did not vary a lot with temperature, in general the variation was less than a factor 10 for all the working contacts, the shape of temperature behaviour varied from one contact to the other. One example is reported in Fig. 6.3b. The bump that can be observed in this case is typical of LSMO and it has been already reported in LSMO based magnetic tunnel junctions [6]. It corresponds to the surface
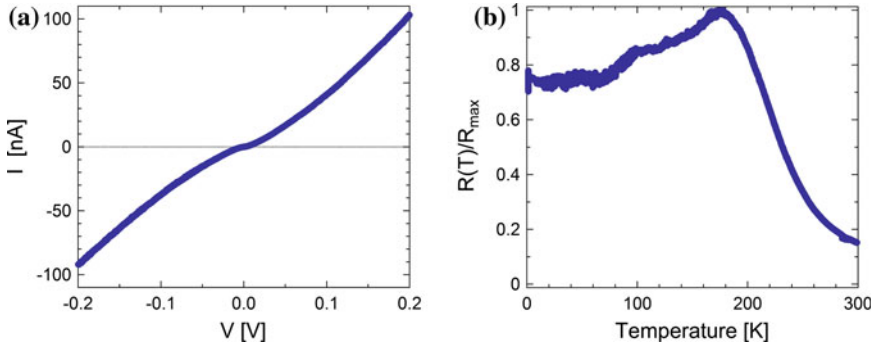
Fig. 6.3 a I(V) characteristic recorded for a LSMO/C12P/Co magnetic tunnel nanojunction at T = 2 K. **b** Example of resistance dependence as a function of temperature for a LSMO/C12P/Co nanojunction. The peak around 180 K corresponds to the surface Curie temperature of LSMO and it is typical of LSMO based MTJs [6]. Since resistance increases with decreasing temperature by less than a factor 10, direct tunnelling is the most likely transport regime

Curie temperature of LSMO. Nevertheless, the almost constant behaviour with temperature allows to exclude thermionic emission and hopping conduction as transport mechanisms since they are characterized by a marked temperature-dependent behaviour. For low applied voltage, the Fowler-Nordheim tunnelling regime is also excluded since the average barrier φ height is expected to be around the eV. The observed transport mechanism in the junction is thus more likely direct tunnelling.

Extraction of Junction Parameters

In order to extract the tunnel barrier parameters, we also tried to analyse the measured I(V) curves using the models presented in Sect. 4.3.1. Nevertheless, when fitting curves recorded at low temperature, it was not possible to fit I(V) features at low bias due to the presence of the zero bias anomaly contribution (see Fig. 6.10a) that is not taken into account in the models. When fitting I(V) curves at room temperature (the zero bias anomaly is less pronounced), fits were not significant since many different sets of parameters could be used. For these reasons we focused on TVS approach, since it allows to directly extract junction parameters from the measured data and the range concerned is mainly the one of high voltage where the zero bias anomaly has the less influence.

One example of Fowler-Nordheim curve obtained from an I(V) characteristic at 2 K is shown in Fig. 6.4. The minima positions are found at $V_{t+} = 0.91$ V and $V_{t-} = -1.03$ V. These values are comparable with the ones reported in the literature and summarized in Table 4.2. By substituting V_{t+} and V_{t-} in Eqs. 4.18 and 4.19, we calculated the energy level position $\varepsilon_0 = 0.84$ eV and the bias asymmetry $\gamma = -0.03$. The level position ε_0 is compatible with barrier values reported in the literature (Table 4.1), while the bias asymmetry is almost zero showing that the level is not strongly coupled to any of the two electrodes. Nevertheless, these estimations can just give a preliminary idea on the structure of the junction, further theoretical investigations will be needed for a better understanding of these parameters.
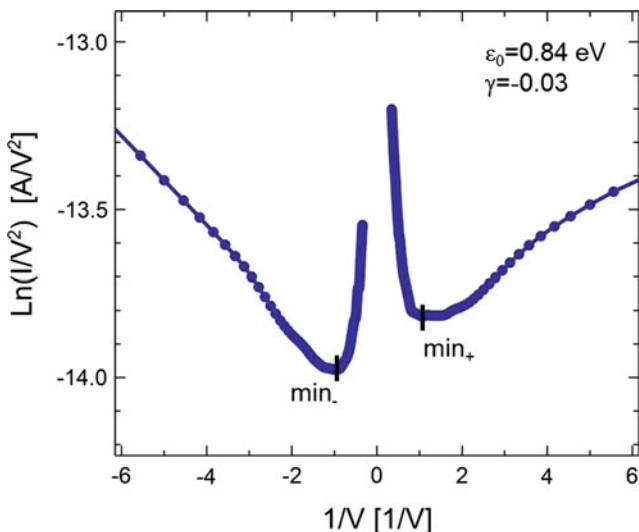
Fig. 6.4 Fowler-Nordheim plot obtained from an I(V) characteristic measured in a LSMO/C12P/Co nanojunction at 2 K. Minima at positive and negative bias correspond to $V_{t+} = 0.91$ V and $V_{t-} = -1.03$ V. From Eqs. 4.18 and 4.19 we calculated the energy level position $\varepsilon_0 = 0.84$ eV and the bias asymmetry $\gamma = -0.03$

6.3.2 Tunnel Magnetoresistance

Magneto-transport properties of the nanojunctions have been also investigated and they gave very promising results. In Fig. 6.5 is presented an example of one tunnel magnetoresistance (TMR) curve recorded at low temperature and low bias (10 mV) for a LSMO/C12P/Co sample. It shows the change of resistance by applying a magnetic field parallel to the junction plane. The TMR is defined following the Jullière's formula as $TMR = (R_{AP} - R_P)/R_P$.

The observed magnetoresistance signal is always positive, meaning that the high resistance state is obtained in an antiparallel configuration of the system ($R_{AP} > R_P$). The first switch of magnetization at low magnetic field is ascribed to the LSMO electrode as we can see by the SQUID measurement performed on the LSMO substrate (Fig. 5.4a). The second switch around ± 100 mT is thus ascribed to the Co electrode. The high value of the coercive field observed cannot be understood if we only consider the magnetic properties of the thin Co film (20 nm), but the high shape anisotropy of the nanocontact must also play a role. The fact that the high resistance state is not perfectly defined is indicative of a progressive switch of the two ferromagnetic electrodes. Electrodes magnetizations are partially coupled and the parallel and antiparallel magnetic configurations are not perfectly defined. Moreover, one can notice that the parallel state is not entirely saturated to a constant value but it presents a slope. This effect is related to the progressive alignment of LSMO surface magnetization [7].
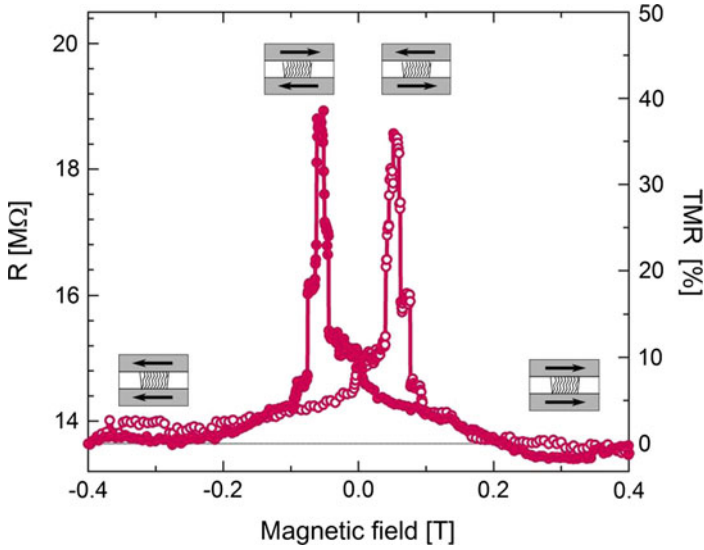
Fig. 6.5 Example of one magnetoresistance curve recorded at 10 mV and 4 K for a LSMO/C12P/Co nanojunction. Resistance change (R ∼ 14 MΩ) is measured while sweeping the magnetic field parallel to the junction plane. Schematic of the junction magnetic polarization switching is represented in the picture. TMR is defined as the Jullière's formula: $TMR = (R_{AP} - R_P)/R_P$

Finally, it is quite remarkable that, despite the technological difficulty to realize the devices due to the nanometric scale and the complexity of the fabrication process where many factors can play a role, results for the "working" contacts are well reproducible. All the contacts present a clear positive magnetoresistance ranging from 20 to 50 % at low temperature. This TMR ratio is comparable to the one found for inorganic magnetic tunnel junctions using LSMO and Co electrodes [8] thus confirming the quality of our contacts and the potential of using SAMs as tunnel barriers in MTJs.

6.3.2.1 TMR Dependence on Angle

In order to define if the observed signal is exclusively due to TMR effects or if anisotropic effect such as AMR or TAMR can play a role, we also performed angle-dependent measurements. In Fig. 6.6 are shown TMR curves recorded maintaining the magnetic field in the plane of the junction and rotating the sample of 0°, 45° and 90° in the plane. As one can see, no appreciable differences can be observed between these curves. On the contrary, if some anisotropic effect would have played a role, a shift in the parallel state and/or an inversion in the magnetoresistance sign should be observed [9]. Thus, it is possible to exclude any consistent contribution coming from anisotropic effects.

Fig. 6.6 Comparison of
magnetoresistance curves for
three different orientations of
the magnetic field in the
LSMO/C12P/Co junction:
0°, 45° and 90°. Magnetic
field is always maintained in
the plane of the junction. No
appreciable difference can be
observed between the three
orientations thus excluding
consistent contributions from
anisotropic effects
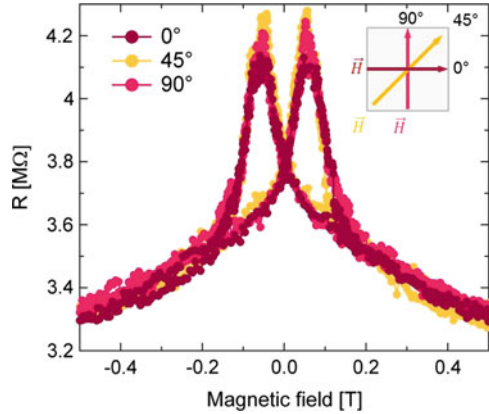

6.3.2.2 TMR Dependence on Temperature

The behaviour of TMR at different temperatures has been also investigated. In
Fig. 6.7a–d are shown TMR curves recorded at: 4, 48, 115, 200 K for 10 mV of applied
bias. Signal starts to become very small above 200 K and it is completely extinguished
at 300 K as expected from the reduced Curie temperature of the LSMO surface. In
Fig. 6.7e the behaviour of TMR decreasing with temperature is also reported and it
is compared with the bare LSMO surface polarization traced in dotted line [10]. As
one can see, TMR decreasing is mainly driven by the LSMO loss of polarization.
According to this observation and as already pointed out [11], the low Curie tem-
perature of the LSMO interface appears to be the main limitation to the observation
of room temperature magnetoresistance effects (see Sect. 1.3.3). This issue could be
solved by replacing LSMO with higher Curie temperature ferromagnets.

6.3.2.3 TMR Dependence on Bias Voltage

Finally, the TMR dependence on bias voltage has been also investigated, giving
unexpected and interesting results. This is reported in Fig. 6.8a and its behaviour
is shown at different temperatures. In Fig. 6.8b, c the TMR curves recorded at 10,
800 mV and 2 V at a temperature of 4 K and 115 K are also compared.

The most striking feature observed throughout all the tested junctions is the
extreme robustness of the TMR effect as a function of the bias voltage. As shown
in the pictures, a clear TMR signal can still be observed in the volt range, while in
previous reports on SAM-based magnetic tunnel junctions [12, 13] or even in most
organic semiconductor-based spintronics devices [14–16], the TMR response almost
vanishes when the bias voltage is increased above a few hundred millivolts.

For magnetic tunnel junctions, a conventional figure of merit is the voltage value
($V_{1/2}$) at which the TMR ratio becomes half of the zero voltage TMR. Here the $V_{1/2}$
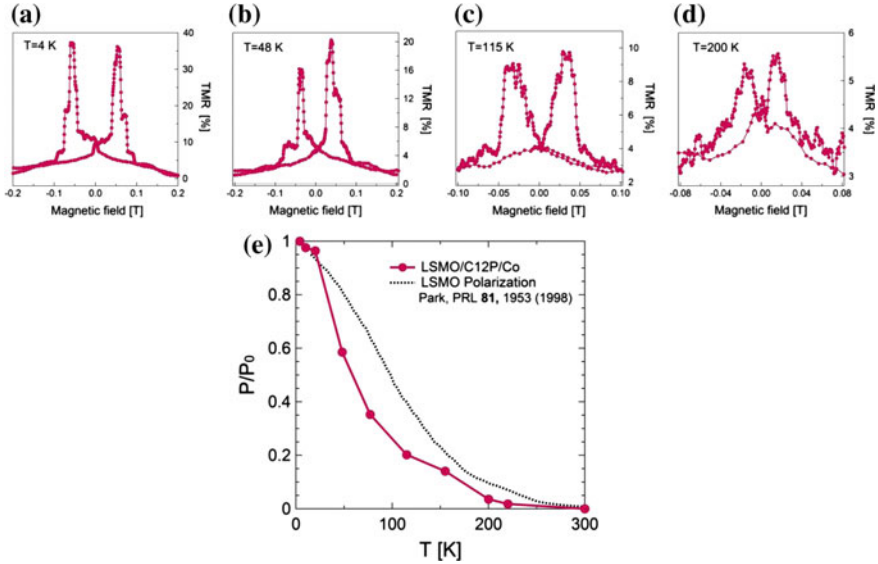
Fig. 6.7 TMR curves recorded at 10 mV for different temperatures: **a** 4 K, **b** 48 K, **c** 115 K, **d** 200 K. **e** In *red*, TMR behaviour with temperature for a LSMO/C12P/Co nanojunction. TMR is normalized with the value at low temperature. In *black* (*dotted line*), comparison with LSMO surface polarization [10]. TMR decreasing with temperature is mainly driven by LSMO loss of polarization thus allowing to ascribe to LSMO the absence of TMR observation at room temperature in the junctions

exceeds 1.5 V, well above the 0.3–0.6 V typical for Al–O tunnel barriers and on par with the best inorganic magnetic tunnel junctions (1.25–1.5 V in Fe/MgO/Fe MTJs [17, 18]).

Even more interestingly, we observe an almost flat dependence of TMR with bias voltage in the volt range and when increasing temperature. A question remains open about the physical origin of this highly unexpected behaviour.

At present, the exact origin of the TMR decrease has not been fully elucidated even in conventional inorganic MTJs. However, it is usually ascribed to magnons [19, 20] whose signature would be the "Zero-Bias Anomaly" (ZBA) described in Sect. 1.3.3. Still, two questions remain unexplained: (i) the weaker bias dependence (high $V_{1/2}$ value) observed in our system in comparison to inorganic LSMO/barrier/Co MTJs and (ii) the flat TMR vs bias behaviour observed at higher temperature.

For what concerns the first question, it was shown that in certain conditions such as experiments through a vacuum barrier (which can be somehow considered as an ideal defect free barrier) the TMR did not decrease with applied voltage [21]. A similar behaviour was also reported for monocrystalline Fe/MgO/Fe magnetic tunnel junctions [18, 22]. Even if not conclusive, this suggests that the high quality barrier and orbital matching may be part of the key to this stability. While possible, it is not obvious to ascribe this origin to our molecular devices.
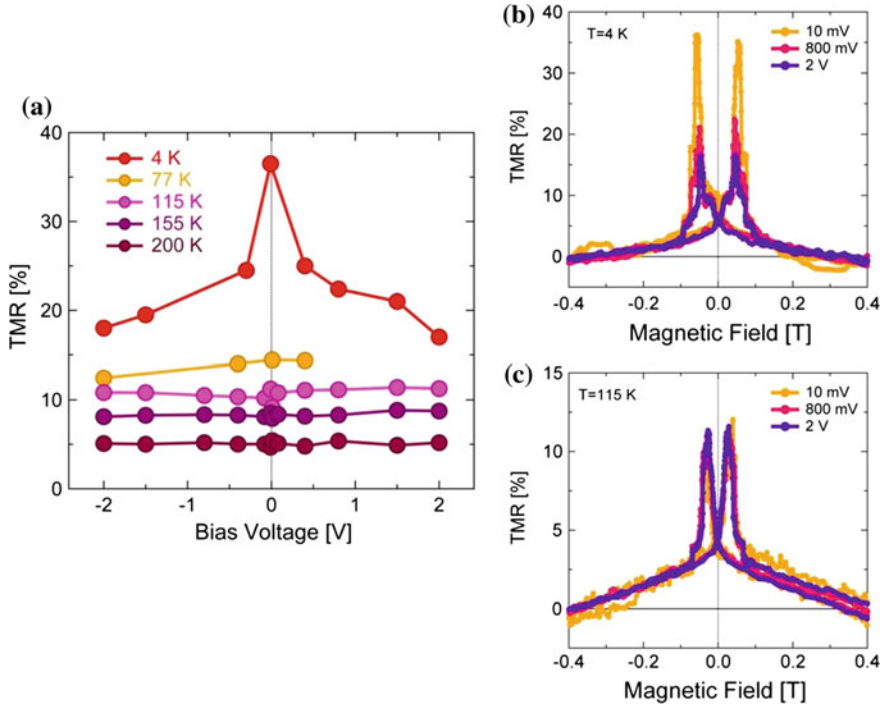
Fig. 6.8 a TMR dependence on bias voltage for different temperatures: 4, 77, 115, 155, 200 K. At very low temperature TMR decreases with the increasing of bias. One of the most remarkable points is that the signal is very robust with still almost 20 % TMR at 2 V and $V_{1/2}$ value exceeding 1.5 V. The other unexpected behaviour is that when temperature increases, TMR presents a flat behaviour. **b** Examples of TMR curves recorded at 4 K for different bias voltage: 10, 800 mV and 2 V. **c** Examples of TMR curves recorded at 115 K for different bias voltage: 10, 800 mV and 2 V

Another hint could also arise from the observation of this stability at high temperature (Fig. 6.8b, c). Following this idea, a possible explanation of this unexpected behaviour could involve molecular vibrations in a beneficial way. Indeed, even in the absence of good orbital matching conditions, magnon excitations could be short-circuited by easily excited molecular vibrations that are known to play predominant roles in molecular junctions.

A schematic view of these two excitation mechanisms is represented in Fig. 6.9. When magnons are excited in one of the two electrodes, electrons lose their energy and their spin polarization (Fig. 6.9a). On the contrary, when electrons excite molecular vibrations in the barrier, they lose their energy but conserve their spin polarization [23] (Fig. 6.9b).

Finally, the conservation of electrons spin polarization when exciting phonons (Fig. 6.9b) could be also at the base of the flat TMR behaviour observed at higher temperature. Indeed, when increasing temperature, molecular vibrations become more and more important, and electrons relaxations by magnons consequently decrease.
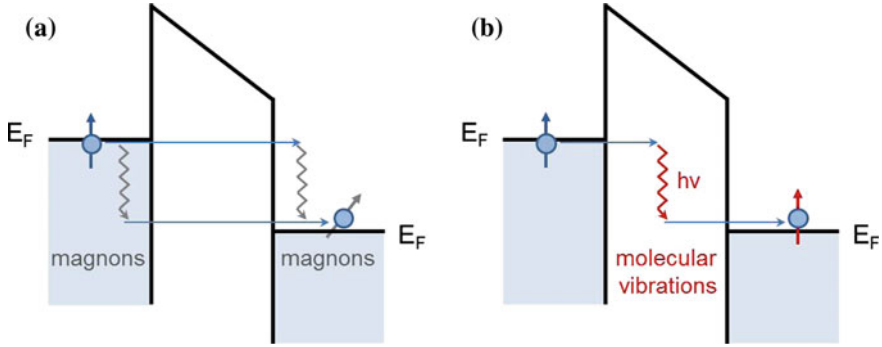
Fig. 6.9 Schematic representation of an electron exciting magnons (**a**) or phonons (**b**) when tunneling through the organic barrier. When magnons are excited, the electron loses its spin polarization (**a**). On the contrary, when molecular vibrations are excited, the electron can maintain its spin polarization [23] (**b**)
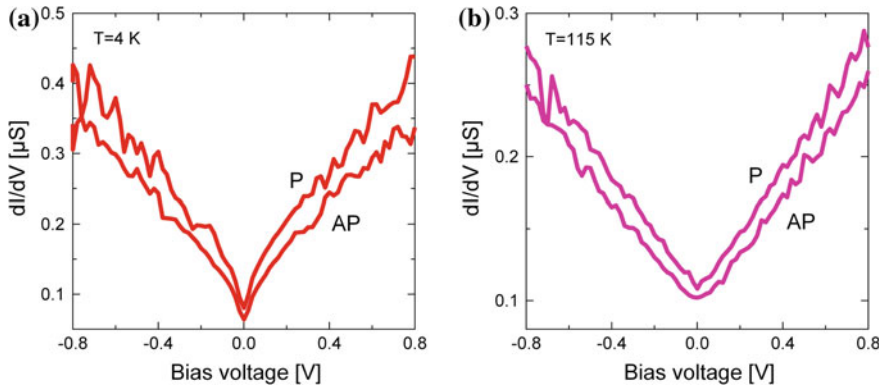
Fig. 6.10 Conductance comparison in the parallel and antiparallel configurations for a LSMO/C12P/Co nanojunctions measured at **a** 4 K and **b** 115 K. Curves are calculated as dI/dV. ZBA is observed only at 4 K

This hypothesis would be also supported by the observation of the conductance curves recorded for this junction at 4 and 115 K and shown in Fig. 6.10. While ZBA anomaly is clearly visible at 4 K (Fig. 6.10a), it is strongly reduced in the curve at 115 K (Fig. 6.10b) thus meaning a decreased number of magnon excitations. Nevertheless, support from theoretical simulations would be needed in order to unravel the exact mechanism.

Reproducibility

In order to show that TMR stability up to the volt range is well reproducible in our system, in the following will be reported examples of TMR dependence on bias voltage measured on others LSMO/C12P/Co nanojunctions.
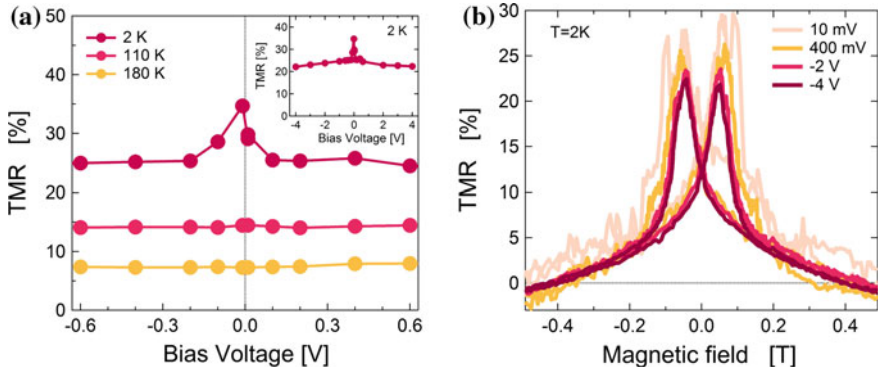
Fig. 6.11 First example of TMR dependence on bias voltage for a different LSMO/C12P/Co nanojunction. **a** TMR dependence on bias voltage for different temperatures: 2, 110, 180 K. At very low temperature TMR decreases with the increasing of bias. One of the most remarkable points is that signal is very robust with still almost 20 % TMR at 4 V (*inset*) and $V_{1/2}$ value well exceeds 2 V. The other unexpected behaviour is that TMR presents a flat behaviour when temperature increases. **b** Examples of TMR curves recorded at 2 K for different bias voltages: 10, 400 mV, -2 and -4 V
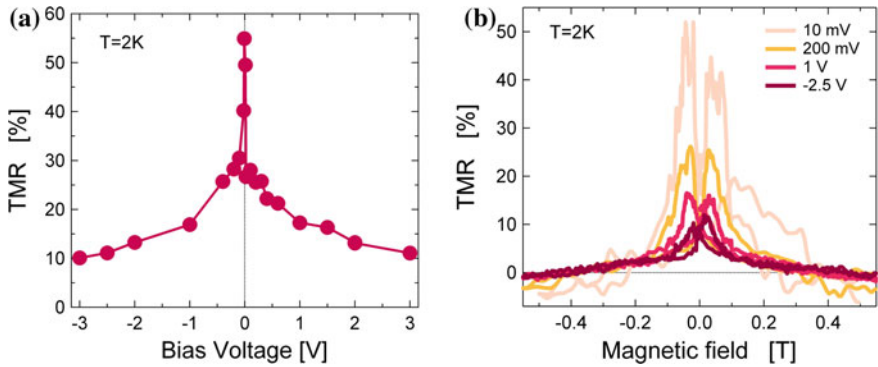
Fig. 6.12 Second example of TMR dependence on bias voltage for a different LSMO/C12P/Co nanojunction. **a** TMR dependence on bias voltage at 2 K. TMR at low bias is about 55 % and the signal can be observed up to 3 V where it has an amplitude of 10 %. **b** Examples of TMR curves recorded at 2 K for different bias voltages: 10, 200 mV, 1 and -2.5 V

A first set of data is shown in Fig. 6.11 while a second one is shown in Fig. 6.12. In Figs. 6.11a and 6.12a are represented the TMR dependence on bias voltage for the two samples, while in Figs. 6.11b and 6.12b are represented the respective TMR curves recorded for different bias at 2 K.

A similar behaviour to the one described before can be observed for both samples. TMR is always positive and at 2 K it symmetrically decreases with the increasing of bias until it reaches a saturation value. When increasing temperature, the flat TMR behaviour ascribed to phonon excitations can be observed again (Fig. 6.11a). One interesting remark is that TMR signal can be robust up to values even higher

than the one presented before. Indeed, in Fig. 6.11b is reported a clear 20 % TMR signal observed at 4 V. TMR intensity can also reach values above 50 % at low bias (Fig. 6.12a, b). The $V_{1/2}$ value probably depends on the quality of the barrier since in the second data set it is around 500 mV while in the first one it exceeds 4 V (inset Fig. 6.11a).

In conclusion, with these experiments we confirmed the robustness of TMR signal. This is very promising since being able to efficiently inject spins into organics at high voltage is particularly exciting for the development of future organic semiconductor spintronic applications such as organic light emitting diodes (spin-OLEDs).

## 6.4 Magneto-Transport Results by Tuning the Molecular Thickness

The investigation of magneto-transport properties in LSMO/C12P/Co magnetic tunnel junctions unveiled the potentiality of this system for spintronics by showing clear and robust magnetoresistance signal up to the volt range. The next important step was to lay the basis towards the tailoring and engineering of the molecular barrier.

On this regard, we started the investigation of barrier tuning with the tailoring of the molecular chain length. This initial step allowed, first, to investigate the magneto-transport properties dependence on the barrier thickness and, second, to validate our technology by verifying the expected exponential increasing of tunnel current with molecular length. To do that, we performed magneto-transport measurements on LSMO/C_nP/Co magnetic tunnel junctions with C10P, C12P, C14P, C16P and C18P alkyl-phosphonic acid molecules where the only change between one molecule to the other was the increasing number of carbon atoms in the body chain (Fig. 6.13).

As it will be described in the following, an exponential increase of the contact resistance with the chain length was observed thus confirming the validity of our system. Moreover, a clear magnetoresistance signal could be detected for every chain length (and a signal above 260 % TMR could be also observed in some case).

6.4.1 Resistance Dependence on Molecular Chain Length

In Fig. 6.14 are shown the measured resistances at low bias and low temperature as a function of the number of carbons in the molecular chain for different contacts. In this graph we have only considered the contacts that presented a non-linear tunnel behaviour in their I(V) curves and no strong dependence on temperature, while we excluded all the contacts in the electrode resistance range (kΩ) and the ones that were completely insulating. The white circles represent the resistance of contacts that showed tunnelling characteristics but no MR signal. The colour gradient in the other points corresponds to the clearness in the observed TMR signal: from the
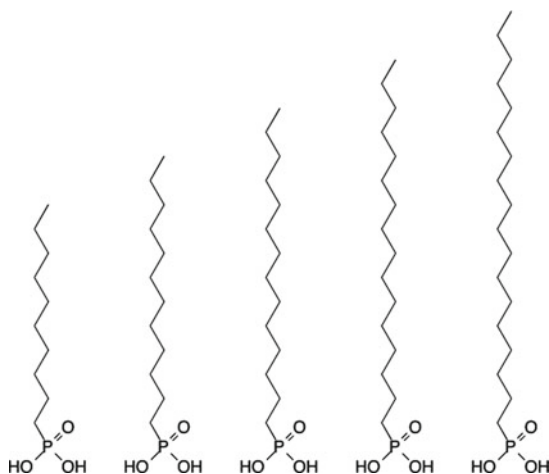
Fig. 6.13 Representation of alkyl-phosphonic acid molecules with carbon chains of different lengths: from C10P to C18P
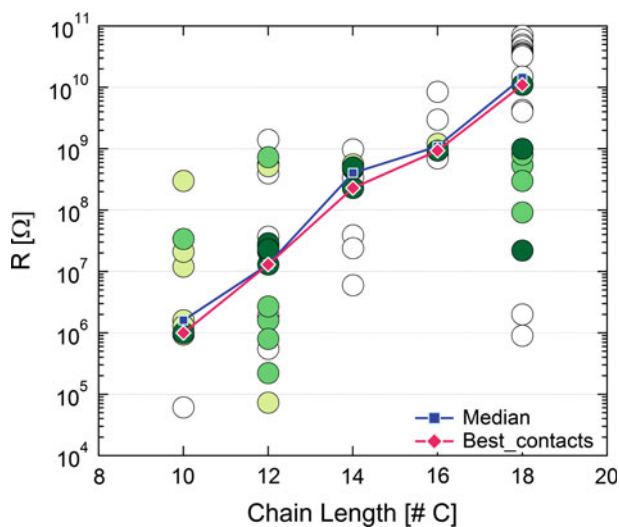
Fig. 6.14 *Circles* correspond to the contact resistances measured at low bias and 2 K as function of the number of carbons in the molecular chain for different contacts. Only contacts that presented a non-linear tunnel behaviour in their I(V) curves and no strong resistance dependence on temperature have been considered in the graph. Resistance of contacts that show tunnelling characteristic but no magnetoresistance signal are reported in *white circles*. The colour gradient in the other points corresponds to the observed TMR signal: from *lightest colours* where signal is quite low, noisy or with coupled peaks, to the *darkest* ones where a clear and clean MR signal is observed. Resistance median for every chain length is also shown as *blue squares* while in *red* is highlighted the resistance of contacts that gave the best magnetoresistance signal for every chain length

lightest colours where signal was quite low or noisy, to the darkest ones where a clean and clear MR signal was observed.

Median values for every chain length are represented as blue squares on the graph. We use the median value to single out non relevant outlier points from the statistics. Moreover, in red we also highlight what we call the "best contacts": the ones where the clearest and highest TMR signal has been recorded for every chain length. We consider these points as the most representative since they are the ones probably related to better quality junctions. Moreover, the similarity between the "best contacts" curve and the median curve values fully supports this choice.

In conclusion, despite the high resistance dispersion, a clear exponential increase of contact resistance with molecular chain length can be observed thus validating our system. A discussion on the possible causes of this dispersion and an estimation of the decay parameter (β) will be provided in the following.

Discussion on the Resistance Dispersion

As said before, contacts present a quite high resistance dispersion (Fig. 6.14). Moreover, due to the complexity of the fabrication process and the number of unsuccessful contacts and samples, we unfortunately had no time yet to have the same statistics for the intermediate chain lengths as we started by mainly characterizing C12P and C18P barriers since almost extremes.

A high resistance dispersion was also reported in SAMs-based MTJs fabricated by nanopore technique, where a dispersion of 2 orders of magnitude larger than our was observed [12]. The causes for such a high dispersion can be various and it is not easy to identify a predominant one. One first reason can be ascribed to the fact that nanojunctions areas depend on the edge shape of the AFM tip, thus varying from one sample (and sometimes contact) to the other. However, this factor can account only for small variations between contacts since AFM tips normally present <10 nm radius variation. Moreover, we usually indented each series of samples with the same tip in order to limit the dispersion and directly compare contacts with almost the same area. Despite in extreme cases the AFM tip radius can range from less than 10 to 100 nm radius thus meaning a resistance change of almost 2 orders of magnitude, this is probably not the main cause for such a high variation.

Another contribution to the dispersion can be probably ascribed to defects inside the molecular barrier. For example, defects can be due to partial Co atom diffusion inside the organic barrier during the top electrode deposition, or to some disorder in the molecular layer assembly. As already highlighted in Sect. 4.4, short chains form more disordered and scarcely packed SAMs than longer ones [24], thus varying the intramolecular and intermolecular transport ratio inside the junction from one contact to the other. This could partially explain the higher resistance dispersion found in C10P and C12P contacts in comparison to C14P and C16P ones that would form more packed and more uniform SAMs. For what concerns C18P, a very high dispersion has been also found but this result is more probably due to the fact that most C18P junctions were in the high measurement limit of the equipment resulting very noisy and difficult to measure. Thus, the major number of contacts that gave a measurable signal were probably made measurable from the presence of defects.

One final important remark is to note that the high resistance dispersion is largely reduced if we consider just junctions that gave a clear MR signal (green dark points + red). As we said, these are probably the most indicative contacts since they should present a better quality barrier. Considering these contacts, resistance dispersion is extremely limited in the case of central chains, while it is still quite high for the two extremes (C10P and C18P). This is not really astonishing since both extremes are in the experimental limits. In one case the molecule starts to be very short and it becomes difficult to distinguish a working junction from a short-circuited one. In the other case, molecules start to be too long and, as remarked before, measurements are in the very limit of the equipment possibilities, so they are often noisy and sometimes impossible to measure.

Calculation of the Decay Coefficient

We also evaluated the decay coefficient β and compared it to values reported in the literature for other alkyl-chain based SAMs, already presented in Sect. 4.4.

In Fig. 6.15 are represented the natural logarithm of median (a) and best contacts (b) curves of Fig. 6.14 with their respective linear fits. Fits are calculated as $ln R = ln R_0 + \beta N$, where N is the number of carbon atoms in the molecular chain, R_0 is the contact resistance and β is the decay coefficient in C^{-1} calculated from the slope of the fits.

Fits considering all the chain lengths (from C10 to C18) are represented as gray dotted lines. The estimated β values for median and best values are extremely similar: $\beta = 1.13 \pm 0.1\,C^{-1}$ for median and $\beta = 1.14 \pm 0.1\,C^{-1}$ in the case of best contacts curve. These values are perfectly in line with the values found in the literature for alkyl-chain molecules that range from $0.7\,C^{-1}$ to $1.71\,C^{-1}$. Looking at Table 4.1, we can also observe that a large number of experiments report a β value very similar to ours, especially if we consider experiments performed by CP-AFM.
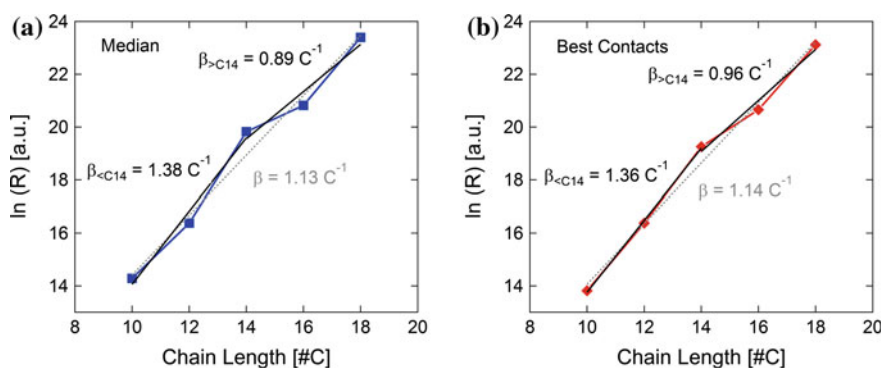
Fig. 6.15 **a** Natural logarithm of the median of the contact resistance as a function of the number of carbons in the molecule chain as shown in Fig. 6.14 (*blue line*). In *gray* is represented the linear fit calculated on the whole curve, while in *black* are represented fits calculated from C10 to C14 and from C14 to C18. **b** Same thing than (**a**) but for the "best contacts" curve (*red*)

From a more accurate analysis, we can also note that a cut in the slope in correspondence of C14 length can be observed in both curves. Separate fits for C10–C14 and C14–C18 lengths are also represented in black lines in Fig. 6.15. The β values found in this case are 1.38 C^{-1} (short) -0.89 C^{-1} (long) and 1.36 C^{-1} (short) -0.97 C^{-1} (long) respectively for the median and the best contact curve. Different slopes between "short" molecules and "long" ones have been already reported in the literature [24] ($\beta = 1.34$ C^{-1} for C8–C12 and $\beta = 0.77$ C^{-1} for C12–C16 in alkyl phosphonate chains on Al–AlOx substrates) and they are very similar to the ones that we found. The higher β value found for short molecules in comparison to long ones is explained in the literature by the higher disorder and tilt of short chains. In this case intermolecular interactions between molecules seem to have a more important contribution to transport than for longer chains and current passing through the molecular barrier is more efficiently attenuated. Moreover, the fact that the point of slope change in the literature is reported to be at C12 while we find it for C14, could be ascribed to the different surface where molecules are grafted, Al_2O_3 in one case and LSMO in the other, that could cause changes in the organization and density of the molecular layer over the surface.

Finally, another interesting proof would be to estimate the decay coefficient of the carbon chain independent from the influence of contacts, β_{body}, as proposed by the multibarrier tunneling model [25]. However, another set of data for a molecule with a different anchoring group would be needed in order to extrapolate this value. This will be an interesting point to check when further tailoring the SAMs barrier.

Still, while the strong similarity between β values estimated from our experiments and the ones reported in the literature appears to confirm the validity of our system, an increased statistics would be necessary to fully confirm this tendency.

6.4.2 TMR Dependence on Molecular Chain Length

After having discussed the resistance dependence on the molecular chain length, we will report here the TMR dependence.

The TMR values recorded at low bias and low temperature for every contact previously considered are represented as a function of the molecular chain length in Figure 6.16. The color code is equivalent to that used in Fig. 6.14, with the median values for every chain length represented with blue points.

From this graph it is possible to observe that, for almost every chain length, most of the good contacts (dark green points) give a TMR signal at low temperature between 30 and 50 %. Contacts that present a small and quite noisy MR signal (light green points) could be related to low quality junctions where defects due to disorder in molecular orientation or partial atomic diffusion in the molecular barrier could induce a loss of spin polarization. The lack of good quality contacts with TMR in the 30–50 % range for C16P is probably due to the low statistics. On the contrary, the fact that C10P contacts showed curves with very similar TMR intensity between 15 and 20 % and presented often coupled peaks (antiparallel state not well defined), could
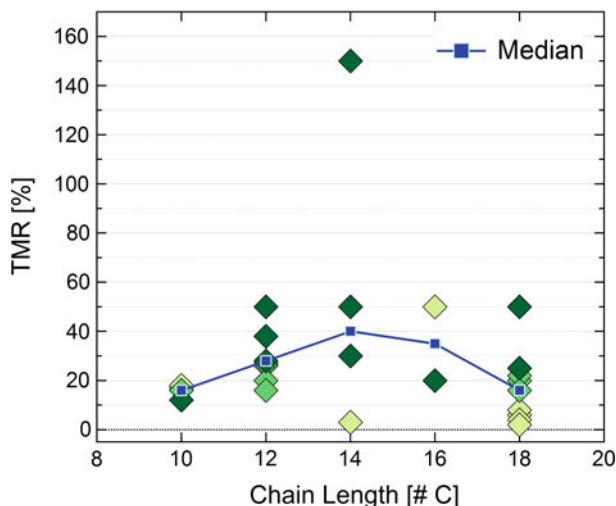
Fig. 6.16 TMR signal represented as a function of the molecule chain length. Points correspond to the TMR signal measured at 10 mV and low temperature for the contacts considered in Fig. 6.14. The color gradient for the points is the same than the one considered before: darker points correspond to contacts that gave the clearest TMR signal. In *blue* are represented the median values for every chain length

be ascribed to the small thickness of the molecular barrier. Finally, a very remarkable point is the extremely high value of TMR (above 150 %) that could be observed in one LSMO/C14P/Co contact.

In Fig. 6.17 are reported examples of TMR curves recorded at low temperature and low bias for the different chain lengths. As one can note, a clear TMR signal can be observed for every chain thickness and its intensity is competitive with the best results obtained in molecular spintronics. A similar behaviour in angle, temperature and bias to the one reported for C12P in Sect. 6.3 could be observed for every chain length.

Finally, if we consider the median curve for TMR values (Fig. 6.16), it looks like there is a peak of MR for C14P but this is more probably just due to the low statistics. Although, a higher statistic would be needed to unambiguously conclude a tendency, in general it seems that there is no remarkable difference of magnetoresistance intensity with the thickness of the tunnel barrier. This is perfectly in line with the theory that the biggest influence on spin polarization properties in molecular spintronics is more likely due to the interface coupling than to the molecular "bulk". Interface effects could be also the cause for the extremely high magnetoresistance observed in one contact.

TVS analysis observations To gain further insight in these results we also tried to analyse the I(V) characteristics recorded for all these contacts using the TVS method presented in Sect. 4.3.2. One interesting observation emerged from this analysis.
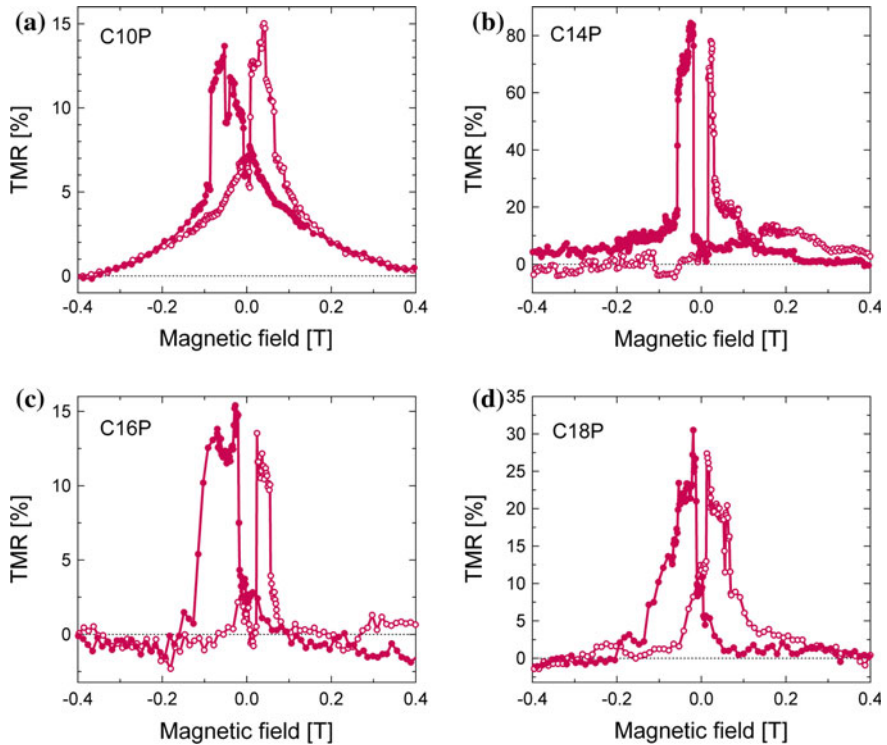
Fig. 6.17 Examples of TMR signal recorded for LSMO/SAM/Co magnetic tunnel junctions where SAMs are alkyl-phosphonic acids with different chain lengths. TMR recorded at 2 K for different alkyl chain tunnel barriers **a** C10P at 10 mV, **b** C14P at 50 mV, **c** C16P at 10 mV, **d** C18P at 50 mV. Every chain length presents a clear magnetoresistance signal and no substantial difference can be detected from one molecule to the other as a function of the number of carbons in their alkyl-chain

Indeed, all the junctions classified as "good contacts" (dark points) in Fig. 6.16, present a transition voltage $V_t > 0.4$ V at low temperature. Moreover, in general, the higher is the V_t value, the clearer is the TMR signal observed. Typical values for "good contacts" are $V_t \simeq 0.7$–1.1 V but in some case it can be higher. These values are in the range of the ones reported in the literature (Table 4.2), even if slightly smaller, maybe due to the fact that LSMO is an oxide [26]. On the contrary, for low and noisy MR contacts, V_t is generally <0.3 V, becoming even much smaller for contacts that do not present any MR signal.

Despite being not trivial to directly link the V_t value to a physical parameter of the junction such as the barrier potential height (φ), this value could represent a first hint towards the indication of the junction quality as already suggested by Ricœur et al. [26]. If this tendency was confirmed, it could be used as a fast tool to gain an idea even at room temperature about the possible quality of TMR signal measured at 2 K.

### 6.4.2.1 Example of Giant TMR Signal in LSMO/C14P/Co MTJ

An example of TMR behaviour in a LSMO/C14P/Co nanocontact will be reported more in details in this section. As shown in Fig. 6.18, in this case an extremely high TMR signal up to 260 % at 10 K could be observed. This high TMR signal can not be explained by Jullière's model since even considering the maximum spin polarization possible for the two electrodes ($P_{LSMO} = 100\%$ and $P_{Co} = 40\%$), a maximum TMR signal of ∼133 % would be expected by Eq. 1.5. Despite the origin of this large effect is still unclear, in analogy to another giant effect observed in an organic MTJ [27], it may be ascribed to a weak coupling at the C14P/Co spinterface (situation described in Fig. 3.5c) that would lead to an enhancement of the spin polarization at the top interface to at least $P_{C14P/Co} \simeq 57\%$. We have to remark that this is an underestimation, since we considered a spin polarization at the bottom interface $P_{LSMO/C14P} = 100\%$, while the real value is more probably lower.

Even more interestingly, when decreasing temperature to 2 K, we could observe an exponential increase of resistance at low bias (<10 mV) and TMR ratio reached giant values as shown in Fig. 6.19a. Here, in solid lines (black and red curves) are reported the TMR behaviour calculated from the difference between the I(V) curves measured in the parallel and antiparallel magnetic configuration of the junction at 2 K (Fig. 6.20a) and 10 K respectively. With symbols are reported the intensities of TMR peaks directly measured in R(H) curves at different bias voltages and different temperatures.

In Fig. 6.19b is also shown an example of MR curve recorded at 2 mV and 6 K where 400 % TMR can be observed. Unfortunately we could not directly measure TMR curves at low bias for lower temperatures since resistance exponentially
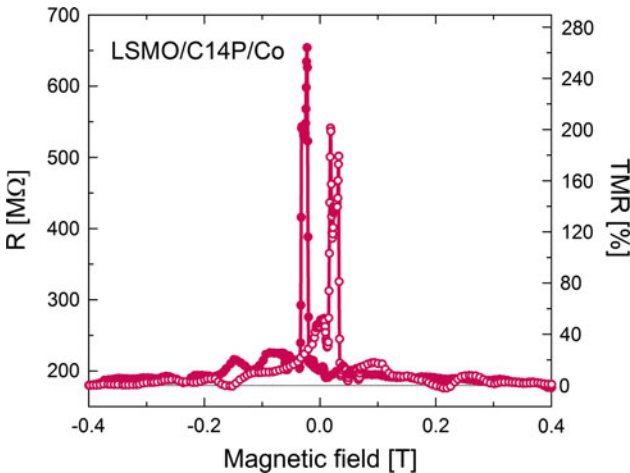

Fig. 6.18 Example of a giant TMR signal up to 260 % recorded in a LSMO/C14P/Co MTJ at 2 mV and 10 K
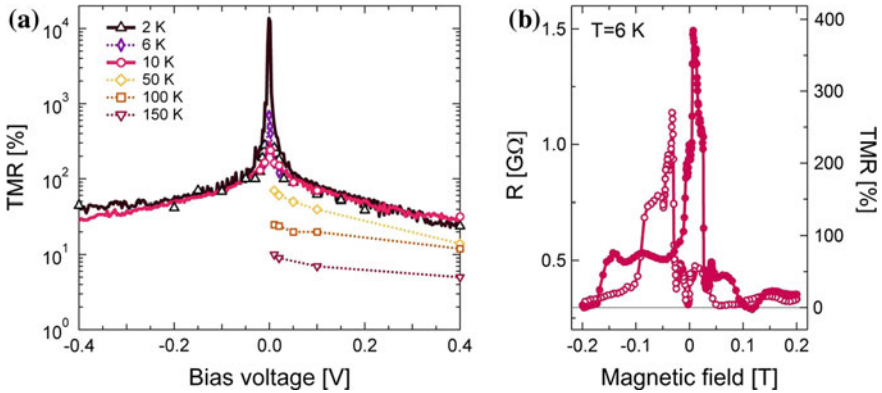
Fig. 6.19 a TMR behaviour as a function of bias and temperature in a LSMO/C14P/Co MTJ. In *solid lines* are represented the TMR values extracted from the difference of I(V) characteristics recorded in the parallel and antiparallel magnetic configuration of the junction for a temperature of 2 K (*black*) and 10 K (*red*). With symbols are reported the TMR values directly measured from R(H) at the different bias voltages and different temperature of 2, 6, 10, 50, 100 and 150 K. As before, TMR presents a flat behaviour when increasing temperature. **b** Example of TMR curve recorded at 2 mV and 6 K

increased in this range when approaching 2 K and we reached the measurement limits of the equipment. The origin of this giant effect at 2 K appears clear if we look at the conductance characteristics of the junction in the parallel and antiparallel configurations shown in Fig. 6.20b. As one can note, a small gap appears in the antiparallel configuration for this bias range and conductance is zero. Nevertheless, the causes of this gap apparition in the antiparallel configuration are still unclear.
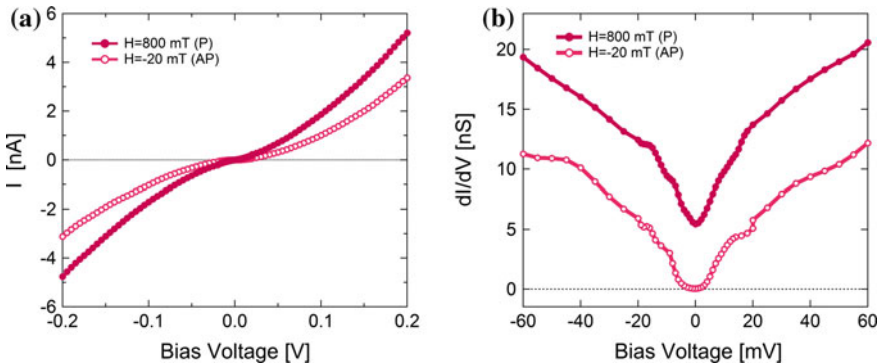
Fig. 6.20 a I(V) characteristic recorded at 2 K in the parallel (800 mT) and antiparallel (−20 mT) magnetic configuration for the LSMO/C14P/Co junction that gave very high TMR signal. **b** Conductance characteristic for this junction in the parallel and antiparallel configuration numerically calculated as dI/dV from curves reported in (**a**). A gap is opened in the antiparallel configuration at low bias and conductance becomes zero
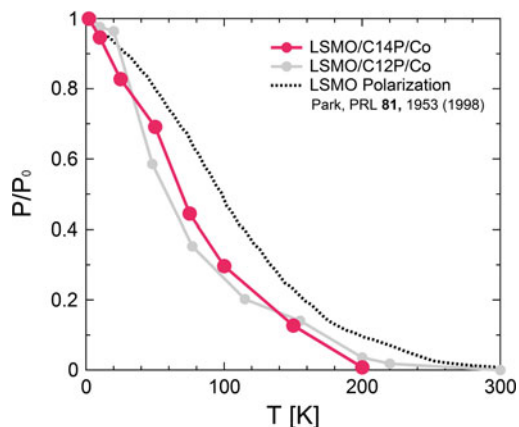
Fig. 6.21 TMR behaviour with temperature for a LSMO/C14P/Co nanojunction (*red*). TMR is normalized with the value at low temperature. This behaviour is the same than the one already reported for LSMO/C12P/Co junction (*gray*) and is compared with LSMO surface polarization [10] (*black dotted line*). Once again it is confirmed that TMR decreasing with temperature is mainly driven by LSMO lost of polarization thus allowing to ascribe to LSMO the absence of TMR observation at room temperature in the junctions

Finally, one important observation is that, for these samples as for all the other chain lengths, we found again the same characteristic features of TMR already described in the case of LSMO/C12P/Co junctions, thus confirming their reproducibility in our system. TMR is found to be robust with the bias voltage and it presents a flat behaviour when increasing temperature. In Fig. 6.21 is also shown the TMR drop with temperature and it is compared with the curve already presented for C12P samples (gray line) and the LSMO surface polarization (black dotted line). A very similar trend is observed for the two chain lengths and, again, the drop is mainly driven by the LSMO surface loss of polarization, thus confirming that LSMO is the main limitation to the observation of a magnetoresistance effect at room temperature.

IETS Measurement

In order to verify that the measured signals were coming from the C14P molecules, we also performed IETS measurement on this junction, as shown in Fig. 6.22.

To assign the observed peaks we compared our result with the ones reported in the literature and shown in Fig. 6.23. Figure 6.23a corresponds to IETS measurement in a Au/SAM/Au crossed-wire tunnel junction of $10\,\mu m$ diameter with SAM constituted by C11 monothiols [3]. Figure 6.23b corresponds to a Au/SAM/Au nanopore junction where SAM is a C8 dithiol [28]. As one can note, the intensity and number of IETS peaks are different in the two curves. This discrepancy was investigated by Yu et al. [29] concluding that the elevate number of peaks in the case of the nanopore device (Fig. 6.23b) could be due to nanoscale metal islands contained in the alkanethiol molecules due to the deposition process of top electrodes. Even if not conclusive, both groups observed peaks that could be ascribed to vibrational
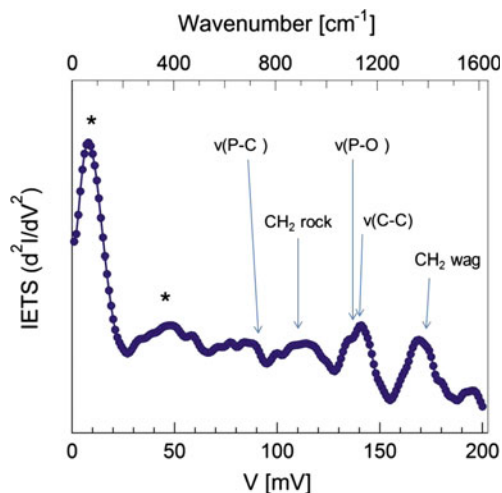
Fig. 6.22 IETS curve measured at 2 K in the same LSMO/C14P/Co junction that gave an extremely high TMR signal. Peaks compatible with the molecular vibrations of the carbon chain and –PO(OH)$_2$ anchoring group have been assigned, while the origin of peaks marked with (∗) remain unassigned
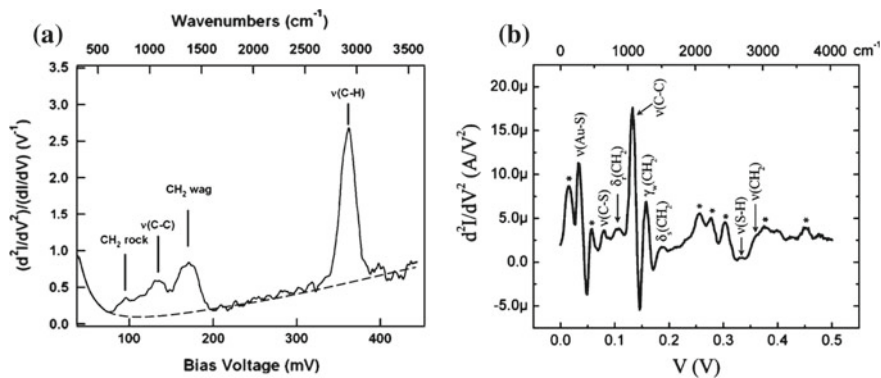
Fig. 6.23 **a** IETS curve measured in a Au/SAM/Au crossed-wire tunnel junction consisting of two 10 μm diameter Au wires where SAMs are C11 monothiols. Reprinted with permission from [3]. Copyright 2004 American Chemical Society. **b** IETS curve measured in a Au/SAM/Au nanopore junction where SAMs are C8 dithiols. Some peaks remain unassigned. Reprinted with permission from [28]. Copyright 2004 American Chemical Society

modes of the carbon chain: CH$_2$ rock ∼ 89–115 mV, ν(C–C) ∼ 130–139 mV, CH$_2$ wag ∼ 152–170 mV [3, 28]. These same vibrational modes could be observed in our junction. Moreover, comparing with values reported in the literature, we could also assign some vibrational modes of P. A first peak is the one around 750 cm^{-1} that would correspond to a ν(P–C) vibration [30]. A second one would be ν(P–O) ∼ 1100 cm^{-1} [31], even if this peak is very close to the ν(C–C) one and they are difficult

to distinguish. Finally, more peaks are also visible at lower bias but in this range they are difficult to assign. They correspond to the voltage range usually associated to the interaction with the surface but their origin remains unclear. They could be also assigned to surface impurities of other defects. In any case, IETS peaks in agreement with literature represent a clear proof that the extremely high TMR effect measured in our device was due to transport through the C14P molecular layer.

6.5 Conclusions

In this first experimental part we demonstrated the potentiality of alkyl-chains (and SAMs in general) MTJs for spintronics. A high TMR signal ranging from 30 to 260 % at low temperature was observed in our devices and represented a strong improvement in comparison to results previously reported in similar systems [12, 13]. Moreover, the most striking observation is probably represented by the robustness of TMR effect in these devices, where a clear signal could be observed up to 4 V. Finally, the study of magneto-transport properties for different chain lengths marked a first step towards the barrier tailoring and represented an indispensable preliminary investigation to probe the validity of our system and confirm the potentiality of SAMs for molecular spintronics. In conclusion, these studies lay the bases for the further investigation of molecular barrier tailoring towards the engineering of the device properties.

References

1. R. Jaklevic, J. Lambe, Molecular vibration spectra by electron tunneling. Phys. Rev. Lett. **17**, 1139–1140 (1966)
2. J. Lambe, R. Jaklevic, Molecular vibration spectra by inelastic electron tunneling. Phys. Rev. **165**(3), 821 (1968)
3. J.G. Kushmerick, J. Lazorcik, C.H. Patterson, R. Shashidhar, D.S. Seferos, G.C. Bazan, Vibronic contributions to charge transport across molecular junctions. Nano Lett. **4**, 639–642 (2004)
4. W. Wang, Electrical characterization of self-assembled monolayers. Ph.D. thesis, Yale University (2004)
5. M.A. Reed, Inelastic electron tunneling spectroscopy. Mater. Today **11**, 46–50 (2008)
6. I. Vera Marún, F. Postma, J. Lodder, R. Jansen, Tunneling magnetoresistance with positive and negative sign in $La_{0.67}Sr_{0.33}MnO_3/SrTiO_3/Co$ junctions. Phys. Rev. B **76**, 064426 (2007)
7. J. Sun, K. Roche, S. Parkin, Interface stability in hybrid metal-oxide magnetic trilayer junctions. Phys. Rev. B **61**, 11244–11247 (2000)
8. J.M. De Teresa, Role of metal-oxide interface in determining the spin polarization of magnetic tunnel junctions. Science **286**, 507–509 (1999)
9. C. Gould, C. Rüster, T. Jungwirth, E. Girgis, G.M. Schott, R. Giraud, K. Brunner, G. Schmidt, L.W. Molenkamp, Tunneling anisotropic magnetoresistance: a spin-valve-like tunnel magnetoresistance using a single magnetic layer. Phys. Rev. Lett. **93**, 117203 (2004)
10. J.-H. Park, E. Vescovo, H.-J. Kim, C. Kwon, R. Ramesh, T. Venkatesan, Magnetic properties at surface boundary of a half-metallic ferromagnet $La_{0.7}Sr_{0.3}MnO_3$. Phys. Rev. Lett. **81**(9), 1953 (1998)

11. V. Garcia, M. Bibes, A. Barthélémy, M. Bowen, E. Jacquet, J.-P. Contour, A. Fert, Temperature dependence of the interfacial spin polarization of $La_{2/3}Sr_{1/3}MnO_3$. Phys. Rev. B **69**, 052403 (2004)
12. J.R. Petta, S.K. Slater, D.C. Ralph, Spin-dependent transport in molecular tunnel junctions. Phys. Rev. Lett. **93**, 136601 (2004)
13. W. Wang, C.A. Richter, Spin-polarized inelastic electron tunneling spectroscopy of a molecular magnetic tunnel junction. Appl. Phys. Lett. **89**, 153105 (2006)
14. V.A. Dediu, L.E. Hueso, I. Bergenti, C. Taliani, Spin routes in organic semiconductors. Nat. Mater. **8**, 707–716 (2009)
15. F.J. Wang, Z.H. Xiong, D. Wu, J. Shi, Z.V. Vardeny, Organic spintronics: the case of $Fe/Alq_3/Co$ spin-valve devices. Synth. Met. **155**, 172–175 (2005)
16. W. Xu, G.J. Szulczewski, P. LeClair, I. Navarrete, R. Schad, G.X. Miao, H. Guo, A. Gupta, Tunneling magnetoresistance observed in $La_{0.67}Sr_{0.33}MnO_3$/organic molecule/Co junctions. Appl. Phys. Lett. **90**(7), 72506 (2007)
17. S. Yuasa, A. Fukushima, T. Nagahama, K. Ando, Y. Suzuki, High tunnel magnetoresistance at room temperature in fully epitaxial Fe/MgO/Fe tunnel junctions due to coherent spin-polarized tunneling. Jpn. J. Appl. Phys. **43**, L588 (2004)
18. C. Tiusan, J. Faure-Vincent, M. Sicot, M. Hehn, C. Bellouard, F. Montaigne, S. Andrieu, A. Schuhl, Spin filtering effects in monocristalline Fe/MgO/Fe magnetic tunnel junctions. Mater. Sci. Eng. B **126**, 112–119 (2006)
19. S. Zhang, P.M. Levy, A.C. Marley, S.S.P. Parkin, Quenching of magnetoresistance by hot electrons in magnetic tunnel junctions. Phys. Rev. Lett. **79**, 3744–3747 (1997)
20. J. Moodera, J. Nowak, R. van de Veerdonk, Interface magnetism and spin wave scattering in ferromagnet-insulator-ferromagnet tunnel junctions. Phys. Rev. Lett. **80**, 2941–2944 (1998)
21. H.F. Ding, W. Wulfhekel, J. Henk, P. Bruno, J. Kirschner, Absence of zero-bias anomaly in spin-polarized vacuum tunneling in Co(0001). Phys. Rev. Lett. **90**, 116603 (2003)
22. S. Yuasa, A. Fukushima, H. Kubota, Y. Suzuki, K. Ando, Giant tunneling magnetoresistance up to 410 % at room temperature in fully epitaxial Co/MgO/Co magnetic tunnel junctions with bcc Co(001) electrodes. Appl. Phys. Lett. **89**, 042505 (2006)
23. A.M. Bratkovsky, Assisted tunneling in ferromagnetic junctions and half-metallic oxides. Appl. Phys. Lett. **72**, 2334–2336 (1998)
24. I. Levine, S.M. Weber, Y. Feldman, T. Bendikov, H. Cohen, D. Cahen, A. Vilan, Molecular length, monolayer density, and charge transport: lessons from Al-AlOx/alkyl-phosphonate/Hg junctions. Langmuir **28**, 404–15 (2012)
25. G. Wang, T.-W. Kim, H. Lee, T. Lee, Influence of metal-molecule contacts on decay coefficients and specific contact resistances in molecular junctions. Phys. Rev. B **76**, 205320 (2007)
26. G. Ricoeur, S. Lenfant, D. Guérin, D. Vuillaume, Molecule/electrode interface energetics in molecular junction: a "transition voltage spectroscopy" study. J. Phys. Chem. C **116**, 20722–20730 (2012)
27. C. Barraud, P. Seneor, R. Mattana, S. Fusil, K. Bouzehouane, C. Deranlot, P. Graziosi, L. Hueso, I. Bergenti, V. Dediu, F. Petroff, A. Fert, Unravelling the role of the interface for spin injection into organic semiconductors. Nat. Phys. **6**, 615–620 (2010)
28. W. Wang, T. Lee, I. Kretzschmar, M.A. Reed, Inelastic electron tunneling spectroscopy of an alkanedithiol self-assembled monolayer. Nano Lett. **4**, 643–646 (2004)
29. L.H. Yu, C.D. Zangmeister, J.G. Kushmerick, Origin of discrepancies in inelastic electron tunneling spectra of molecular junctions. Phys. Rev. Lett. **98**, 206803 (2007)
30. R. Luschtinetz, G. Seifert, E. Jaehne, H.-J.P. Adler, Infrared spectra of alkylphosphonic acid bound to aluminium surfaces. Macromol. Symp. **254**, 248–253 (2007)
31. P. Thissen, M. Valtiner, G. Grundmeier, Stability of phosphonic acid self-assembled monolayers on amorphous and single-crystalline aluminum oxide surfaces in aqueous solution. Langmuir **26**, 156–64 (2010)

Part III
Room Temperature Spin Injection in Organic Semiconductors

In parallel to the investigation on self-assembled monolayers, we also turned our attention towards another hot topic of organic spintronics field. Indeed, the achievement of good magnetoresistance signal at room temperature is an important requirement for the possible future development of organic devices for applications. Until now only few works reported room temperature MR effect in organic spin valves (OSVs). In this regard, we also dedicated a part of our work to the investigation of Alq_3-based OSVs. We chose Alq_3 molecule since it is a standard material in the field. Moreover the fabrication of large area devices (50×50 and 100×100 μm^2) by shadow mask using an in situ deposition technique allowed us to use ferromagnetic metals at room temperature, such as Co, for both electrodes without any oxidation problems.

The results obtained in these devices will be presented in the third part of this manuscript. A brief state of the art in Alq_3 devices for spintronics will be introduced in Chap. 7 showing very heterogeneous results difficult to compare due to the different approaches adopted by each group.

For this reason we decided to perform a systematic study on Co/Alq_3/Co OSVs that will be presented in Chap. 8 showing room temperature MR results. Moreover, inelastic electron tunneling spectroscopy (IETS) technique will be used to prove spin injection into the organic layer. Finally, an insulating oxide barrier (Al_2O_3 or MgO) will be also inserted at the bottom or top interface. This will allow to separately investigate the specific role of ferromagnetic metal/molecule hybridization at each interface and understand its influence on the spin polarization properties.

Chapter 7
State of the Art in Alq$_3$-Based Spintronic Devices

7.1 State of the Art in Alq$_3$-Based Spintronic Devices

Since the first observation of a magnetoresistance signal in a vertical organic spin valve in 2004 [1], tris (8-hydroxyquinoline) aluminium (Alq$_3$) molecule has become a standard material for organic spintronics devices. The choice of Alq$_3$ arises from the fact that this organic semiconductor is widely used as electron transporting and light-emitting material in OLEDs and it has been studied in this field more than any other material over the past 20 years. Moreover, its successful employment in organic spin valves is probably due to the high-quality thin films that can be grown on various ferromagnetic substrates by standard ultrahigh vacuum evaporation.

In this chapter we will briefly present the state of the art on Alq$_3$-based spintronic devices and the different approaches applied through the years to try to optimize these systems. We will see that, despite extensively investigated, many fundamental questions regarding the spin injection and transport mechanisms through the organic layer are still unclear. We will present some of the most controversial topics in the organic spintronic area and we will highlight how great margins for improvement are still possible, especially for what concerns interface control and the value of MR signal at room temperature.

7.1.1 First Results in Alq$_3$-Based Organic Spin Valves

As already presented in Chap. 3, the first successful vertical spin valve was reported by the group of Z.V. Vardeny in 2004 [1]. In this article, authors observed a clear -40% MR signal at low temperature (Fig. 3.2) in a $2 \times 3\,mm^2$ LSMO/Alq$_3$(130 nm)/Co spin valve realized by shadow mask. This break through result motivated an increasing interest in organic spintronics field and in particular in the use of Alq$_3$ molecules as organic barrier.

Since then, a large number of studies have been focused on the investigation and optimization of this kind of devices, however reporting very heterogeneous results. A summary of some of them is reported in Table 7.1.

For example, a negative MR signal was observed by different groups [2–5], an inversion of the MR sign depending on the applied bias voltage was also reported by Vinzelberg et al. [6], or even a complete absence of the MR effect was claimed by Jiang et al. [7]. This absence was ascribed by the authors to a large conductivity mismatch between the metal electrodes and the organic semiconductor that would prevent any spin injection.

Table 7.1 Examples of works on Alq$_3$ based devices reported in the literature

Structure	MR signal	Temperature	Reference
No tunnel barrier			
LSMO/Alq$_3$ (130 nm)/Co	−40 %	11 K	Xiong et al. 2004 [1]
LSMO/Alq$_3$ (130 nm)/Co	−33 %	5 K	Majumdar et al. 2006 [2]
Fe/Alq$_3$ (140 nm)/Co	−5 %	11 K	Wang et al. 2005 [4]
Ni/Alq$_3$ (25 nm)/Co	−0.4 to +0.1 %	1.9 K	Pramanik et al. 2006 [20]
LCMO/Alq$_3$ (150 nm)/Co	−50 %	30 K	Zhi-Yong et al. [5]
LSMO/Alq$_3$ (10 nm)/Co	−15 %	11 K	Xu et al. 2007 [3]
Co/Alq$_3$ (50 nm)/Fe	0		Jiang et al. 2008 [7]
LSMO/Alq$_3$ (150 nm)/Co	−15 to +3 %	4.2 K	Vinzelberg et al. 2008 [6]
LSMO/Alq$_3$ (2 nm)/Co	+300 %	2 K	Barraud et al. 2010 [21]
LSMO/Alq$_3$ (93 nm)/BLAG Co/Co	−300 %	2 K	Sun et al. 2010 [12]
NiFe/Alq$_3$ (100 nm)/Fe	−2 %	50 K	Zhang et al. 2014 [22]
Fe/Alq$_3$ (100 nm)/Co	+1 %	290 K	Liu et al. 2009 [23]
LSMO/Alq$_3$ (40 nm)/Co	−0.07 %	300 K	Wang et al. 2011 [13]
LSMO/Alq$_3$ (50 nm)/Co	−2 %	300 K	Chen et al. 2013 [24]
Barrier at the bottom interface			
Co/Al$_2$O$_3$/Alq$_3$ (96 nm)/Co	+19 %	5 K	Zhang et al. 2011 [15]
NiFe/LiF/Alq$_3$ (200 nm)/TPD/CoFe	+0.3 %	90 K	Drew et al. 2009 [25]
Co/Al$_2$O$_3$/Alq$_3$ (1.6 nm)/NiFe	+4.6 %	300 K	Santos et al. 2007 [16]
CoFeB/MgO/Alq$_3$ (2 nm)/NiFe	+13 %	300 K	Szulczewski et al. 2009 [17]
CoFeB/Al$_2$O$_3$/Alq$_3$ (1 nm)/NiFe	+9 %	300 K	Szulczewski et al. 2009 [17]
CoFeB/Al$_2$O$_3$/Alq$_3$ (2 nm)/NiFe	+4 %	300 K	Schoonus et al. 2009 [18]
Fe$_3$O$_4$/Al$_2$O$_3$/Alq$_3$ (2 nm)/Co	+6 %	300 K	Zhang et al. 2014 [19]
Barrier at the top interface			
LSMO/Alq$_3$ (100 nm)/Al$_2$O$_3$/Co	−0.15 %	300 K	Dediu et al. 2008 [11]

In the Table is generally reported the maximum value of MR signal observed in these works. In the case of results at room temperature the value at 300 K is reported. For studies on Alq$_3$-based MTJs with different thickness of the barrier, when possible, a thickness of 2 nm Alq$_3$ has been considered for a better comparison between results
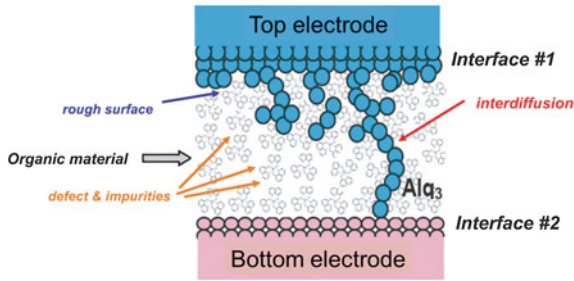
Fig. 7.1 Schematic representation of a "real device" highlighting some of the main problems related to poorly defined interfaces, such as inter-diffusion or metallic inclusions of the top electrode atoms, defects and impurities. Adapted from [10] with permission of The Royal Society of Chemistry

In analogy to inorganic MTJs where the TMR value has been substantially enhanced by tailoring the FM/MgO interfaces [8, 9], in organic spintronics the poor quality and control of the interfaces (Fig. 7.1) has been claimed as the main cause for the low reproducibility and limited efficiency of Alq₃ spin valves, as well as the loss of spin polarization at room temperature. In this scenario, different approaches have been adopted to try to improve the interface quality and the performances of these devices and they will be described in the next section.

7.1.2 Towards the Optimization of Alq₃-Based Spintronic Devices

7.1.2.1 Improvement of the Top Interface

With the aim of obtaining a well defined ferromagnetic metal/molecule interface, a particularly problematic question is the degree of interdiffusion of the top FM electrode into the much softer organic layer during sample fabrication. The penetration of the energetic atoms into the organic gives rise to an "ill-defined" layer whose thickness can reach 100 nm [6] and often obliges the deposition of a very thick organic layer to avoid short-circuited junctions.

One approach to limit this problem is the insertion of a buffer layer between the top FM electrode and the organic. The first to propose this approach was the group of A. Dediu in 2008 [11] with the fabrication of LSMO/Alq₃(100 nm)/Al₂O₃/Co OSVs. Thanks to the insertion of the Al₂O₃ tunnel barrier that limited the Co diffusion, authors could observe a −9 % MR signal at low temperature and −0.15 % MR at 300 K (Fig. 7.2). This was the first time that a MR effect could be observed at room temperature in OSVs.
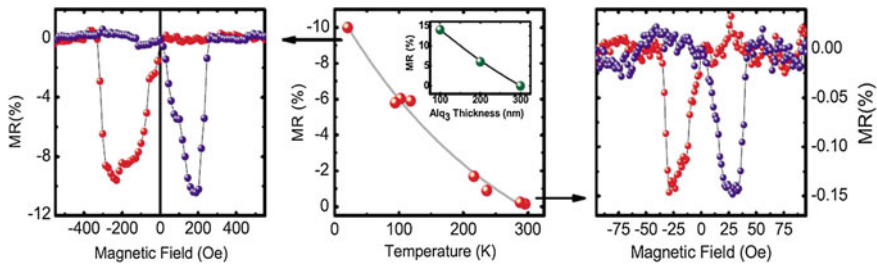
Fig. 7.2 Temperature dependence of the MR signal obtained in a LSMO/Alq$_3$(100 nm)/Al$_2$O$_3$/Co OSVs. *On the left*, MR curve recorded at 20 K. *On the right*, MR curve recorded at 300 K. The MR behaviour with temperature is represented in the *middle* and in the inset is reported the MR decrease with increasing Alq$_3$ thickness. Reprinted figure with permission from [11]. Copyright 2008 by the American Physical Society

Another attempt to optimize the top Alq$_3$/Co interface was proposed by Sun et al. [12]. This group deposed Co nanoparticles to form a BLAG layer (BLAG = buffer layer assisted growth) on Alq$_3$ before the deposition of the top Co electrode (Fig. 7.3a). In this way, nanoparticles with their large size protected the molecular layer from Co atom diffusion and formed the top ferromagnetic electrode. Very promising MR results of −300 % (−75 % following the standard Jullière's definition) could be observed with this kind of system as shown in Fig. 7.3b.

A good improvement could be also obtained limiting the energy of the incident top electrode Co atoms on the organic layer by using the indirect deposition method. This method consists in the introduction of an inert gas into the evaporation chamber during the top electrode deposition. The vaporized high temperature atoms collide with the inert gas several times, release their energies and "softly" land on the mole-
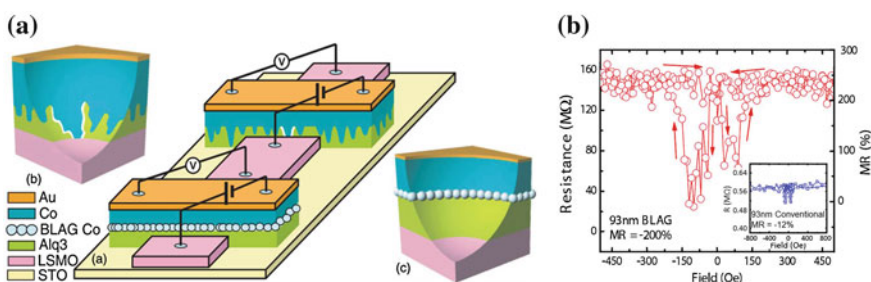
Fig. 7.3 **a** Schematic representation of two LSMO/Alq$_3$/Co spin valves. One (*on the left*) fabricated following the standard fabrication process where Co atoms diffuse into the organic barrier. The other (*on the right*) fabricated with the BLAG layer of Co nanoparticles that protect the organic barrier from the atom diffusion producing a well defined interface. **b** MR curve recorded at 2 K in a junction with Co nanoparticles at the interface. The blue curve in the inset shows the same measurement but in a junction without the nanoparticle barrier. Reprinted figure with permission from [12]. Copyright 2010 by the American Physical Society (color figure online)

cular layer. Using this method Wang et al. [13] fabricated LSMO/Alq$_3$(40 nm)/Co OSVs and could observe a very small MR effect of -0.07% at room temperature.

Finally, a small MR signal at room temperature could be also recorded by Liu et al. [14] in a Co/Alq$_3$(64 nm)/Fe OSV. In order to stabilize the OSC film during evaporation and to reduce the potential penetration of Co atoms into the organic layer, authors used chilled water to keep the substrate holder at a temperature of 20°C during the top electrode deposition. A positive magnetoresistance of $+9\%$ was reported for these junctions at low temperature and the effect persisted up to room temperature with 1% MR measured at 290 K.

7.1.2.2 Improvement of the Bottom Interface

A complementary approach has been to improve the ferromagnetic metal/molecule bottom interface through the insertion of a thin oxide layer.

For example, Zhang et al. [15] fabricated Co/Al$_2$O$_3$/Alq$_3$(96 nm)/Co OSVs where they observed $+19\%$ MR signal at 5 K, while the effect disappeared above 80 K. Spin valves without any oxide barrier were also investigated but no MR effect could be observed in this case.

The insertion of a thin oxide barrier at the bottom interface is also a common habit in the fabrication of large area organic MTJs. The first to adopt this method were Santos et al. in 2007 [16] when they reported a positive $+7.5\%$ TMR signal in Co/Al$_2$O$_3$/Alq$_3$(1.6 nm)/NiFe magnetic tunnel junction ($300 \times 300\,\mu m^2$) at low temperature that was maintained up to room temperature with $+4.6\%$ TMR (Fig. 7.4a). Authors also showed that the signal in a Co/Alq$_3$/NiFe junction without the Al$_2$O$_3$ barrier was seriously degraded with a loss of the estimated spin polar-
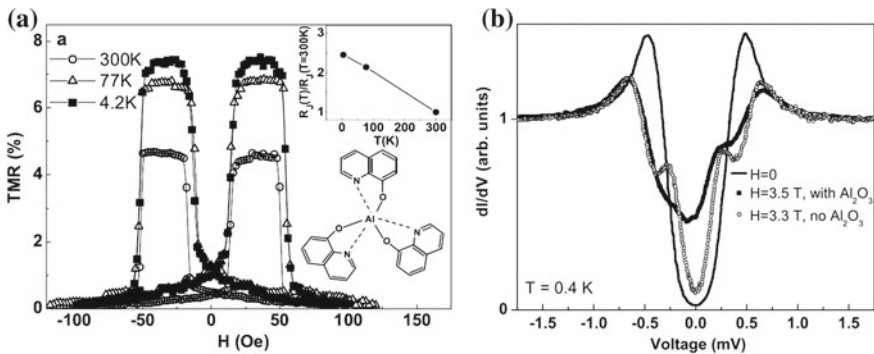
Fig. 7.4 a TMR curve recorded in a Co/Al$_2$O$_3$ (0.6 nm)/Alq$_3$ (1.6 nm)/NiFe MTJ at different temperatures (300, 77 and 4.2 K). The resistance dependence with temperature is represented in the *inset*, as well as the picture of an Alq$_3$ molecule. **b** Curve obtained with a Meservey–Tedrow experiment on a Al/Al$_2$O$_3$/Alq$_3$ (1.5 nm)/Co and a Al/Alq$_3$(3.7 nm)/Co junction to directly determine the spin polarization P for the tunnel current from Co electrode through the Alq$_3$ barrier. Reprinted figure with permission from [16]. Copyright 2007 by the American Physical Society

ization of the bottom interface from $P_{Co/Al_2O_3/Alq3} = 27\%$ with the Al$_2$O$_3$ tunnel
barrier to $P_{Co/Alq3} = 6\%$ without the tunnel barrier.

In the case of Co/Alq$_3$ direct contact, this degradation was explained with the
formation of localized states at the interface that decreased the spin polarization
of the tunnel current. According to authors, the role of Al$_2$O$_3$ was to decouple the
two layers and lower the barrier height to promote the electron injection across the
interface. Moreover, Al$_2$O$_3$ barrier would have also assured a better adhesion of the
Alq3 layer in comparison to the clean Co surface.
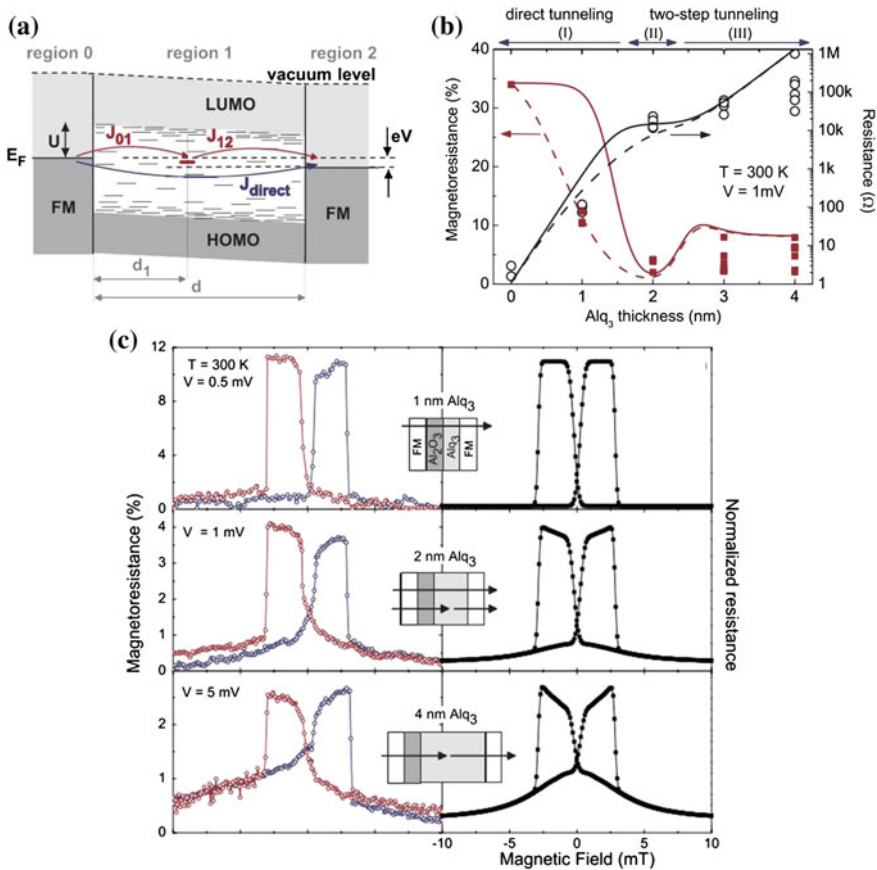
Fig. 7.5 a Schematic representation of the transport mechanisms that can occur in a FM/Alq$_3$/FM
junction. The *black arrow* represents the direct tunneling, while the *red arrow* represents the 2-step
tunneling with electron hopping between localized states inside the organic barrier. **b** Room tempera-
ture MR and resistance dependence on the Alq$_3$ barrier thickness recorded in CoFeB/Al$_2$O$_3$/Alq$_3$/Co
junctions. **c** MR curves measured (*on the left*) and calculated (*on the right*) for junctions with an
Alq$_3$ thickness of 1, 2 and 4 nm. Reprinted figure with permission from [18]. Copyright 2009 by
the American Physical Society

Similar results were later reported by Szulczewski et al. [17] where a positive MR signal up to room temperature was observed in CoFeB/MgO/Alq$_3$/Co and CoFeB/Al$_2$O$_3$/Alq$_3$/Co MTJs of increasing Alq$_3$ thickness from 0 to 8 nm. A study was also reported by Schoonus et al. [18] where CoFeB/Al$_2$O$_3$/Alq$_3$/Co OSVs with an Alq$_3$ thickness from 0 to 4 nm were investigated. In this work, authors studied the change from direct tunneling to 2-step tunneling as function of the increasing Alq$_3$ thickness (Fig. 7.5) and they observed a decrease of the MR signal of at least a factor 4 from one regime to the other. Moreover, they discussed how hyperfine fields could influence the spin transport in organic semiconductors.

Finally, more recently Zhang et al. [19] also reported Fe$_3$O$_4$/Al$_2$O$_3$/Alq$_3$/Co devices with an Alq$_3$ thickness of 2, 5, 10 and 20 nm. Here authors observed a MR ratio that decreased monotonously with increasing Alq$_3$ layer thickness. The largest MR ratio measured at room temperature was 6 % for an Alq$_3$ thickness of 2 nm, and the signal decreased to 0.4 % for devices with a 20 nm thick Alq$_3$ layer.

7.2 Puzzling Results

As one can see from the scenario described above, very heterogeneous results are reported in the literature and they are often difficult to compare due to the lack of common metrology rules. Many points, as the control of device interfaces and the spin injection mechanisms in the organic semiconductor layer, are still unclear and contradictory. Below, we will present and discuss some of these hot topics that are still object of large debates among the organic spintronic community.

7.2.1 Magnetoresistance Sign

The observation and cause of the different MR sign observed in these devices animated for many years a large debate in organic spintronics community.

The negative MR firstly reported by the group of Vardeny in a LSMO/Alq$_3$/Co [1] OSV was interpreted with a model inspired from Jullière's one. Since LSMO is an half-metal with a positive spin polarization P $\simeq$ 100 %, the negative sign was ascribed to a negative spin polarization at the Alq$_3$/Co interface. This result seemed to be confirmed by other works on LSMO/Alq$_3$/Co OSVs [2, 3].

On the other hand, Santos et al. [16] measured a positive spin polarization at the Alq$_3$/Co interface in Meservey-Tedrow experiments on Al/Alq$_3$/Co tunnel junctions (Fig. 7.4b). This contradiction was firstly ascribed to the different thickness of the organic layer implying a tunnel transport regime instead of a diffusion one. However, other works showed that MR sign seemed to be independent on the organic layer thickness and even an inversion of MR signal with bias voltage could be observed in LSMO/Alq$_3$/Co spin valves with an Alq$_3$ thickness of 150 nm [6] (Fig. 7.6). Finally, a positive TMR signal of +300 % was reported in a LSMO/Alq$_3$/Co nanojunction [21].
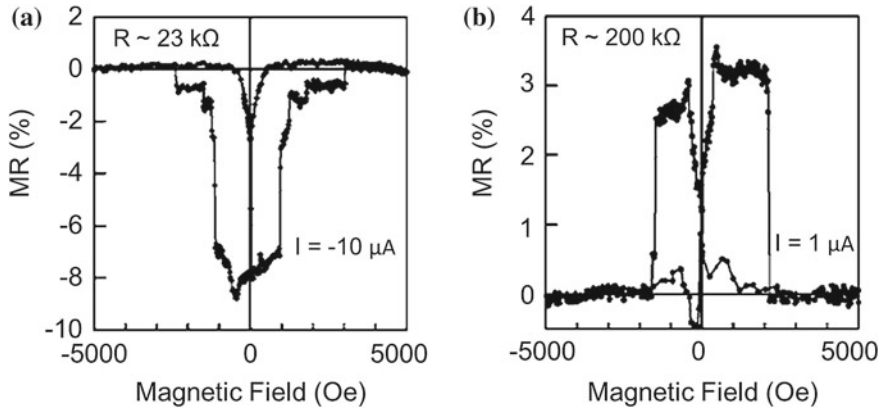
Fig. 7.6 Magnetoresistance curves measured at T = 4.2 K and different bias voltages in LSMO/Alq$_3$ (150 nm)/Co OSVs. A positive and negative MR signal could be recorded for spin valves with the same structure. Figure reprinted from [6]

From this scenario two fundamental questions arise: (i) the first one is about the sign of the spin polarization at the Alq$_3$/Co interface (ii) the second one is about the origin of the positive or negative MR signal in LSMO/Alq$_3$/Co junctions with the same structure.

Different interpretations have been proposed to explain these phenomena [26]. For example, the model proposed by Barraud et al. [21] and already presented in Sect. 3.2.1 shows that the interface plays a key role and ascribes the origin of positive and negative MR to the spin dependent hybridization at the ferromagnetic metal/molecule interface. Indeed, as it has been shown, the spin polarization of an interface can be enhanced or change sign depending on the FM metal/molecule coupling.

To answer the first question, authors started by the consideration that the effective spin polarization at the Alq$_3$/Co interface was positive according to Meservey-Tedrow experiments performed by Santos et al. [16]. On the other hand, authors considered the experiments performed on large area LSMO/Alq$_3$/Co and LSMO/Alq$_3$/Al$_2$O$_3$/Co junctions [11] which both showed a negative MR sign. This suggested that the negative MR could not come from the Alq$_3$/Co interface and hence it was deduced a negative sign of the spin polarization at the LSMO/Alq$_3$ interface due to a strong coupling between the LSMO electrode and the Alq$_3$ molecule.

The last point to explain was the change of MR sign observed in LSMO/Alq$_3$/Co junctions. Authors ascribed its cause to the statistical distribution of the molecular orbitals at the interface due to dipole fluctuations. This would lead to a statistical behaviour of the MR effect depending on the states selected in each specific case. To understand this point one can look at the DOS of the metal/Alq$_3$ interface shown in Fig. 7.7 [27]. The states near the Fermi level of the electrode are highlighted in red. These states are the ones mainly involved in transport since they correspond to the spin polarized molecular orbitals that are resonant to the Fermi level. Hence, even if
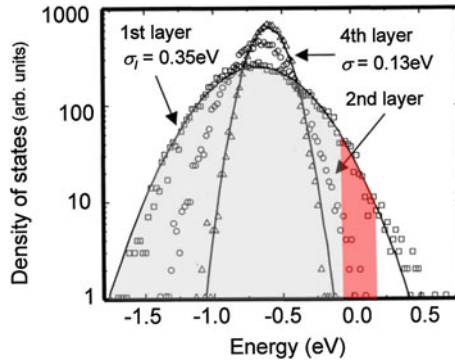
Fig. 7.7 Effect of the interface dipoles on the electron-energy distribution at the metal/Alq$_3$ interface. The distribution in the first few organic monolayers is considerably broadened. In *red* are highlighted the states that are resonant with the Fermi level (E = 0) while in *gray* are represented the non-resonant states. Reprinted figure with permission from [27]. Copyright 2001 by the American Physical Society

they represent a minority in comparison to the whole statistics, they are responsible for the transport of almost all the spin polarized current density. For this reason they behave as "hot spots" and they become responsible for the global behaviour of the junction. Since resonant, these states are also responsible for the inversion of the spin polarization at the interface (case of Fig. 3.5b according to the model presented in Sect. 3.2.1), thus explaining the measurement of a negative MR effect.

Finally, due to the broadening of the DOS, there could be situations where none of these resonant states are probed during transport. This is more likely the case in a nanojunction as the one presented in Fig. 3.7a. In this case the reduced area of the junction makes that only few levels of the whole statistics are probed and the most probable case is that these levels are non-resonant (gray area in Fig. 7.7). According to the model, this would lead to the enhancement of the spin polarization and not to a sign inversion resulting in a positive MR effect (case represented in Fig. 3.5c). If many more samples were measured, statistically there would be cases where a resonant level would be probed and the MR sign would be inverted also for this kind of systems.

The interesting discovery of the possibility to tune the spin polarization properties for a same device depending on the interface coupling, unveiled a new potentiality in organic spintronics field. This gave rise to the new field of "spinterface" and motivated specific studies on the FM metal/molecule interface, both from an experimental point of view, like the ones performed by 2-photon photoemission to determine the spin-filtering properties of Co/Alq$_3$ interfaces [28], and from a theoretical point of view [29, 30]. Nevertheless, nowadays the understanding and control of the interfacial mechanisms for spin polarization manipulation still represents an exciting and open challenge.

7.2.2 Magnetoresistance Origin

Another hot topic in the organic spintronics community during the last years concerns the demonstration of spin injection and propagation mechanisms into organic semiconductors.

Although the feasibility to inject spin-polarized carriers into OSCs has been shown in various experiments, for example using muon-spin rotation [25] or two-photon photoemission [31], these are considered not enough to prove that spin polarization is the cause of the MR effect observed in OSVs. Indeed, many points are still unclear about the mechanisms underlying the spin injection into OSCs and in the last years it is quite controverted if in vertical OSVs, tunneling-based magnetoresistance effects (TMR or TAMR) or actual spin injection and thus GMR is the origin of the observed effects.

Indeed, a GMR effect would be expected in OSVs due to the large thickness of the organic layer. However many of these devices present a weak resistance dependence with temperature that is more likely compatible with TMR transport. Moreover, it was also observed that it is strange that in these devices conduction can be measured even at few tens of mV [32].

Finally, it is also surprising that the top interface and metal atom diffusion during electrode deposition is no more critical when inserting an oxide barrier at the bottom interface allowing the deposition of thin organic layers down to 1 nm. Indeed, the absence of short-circuits in these devices is often justified by the scalability of contact resistance with the organic layer thickness. Nevertheless, it must be remarked that the number of pinholes statistically depends on the organic thickness [33]. For thicker layers the number of pinholes and thus the device resistance and the MR contribution are reduced and this could be erroneously interpreted as transport through the organic layer.

All these unexplained points made recently call into question the origin of the observed MR in OSVs. Moreover, in analogy to inorganic semiconductors field, it was suggested that the final proof to assure the effective spin injection into the organic semiconductor layer is the observation of the Hanle effect in these systems [33, 34].

7.2.3 Conclusions

In conclusion, we have seen in this chapter that a significant effort has been dedicated in the last years to the study and optimization of spintronic devices, in particular to the ones based on Alq$_3$ organic semiconductor. Important improvements have been achieved as the explanation of the origin of the MR sign or the observation of a MR signal at room temperature even if still very small, leaving a large margin for optimization. However, many questions are still open as the control and manipulation of the interfaces or the understanding of the mechanisms for the spin injection into the organic layer.

   Very heterogeneous results emerge from these studies and they are often difficult
to compare due to the high structural variation and different approaches adopted. For
example, at the origin of the low reproducibility of results seems to be the uncertainty
about the reliability of the device interfaces. On one hand it seems that the main
issue preventing the observation of good MR results is the atomic diffusion into the
organic barrier during the top electrode deposition that obliges the deposition of a
thick organic layer or the insertion of a protection oxide barrier at the top interface to
avoid the short-circuit formation. On the other hand, another approach is to improve
the bottom interface with the insertion of a thin oxide barrier between the organic
layer and the bottom electrode. It looks amazing how in this case the top interface
seems no more critic and pinhole problem seems completely solved allowing the
deposition of thin organic layers down to 1 nm.

   In this scenario, a systematic study of this kind of devices for trying to gain a
global vision on all these effects is missing and it will be the object of this second
experimental part.

References

 1. Z.H. Xiong, D. Wu, Z.V. Vardeny, J. Shi, Giant magnetoresistance in organic spin-valves.
    Nature **427**, 821–824 (2004)
 2. S. Majumdar, H.S. Majumdar, R. Laiho, R. Osterbacka, Comparing small molecules and poly-
    mer for future organic spin-valves. J. Alloys Compd. **423**, 169–171 (2006)
 3. W. Xu, G.J. Szulczewski, P. LeClair, I. Navarrete, R. Schad, G.X. Miao, H. Guo, A. Gupta,
    Tunneling magnetoresistance observed in La0.67Sr0.33MnO3/organic molecule/Co junctions.
    Appl. Phys. Lett. **90**(7), 72506 (2007)
 4. F.J. Wang, Z.H. Xiong, D. Wu, J. Shi, Z.V. Vardeny, Organic spintronics: the case of Fe/Alq$_3$/Co
    spin-valve devices. Synth. Met. **155**, 172–175 (2005)
 5. P. Zhi-Yong, C. Yan-Xue, L. Tian-Tian, Z. Yun-Pang, X. Shi-Jie, Y. Shi-Shen, H. Sheng-
    Hao, Giant magnetoresistance in LaCaMnO/Alq$_3$/Co sandwiched-structure organic spin valves.
    Chin. Phys. Lett. **23**, 1566 (2006)
 6. H. Vinzelberg, J. Schumann, D. Elefant, R.B. Gangineni, J. Thomas, B. Büchner, Low temper-
    ature tunneling magnetoresistance on (La, Sr)MnO$_3$/Co junctions with organic spacer layers.
    J. Appl. Phys. **103**, 93720 (2008)
 7. J.S. Jiang, J.E. Pearson, S.D. Bader, Absence of spin transport in the organic semiconductor
    Alq$_3$. Phys. Rev. B **77**, 035303 (2008)
 8. S. Yuasa, T. Nagahama, A. Fukushima, Y. Suzuki, K. Ando, Giant room-temperature magne-
    toresistance in single-crystal Fe/MgO/Fe magnetic tunnel junctions. Nat. Mater. **3**, 868–871
    (2004)
 9. S.S.P. Parkin, C. Kaiser, A. Panchula, P.M. Rice, B. Hughes, M. Samant, S.-H. Yang, Giant
    tunnelling magnetoresistance at room temperature with MgO (100) tunnel barriers. Nat. Mater.
    3(12), 862–867 (2004)
10. D. Sun, E. Ehrenfreund, Z. Valy, The first decade of organic spintronics research. Chem.
    Commun. **50**, 1781–1793 (2014)
11. V.A. Dediu, L.E. Hueso, I. Bergenti, A. Riminucci, F. Borgatti, P. Graziosi, C. Newby, F. Casoli,
    M.P. De Jong, C. Taliani, Y. Zhan, Room-temperature spintronic effects in Alq$_3$-based hybrid
    devices. Phys. Rev. B **78**, 115203 (2008)
12. D. Sun, L. Yin, C. Sun, H. Guo, Z. Gai, X.-G.G. Zhang, T.Z. Ward, Z. Cheng, J. Shen, Giant
    magnetoresistance in organic spin valves. Phys. Rev. Lett. **104**, 236602 (2010)

13. S. Wang, Y.J. Shi, L. Lin, B.B. Chen, F.J. Yue, J. Du, H.F. Ding, F.M. Zhang, D. Wu, Room-temperature spin valve effects in La$_{0.67}$Sr$_{0.33}$MnO$_3$/Alq$_3$/Co devices. Synth. Met. **161**, 1738–1741 (2011)

14. Y. Liu, T. Lee, H.E. Katz, D.H. Reich, Effects of carrier mobility and morphology in organic semiconductor spin valves. J. Appl. Phys. **105**, 07C708 (2009)

15. X. Zhang, S. Mizukami, T. Kubota, M. Oogane, H. Naganuma, Y. Ando, T. Miyazaki, Spin transport in Co/Al$_2$O$_3$/Alq$_3$/Co organic spin valve. IEEE Trans. Magn. **47**, 2649–2651 (2011)

16. T.S. Santos, J.S. Lee, P. Migdal, I.C. Lekshmi, B. Satpati, J.S. Moodera, Room-temperature tunnel magnetoresistance and spin-polarized tunneling through an organic semiconductor barrier. Phys. Rev. Lett. **98**, 016601 (2007)

17. G. Szulczewski, H. Tokuc, K. Oguz, J.M.D. Coey, Magnetoresistance in magnetic tunnel junctions with an organic barrier and an MgO spin filter. Appl. Phys. Lett. **95**, 202506 (2009)

18. J.J.H.M. Schoonus, P.G.E. Lumens, W. Wagemans, J.T. Kohlhepp, P.A. Bobbert, H.J.M. Swagten, B. Koopmans, Magnetoresistance in hybrid organic spin valves at the onset of multiple-step tunneling. Phys. Rev. Lett. **103**, 146601 (2009)

19. X. Zhang, S. Mizukami, Q. Ma, T. Kubota, M. Oogane, H. Naganuma, Y. Ando, T. Miyazaki, Spin-dependent transport behavior in C$_{60}$ and Alq$_3$ based spin valves with a magnetite electrode. J. Appl. Phys. **115**, 172608 (2014)

20. S. Pramanik, S. Bandyopadhyay, K. Garre, M. Cahay, Normal and inverse spin-valve effect in organic semiconductor nanowires and the background monotonic magnetoresistance. Phys. Rev. B **74**, 235329 (2006)

21. C. Barraud, P. Seneor, R. Mattana, S. Fusil, K. Bouzehouane, C. Deranlot, P. Graziosi, L. Hueso, I. Bergenti, V. Dediu, F. Petroff, A. Fert, Unravelling the role of the interface for spin injection into organic semiconductors. Nat. Phys. **6**, 615–620 (2010)

22. H. Zhang, P. Desai, Y.Q. Zhan, A.J. Drew, W .P. Gillin, T. Kreouzis, The importance of holes in aluminium tris-8-hydroxyquinoline (Alq$_3$) devices with Fe and NiFe contacts. Appl. Phys. Lett. **104**, 013303, (2014)

23. Y. Liu, S.M. Watson, T. Lee, J.M. Gorham, H.E. Katz, J.A. Borchers, H.D. Fairbrother, D.H. Reich, Correlation between microstructure and magnetotransport in organic semiconductor spin-valve structures. Phys. Rev. B **79**, 075312 (2009)

24. B.B. Chen, Y. Zhou, S. Wang, Y.J. Shi, H.F. Ding, D. Wu, Giant magnetoresistance enhancement at room-temperature in organic spin valves based on La$_{0.67}$Sr$_{0.33}$MnO$_3$ electrodes. Appl. Phys. Lett. **103**(7), 72402 (2013)

25. A.J. Drew, J. Hoppler, L. Schulz, F.L. Pratt, P. Desai, P. Shakya, T. Kreouzis, W.P. Gillin, A. Suter, N.A. Morley, V.K. Malik, A. Dubroka, K.W. Kim, H. Bouyanfif, F. Bourqui, C. Bernhard, R. Scheuermann, G.J. Nieuwenhuys, T. Prokscha, E. Morenzoni, Direct measurement of the electronic spin diffusion length in a fully functional organic spin valve by low-energy muon spin rotation. Nat. Mater. **8**(2), 109–114 (2009)

26. L. Schulz, L. Nuccio, M. Willis, P. Desai, P. Shakya, T. Kreouzis, V.K. Malik, C. Bernhard, F.L. Pratt, N.A. Morley, A. Suter, G.J. Nieuwenhuys, T. Prokscha, E. Morenzoni, W.P. Gillin, A.J. Drew, Engineering spin propagation across a hybrid organic/inorganic interface using a polar layer. Nat. Mater. **10**, 39–44 (2011)

27. M.A. Baldo, S.R. Forrest, Interface-limited injection in amorphous organic semiconductors. Phys. Rev. B **64**, 1–17 (2001)

28. S. Steil, N. Großmann, M. Laux, A. Ruffing, D. Steil, M. Wiesenmayer, S. Mathias, Spin-dependent trapping of electrons at spinterfaces. Nat. Phys. **9**, 242–247 (2013)

29. S. Müller, S. Steil, A. Droghetti, N. Großmann, V. Meded, A. Magri, B. Schäfer, O. Fuhr, S. Sanvito, M. Ruben, M. Cinchetti, M. Aeschlimann, Spin-dependent electronic structure of the Co/Al(OP)$_3$ interface. New J. Phys. **15**, 113054 (2013)

30. A. Droghetti, S. Steil, N. Großmann, N. Haag, H. Zhang, M. Willis, W.P. Gillin, A.J. Drew, M. Aeschlimann, S. Sanvito, M. Cinchetti, Electronic and magnetic properties of the interface between metal-quinoline molecules and cobalt. Phys. Rev. B **89**, 094412 (2014)

31. M. Cinchetti, K. Heimer, J.-P. Wüestenberg, O. Andreyev, M. Bauer, S. Lach, C. Ziegler, Y. Gao, M. Aeschlimann, Determination of spin injection and transport in a ferromagnet/organic semiconductor heterojunction by two-photon photoemission. Nat. Mater. **8**(2), 115–119 (2009)

32. H. Jiang, G. Hu, S. Xie, Effect of electron delocalization in quasi-one-dimensional organic ferromagnet. Phys. B: Condens. Matter **405**(11), S299–S302 (2010)
33. M. Grünewald, R. Göckeritz, N. Homonnay, F. Würthner, L.W. Molenkamp, G. Schmidt, Vertical organic spin valves in perpendicular magnetic fields. Phys. Rev. B **88**, 085319 (2013)
34. A. Riminucci, M. Prezioso, C. Pernechele, P. Graziosi, I. Bergenti, R. Cecchini, M. Calbucci, M. Solzi, V.A. Dediu, Hanle effect missing in a prototypical organic spintronic device. Appl. Phys. Lett. **102**, 92407 (2013)

Chapter 8
Magneto-Transport Results in Alq$_3$ Based OSVs

In this second experimental section we will report results on large area Alq$_3$ OSVs. The study of these devices represents a large part of organic spintronics research and it is mainly oriented to their implementation in devices as spin-OLEDs or to the investigation of spin transport over long distances. Despite largely studied, these systems are extremely complex and the phenomena governing them are still unclear.

We have seen in Chap. 7 that results reported until now are very heterogeneous and often difficult to compare due to the different approaches adopted by each group. For this reason we decided to perform a systematic study of Co/Alq$_3$/Co OSVs in order to investigate the specific role of ferromagnetic metal/molecule hybridization at the top and bottom interface and their influence on the spin polarization. The use of Co electrodes, with a Curie temperature well above 300 K, also allowed to investigate MR signal at room temperature. This represents one of the main targets of OSVs but, for the moment, only few works could report room temperature MR effect in OSVs [1–3] with a very limited signal amplitude ($\leq |1|\%$), leaving a large margin for improvement.

In Sect. 8.1 we will start by presenting the device fabrication and Alq$_3$ characterization in order to verify that the properties of the molecule are maintained after evaporation. Then, a statistical study of the resistance dependence on the Alq$_3$ thickness in Co/Alq$_3$/Co OSVs will be presented, with a thickness of the organic barrier ranging from 12 to 160 nm and an active area of the device of 50×50 and $100 \times 100\,\mu m^2$. We will finally focus on Alq$_3$ thickness of 12–20 nm as standard device and we will investigate the spin polarized effects into this system.

In Sect. 8.2 we will show very successful and reproducible MR signal at room temperature in devices where a tunnel barrier (TB) is inserted at the bottom interface in Co/TB/Alq$_3$/Co OSVs, using a similar approach to the one adopted in large area organic MTJs [4, 5]. In Sect. 8.3, the spin injection into the organic layer will be proved using IETS measurement and the importance to be extremely careful when interpreting MR results in such devices will be also highlighted.

In Sect. 8.4 we will finally report MR at room temperature in Co/Alq$_3$/Co OSVs. In this section we will also discuss the origin of positive and negative MR observed and we will show that another effect, TAMR, can be detected in these complex systems.

## 8.1 Fabrication and Characterization of Alq$_3$ Based OSVs

8.1.1 Device Fabrication

In order to perform a systematic study to investigate the influence of interface hybridization on spin polarization and compare results with the ones reported in the literature, we chose to use standard materials for organic spintronics, Alq$_3$ as organic semiconductor and Co as ferromagnetic electrodes, to fabricate large area OSVs. In this aim, we used a completely in-situ technique to fabricate vertical organic spin valves by shadow mask where metal quinolines are deposited by evaporation. The main advantage of this process is that, since it is entirely performed under high vacuum, it is compatible with the use of ferromagnetic transition metals, as Co, whose use is often prevented in these devices by their easy oxidation under ambient atmosphere. Moreover, standard oxide barriers such as Al$_2$O$_3$ or MgO have been eventually introduced at the top or bottom interface in order to separately investigate the FM metal/molecule interface hybridization.

A schematic of the junction used in this study is shown in Fig. 8.1b, while in Fig. 8.1a it is shown a picture of a whole real sample. On every substrate (a Si/SiO$_2$(400 nm) 2" wafer) are fabricated 140 Co/(TB)/Alq$_3$/(TB)/Co junctions to have a large statistics. Half of the junctions present an area of $50 \times 50 \, \mu m^2$ and the other half $100 \times 100 \, \mu m^2$. The equipment used to realize the devices is shown in Fig. 8.2.

The fabrication process starts with the bottom electrode deposited by sputtering (the characteristic of this technique has already been discussed in Sect. 5.4.4). The bottom electrode is patterned by shadow mask in stripes of 50 and 100 μm width. It is composed by a thin layer of Co (3 nm) that is oxidized under a controlled oxygen plasma and covered with a 50 nm Co layer. Co oxide is antiferromagnetic at low temperature and its function is to increase the coercive field of the bottom electrode, making the junction not completely symmetric and facilitating an antiparallel magnetic configuration.

Once the bottom electrode is deposited, the shadow mask is changed under vacuum and sample is transferred into the evaporator for the deposition of the organic barrier. Here the Alq$_3$ organic layer (from 12 to 160 nm) is deposited by thermal evaporation. The Alq$_3$ powder (a Sigma Aldrich commercial 4N5 99,995 % pure one not re-purified before deposition) is situated into a crucible surrounded by an electric filament. The evaporation temperature is about 270 °C and it is adjusted to reach an evap-
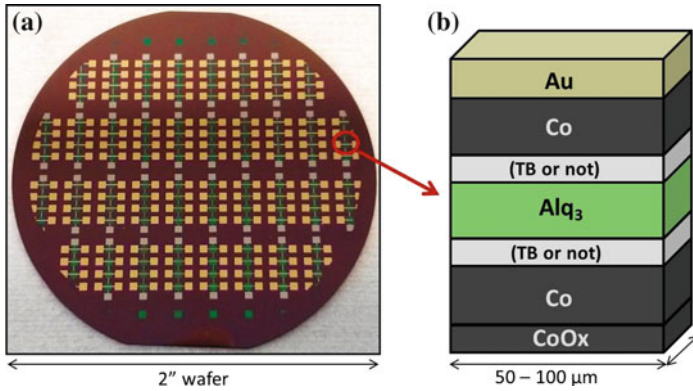
Fig. 8.1 **a** Picture of one sample fabricated by shadow-mask. Each sample contains 140 OSVs in order to obtain a large statistics. These junctions are divided in groups of four for an easier measurement into the cryostat and the junction area is 50×50 and $100 \times 100 \, \mu m^2$. **b** Schematic representation of one Co/(TB)/Alq$_3$/(TB)/Co OSVs. An oxide tunnel barrier (TB) can eventually be inserted at the bottom or top interface to separately study the properties of the other interface in the junction
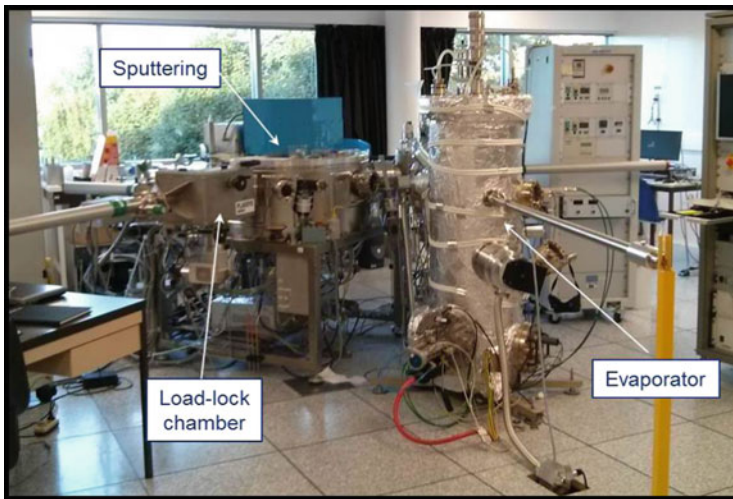
Fig. 8.2 Picture of the equipment used to fabricate Co/(TB)/Alq$_3$/(TB)/Co OSVs by shadow-mask. The device is maintained under vacuum for the whole fabrication process. Masks can be removed and replaced in the load-lock chamber and sample can be transferred from the sputtering machine to the evaporator without breaking the vacuum

oration rate of $\sim$40 pm/s. Alq$_3$ is deposited on the upstanding sample under a pressure of $\sim 10^{-6}$ mbar and the layer thickness is controlled by a quartz-crystal oscillator.

Finally, shadow mask is changed again without breaking the vacuum and the top electrode, a Co(15 nm)/Au(10 nm) bilayer, is deposited by evaporation and capped

with a Au (70 nm) layer by sputtering. Contrarily to molecule evaporation, inorganic materials are heated by an electron-beam. The deposition by evaporation of the top layer directly in contact with the organic one is extremely important to limit the metal atoms diffusion into the organic. This is because evaporation is a much softer deposition technique compared to sputtering. To give an idea, evaporated atoms arrive with an energy of about 0.1 eV over the sample, while atoms deposited by sputtering have a large energy distribution with a peak at 10 eV and queues that can reach even 300 eV. Sputtering layers are thus more uniform and dense than evaporated ones, but it is clear the destructive effect that such energetic atoms could have on soft organic layers.

Additionally, before or after the Alq₃ deposition, an oxide barrier of Al_2O_3 or MgO can be also added in order to decouple one of the two metal/molecule interfaces and study the hybridization properties of the other one. Alumina barrier is formed from an Al layer (1.5 nm) deposited by sputtering and then oxidized by an oxygen plasma, while MgO barrier is deposited by evaporation starting directly from an MgO charge with a deposition technique equivalent to that of evaporated metals.

8.1.2 Alq₃ Characterization

In order to confirm the quality of our organic material and to be sure that molecules are not damaged during the evaporation process, samples of evaporated Alq₃ have been characterized by infrared and Raman spectroscopy and they have been compared to bulk material and literature results. Moreover, in Sect. 8.3 we will see how these characterizations have been also used to assign the vibrational modes electrically detected by IETS in the measured junctions.

Infrared spectroscopy (IR): IR technique is used to gain information about the specific vibrational modes of molecules, exploiting the fact that molecules absorb specific frequencies that correspond to transition energy of the bond or group that vibrates. In Fig. 8.3 are compared spectra of Alq₃ powders before and after evaporation. In these spectra we can observe all the typical peaks reported in the literature [6] and no substantial change could be detected before and after evaporation, thus confirming that molecules are not damaged during the deposition process. A summary of the vibrational modes observed in these spectra is reported in Table 8.1.

Raman spectroscopy: We also characterized evaporated Alq₃ by Raman spectroscopy. This technique is based on inelastic scattering (Raman scattering) of monochromatic light. In a Raman experiment, a photon excites the molecule from the ground state to a virtual energy state. When the molecule relaxes, it emits a photon and it returns to a different rotational or vibrational state. The difference in energy between the original state and this new state leads to a shift in the emitted photon's frequency away from the excitation wavelength. The shift in energy gives information about the vibrational modes in the system. For selection rules, the vibrational modes that are observed by Raman spectroscopy are complementary to the ones observed by IR spectroscopy.

Fig. 8.3 *Top* Normalized IR spectrum of an Alq$_3$ bulk sample before evaporation. *Bottom* Normalized IR spectrum measured on Alq$_3$ powder after evaporation. No significant difference can be observed between the two spectra thus suggesting that Alq$_3$ molecule is not damaged by the evaporation process
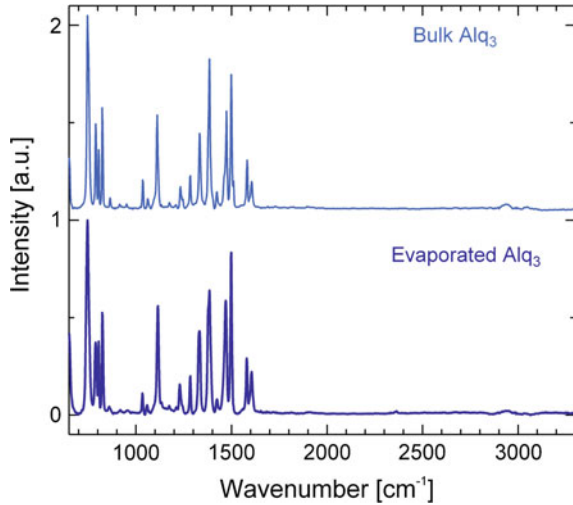
Using Raman spectroscopy we analysed an Alq$_3$ layer deposited over a Co electrode in order to have the same conditions for Alq$_3$ to the ones analysed by IETS. In Fig. 8.4 the Raman spectrum recorded for this sample using a $\lambda = 514$ nm excitation laser is reported. The low resolutions of the peaks is due to the difficulty to obtain a clear signal for a thin layer of Alq$_3$ ($\sim$80 nm). In any case, some peaks can be distinguished and they correspond to values reported in the literature [7]. These modes are also summarized in Table 8.1.

Raman and IR modes will be compared in Sect. 8.3 to the peaks corresponding to the molecular vibrations electrically measured in the devices using the IETS technique.

8.1.3 Preliminary Considerations on Device Resistance Statistics

One of the main issues in the fabrication of large area organic devices is the high probability of short-circuit formation due to the top electrode atom diffusion into the organic barrier. To avoid this problem people are often obliged to deposit a thick organic layer of about 100 nm.

However, in our system thanks to the limited size of the junctions (50×50 and $100 \times 100 \, \mu m^2$) and to the large number of contacts fabricated for every sample (140 contacts/sample), we were able to measure non short-circuited OSVs with an Alq$_3$ thickness down to 12 nm without the addition of any protection barrier. The statistics that we will show are grouped for runs since results can statistically vary from one sample to the other.

**Table 8.1** Summary of the peaks that could be observed by IR and Raman spectroscopy characterization of Alq$_3$

IR		Raman		Peaks assignment
(cm^{-1})	(meV)	(cm^{-1})	(meV)	
		522	65	$\delta_{ring} + \nu$(Al-O)
		642	80	ν(Al-O)$ + \nu$(Al-N)$ + \delta_{ring}$
746	92	752	93	ν_{ring}
789	98			δ(C-H)$_{wag}$
804	100			δ(C-H)$_{wag} + \delta_{ring}$
823	102			δ(C-H)$_{wag}$
863	107			δ(C-H)$_{wag}$
1034	128			δ(C-H)$ + \nu_{ring}$
1060	131	1053	131	δ(C-H)$ + \nu_{ring}$
1110	138			δ(C-H)$ + \nu_{ring}$
1132	140	1131	140	δ(C-H)
1174	146			δ(C-H)
1209	150			δ(C-H)$ + \nu_{ring}$
1232	153			ν(C-N)$ + \delta$(C-H)
1284	159	1282	159	δ(C-H)$ + \nu_{ring} + \nu$(C-O)
1332	165	1327	165	δ(C-H)$ + \nu_{ring}$
1385	172	1387	172	ν_{ring}
1424	177	1422	176	δ(C-H)$ + \nu_{ring}$
1473	183	1470	182	δ(C-H)$ + \nu_{ring}$
1498	186	1498	186	δ(C-H)$ + \nu_{ring}$
1581	196			ν_{ring}
		1591	197	δ(C-H)$ + \nu_{ring}$
1605	199			ν_{ring}
2939	364			–
		3051	378	–

ν and δ correspond respectively to stretching and bending vibrational modes. Peaks have been assigned by comparison with the values tabulated in the literature [6, 7]

In Fig. 8.5 is shown the typical trend for the percentages of short-circuited (gray), measurable (green) and insulating (red) contacts measured in Co/Alq$_3$/Co spin valves with different Alq$_3$ thicknesses. As expected, the number of short-circuited contacts decreases with the increasing thickness, while the number of contacts that become too resistive to be measured increases. Astonishingly about 20 % of the contacts (with variations from one sample to the other) were still measurable with resistances in the 100 kΩ–100 MΩ range for an Alq$_3$ thin layer of 12 nm. For our devices we finally chose to focus on junctions with a thickness of 12–20 nm for the Alq$_3$ barrier. This is because: (i) the estimated spin diffusion length in Alq$_3$ is in the order of some tens of nm [8]. (ii) The increasing number of insulating contacts measured in our
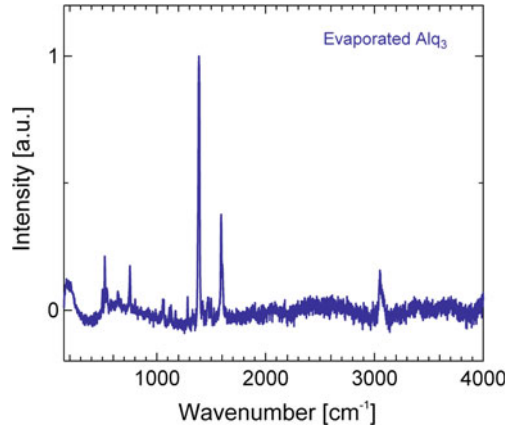
Fig. 8.4 Normalized Raman spectrum recorded on a Co/Alq$_3$(80 nm) sample where Alq$_3$ layer is deposited by evaporation with the same conditions used to fabricate Co/Alq$_3$/Co OSVs. Background has been subtracted in the graph
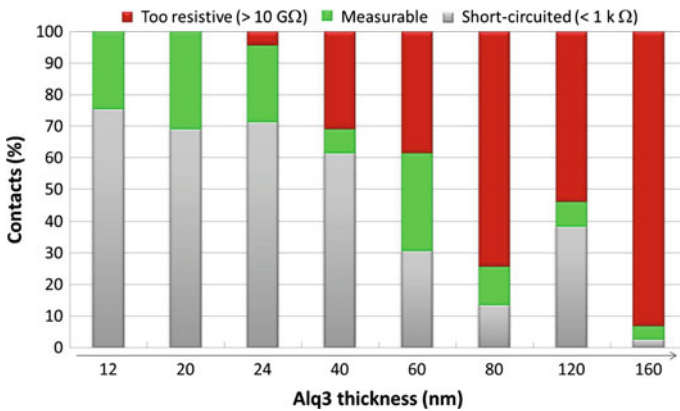
Fig. 8.5 Typical trend for the percentage of short-circuited (*gray*), measurable (*green*) and highly resistive (>10 GΩ) (*red*) contacts in Co/Alq$_3$/Co samples for an increasing thickness of Alq$_3$ barrier. The percentage of each sample is calculated on a statistics of 140 contacts

system for an Alq$_3$ thickness >20 nm, suggests that "good contacts" with no or little inclusions could be too resistive to be measured above this limit. This would mean that the "measurable contacts" in junctions with Alq$_3$ >20 nm would be measurable only when defects are present in the barrier. On the contrary, even if the presence of pinholes in devices with an Alq$_3$ thickness of 12–20 nm can not be excluded, there is a higher probability that measurable contacts in these junctions present a less damaged interface, since otherwise they would probably result in short-circuited junctions.

The ability to measure non short-circuited large area devices with an Alq$_3$ thickness down to 12 nm and without any protection barrier at the interface represents

a strong improvement in device fabrication. To compare, the smallest thickness reported in the literature for similar devices is 40 nm where an indirect deposition of the top electrode had to be applied to avoid short-circuits formation on an area of 1×1 mm^2 [2].

Nevertheless, the resistance dispersion between the measurable contacts is still relatively high in Co/Alq$_3$/Co samples.

Effect of a tunnel barrier at the top interface on the device resistance statistics: Following the approach proposed by Dediu et al. [1], we tried to insert a thin MgO barrier at the top interface to investigate its effect on the device resistance statistics. In Fig. 8.6a are shown the percentages of short-circuited, measurable and insulating contacts probed in Co/Alq$_3$/Co and Co/Alq$_3$/TB/Co junctions of a same run. The analysed junctions are part of a unique sample where a portion of the contacts has been masked from the TB deposition. This assures that all the contacts were subjected to the same fabrication conditions and allows a direct comparison.

As expected, what we observe is an increase in the number of measurable contacts in the case of the TB insertion. This effect can be due both to the protective impact of the tunnel barrier or to the measurement of insulating filaments.

Effect of a tunnel barrier at the bottom interface on the device resistance statistics: The second approach that we tested was to insert a thin tunnel barrier at the bottom interface. In Fig. 8.6b are compared contacts resistance measured in Co/Alq$_3$/Co and Co/TB/Alq$_3$/Co devices (TB = Al$_2$O$_3$ or MgO), again taken from a same sample. What we observe is a large and very reproducible increase of the number of
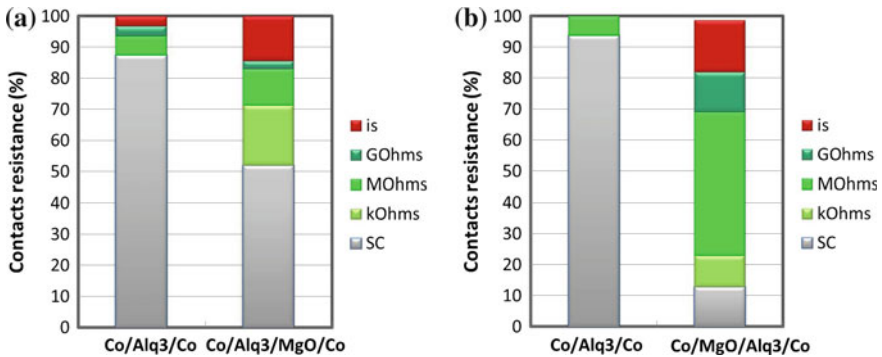
Fig. 8.6 a Comparison of the percentage of short-circuited (*gray*), measurable (scale of *green*) and insulating (*red*) contacts in Co/Alq$_3$(20 nm)/Co (statistics on 32 contacts) and Co/Alq$_3$(20 nm)/MgO(2 nm)/Co junctions (statistics on 78 contacts) for a same run. The barrier protects the organic layer from atom diffusion and increases the number of measurable contacts. However, the resistance dispersion is still very high. **b** Same color scale but this time the comparison is between Co/Alq$_3$(20 nm)/Co and Co/MgO(2 nm)/Alq$_3$(20 nm)/Co junctions. In this case the number of contacts in the MΩ range significantly increases. The slight difference between the number of contacts in the MΩ and insulating range in Co/Alq$_3$/Co junctions of (**a**) and (**b**) is due to the statistical variation observed in samples coming from different runs

measurable contacts with a very strong increase of the number of contacts in the MΩ range. The increase of the total number of non short-circuited junctions is not really astonishing since the formation of a pinhole into the organic layer would lead to the measurement of the underlying oxide tunnel barrier. On the contrary, what is quite remarkable is the decrease of resistance dispersion with a clear increase of contacts in the MΩ range. If what we were measuring was just the resistance of the tunnel barrier, we would expect an increase of the measured resistance but there would be no reason for a decrease of its dispersion. In this regard one possible explanation could be the one suggested by the group of Moodera [4] of a different growth mode of Alq₃ molecules on the oxide layer than in direct contact with the Co surface.

## 8.2 Efficient Room Temperature Spin Injection in Organic Semiconductors

Since Co/TB/Alq₃/Co contacts gave the most homogeneous resistance results, we started from these junctions for the investigation of spin injection at room temperature. A very efficient and reproducible room temperature MR signal could be observed in these devices with both MgO or Al₂O₃ barrier.

In Fig. 8.7a is shown a MR signal up to 8 % recorded in a Co/MgO/Alq₃/Co spin valve at 300 K. This signal is very clear, stable and can be reproducibly observed in this kind of junctions always showing a positive sign up to ±600 mV. In the inset the MR signal measured at 2 K is also shown. The peak asymmetry in the low temperature curve is due to the presence of Co oxide below the bottom Co electrode. At low temperature Co oxide becomes antiferromagnetic and the coercive field of the bottom electrode increases. This effect disappears at room temperature, here the electrodes are partially coupled and they are never really in the antiparallel configuration. In Fig. 8.7b is also shown the MR behaviour with bias voltage of this junction at 300 and 2 K. As expected, MR signal decreases with increasing bias and temperature.

An analogous behaviour was also observed in Co/Al₂O₃/Alq₃/Co OSVs as shown in Fig. 8.8. Once again, a clear and reproducible MR signal could be recorded at room temperature. MR sign is always positive and the same behaviour with bias voltage and temperature than the previous one could be observed, thus confirming the reproducibility of the results. The lower magnitude of MR curve in these junctions compared to the previous ones could be ascribed to a weaker spin polarization at Co/Al₂O₃ interface than Co/MgO one.
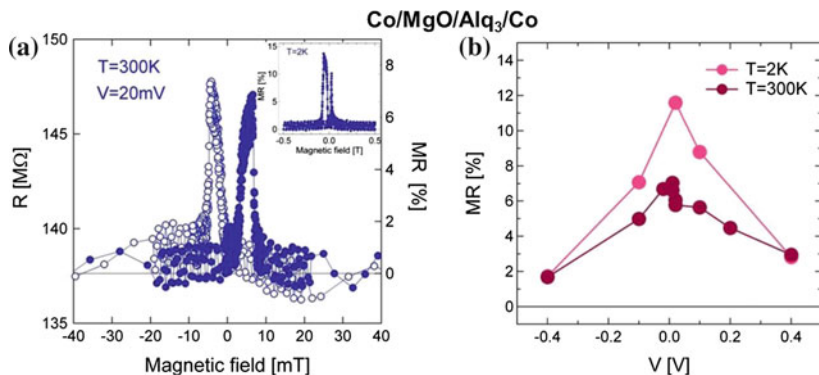
Fig. 8.7 **a** Room temperature MR signal recorded in a Co/MgO(2 nm)/Alq₃(20 nm)/Co OSV with an applied bias of 20 mV. The section of the junction is $50 \times 50 \, \mu m^2$. In the *inset* is shown the same MR signal recorded at 20 mV and 2 K. **b** MR dependence with bias voltage for the two temperatures of 2 and 300 K
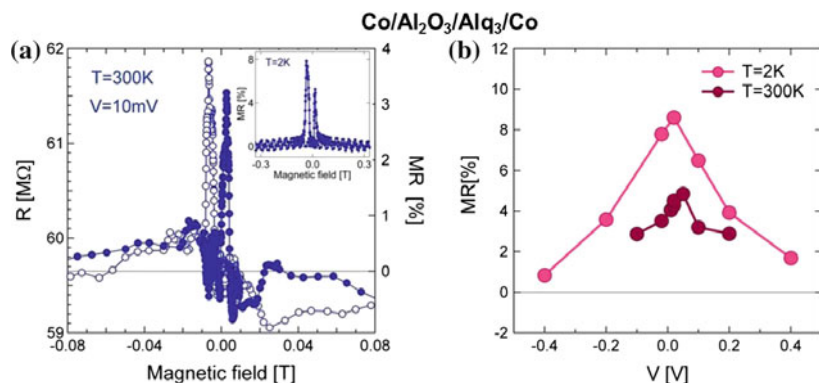

Fig. 8.8 **a** Room temperature MR signal recorded in a Co/Al₂O₃(1.5 nm)/Alq₃(20 nm)/Co OSV with an applied bias of 20 mV. The section of the junction is $100 \times 100 \, \mu m^2$. In the *inset* is shown the same MR signal recorded at 20 mV and 2 K. **b** MR dependence with bias voltage at 2 and 300 K

8.3 How to Detect Spin Injection in Organic Semiconductors

As remarked before, one of the most controverted points in the organic spintronics community is the demonstration of spin injection through the organic layer. In analogy to inorganic semiconductors field some people sustain that the observation of the Hanle effect (HE) is the only reliable proof for spin injection. Nevertheless, no observation of HE in organic materials could be reported until now [9, 10]. Some theoretical work also advanced the hypothesis that the non observation of an HE evidence could be normal in organic devices [11]. The meaning of this lack of results is consequently still unclear.

Fig. 8.9 Schematic representations of: **a** a "good" Co/TB/Alq$_3$/Co contact and **b** a Co/TB/Alq$_3$/Co contact where Co atoms inclusions create a short-circuit through the organic layer. Contact (**b**) is the equivalent of a Co/TB/Co MTJ
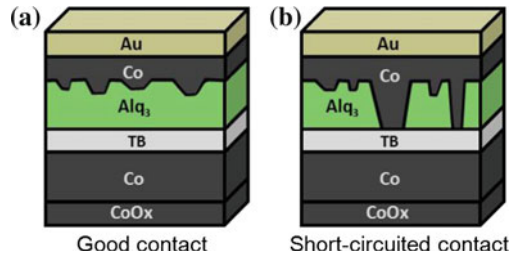
We propose to use the IETS measurements as an alternative to prove the spin transport through the organic layer. This method allows to make the difference between a MR signal due to a real spin injection through the organic barrier (Fig. 8.9a) and a signal just coming from the oxide tunnel barrier measured through a short-circuit into the molecules (Fig. 8.9b). In the following we will see more in details how it is possible to make this difference.

One argument commonly used to make the difference between the two situations is the comparison between the resistance of a short-circuited contact that is normally much lower and the one of the junction. However, in a TB/organic bilayer this condition could not be true if the short-circuit through the molecules is just due to few atoms inclusions resulting in a very small cross section.

Another commonly used argument is to verify the scalability of contact resistance with the organic layer thickness, but even this method is not reliable since the number of pinholes statistically depends on the organic thickness.

Finally, transition electron microscopy (TEM) investigation on a contact section has been also used to show the absence of atomic inclusions into the organic barrier. However, this technique can give an idea on the general quality of the interface but it can not exclude the presence of few pinholes outside the imaged section.

To avoid all these doubts, we propose to use IETS measurements to verify the spin injection into the Alq$_3$ layer. As seen in Sect. 6.2, IETS technique allows to relate the second derivative of current electrically measured in the junction to the molecular vibrations excited by the electrons transiting through the organic barrier. This results in a curve where peaks appear in correspondence of these excitation energies. Moreover, IETS also allows to directly check transport through molecules for a given contact. For these reasons this analysis can be used as a fingerprint of the transport through molecules inside each junction. Thanks to these great advantages, IETS method is recently increasing its popularity in the field of molecular electronics and organic spintronics [12–15]. However, no results have been yet reported on Alq$_3$ based devices.

In Fig. 8.10a is shown the IETS spectrum (red curve) measured in the Co/Al$_2$O$_3$/Alq$_3$/Co contact presented in the previous section. For simplicity we will call this sample "Sample 1". As one can see, peaks appear in the spectrum while they are totally absent in the IETS curve recorded in a Co/Al$_2$O$_3$/Co junction made under the same conditions (black curve). This observation suggests that the peaks observed in Sample 1 come from the organic layer and they represent the vibrational modes
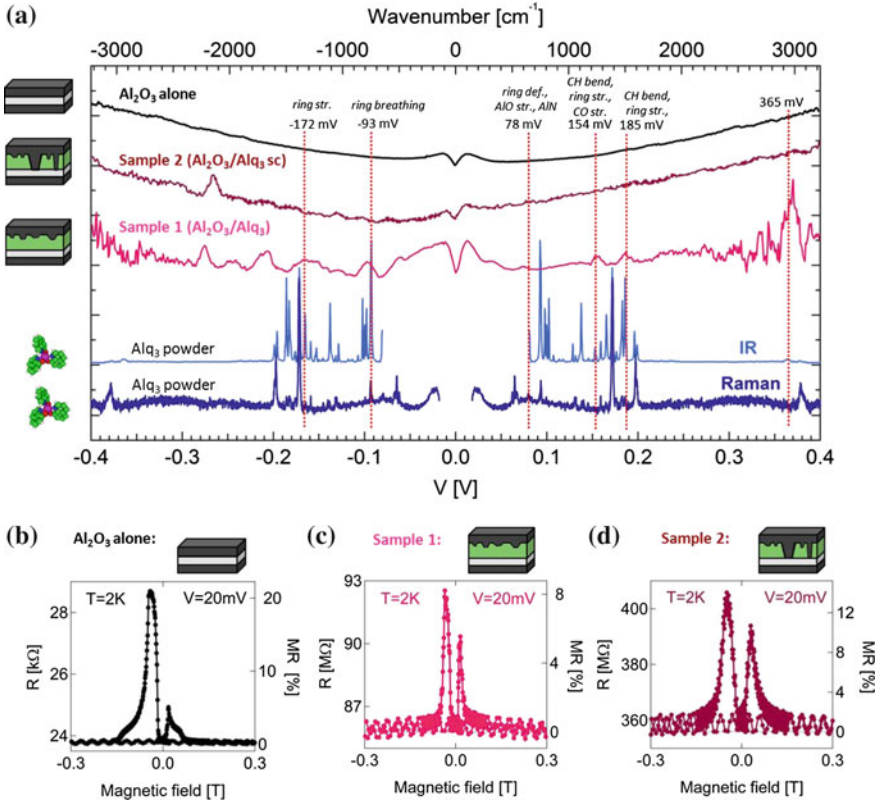
Fig. 8.10 a IETS curves for three samples (Sample1, Sample 2, Co/Al₂O₃/Co) recorded at 2 K and Raman and IR spectra of Alq₃. **b–d** MR curves for the three different samples. The peaks highlighted in the IETS curve of Sample 1 correspond to the molecular vibrations. None of these peaks can be observed in the IETS curve of Sample 2, meaning that this contact is short-circuited

excited by electrons when crossing this barrier. To assign the vibrational modes we compared the peaks position to the modes tabulated by IR and Raman spectroscopy (Table 8.1). Additionally, for comparison, we added to Fig. 8.10a the IR and Raman spectra of Alq₃ (Figs. 8.3 and 8.4). These spectra have been duplicated symmetrically for positive and negative bias since excitations can take place in both cases.

Tens of IETS curves measured in different Alq₃ based junctions have been analysed and compared to assign Alq₃ modes. This process must be extremely careful since each curve results from the sum of different contributions. First of all, the peak resolution is much lower that the one obtained by IR or Raman spectroscopy resulting in peaks enlarged in energy. Then, the peak intensity varies from one contact to the other since it represents the contribution of all the molecules involved in transport inside the junction. The number of probed molecules can vary in each device especially for the Co diffusion that modifies the probed Alq₃ thickness. Moreover,

Alq$_3$ is deposited in an amorphous layer resulting on a random disposition of molecules, while IETS technique is more sensitive to modes perpendicular to the current direction. Finally, some peaks can be also due to defects or charge traps inside the barrier, making the interpretation even more difficult. In Fig. 8.10a we assigned only the peaks that could be observed in all the analysed junctions and that we concluded to be related to the Alq$_3$ vibrations.

In order to illustrate that IETS is a powerful tool to discriminate between spin injection into the organic layer and a short-circuited contact, in Fig. 8.10a we also report the IETS spectrum (dark red curve) of another Co/Al$_2$O$_3$/Alq$_3$/Co contact that we name "Sample 2". Sample 1 and Sample 2 present the same structure and they have been grown exactly under the same conditions since they come from the same wafer. The MR curve measured in Sample 2 at low temperature is shown in Fig. 8.10d, while in Fig. 8.10c, b are respectively reported the MR curves measured in Sample 1 and in a Co/Al$_2$O$_3$/Co junction under the same conditions. No substantial difference can be detected between MR curves of Sample 1 and Sample 2 and they also present a similar contact resistance in the 100 MΩ range. Nevertheless, if we look at the IETS spectrum of Sample 2 we discover that none of the peaks corresponding to molecular vibrations appear and the curve is almost flat as the one of Co/Al$_2$O$_3$/Co junction. Only one peak can be observed at an energy around -260 mV but this is probably due to some surface contamination or charge trapping since it is visible for both samples but it does not correspond to any Alq$_3$ tabulated vibrational mode. From these observations we can conclude that what we are measuring in Sample 2 is the equivalent of a Co/TB/Co MTJ due to a short-circuit through the organic layer (case of Fig. 8.9b). From a rapid calculation comparing the resistance of this short-circuited contact to the one of the Co/Al$_2$O$_3$/Co junction (Fig. 8.10b), we can estimate that the equivalent area of this junction is about $1 \times 1\,\mu m^2$.

In conclusion, with these experimental results we want to highlight the importance to be extremely careful when interpreting the MR results in such devices since it can be easily confused to the one of an equivalent oxide TB. Moreover, we also demonstrated that the observation of a MR signal, the high contact resistance and its scalability with the organic barrier thickness are not enough to distinguish a short-circuited contact to one where spin is really injected in the organic layer. In this scenario, IETS technique results to be a very useful (or indispensable) characterization tool.

## 8.4 Spin Polarization Properties of Co/Alq$_3$/Co Organic Spin Valves

After having shown very successful and reproducible spin injection at room temperature in Co/TB/Alq$_3$/Co spin valves and having verified that the signal is really coming from transport through the organic layer, here we will discuss the spin injection in "pure" Co/Alq$_3$/Co devices.

This kind of junctions present less homogeneous results than the previous ones probably due to the higher difficulty to obtain well defined interfaces. Between the contacts that gave a measurable signal we can distinguish two categories. The first one represents almost 47 % of these contacts and it consists in junctions where a strong resistance increase with decreasing temperature is observed, compatible with charge transport through the organic semiconductor. The second category is formed by the other 53 % of contacts that present a weak change of their resistance with temperature, probably due to some Co atom diffusion inside the barrier which makes the probed Alq₃ thickness thinner than the nominal value, eventually leading to tunnel behaviour. In addition to these samples there are many others that are already too much resistive at room temperature.

Junctions with Expected OSV Behaviour

First of all we will start by considering the first category of samples since their temperature behaviour corresponds to the one expected in OSVs. Their resistance strongly increases at low temperature, reaching the GΩ range. Contrarily to the curves recorded in the junctions showed before, in Co/Alq₃/Co devices we could observe both positive and negative MR effect and often the signal changed sign with the applied bias. One example is reported in Fig. 8.11 where MR curves recorded at ±100 mV for the same junction are shown. A MR inversion with bias voltage was already reported in the literature by Vinzelberg et al. [16] who observed this phenomenon in some LSMO/Alq₃/Co OSVs.

Moreover, in about 60 % of the junctions a gap could be observed in the IV characteristic at low bias and low temperature. In Fig. 8.12 are shown examples of IV characteristics for junctions presenting a classical non linear behaviour (Fig. 8.12a) and the ones presenting a gap at low bias that typically reaches values of 100–200 mV (Fig. 8.12b). Both kind of junctions present similar MR results and sign inversion with bias voltage.
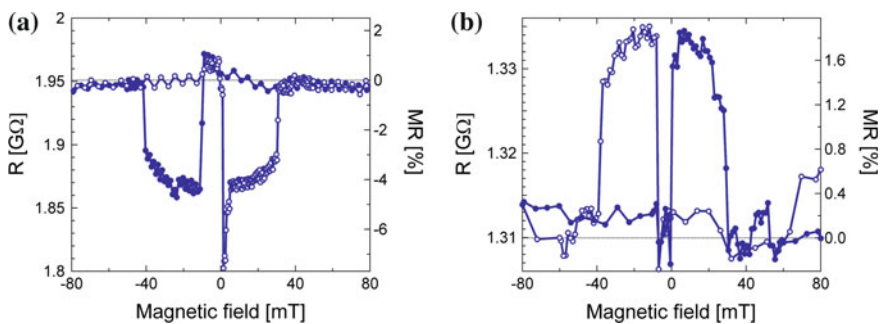
Fig. 8.11 MR curves recorded at 2 K in a Co/Alq₃(20 nm)/Co OSV that presents the expected resistance behaviour for transport through an OSC. MR changes sign with applied bias voltage: **a** V = 100 mV. **b** V = −100 mV
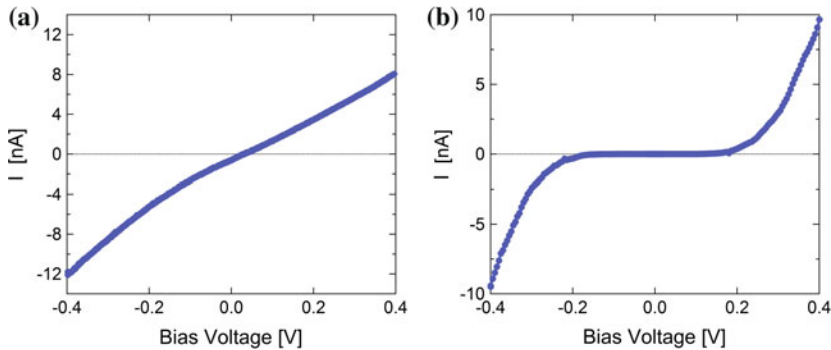
Fig. 8.12   a IV characteristic measured at 2 K in a Co/Alq$_3$(12 nm)/Co OSV that presents a classical non linear behaviour. **b** IV characteristic measured at 2 K in a Co/Alq$_3$(12 nm)/Co OSV that presents a gap at low bias voltage and low temperature. For both junctions resistance strongly increases with decreasing temperature

While most of the results reported in the literature present a resistance behaviour compatible with tunnel transport inside the junction, the MR observed in these devices, even if it is only at low temperature, is very promising since it could indicate a possible spin transport through the organic layer. Nevertheless, we have to point out that signals in these junctions are often noisy and difficult to measure due to the high resistance, thus making their study very difficult. For this reason in the following we will focus on the second category of contacts.

Junctions with a Tunnel Like Behaviour

This second category of junctions presents a weak resistance dependence with temperature, hence we can consider them as Co/Alq$_3$/Co MTJs with an estimated Alq$_3$ thickness of just few nm instead of tens of nm. Their study is very useful since they present a measurable MR signal at low temperature and even room temperature, and the low Alq$_3$ thickness allows to focus on the interface properties of the devices.

As shown in Fig. 8.13, a MR signal at room temperature could be also observed in these junctions. This is a very promising result since the reports of room temperature MR effects in FM/organic/FM devices are still very limited in organic spintronics [17]. Moreover, the amplitude of -4% MR represents the highest value obtained until now at 300 K in a device without any tunnel barrier.

As in the case of large resistance devices, we could observe in these MTJs a large range of results with MR signals that present a positive, negative, or change sign with the applied bias. For example, in Fig. 8.14 are shown MR curves where the sign is inverted when applying a different bias voltage on the junction.

In order to enlighten the origin of this spin polarization inversion and to investigate the different contribution of top and bottom interface hybridization on the spintronic properties of these devices, we compared these results to junctions where one of the two interfaces has been decoupled by the insertion of a tunnel barrier.
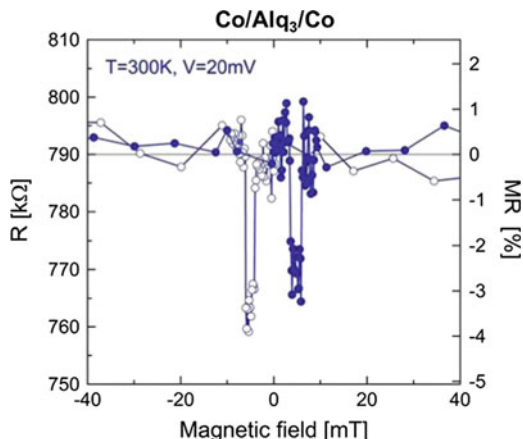
Fig. 8.13 Room temperature MR signal recorded at 20 mV in a Co/Alq₃(12 nm)/Co OSV where the resistance behaviour with temperature is compatible with the one of a tunnel junction
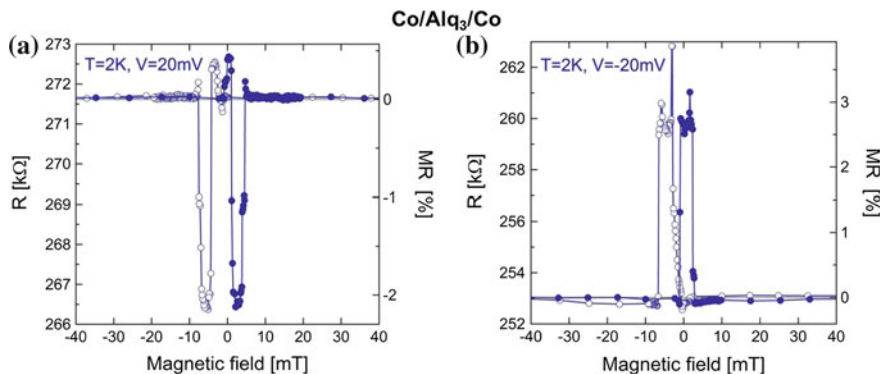
Fig. 8.14 Example of MR signal recorded at 2 K for a same Co/Alq₃(12 nm)/Co contact whose resistance behaviour with temperature is compatible with the one of a tunnel junction. **a** V = 20 mV. **b** V = −20 mV. MR signal changes sign depending on the applied bias voltage

8.4.1 Interfaces Influence on the MR Sign

The importance of interface ferromagnetic metal/molecule hybridization on the spin polarization properties of a device has been already discussed in Sect. 3.2.1. We saw that the spin polarization on an interface can be enhanced or inverted depending on the FM metal/molecule coupling. In order to investigate the different role of the top and bottom interface we decoupled one of them with the insertion of a tunnel barrier to analyse the effects of the other one.

Tunnel Barrier at the Bottom Interface

The insertion of a tunnel barrier between the bottom electrode and the organic layer allowed to study the properties of the top Alq$_3$/Co interface. As already shown in Figs. 8.7 and 8.8, in this kind of devices a positive and very stable MR signal was always observed at low bias. This result suggests that the MR inversion often observed in Co/Alq$_3$/Co junctions is not due to the top interface. Hence, we can conclude that the top Alq$_3$/Co interface has a positive spin polarization, whereas an inversion occurs at the bottom one. The coupling between the molecular levels and top electrode is weak at this interface and a small variation on level position does not impact on spin polarization sign, explaining why observed MR signal is always positive at low bias.

Tunnel Barrier at the Top Interface

In order to investigate the properties of the bottom interface we fabricated Co/Alq$_3$/TB/Co OSVs. In this kind of devices we could observe the whole range of results observed in Co/Alq$_3$/Co junctions where MR signal can be positive, negative, or change sign with bias voltage. An example of negative MR curve observed in a Co/Alq$_3$/TB/Co junction is shown in Fig. 8.15a, while an example of a positive one recorded at room temperature in a different contact is shown in Fig. 8.15b.

These results point out that the bottom interface is much more sensitive to spin-dependent hybridization than the top one. We have to remark that the MR sign inversion often observed in our large area devices is scarcely reported in the literature [16]. This could be ascribed to a different alignment and coupling at the Co/Alq$_3$ interface in comparison to LSMO/Alq$_3$ one where a negative MR is almost always observed, or to Fe/Alq$_3$ interface where a positive MR is reported in Fe/Alq$_3$/Co junctions. Indeed, MR inversion suggests that bottom Co/Alq$_3$ interface is very sensitive to levels alignment and molecular levels are probably almost resonant to the
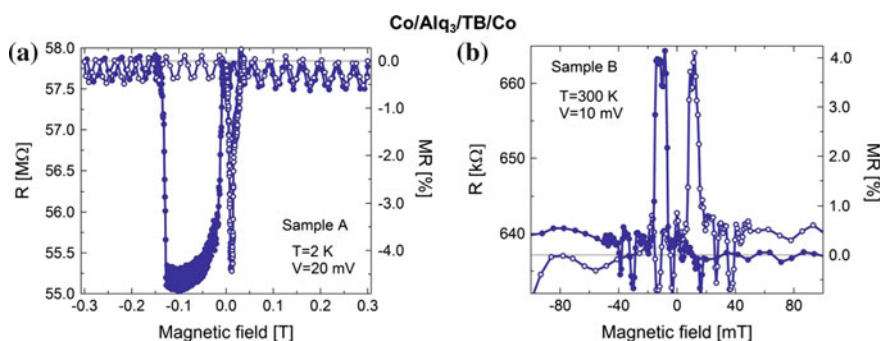
Fig. 8.15 **a** Example of negative MR signal observed in a Co/Alq$_3$(20 nm)/MgO(2 nm)/Co OSV at 20 mV and 2 K. IETS measurement were made to prove that the junction was not short-circuited. **b** Example of positive MR signal detected in another Co/Alq$_3$(12 nm)/MgO(2 nm)/Co OSV measured at 10 mV and 300 K

Co Fermi energy of the bottom electrode. In these conditions a little energy shift has dramatic effects on the spin polarization sign of this interface.

8.4.1.1 Summary of the Section

To summarize, from these observations we demonstrated that the top Alq_3/Co interface is always positive, confirming the previous reports [4, 5, 18]. Moreover, we also proved that *the most "active" interface for what concerns spin polarization tailoring is the bottom one*. This could be explained with the hypothesis that deposed molecules are more strongly coupled to the bottom interface than the top one, thus resulting in a possible spin polarization inversion. A schematic representation of this situation is summarized in Fig. 8.16. From these experiments it becomes also clear how the *direct coupling* between the bottom electrode and the molecular layer is fundamental to be able to exploit the tailoring opportunities of organic materials and engineer the spin polarization properties of spintronic devices.

8.4.2 Magnetoresistance Inversion with Bias Voltage

In the previous sections we have explained qualitatively the MR behaviour observed in Co/Alq_3/Co junctions. In an effort to investigate more in detail the relevant parameters behind these different MR behaviours, we have tried to extract parameters from a simple spin dependent model. We intentionally focused on the simplest samples where transport properties could be fitted without involving too many parameters as the real thickness of Alq_3 was small enough to consider a tunnel regime. In this case the two interfaces merge and the model presented above (and in Sect. 3.2.1) is reduced to a single level transport in the tunneling regime.
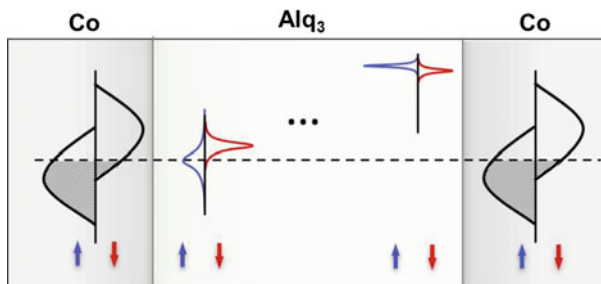
Fig. 8.16 Summary of the level alignment at the two interfaces in a Co/Alq_3/Co junction estimated by previous investigation in devices where a TB was inserted. From these observations it becomes clear the important role played by the bottom interface where a small variation of levels alignment can lead to a change of the spin polarization. On the contrary, molecular levels at the top interface, since less coupled, do not impact on spin polarization sign

With these approximations, we used a spin dependent adaptation of an unidimensional model based on the single molecular level coherent transport model described in Sect. 4.3.1.[1] According to spinterface model described in Sect. 3.2.1, in an organic system we also have to take into account the characteristic metal/molecule hybridization at the interfaces which creates a spin dependent shift and broadening of the molecular level. With these considerations, we can describe the current flowing through the barrier using a modified Eq. 4.17 where the contributions of spin ↑ and ↓ at the interfaces are also taken into account:

$$I_{\uparrow\uparrow(\downarrow\downarrow)}(V) \simeq \frac{4\Gamma_{L\uparrow(\downarrow)}\Gamma_{R\uparrow(\downarrow)}}{\Gamma_{L\uparrow(\downarrow)} + \Gamma_{R\uparrow(\downarrow)}} \left\{ \arctan\left(\frac{V - 2(\varepsilon_0 + \delta\varepsilon_{L\uparrow(\downarrow)} + \delta\varepsilon_{R\uparrow(\downarrow)}) - 2V\eta}{\Gamma_{L\uparrow(\downarrow)} + \Gamma_{R\uparrow(\downarrow)}}\right) \right.$$
$$\left. + \arctan\left(\frac{V + 2(\varepsilon_0 + \delta\varepsilon_{L\uparrow(\downarrow)} + \delta\varepsilon_{R\uparrow(\downarrow)}) + 2V\eta}{\Gamma_{L\uparrow(\downarrow)} + \Gamma_{R\uparrow(\downarrow)}}\right) \right\}$$

(8.1)

where ε_0 is the energy level position and $\delta\varepsilon_{L\uparrow(\downarrow)} = +(-)\frac{\delta\varepsilon_L[1+(-)P_L]}{2}$, $\delta\varepsilon_{R\uparrow(\downarrow)} = +(-)\frac{\delta\varepsilon_R[1+(-)P_R]}{2}$ are the spin dependent shift contributions at the left (L) and right (R) interface to the position of ε_0. $\Gamma_{L\uparrow(\downarrow)} = \frac{\Gamma_L[1+(-)P_L]}{2}$, $\Gamma_{R\uparrow(\downarrow)} = \frac{\Gamma_R[1+(-)P_R]}{2}$ are the contributions to level broadening at left (L) and right (R) interface and P_L, P_R are the spin polarizations of the electrodes. Spin polarization influences $\delta\varepsilon_{L(R)\uparrow(\downarrow)}$ and $\Gamma_{L(R)\uparrow(\downarrow)}$ to take into account the effective polarization of the interfaces. Finally, η is the position of the level inside the organic barrier and takes into account the different weight of left and right electrode on the molecular level. The value of this parameter ranges between $-0.5 < \eta < 0.5$ and $\eta = 0$ means that the level is in the middle of the barrier and left and right electrodes have the same contribution on the bias drop.

Using Eq. 8.1 we can calculate the current in the parallel ($I_{\uparrow\uparrow} + I_{\downarrow\downarrow}$) and antiparallel ($I_{\uparrow\downarrow} + I_{\downarrow\uparrow}$) configuration of the system and, substituting it in Eq. 1.5, we obtain MR as:

$$MR = \frac{I_P - I_{AP}}{I_{AP}} = \frac{(I_{\uparrow\uparrow} + I_{\downarrow\downarrow}) - (I_{\uparrow\downarrow} + I_{\downarrow\uparrow})}{(I_{\uparrow\downarrow} + I_{\downarrow\uparrow})}$$

(8.2)

In Fig. 8.17 are shown examples of MR behaviours with bias voltage measured in two different Co/Alq₃/Co junctions presenting a tunnel characteristic with temperature and that we considered could correspond to our approximation. More complex features were also observed in other junctions but in that case the modelization becomes too difficult (already in the simplest case it depends on 8 parameters) and fits would probably become not significant.

In the first example shown in Fig. 8.17a we observe an inversion of MR sign with bias voltage. The fit curve obtained by Eq. 8.2 is shown in red. To simplify the fit we fixed both Co electrode spin polarizations to a value of 0.40 but similar results were also obtained by slightly tuning this value. A first observation that we can point out from fit parameters is the small value of $\varepsilon_0 = 71$ meV which indicates

---

[1]The results of this model are similar to the resonant tunneling inversion that was introduced for inorganic semiconductor MTJs [19, 20].
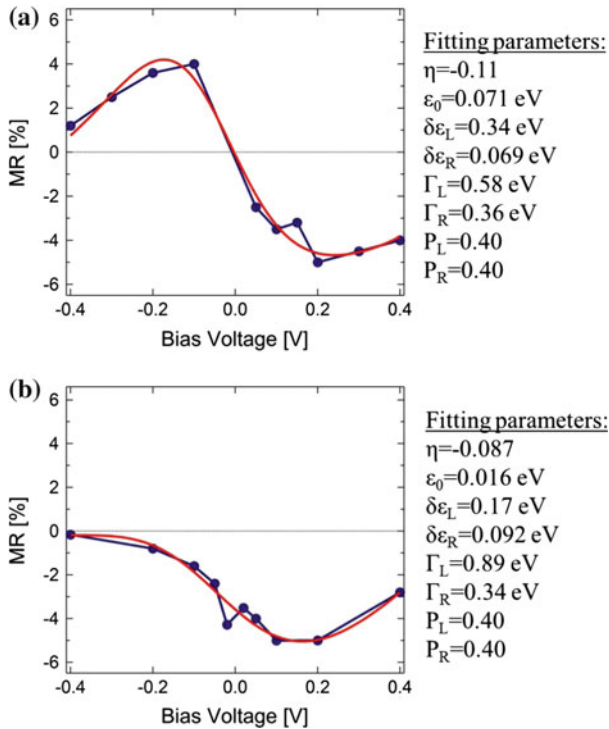
Fig. 8.17 a, b Examples of MR versus bias voltage characteristics for two different Co/Alq₃/Co OSVs which present a tunnel behaviour with temperature. Experimental data (*blue*) and fit (*red*) obtained by Eq. 8.2 are shown. Fitting parameters obtained for each curve are reported on the right. Electrodes spin polarization $P_{L(R)}$ has been fixed to 0.40 to simplify the fitting

that the molecular level is close to the Fermi energy. This observation is particularly interesting since it seems to confirm the assumption made in the previous section where we ascribed the MR inversion to a situation similar to the one described by Fig. 3.5b in the spinterface model which predicts a position of the molecular level close to the Fermi energy and a large broadening Γ of the level that we also find in this fit ($\Gamma \sim 360 - 580$ meV). Finally, we can also observe by the fit parameters that the junction is not symmetric but it seems that the molecular level is more coupled to the left electrode. This results in a larger shift of the level ($\delta\varepsilon_L > \delta\varepsilon_R$), a larger broadening ($\Gamma_L > \Gamma_R$) and a parameter $\eta = -0.11$. This also seems to confirm the situation estimated in Fig. 8.16 where we consider that the molecular levels are more strongly coupled to one of the two electrodes, the bottom one.

We now focus on the second MR versus bias behaviour reported in Fig. 8.17b. As one can note, in this case the MR signal does not change its sign but it is negative for every bias voltage. What we would expect according to predictions of spinterface model (Fig. 3.5b) would be an even closer position of the molecular level to the Fermi level and thus stronger coupling at the interfaces. Again, we fitted this curve using

Eq. 8.2 and fixed the spin polarization of the two electrodes $P_L = P_R = 0.40$ to simplify the system. As one can see in the picture, the fitting parameters obtained go exactly in the expected direction: the energy position of the molecular level is even closer to the Fermi level ($\varepsilon_0 = 16\,\text{meV}$) and the molecular level has a much larger broadening ($\Gamma_L = 890\,\text{meV}$) at one of the two interfaces. The always negative MR behaviour could be thus explained by a stronger interaction of the molecular level with the bottom electrode than in the case shown in Fig. 8.17a.

The coherence of these results with predictions made by spinterface model (see Sect. 3.2.1) looks encouraging to improve the understanding of interfacial properties of these systems. Nevertheless, we have to recall that the considered model is an extreme simplification of the complex real OSV. For example, we considered the presence of a single molecular level while we should have taken into account the fact that a distribution of many more levels may contribute in parallel at the interface (depending on the device area) and this probably contributes to the level broadening. Finally, we considered a tunnel behaviour where just merged spin injection/detection plays a role. If we would consider spin transport through the organic barrier, the system would quickly become way too complicated to describe.

8.4.3 TAMR Effects in Alq$_3$ Based OSVs

To make things even more complicated, an effect of Tunneling Anisotropic Magnetoresistance (TAMR) that goes to add to the total MR signal could be also observed in our Co/Alq$_3$/Co devices. It is interesting to analyse more in details this effect in order to better understand all the contributions that can play a role in the observed MR signal. Until now only one work reported in the literature the investigation of TAMR in Alq$_3$ based OSVs (LSMO/Alq$_3$/Co) [9].

TAMR origin stems from the fact that the density of states in strongly spin-orbit coupled materials is anisotropic with respect to the orientation of their magnetization. For this reason TAMR occurs when charge carriers tunnel from a ferromagnetic material with crystalline anisotropy in the presence of spin-orbit coupling. This effect can be observed in structures with only one ferromagnetic layer, it can be either positive or negative in amplitude and it depends on the exact orientation of the magnetization in the ferromagnetic layer [21].

In a standard device with no TAMR effect, the resistance when applying a magnetic field large enough to saturate electrode magnetization ($R_\parallel$) does not change with the electrode magnetization direction ($R_\parallel(\theta) = \text{const}$). This is not the case for a device where TAMR is observed. In Fig. 8.18 is represented the typical behaviour of this kind of devices. As one can see, two resistance states appear ($R_\parallel$ and $R_\perp$) corresponding to a parallel and orthogonal magnetization to the magnetic field. When turning the sample by 90° the starting situation becomes inverted and the TAMR spin-valve-like signal is also inverted.
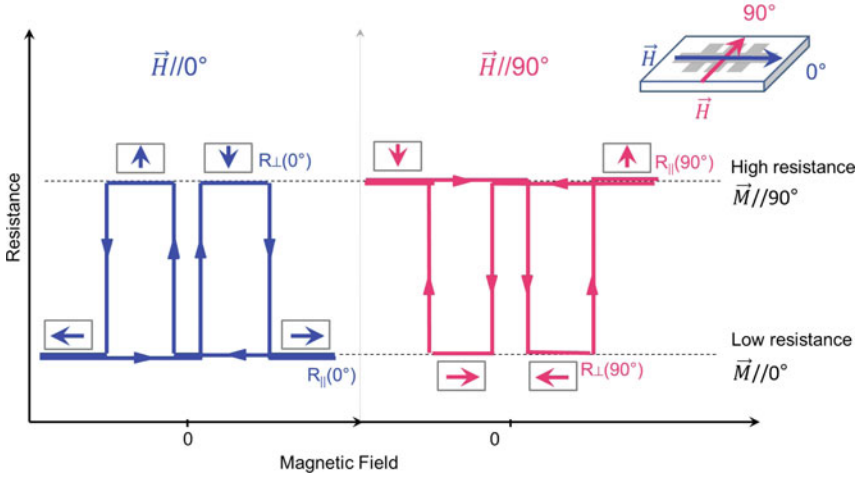
Fig. 8.18 Schematic representation of a typical TAMR curve in a device with only one ferromagnetic electrode and a biaxial anistropy. The device presents two resistance states for a parallel or orthogonal orientation of the applied magnetic field to electrodes magnetization. This results in an inversion of TAMR effect when turning the sample of 90°. *On the top* schematic representation of the measurement geometry. $\theta = 0°$ is considered when the external magnetic field is applied parallel to the easy axis of the bottom electrode

The TAMR contribution is added to the total MR signal and it is difficult to separate both. In devices with a large tunnel barrier height (up to eV) this effect can not be observed since the small energy shift of the chemical potential ($\delta\mu \sim 1$ meV) that occurs when changing the orientation of electrode magnetization is negligible in front of the barrier height and the effect is too small to be detected. On the contrary, in our devices the molecular levels are almost resonant with the Fermi level of the electrode and the small energy shift can produce a significant effect on the observed MR (Fig. 8.16).

One example is shown in Fig. 8.19a where MR curves are recorded at 100 mV and for two direction fields (0° and 90°). TAMR effect induces a shift of ~ 0.1 MΩ in R$_\parallel$ when changing the orientation of the external magnetic field. Since TAMR effect is smaller than the real spin-valve effect of the device, the observed MR signal often does not change the sign for the two orientations.

The MR behaviour with bias voltage is also shown in Fig. 8.19b and it is compared with the TAMR$_{angle}$ signal deduced in the device. This last is calculated as: TAMR$_{angle} = \frac{R_\parallel(0°) - R_\parallel(90°)}{R_\parallel(0°)}$ and MR for a given angle is $MR = \frac{R_{AP}(\theta) - R_P(\theta)}{R_P(\theta)}$. As one can note, the TAMR contribution in our device is one order of magnitude smaller than the spin-valve MR effect.

In order to investigate the origin of the TAMR effect in these contacts we also studied the angle behaviour of MR signal in devices where a tunnel barrier is inserted at one of the two interfaces. In Fig. 8.20a are reported MR signals recorded in a
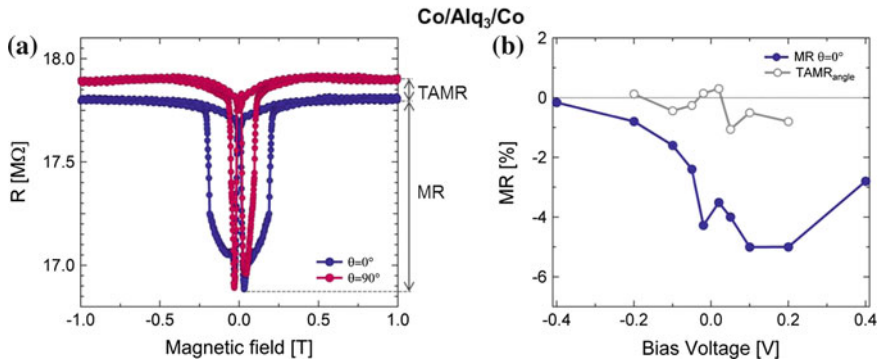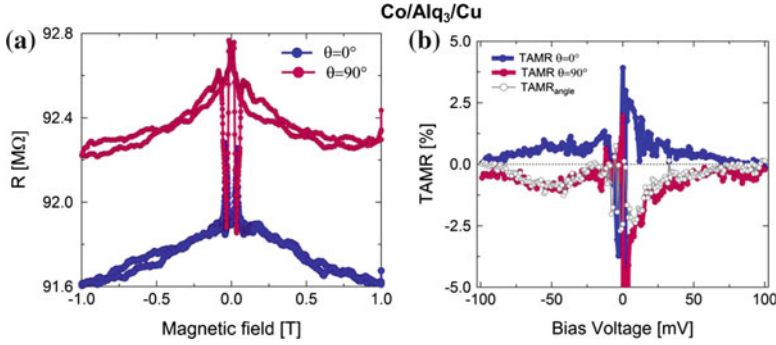
Fig. 8.19 a MR curves recorded at 100 mV and 2 K in a Co/Alq$_3$(20 nm)/Co OSV for two different orientations of the external magnetic field: parallel to the bottom electrode ($\theta = 0°$) and perpendicular to it ($\theta = 90°$). The shift of the saturated resistance at high magnetic field is due to a TAMR effect contribution. **b** MR behaviour of bias voltage at $\theta = 0°$ (*blue curve*) and TAMR$_{angle}$ contribution to the MR effect with bias voltage (*gray curve*). This contribution is one order of magnitude smaller than the MR effect
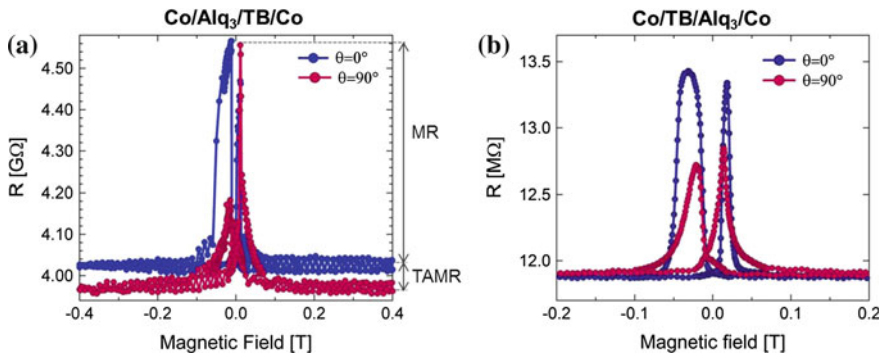
Fig. 8.20 MR curves recorded at 100 mV and 2 K in **a** a Co/Alq$_3$(12 nm)/TB/Co OSV and **b** a Co/TB/Alq$_3$(20 nm)/Co OSV for two different orientations of the external magnetic field: parallel to the bottom electrode ($\theta = 0°$) and perpendicular to it ($\theta = 90°$). **a** The shift of the saturated resistance at high magnetic field is due to a TAMR contribution to the total MR. **b** No shift can be detected for the saturated resistance at high magnetic field in the two angles. No TAMR contribution to the total MR effect can be observed in this case

Co/Alq$_3$/TB/Co for a same bias at $\theta = 0°$ and $\theta = 90°$. As one can see, a shift of R$_\parallel$(400 mT) ($\sim$1 %) can be again observed. On the contrary, in Fig. 8.20b are reported MR curves recorded in a Co/TB/Alq$_3$/Co for the two angle orientations. In this case no difference in the saturated resistances (R$_\parallel$(200 mT)) can be observed. These considerations suggest that the origin of the TAMR effect can be attributed to the bottom electrode.

Finally, in order to verify this assumption we also realized Co/Alq$_3$/Cu devices with only one FM electrode at the bottom interface. A typical TAMR signal could be

Fig. 8.21 a TAMR curves recorded at −10 mV and 2 K in a Co/Alq₃(20 nm)/Cu structure for two different orientations of the external magnetic field: parallel to the bottom electrode ($\theta = 0°$) and perpendicular to it ($\theta = 90°$). The device presents only one FM electrode and the spin-valve-like effect observed is pure TAMR which presents the typical inversion for parallel and orthogonal configurations (Fig. 8.18). **b** TAMR behaviour with bias voltage at $\theta = 0°$ (*red curve*) and $\theta = 90°$ (*blue curve*) showing the typical inversion. TAMR$_{angle}$ contribution is also calculated and it perfectly matches with the TAMR curve meaning that the effect observed is totally due to TAMR effects

detected in these devices, as one can see in Fig. 8.21a where TAMR curves recorded at 0° and 90° are compared showing the typical inversion (as shown in the schematic representation of Fig. 8.18). In Fig. 8.21b TAMR behaviour with bias voltage recorded at 0° and 90° are also reported (where TAMR$(\theta) = \frac{R_\perp(\theta) - R_\parallel(\theta)}{R_\parallel(\theta)}$) and one can clearly observe the symmetric inversion of the TAMR sign in the two configurations. The TAMR$_{angle}$ behaviour calculated as before is also shown and it perfectly matches with the TAMR curve, proving that the measured signal is pure TAMR effect.

In conclusion, in these experiments we observed a TAMR signal contribution in Co/Alq₃/Co and Co/Alq₃/TB/Co devices. With the observation of TAMR effects in Co/Alq₃/Cu devices we could definitely prove that TAMR contribution comes from the bottom electrode. The observation of a quite large TAMR effect (up to ∼3 %) also confirms the estimated molecular level position at the bottom interface close to the Fermi energy. This situation is schematically represented in Fig. 8.22a where it can be seen that even a small energy shift of the chemical potential $\delta\mu$ of the electrode, which depends on magnetization orientation, can have a strong influence on the spin polarization properties of this interface.[2] This overall picture is supported by the absence of observable TAMR effects in devices where only the top interface was investigated which confirms that the level position in this case is far from the Fermi level and energy shift has negligible effects on the spin polarization properties of this interface (Fig. 8.22b). This contributes to confirm the estimations previously made by the study of MR signal and summarized in Fig. 8.16.

---

[2]For a more complete picture, one would have to consider that coupling strength of different orbitals will also be magnetization orientation dependent.
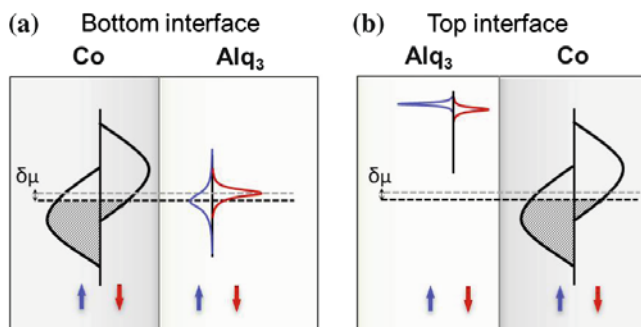
Fig. 8.22 a Schematic representation of TAMR effect at the bottom interface. The molecular level is close to the Fermi level and a little shift $\delta\mu$ has a strong influence on the spin polarization properties of this interface. **b** Schematic representation of the estimated situation at the top interface. Molecular level is far from the Fermi energy and a little shift has no influence on its spin polarization properties. This would explain the absence of TAMR effect in $Co/TB/Alq_3/Co$ devices

8.5 Conclusions

With these experiments we demonstrated that very interesting properties for spin polarization inversion lie in the strongly coupled (here bottom) interface. That is why, despite most of the results of MR signal at room temperature have relied on the insertion of an oxide barrier at the bottom interface, it will be a key issue to be able to get rid of it if one wants to exploit and unleash the tailoring potential offered by molecules. In this regard, our preliminary observation of MR effects at room temperature in $Co/Alq_3/Co$ OSVs is very encouraging towards this direction.

References

1. V.A. Dediu, L.E. Hueso, I. Bergenti, A. Riminucci, F. Borgatti, P. Graziosi, C. Newby, F. Casoli, M.P. De Jong, C. Taliani, Y. Zhan, Room-temperature spintronic effects in Alq_3-based hybrid devices. Phys. Rev. B **78**, 115203 (2008)
2. S. Wang, Y.J. Shi, L. Lin, B.B. Chen, F.J. Yue, J. Du, H.F. Ding, F.M. Zhang, D. Wu, Room-temperature spin valve effects in $La_{0.67}Sr_{0.33}MnO_3/Alq_3/Co$ devices. Synth. Met. **161**, 1738–1741 (2011)
3. Y. Liu, T. Lee, H.E. Katz, D.H. Reich, Effects of carrier mobility and morphology in organic semiconductor spin valves. J. Appl. Phys. **105**, 07C708 (2009)
4. T.S. Santos, J.S. Lee, P. Migdal, I.C. Lekshmi, B. Satpati, J.S. Moodera, Room-temperature tunnel magnetoresistance and spin-polarized tunneling through an organic semiconductor barrier. Phys. Rev. Lett. **98**, 016601 (2007)
5. G. Szulczewski, H. Tokuc, K. Oguz, J.M.D. Coey, Magnetoresistance in magnetic tunnel junctions with an organic barrier and an MgO spin filter. Appl. Phys. Lett. **95**, 202506 (2009)
6. Y. Sakurai, Y. Hosoi, H. Ishii, Y. Ouchi, G. Salvan, A. Kobitski, T.U. Kampen, D.R.T. Zahn, K. Seki, Study of the interaction of tris-(8-hydroxyquinoline) aluminum (Alq_3) with potassium

using vibrational spectroscopy: examination of possible isomerization upon K doping. J. Appl. Phys. **96**, 5534 (2004)

7. R.J. Davis, J.E. Pemberton, Surface Raman spectroscopy of the interface of tris-(8-hydroxyquinoline) aluminum with Mg. J. Am. Chem. Soc. **131**(29), 10009–10014 (2009)

8. Z.H. Xiong, D. Wu, Z.V. Vardeny, J. Shi, Giant magnetoresistance in organic spin-valves. Nature **427**, 821–824 (2004)

9. M. Grünewald, R. Göckeritz, N. Homonnay, F. Würthner, L.W. Molenkamp, G. Schmidt, Vertical organic spin valves in perpendicular magnetic fields. Phys. Rev. B **88**, 085319 (2013)

10. A. Riminucci, M. Prezioso, C. Pernechele, P. Graziosi, I. Bergenti, R. Cecchini, M. Calbucci, M. Solzi, V.A. Dediu, Hanle effect missing in a prototypical organic spintronic device. Appl. Phys. Lett. **102**, 92407 (2013)

11. Z.G. Yu, Suppression of the Hanle effect in organic spintronic devices. Phys. Rev. Lett. **111**, 016601 (2013)

12. J.G. Kushmerick, J. Lazorcik, C.H. Patterson, R. Shashidhar, D.S. Seferos, G.C. Bazan, Vibronic contributions to charge transport across molecular junctions. Nano Lett. **4**, 639–642 (2004)

13. W. Wang, Electrical characterization of self-assembled monolayers. Ph.D. thesis, Yale University (2004)

14. K.-S. Li, Y.-M. Chang, S. Agilan, J.-Y. Hong, J.-C. Tai, W.-C. Chiang, K. Fukutani, P.A. Dowben, M.-T. Lin, Organic spin valves with inelastic tunneling characteristics. Phys. Rev. B **83**, 172404 (2011)

15. K.V. Raman, Spin injection and manipulation in organic semiconductors. Ph.D. thesis, MIT (2011)

16. H. Vinzelberg, J. Schumann, D. Elefant, R.B. Gangineni, J. Thomas, B. Büchner, Low temperature tunneling magnetoresistance on (La, Sr)MnO₃/Co junctions with organic spacer layers. J. Appl. Phys. **103**, 93720 (2008)

17. M. Palosse, Élaboration et étude de vannes de spin organiques: vers le transport de spin à température ambiante. Ph.D. thesis, Université de Toulouse (2013)

18. J.J.H.M. Schoonus, P.G.E. Lumens, W. Wagemans, J.T. Kohlhepp, P.A. Bobbert, H.J.M. Swagten, B. Koopmans, Magnetoresistance in hybrid organic spin valves at the onset of multiple-step tunneling. Phys. Rev. Lett. **103**, 146601 (2009)

19. E.Y. Tsymbal, A. Sokolov, I.F. Sabirianov, B. Doudin, Resonant inversion of tunneling magnetoresistance. Phys. Rev. Lett. **90**(18), 186602 (2003)

20. V. Garcia, H. Jaffrès, J.-M. George, M. Marangolo, M. Eddrief, V. Etgens, Spectroscopic measurement of spin-dependent resonant tunneling through a 3d disorder: the case of MnAs/GaAs/MnAs junctions. Phys. Rev. Lett. **97**, 246802 (2006)

21. C. Gould, C. Rüster, T. Jungwirth, E. Girgis, G.M. Schott, R. Giraud, K. Brunner, G. Schmidt, L.W. Molenkamp, Tunneling anisotropic magnetoresistance: a spin-valve-like tunnel magnetoresistance using a single magnetic layer. Phys. Rev. Lett. **93**, 117203 (2004)

Conclusions

The work of this thesis has been mainly inspired by the fascinating opportunities pre-
dicted and offered by the spin dependent metal/molecule hybridization (now coined
as spinterface), also aiming to foresee the development of future possible applica-
tions. In this regard, two different topics were treated during my PhD.

The first experimental part concerns the study and development of SAMs-based
magnetic tunnel nanojunctions. This work aims at demonstrating the validity of these
systems for spintronics and, thanks to SAMs modularity, to set the basis towards the
future possibility to engineer at the molecular level the spin polarization properties
of these devices.

Thanks to the nanoindentation technique we could fabricate successful LSMO/
SAM/Co magnetic tunnel nanojunctions with an active area of about $20 \times 20 \, nm^2$.
Using dodecyl-phosphonic acids (C12P) SAMs as tunnel barrier we measured high
TMR signals up to 50 % at 2 K, showing a strong improvement in comparison to
results previously reported in the literature [1, 2].

We also observed a TMR signal up to 200 K and we correlated the decrease of TMR
signal for increasing temperature with the LSMO surface spin polarization drop. This
is probably one of the main reasons which prevented us to observe a TMR effect
at room temperature and it is very encouraging for future improvements. Indeed, it
would be probably sufficient to replace LSMO with a metal which maintains its spin
polarization at room temperature to obtain TMR signal at 300 K.

An interesting observation in this kind of devices was also the flat TMR behav-
iour with bias voltage at T > 100 K. Despite the origin of this phenomenon remains
hypothetically attributed to vibrations, the stability of TMR effect at high temperature
represents another potential offered by organic materials.

But maybe the most striking and potentially applicable effect observed in this
system resulted to be the robustness of the TMR signal with bias voltage. TMR
values above 20 % could be observed at 4 V and $V_{1/2}$ parameter was found in the
voltage range for some junctions, comparable with best results in inorganic MTJs.

Finally, after having overcome all the technological barriers and having demon-
strated the feasibility to fabricate successful SAMs-based devices, we started to tune
the thickness of the aliphatic chain from 10 to 18 carbon atoms chain. First, the

observed exponential increase of device resistance with chain length described by a
decay coefficient $\beta \simeq 0.9 \,\text{Å}^{-1}$, is perfectly in line with results reported in the litera-
ture and allowed us to validate our system. Second, this represents a first step towards
the tailoring of the barrier properties. A TMR signal normally ranging between 30
and 50 % could be observed for all the chain lengths. Although no particular dif-
ference was reported between the different molecules tested, poorer results were
obtained with the longest C18P and shortest C10P chains, probably because worse
adapted to our measurement conditions.

An extremely high TMR signal above 260 % could be also recorded in a
LSMO/C14P/Co junction at low temperature. This result unveils once more the
strong potential of these systems for spintronics.

The second experimental part concerns the study of organic semiconductor spin-
tronic devices formed by standard materials as Co/Alq$_3$/Co OSVs. This, on one hand,
allowed us to investigate magneto-transport properties at room temperature using a
FM material as Co whose Curie temperature is well above 300 K. On the other hand,
we tried to improve the understanding of the two interfaces contributions on spin
polarization properties. Indeed, the comprehension of the role of each contribution
in these phenomena is extremely interesting for the future possibility to modulate
interfacial spin polarization exploiting the versatility of molecules.

In our study we adopted a systematic approach with the fabrication of Co/Alq$_3$(12–
20 nm)/Co OSVs of 50×50 and $100 \times 100 \ \mu\text{m}^2$ using an all in-situ technique by
shadow mask that allowed us to realize 140 junctions at the same time. The insertion
of a thin oxide tunnel barrier (Al$_2$O$_3$ or MgO) at the bottom or top interface was also
experimented to asses its influence in the device properties, as well as to separately
study the spin-polarization of the bottom and top interfaces.

In our investigation, first we statistically observed an increase in the number of
non short-circuited devices with the insertion of a tunnel barrier and in particular we
observed a decrease of resistance dispersion when the tunnel barrier was inserted at
the bottom interface.

Next, we used IETS measurements to investigate the spin injection into the organic
layer and we remarked the importance to be extremely careful when interpreting a
MR signal in OSVs where an oxide tunnel barrier is inserted. We demonstrated that
the most common arguments usually applied to exclude that observed MR signal is
not merely coming from the oxide barrier, are often not enough. In this regard, we
highlighted IETS as one valid (if not indispensable) technique to prove the real spin
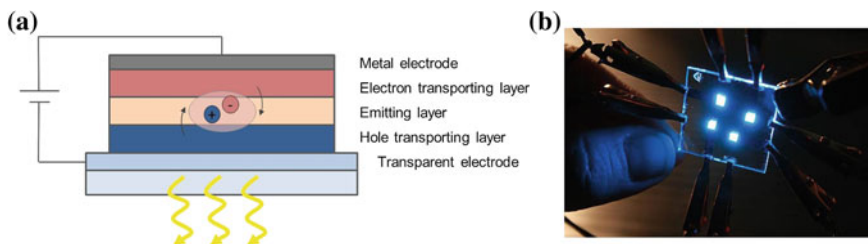injection into organic materials.

Moreover, we could report +8 and +4 % MR signal at room temperature respec-
tively in Co/MgO/Alq$_3$ (20 nm)/Co and Co/Al$_2$O$_3$/Alq$_3$ (20 nm)/Co OSVs after hav-
ing verified by IETS the real spin-injection into the organic layer. A signal of −4 %
MR at room temperature was also observed in a Co/Alq$_3$(12 nm)/Co OSV, represent-
ing the highest value reported until now in a FM metal/molecule/FM metal device
without the insertion of any oxide tunnel barrier. This represents a strong improve-
ment since room temperature MR signals for this kind of devices are still scarcely
reported in the literature.

Finally, we also investigated more in details the interfacial spin polarization properties of these devices. We could achieve that with the insertion of the oxide tunnel barrier at the bottom (top) interface to decouple it and study the properties of the top (bottom) one. It was previously shown that a weak coupling (occurring at the top interface) could lead to a spin polarization enhancement [3]. From these studies we found that a spin polarization inversion could also occur in our devices. Interestingly, we isolated the phenomenon and found that only the bottom interface would present a strong enough coupling to lead to this inversion. More importantly, this coupling was shown to be strong enough to persist even at room temperature, holding great promise for spinterface applications. In future works, the microscopic mechanisms behind the differences between these two interfaces will have to be studied and controlled. But we can see that the potential is already here.

Indeed, the main perspective of this work is to go towards the active control of interfacial properties for the future development of muntifunctional devices.

More in detail, for what concerns perspectives of SAMs studies on the short term, the next step will be to further tune the molecular barrier with the aim to investigate and optimize its properties. One first step could be the tailoring of the SAMs body with the introduction of aromatic rings into the aliphatic carbon chain. Indeed, it has been theoretically predicted [4, 5] that the introduction of localized states in the barrier could have a beneficial effect on the TMR signal. Another possible modification would be the tailoring of the molecular head to tune the level alignment and spinterface properties at the top electrode. Finally, the substitution of LSMO bottom electrode with a FM metal at room temperature could allow the observation of the TMR effect up to 300 K. This would also allow a larger choice of anchoring groups and thus the tuning of bottom interface metal/molecule hybridization would become possible. Essentially, almost unlimited tailoring opportunities can be envisaged and the improvement in the understanding and prediction of spinterface properties will be a strong support towards the optimization and customization of molecular spintronics device properties.

On the longer term, spin-dependent hybridization is expected to be used in the tailoring of the resistive and magnetoresistive response of spintronics devices using functional molecules. In these new crafted systems, a single multi-functional device could provide many spintronic functionalities. Indeed, spin-dependent broadening and shifting of the hybridized states could be tailored at will by molecular engineering and then tuned later on by external stimuli such as light, temperature, magnetic or electric field. Hence for example, with molecules such as di-azobenzenes, one could expect to switch the molecular conformation by light or electric field controlling the coupling strength (weak/strong) and hence the spinterface response. Similarly, with redox molecules, one could electrically charge or discharge a carrier from the interface to the molecule, shifting the levels and modifying the coupling of the spinterface. Finally, with molecules such as spin crossovers complexes one could achieve the spinterface tailoring in a multiple way, optically, electrically, magnetically or thermally.

(a)

Metal electrode
Electron transporting layer
Emitting layer
Hole transporting layer
Transparent electrode

(b)

Fig. 1 **a** Schematic representation of a classical OLED. It is formed by a vertical structure based on two metallic electrodes (cathode and anode) separated by an organic active layer. The cathode electrode is an electron injector, while the anode electrode is an hole injector and it is transparent to allow the light to exit. In the active layer electrons and holes recombine forming an electron-hole pair called exciton. The radiative recombination of excitons leads to light emission with a color depending on the HOMO-LUMO gap of the organic material. **b** Example of an OLED device

Moreover, one can also envision spinterface as a way to tailor and enhance the spin injection into devices such as transistors or OLEDs. This is one of the main directions for the development of Alq_3-based OSVs.

For example, due to selection laws, the radiative recombination efficiency of classical OLEDs (Fig. 1) is limited to 25 %. This because, depending on the spin of electron and holes, exciton can be either a singlet (spin $S = 0$) or a triplet (spin $S = 1$) but only single excitons (which are the 25 % of the total) decay emitting a photon, while triplet excitons decay non-radiatively. As proposed by Bergenti et al. [6], a solution to improve OLED efficiency would be the fabrication of spin-OLEDs. Indeed, the injection of spin polarized current in these devices could increase the singlet-to-triplet ratio and enhance their efficiency. The ability to fabricate large-area devices working at room temperature is hence essential for the development of these systems. Nevertheless, another main limitation is represented by the incompatibility between the voltage range where MR signal is observed in organic spintronic devices (generally behind 1 V), and the voltage range where OLEDs emit light ($\sim$10 V).

In this regard, the observation of robust MR signal up to 4 V in our SAMs-based MTJs is very promising. In SAMs based MTJs a bias in the 1 V range corresponds to an electric field of the order of $E = 10^9$ V m^{-1}. This in turn corresponds to 100–200 V for the average 100–200 nm spacer found in most of the organic semiconductor-based devices and then should be more than enough to inject spins into devices working in the 10 V range such as OLEDs. In this scenario, the implementation of a SAM spin injector layer in a spin-OLED represents a promising perspective and could be envisaged as a possible solution to spin injection problems in these devices.

References

1. J.R. Petta, S.K. Slater, D.C. Ralph, Spin-dependent transport in molecular tunnel junctions. Phys. Rev. Lett. **93**, 136601 (2004)
2. W. Wang, C.A. Richter, Spin-polarized inelastic electron tunneling spectroscopy of a molecular magnetic tunnel junction. Appl. Phys. Lett. **89**, 153105 (2006)
3. C. Barraud, P. Seneor, R. Mattana, S. Fusil, K. Bouzehouane, C. Deranlot, P. Graziosi, L. Hueso, I. Bergenti, V. Dediu, F. Petroff, A. Fert, Unravelling the role of the interface for spin injection into organic semiconductors. Nat. Phys. **6**, 615–620 (2010)
4. A.R. Rocha, V.M. García-Suárez, S.W. Bailey, C.J. Lambert, J. Ferrer, S. Sanvito, Towards molecular spintronics. Nat. Mater. **4**(4), 335–339 (2005)
5. A.R. Rocha, S. Sanvito, Resonant magnetoresistance in organic spin valves (invited). J. Appl. Phys. **101**(9), 09B102 (2007)
6. I. Bergenti, V. Dediu, E. Arisi, T. Mertelj, M. Murgia, A. Riminucci, G. Ruani, M. Solzi, C. Taliani, Spin polarised electrodes for organic light emitting diodes. Org. Electron. **5**, 309–314 (2004)